UNSTEADY MULTIPHASE FLOW MODELING OF IN-SITU AIR SPARGING SYSTEM IN A VARIABLY SATURATED SUBSURFACE ENVIRONMENT

A Thesis
Presented to
The Academic Faculty

By

Wonyong Jang

In Partial Fulfillment
Of the Requirements for the Degree
Doctor of Philosophy in Environmental Engineering
School of Civil and Environmental Engineering

Georgia Institute of Technology

December 2005

UNSTEADY MULTIPHASE FLOW MODELING OF IN-SITU AIR SPARGING SYSTEM IN A VARIABLY SATURATED SUBSURFACE ENVIRONMENT

Approved by:

Dr. Mustafa M. Aral, Advisor
School of Civil and Environmental Engineering
Georgia Institute of Technology

Dr. Spyros Pavlostathis
School of Civil and Environmental Engineering
Georgia Institute of Technology

Dr. Sotira Yiacoumi
School of Civil and Environmental Engineering
Georgia Institute of Technology

Dr. Ching-Hua Huang
School of Civil and Environmental Engineering
Georgia Institute of Technology

Dr. Turgay Uzer
School of Physics
Georgia Institute of Technology

Date Approved: 11/12/2005

To my parents and wife, for their guidance, support, and love.
Without these things this thesis could not have been possible.

ACKNOWLEDGMENTS

I would like to express my sincere gratitude and appreciation to my advisor Dr. Mustafa M. Aral for his invaluable guidance, continuous support, and patience throughout my studies. Without these, this thesis could never been made this far.

I would also like to thank my committee members: Dr. Spyros Pavlostathis, Dr. Sotira Yiacoumi, Dr. Ching-Hua Huang, and Dr. Turgay Uzer. Dr. Pavlostathis's expertise in microbiology and Dr. Yiacoumi's guidance in reaction processes were extremely valuable. Comments and suggestions of my committee members were indeed helpful in improving this thesis.

I acknowledge with gratitude the guidance and encouragement given by my professors from Korea Advanced Institute of Science and Technology, Dr. Ja-Kong Koo and Dr. Hang-Sik Shin.

I would like to express my gratitude to my undergraduate professors from Pusan National University, Dr. Ok-Hyun Park, Dr. Chang-Won Kim, Dr. Kwang-Joong Oh, Dr. Tae-Joo Park, and Dr. Dong-Yoon Kim. Their excellence in teaching had a great influence on me to pursue graduate studies in Environmental Engineering.

I also appreciate the friendship and support of Dr. Nam-Hoon Lee, Anyang University and my former colleagues, Dr. Chul-Hyo Lee and Dr. Kang-Pyo Lee.

I want to gratefully acknowledge my past and current MESL members, Dr. Chan-hee Park, Elcin, Kijin, Sinem, Scott, Jinjun, Recep, SoonChul, and Dr. Guan for their help and valuable comments.

Especially, I would like to give my special thanks to my wife Hyunsook Yang, daughter Janice, son Alec, mother Young-Ae Choi, sisters, and brothers-in-law. Their patient love enabled me to complete this thesis.

TABLE OF CONTENTS

LIST OF TABLES

LIST OF FIGURES

LIST OF NOTATIONS

a_i An auxiliary variable

a_{io} Initial conditions of species *i* concentration [ML^{-3}]

a_{ib} Boundary conditions of species *i* concentration [ML^{-3}]

b_{wo} Specified dispersive flux of contaminants in water phase on boundaries [$ML^{-2}T^{-1}$]

b_{go} Specified dispersive flux of contaminants in gas phase on boundaries [$ML^{-2}T^{-1}$]

b_{wo} Contaminant flux across a groundwater table boundary [$ML^{-2}T^{-1}$]

DCE Dichloroethylene

cDCE *cis*-1,2-dichloroethylene

c Specific heat capacity for each component [$J/kg/K$]

c_k Klinkenberg factor

C^* Specified concentrations of contaminants at a source/sink [ML^{-3}]

C' Dimensionless contaminant concentration

C_{atm} Contaminant concentration in the atmosphere [ML^{-3}]

C_g Contaminant concentration in water phase [ML^{-3}]

C_{ge} Maximum concentration of a contaminant in gas phase [ML^{-3}]

C_{go} Specified contaminant concentrations in gas phase on boundaries [ML^{-3}]

C_{gs} Contaminant concentration in soil gas phase at the ground surface [ML^{-3}]

C_s Concentration of sorbed contaminant in soil phase [$M_{compound}M_{soil}^{-1}$]

C_w Contaminant concentration in water phase [ML^{-3}]

C_{we} Maximum concentration (solubility) of a contaminant in aqueous phase [ML^{-3}]

C_{wt} Contaminant concentrations in water phase at the top of a boundary layer [ML^{-3}]

C_{wb} Contaminant concentrations in water phase at the bottom of a boundary layer [ML^{-3}]

C_{wo} Specified contaminant concentrations in water phase on boundaries [ML^{-3}]

Cr Courant number

D Dispersion tensor [L^2T^{-1}]

D^* Molecular diffusion coefficient [L^2T^{-1}]

D_w^* Effective aqueous dispersion coefficient [L^2T^{-1}]

f_g Gas pressure head gradient

f_w Water pressure head gradient

g Gravitational constant [LT^{-2}]

h_{Lat} Specific enthalpies of vaporization [J/kg]

h_f Specific enthalpy of phases [J/kg]

H Dimensionless Henry's law coefficient

H_c Depth of injection screen center as a characteristic length [L]

I_g Mass transfer of contaminants between phases [$ML^{-3}T^{-1}$]

IAS In situ air sparging

J_v Flux of water vapor in gas phase [$ML^{-2}T^{-1}$]

J_o Flux of organic vapor in gas phase [$ML^{-2}T^{-1}$]

k Maximum specific rate of substrate degradation [$M_{substrate}\ M^{-1}_{cell}\ T^{-1}$]

k' Maximum bioreaction rate [MT^{-1}]

k_i Pseudo-first-order reaction coefficient of i^{th} chemical [T^{-1}]

k_B Maximum bioreaction rate [$ML^{-3}T^{-1}$]

k_m Intrinsic permeability tensor for soil media [L^2]

k_r Relative permeability

k_{rg} Relative permeability of gas phase

k_{rw} Relative permeability of liquid phase

K Thermal conductivity [$W/m/K$]

K_A Overall conductivity of soil matrix [$W/m/K$]

K_D Sorption coefficient [$L^3 M^{-1}_{soil}$]

K_f Heat conductivity of each phase [$W/m/K$]

K_S Half-saturation constant for the substrate of the bioreaction [ML^{-3}]

m Empirical parameters for van Genuchten equation

M Molecular weight of a chemical component

M_g Averaged molecular weight of a gas mixture

n Empirical parameters for van Genuchten equation

n Total number of chemical species

$\vec{n}$ Unit vector normal to a boundary [L]

N Total number of contaminants

N_g Dimensionless gravity number of gas phase

NAPL Nonaqueous phase liquid

P_c Capillary pressure [$ML^{-1}T^{-2}$]

P_{cgw} gas-water capillary pressure [$ML^{-1}T^{-2}$]

P_{cnw} Nonaqueous phase liquid-water capillary pressure [$ML^{-1}T^{-2}$]

P_n Nonaqueous phase liquid pressure [$ML^{-1}T^{-2}$]

P_d Displacement pressure for Brook-Corey equation [$ML^{-1}T^{-2}$]

P_g Gas pressure [$ML^{-1}T^{-2}$]

P_w Water pressure [$ML^{-1}T^{-2}$]

Pe Grid Peclet number

PCE Tetrachloroethylene

q Darcy flux [LT^{-1}]

q_{gn} Darcy fluxes of gas on boundaries [LT^{-1}]

q_{wn} Darcy fluxes of water on boundaries [LT^{-1}]

Q Strength of sources/sinks [T^{-1}]

Q_g Air injection rate [L^3T^{-1}]

Q_S heat source/sink per unit volume due to heated air injection/extraction [$J/m^3/s$]

Q_w Strength of sources/sinks of water phase [T^{-1}]

$Q^{'}$ Strength of sources/sinks of mass [$ML^{-3}T^{-1}$]

r Radius [L]

r' Dimensionless radius

r_b Rate of bioreactions [$ML^{-3}T^{-1}$]

ROI Radius of influence

s Saturation degree

S Substrate concentration [ML^{-3}]

X Active microbial concentration [ML^{-3}]

s_g Gas saturation

s_n Saturation of nonaqueous phase liquid

S_s Specific volumetric storativity [L^{-1}]

s_w Water saturation

s_{we} Effective water saturation

s_{wr} Irreducible water saturation

S_h Overall heat capacity [$J/m^3/K$]

t Time [T]

T Temperature [$\circ C$ or K]

T_{ref} Reference absolute temperature [K]

TCE Trichloroethylene

TEV Thermal-enhanced venting

v Pore velocity of fluid [LT^{-1}]

V_t Bulk volume of porous media element [L^3]

VC Vinyl chloride

VOC Volatile organic compound

x, y, z Directions in a Cartesian coordinate system

x_i Fractional molar concentration of i^{th} species

Δx Length of an element in x-direction [L]

y_i Stoicheometric yield factor

Δy Length of an element in y-direction [L]

Y_1 Lower limit of a contaminant source zone in y-direction [L]

Y_2 Upper limit of a contaminant source zone in y-direction [L]

Δz Length of an element in z-direction [L]

Z_1 Lower limit of a source zone in z-direction [L]

Z_2 Upper limit of a source zone in z-direction [L]

α Empirical parameter for van Genuchten equation [L^{-1}]

α Soil matrix compressibility [LT^2M^{-1}]

α_L Longitudinal dispersivity of soil media

α_T Transversal dispersivity of soil media

β_w Compressibility of water under an isothermal condition [LT^2M^{-1}]

γ_g Compressibility of gas phase [T^2L^{-2}]

δ_{mn} Kronecker delta.

δ_g Thickness of a stagnant boundary layer of gas phase at the ground surface

δ_w Thickness of the groundwater table boundary layer

ε_a Absolute error

ε_r Relative error

λ Fitted parameter for Brook-Corey equation

λ_B First-order biological transformation coefficient [T^{-1}]

λ_D First-order coefficient for dissolution of NAPL contaminants [T^{-1}]

λ_H First-order mass transfer coefficients between water and gas phases [T^{-1}]

λ_V First-order coefficient for evaporation of NAPL contaminants [T^{-1}]

μ Dynamic viscosity [$ML^{-1}T^{-1}$]

ρ_{air} Air density [ML^{-3}]

ρ_b Bulk density of the soil phase [$M_{soil}L^{-3}$]

ρ_n Density of nonaqueous phase liquid [ML^{-3}]

ρ_v Density of pure vapor of a contaminant [ML^{-3}]

τ Tortuosity of porous media

τ Dummy variable of integration for time integral

ϕ Porosity

ψ_g Water-equivalent pressure head of gas phase [L]

ψ_w Water-equivalent pressure head of water phase [L]

$\psi_{g\Gamma}$ Gas pressure head on a boundary [L]

$\psi_{w\Gamma}$ Water pressure head on a boundary [L]

∇ Gradient operator

SUMMARY

Volatile organic compounds (VOCs) such as chlorinated solvents are among major contaminants found in contaminated sites. Groundwater contamination by VOCs has become a major environmental issue due to the toxicity of VOCs at very low concentrations. Once VOCs enter the ground, they will spread out through porous soil media by complicated processes including advection, dispersion, and partitioning. These processes may accelerate groundwater contamination by VOCs over time. In order to preserve groundwater resources from such contamination and to clean up sites contaminated with VOCs, it is necessary to understand the fate and transport of contaminants in the subsurface systems and physicochemical processes involving remediation technologies. To enhance our understanding, in this work, numerical studies were performed on the following important topics: (i) multiphase flow and contaminant transport in subsurface environments; (ii) biological transformations of contaminants; (iii) in-situ air sparging (IAS); and, (iv) thermal-enhanced venting (TEV). Among VOCs, due to the wide use of trichloroethylene (TCE) as a solvent, TCE is one of the most-frequently-detected chemicals in the contaminated groundwater. In this study, TCE and its daughter products (*cis*-1,2-dichloroethylene (cDCE) and vinyl chloride (VC)) are chosen as target contaminants. cDCE and VC are more toxic than TCE.

Density-driven advection of gas phase is generated by the increase in gas density due to vaporization of high-molecular weight contaminants such as TCE in the unsaturated zone. This study investigated the effect of the density-driven advection on the fate and transport of TCE in the unsaturated/saturated zones. The effect of some

important factors including infiltration and permeability on the density-driven transport of TCE were analyzed. The density-driven advection of gas phase played an important role in TCE transport into the atmosphere and into the saturated-zone groundwater near a contaminant source area.

Biological transformations of contaminants can generate byproducts, which may become new toxic contaminants in subsurface systems. Sequential biotransformations of TCE, cDCE, and VC are considered, which are expressed by first-order relationships and Michaelis-Menten kinetics. Under different reaction rates for the two bioreaction kinetics, temporal and spatial concentration profiles of parent and daughter contaminants were examined to evaluate the effect of biotransformations on multispecies transport. The concentration profiles of the contaminants varied with the magnitude of bioreaction coefficients, and the locations of the highest concentration zones of daughter contaminants depended on bioreaction kinetics.

IAS injects clean air into the subsurface below the groundwater table to remediate contaminated soil and groundwater. In this study, through the application of numerical models, the movement of gas and the groundwater as a multiphase flow in the saturated zone and the removal of TCE by IAS application were investigated. A multiphase flow under IAS was examined in terms of saturation levels and fluid velocity profiles of each phase in a three-dimensional domain. Several scenarios for IAS systems were simulated to evaluate remedial performance of the systems in terms of several IAS-related factors, such as injection-well types, flow rates, injection-point depths, injection methods, and well-to-well distances. In this study, IAS using multiple-injection wells showed superior remedial performances over IAS using single-injection well.

TEV is used to clean up soil contaminated with a nonaqueous phase liquid (NAPL) in the unsaturated zone. Transport of heat energy in porous media and the effect of TEV application on TCE NAPL removal were analyzed under different operational conditions regarding air injection rate and relative humidity. In terms of the variations of temperature and NAPL saturation, TEV was compared with normal soil venting at an ambient temperature. Under modeling conditions used here, TEV was effective to deliver thermal energy to contaminated zones. Thus, TEV increased TEC removal rates in the domain and reduced remedial times.

For numerical studies conducted in this thesis, the governing equations for flow of water, gas, and NAPL phases and transport of multispecies and heat energy in porous media were developed and solved using Galerkin finite element method. A three-dimensional numerical model, called TechFlow^{MP} model, has been developed. For each research topic, the model has been verified and validated using analytical solutions and experimental data published in the literature.

CHAPTER I

INTRODUCTION

This chapter provides introduction to soil and groundwater contamination in subsurface environments and two remedial technologies (in-situ air sparing and thermal-enhanced venting) that may be used to clean up contaminated zones. The chapter concludes with a discussion of the scope of the present study.

1.1 Soil and Groundwater contamination

Groundwater is an important fresh water resource throughout the world. It is used for public and domestic water supply systems, and agricultural and industrial purposes. In the United States in 1995, the USGS reported that approximately 77 billion gallons of fresh groundwater was withdrawn daily; nearly half of the nation's overall population and about 99% of the population in rural areas used groundwater as drinking water; nineteen states obtained more than 25% of their overall water supply from groundwater; and ten states obtained more than 50% of their total water supply from groundwater [Solley et al., 1998; EPA, 2000]. Such large utilization of groundwater comes from its advantageous characteristics such as: (i) its availability at extended areas; (ii) relatively constant supply through years; and (iii) its high quality due to the purification processes by soil matrix [Wiener, 1972; Bear, 1979].

In many areas of the U.S., the future sustainability of groundwater resources is at risk from overuse and contamination. Major sources of groundwater contamination most frequently cited as being of greatest concern include underground storage tanks, septic

tanks, hazardous waste sites and landfills, surface impoundments, chemical manufacturing and storage facilities, fertilizer and pesticide applications, and salt water intrusion. According to EPA report [2000], underground storage tanks (USTs) represented the highest number of potential sources of groundwater contamination. Of over 85,000 UST sites reported in 72 hydrogeologic settings in 22 states, 57 % were characterized as confirmed contaminant releases to the environment and 18 % had releases that adversely affected groundwater quality.

Volatile organic compounds (VOCs), such as solvents and hydrocarbon fuels, are among major chemicals found in many contaminated sites. Subsurface contamination of VOCs is usually caused by spills, leakage from transport and storage facilities, or release from uncontrolled hazardous landfills [Lorah, 1997; Wu and Schaum, 2001; Dinicola et al., 2002]. Typically, VOCs are released as a non-aqueous phase liquid (NAPL) into the ground. Due to capillary forces in pore space, when VOCs migrate in the form of NAPL through porous media, they leave behind an immobilized residual suspended in soil pore structures. Through partitioning processes such as dissolution, vaporization, and adsorption onto soil particles, the residual NAPL becomes a long-lasting source of soil and groundwater contamination [Mendoza and Frind, 1990a; Thomson et al., 1997].

VOCs have drawn our concern because of their toxicity at low concentrations. Among VOCs, trichloroethylene (TCE) widely used as a solvent in industry is one of the most frequently detected contaminants in the groundwater [Wu and Schaum, 2001]. TCE has been found in at least 861 sites of the 1,428 hazardous waste sites that make up the National Priorities List and are targeted for long-term federal clean-up [ATSDR, 1997]. Based on available Federal and State surveys, ATSDR [1997] estimated that between 9 %

and 34 % of the drinking water supply sources tested in the U.S. may have some TCE contamination.

In the subsurface near contaminant source zones, VOCs often exist in multiple phases (water, gas, and NAPL). These phases have distinct flow patterns, generating multiphase flow. Multiphase flow means a simultaneous flow of two or more immiscible fluids. Transport of VOCs in a multiphase flow occurs as a result of complex mechanical, chemical, and biological processes such as advection, diffusion, sorption, and biological transformations [Thomson et al., 1997]. Molecular diffusion, which is generated by a concentration gradient, or advection of gas phase, which is created by pressure- or density-gradients, is often a primary driving force for contaminant transport in the unsaturated zone while groundwater flow has a dominant effect on contaminant transport in the saturated zone. The density-driven advection of gas, which is generated by high concentration of dense VOCs like TCE near source zones, has a significant effect on spreading contaminants [Mendoza and Frind, 1990a]. Biological transformations of VOCs can introduce toxic daughter contaminants into groundwater systems. For instance, under anaerobic conditions, the dehalogenation of TCE produces intermediates such as dichloroethylenes (DCEs) and vinyl chloride (VC) [Vogel et al., 1987]. DCEs are more toxic than TCE, and VC is a known human carcinogen [Montgomery, 2000].

The understanding of the processes that influence fate and transport of contaminants in groundwater systems and proper modeling of these processes is essential to evaluate the effectiveness of recommended clean-up processes. In turn these models can then be effectively used in management decisions that may prevent soil and groundwater from pollution or they may be used in decisions to effectively remediate a

contaminated site. Thus, extensive researches have been carried out to predict the behavior of VOCs in the subsurface [Corapcioglu and Baehr, 1987; Mendoza and Frind, 1990a; Lenhard et al., 1995; Altevogt et al., 2003; Jellali et al., 2003] and to identify biological transformation of VOCs, especially halogenated hydrocarbons [Vogel et al., 1987; Pavlostathis and Prytula, 2000; Alvarez-Cohen and Speitel, 2001; He et al., 2003]. However, contaminant transport modeling still has many challenges to represent its migration in multiple phase environments [Miller et al., 1998]. Even though contaminant transport in gas phase has significant effects on the spreading of dense VOCs in the unsaturated and saturated zones, the transport has not been taken into much consideration. Up to now, currently available models are mainly focused on groundwater flow in the saturated zone and contaminant transport in water phase [Mulligan and Yong, 2004]. In studies on contaminant transport in the unsaturated zone, only gas-phase contaminant transport was considered without interactions between gas and water flows [Mendoza and Frind, 1990a, b], or biological processes in the unsaturated have been neglected [Thomson et al., 1997]. To enhance our understanding of transport and reaction processes of VOCs in the unsaturated and saturated zones, in Chapter III and IV, the following important processes are reviewed: (i) interaction between density-driven gas flow and water flow in a variably saturated zone; (ii) contaminant transports in each phase and mass transfer between phases; and (iii) biological transformation of contaminants within water phase.

1.2 Remedial technologies for contaminated zones

In the United States, the development of remedial technologies for contaminated sites has been driven by increased environmental awareness and national hazardous waste cleanup programs managed by Environmental Protection Agency (EPA). The programs have been regulated by Comprehensive Environmental Response, Compensation, and Liability Act (CERCLA or Superfund), Resource Conversation and Recovery Act (RCRA), Oil Pollution Act (OPA), and Underground Storage Tank (UST) program. Under these programs a variety of remediation technologies have been used or recommended. These remediation technologies include: (i) pump-and-treatment for groundwater; (ii) soil vapor extraction; (iii) bioventing; (iv) chemical and biological treatments; (v) bioremediation; (vi) in-situ air sparging; (vii) thermal-enhanced venting; and (viii) monitored natural attenuation.

In-situ air sparging (IAS) is a cost-effective remedial technology applied to remove VOCs dissolved in the groundwater and NAPL both above and below the groundwater table [Unger et al., 1995; Kirtland and Aelion, 2000]. It has been used at many sites contaminated by chlorinated solvents and petroleum hydrocarbons [Bass et al., 2000]. Contaminant removal by IAS commonly relies on two primary mechanisms; volatilization and biodegrdation of contaminants [Roosevelt and Corapcioglu, 1998]. IAS injects contaminant-free air below the groundwater table. As the air rises through the saturated zone, contaminants in aqueous phase or NAPL diffuse into the air due to concentration gradient and are then carried out into the unsaturated zone above the groundwater table. Typically, in the unsaturated zone, the air containing the contaminants are withdrawn by soil vapor extraction (SVE), and the contaminants are treated by post-

treatment units. IAS may enhance the aerobic biodegradation of contaminants in the subsurface by transferring oxygen to the groundwater. Kirtland et al. [2001; 2005] examined the biodegradation of petroleum hydrocarbons through a field-pilot test for IAS/SVE and the biodegradation of recalcitrant organic compounds such as dichloroethylene.

In IAS, injected air causes dynamic movement of groundwater and air by displacing water in soil matrix. The lateral and upward movements of the air are an important factor to determine the radius of influence and the degree of contact between the injected air and the contaminated groundwater, which control the efficiency of IAS [McCray, 2000]. Before a full-scale air sparging system is installed, sparging pilot tests should be performed to obtain field data about feasibility of IAS, radius of influence, and mechanical requirements such as pressure and flow rates. Based on case studies of IAS, Bass et al. [2000] pointed several difficulties in IAS application; For examples, sparging well density, a rebound of groundwater concentrations, and remediation times with different initial concentration of dissolved contaminants. Numerical modeling is a valuable tool in predicting complex processes regarding fluid flow, contaminant transport, and nonequilibrium reactions and in solving problems occurring during IAS [Benner et al., 2002]. Especially, the understanding of dynamic behavior of gas and water fluids is essential to determine the applicability of IAS and to design IAS system under certain hydrogeologic situations.

Thermal-enhanced venting (TEV) is a remedial technique used to enhance removal or recovery of less-volatile residual hydrocarbon contaminants such as naphthalene and dodecane in the unsaturated zone. TEV applies heated air to the

contaminated zone while soil venting uses ambient air. As heat energy is introduced into the ground, many physicochemical properties of fluids and VOCs are changed under nonisothermal environments. In a case of vapor pressure of an organic compound highly depending on temperature, the temperature increase of 20-30°C leads the increase in the gas-phase concentrations of a less-volatile contaminant by three- or five-fold [Kaluarachchi and Islam, 1995]. Thermal energy plays important roles in increasing remediation efficiency and in reducing remediation time of the contaminated unsaturated zone.

1.3 Scope of the Study

The study area of this thesis is divided into two main parts; The first part focuses on how organic contaminants naturally migrate and are biologically transformed, and the second part concentrates on how two remediation technologies (IAS and TEV) work to clean up contaminated soil and groundwater and how we can improve their performance.

In these two parts, the objectives of this study is: (i) to investigate biological transformations of multi-species by sequential reactions and density-driven advective transport of contaminants in multiphase flow in a variably saturated zone; and, (ii) to analyze dynamic fluid flows and contaminant transport under isothermal or nonisothermal conditions in two remediation technologies, IAS and TEV.

In this study, fully coupled flow equations for mobile and immobile phases, advective-dispersive transport equations of multi-species, and heat transport equations in variably saturated zones are developed. Multiphase flow equations are coupled by capillary pressure and saturation degree, and the equations are linked with transport

equations with concentration terms. In the transport equations, non-equilibrium processes such as biological transformation and mass transfers between phases are expressed by a first-order relationship or Michaelis-Menten equation. For nonisothermal conditions, heat transport equation is solved to take into account the variation in properties of fluid and chemicals due to the change in temperature. The governing equations for flow, and contaminant and heat transport are numerically solved using Galerkin finite element method (FEM), and a three-dimensional FEM-based model, referred to as TechFlow^{MP}, was developed. The model was verified using experimental data, analytical solutions, and numerical results found in literature, and it was used to run a variety of simulation problems.

In Chapter II, a comprehensive literature review related to research topics of this thesis: (i) multiphase flow and density-driven transport; (ii) biological transformation of contaminants; (iii) in-situ air sparging; and (iv) thermal-enhanced venting system is presented.

In Chapter III, the governing equations for multiphase flow and contaminant transport are developed, and numerical methods used to solve the equations are given. The chapter addresses the effect of density-driven advection of gas phase on contaminant transport in the unsaturated and saturated zones. Especially, the transport profiles of conservative-contaminant by two mechanisms (density-driven transport and diffusion-only transport) are compared. In addition to the density-driven advection of gas, the effects of infiltration and permeability on contaminant transport are investigated. Biological transformations of multi-species (TCE, DCEs, and VC) by sequential reactions are considered in Chapter IV. Transports of three reactive contaminants in

three-dimensional domain are verified using analytical solutions. Spatial and temporal distributions of all contaminants in gas and water phases are also analyzed.

Chapter V focuses on multiphase flow and contaminant removal in IAS systems. In this chapter, the interactive movement of water and air fluids during air sparging and contaminant transport in the two fluids are addressed. The system design parameters such as influence of radius, gas saturation level, and gas flow velocity are estimated for several options of IAS system. Based on contaminant removal rates and residual concentration in gas and groundwater, the remedial efficiency of each option is evaluated, and effective design methods of IAS are suggested.

In addition to flow and transport equations, in Chapter VI, heat transport equation is formulated and solved to describe heat conduction through soil matrix, heat convection due to gas flow, and heat exchange due to vaporization or condensation of water and NAPL in pore spaces. Experimental data found in literature were used to validate TechFlow^{MP} on the variation in temperature due to volatilization of NAPL. Simulation results of several TEV systems are analyzed in terms of three topics; air flow through porous media under nonisothermal conditions, the temperature change of soil matrix due to heat input and vaporization/condensation of a chemical or water, and concentration evolution of a contaminant in TEV system.

Finally, in Chapter VII, conclusions and recommendations for further research are given.

CHAPTER II

LITERATURE REVIEW

In this chapter, a review of studies related to the migration of volatile organic compounds in the subsurface and two remediation technologies are given. The topics covered are: (i) density-driven transport of contaminants; (ii) biological transformation of contaminants; (iii) in-situ air sparging system; and, (iv) thermal-enhanced venting system.

2.1 Density-driven Transport of Contaminants

Soil and groundwater contamination is often initiated by an accidental spill or leakage of volatile organic compounds (VOCs) such as organic solvents and hydrocarbon fuels. The contaminants may percolate into the ground as a non-aqueous phase liquid (NAPL), which migrates downward under the influence of gravity and, to some extent, spreads laterally due to the effect of capillary forces [Abriola, 1989]. According to its density, NAPL is generally divided into two groups; light non-aqueous phase liquid (LNAPL), which is lighter than water, and dense non-aqueous phase liquid (DNAPL), which is heavier than water. The density of NAPL plays an important role in its movement in the subsurface. LNAPL and DNAPL behave similarly in the unsaturated zone, disregarding percolation velocities as a result of different viscosities. When they reach the saturated zone, however, LNAPL forms a pool on the groundwater table while DNAPL sinks into the saturated zone below the groundwater table [Yaron et al., 1984]. While NAPLs migrate through porous soil media, some fraction of them will be

continuously retained in the soil pore spaces due to surface tension effects [Falta et al., 1989]. After reaching the final spreading stage of NAPLs, they eventually become immobile in a condition of residual saturation. The residual saturation may be at about 2-20 % of the available pore spaces [Schwille, 1988].

Residual NAPL contaminants trapped in the pore spaces will volatilize into the surrounding soil gas and dissolve into water phase. Fate and transport of contaminants in gas and water phases occurs as a result of complex processes such as advection, diffusion, partitioning, and biological transformations in the subsurface environment [Thomson et al., 1997]. Typically, groundwater flow is created by hydraulic head gradients, having a primary effect on contaminant transport in the saturated zone. Gas flow in the subsurface can be generated by a variety of factors such as density gradients of gas, barometric pressure changes, groundwater table fluctuations, and vapor extraction/injection [Mendoza and Frind, 1990a; van Dijke et al., 1995; Auer et al., 1996; Thomson et al., 1997; Rathfelder et al., 2000]. Especially, the gas flow induced by the density gradient of gas is called density-driven advection, which is associated with high concentrations of contaminants in gas near a contaminant source. In the unsaturated zone, without considering atmospheric pressure gradient, vapors less dense than air may rise to the ground surface while those more dense than air may sink towards the groundwater table [Sleep and Sykes, 1989].

Density-driven transport of a contaminant refers to its transport that is mainly governed by density-driven advection. Since VOCs have high vapor pressures, the changes in gas density due to contaminants are larger in the soil gas than in the groundwater. The effect of density changes on density-driven advection is also larger in

gas phase than in water phase. Density-driven advection plays an important role in spreading dense VOCs such as trichloroethylene (TCE) and tetrachloroethylene (PCE) in the unsaturated and saturated zone [Falta et al., 1989].

Many experimental studies were carried out to investigate density-driven transport of VOCs in porous soil media and its effects on groundwater contamination [Lenhard et al., 1995; Conant et al., 1996; Smith et al., 1996; Jellali et al., 2001; Altevogt et al., 2003; Jellali et al., 2003]. Lenhard et al. [1995] analyzed the transport of TCE in the unsaturated zone using a vertical two-dimensional experimental cell. The comparison of their experiments and numerical results demonstrated that the density-driven advective flow of gas phase was significant in the downward movement of TCE gas-plume. Altevogt et al. [2003] examined the transport of a dense gas (Freon-113) in a sand column in three primary flow directions (horizontal, vertically upward, and vertically downward), and they identified that advective driving force causing the downward flow of the dense gas retards transport of the gases in the upward direction. Large-scale experiments, done by Jellali et al. [2001; 2003], demonstrated that the downward propagation of TCE vapor plumes leads to increase TCE concentrations with depth. Jellali et al. [2003] reported that mass transfer of TCE from the unsaturated zone into the saturated zone is governed almost equally by molecular diffusion and vertical dispersion, and, even though the mass transfer is small, it may be significant potential for groundwater pollution. Temperature variations have a significant impact on the transport of contaminant vapors because gas density and vapor pressure of contaminants highly depend on temperature. Through field experiments, Conant et al. [1996] investigated the temperature effect of two seasons (winter and summer) on the transport of TCE vapors in

the unsaturated zone. In the winter (subsurface temperatures ranged less than zero to 10 ºC at the ground surface to the depth of 3.5 m), a decrease in subsurface temperatures reduced the vapor pressure of TCE and its diffusion coefficient in gas phase with the increase in sorption. Thus, molecular diffusion became dominated on TCE transport, and the spreading of TCE vapor was relatively small. During the summer months (subsurface temperatures ranged about 24 to 10 ºC at the ground surface to the depth of 3.5 m). An increase in subsurface temperatures caused high vapor concentrations of TCE in the source area, resulting in a greater driving force for both dispersion and density-driven advection, and a decrease in retardation due to vapor dissolution and sorption. Thus, vaporized TCE plume was widely spread out in the unsaturated zone. Since temperature is a critical factor to raise the vaporization of various VOCs, high temperature is often used to accelerate the remediation of contaminated sites [EPA, 1991]. The effect of temperature on the removal of VOCs, especially TCE, is addressed in Chapter VI.

Analytical solutions of VOCs transport in the unsaturated zone are available in the literature [Jury et al., 1983; 1984; 1990; Shoemaker et al., 1990; Shan and Stephens, 1995]. Jury et al. [1983] developed a one-dimensional transport solution on the assumptions of linear, equilibrium partitioning between gas, water, and adsorbed phases, first-order degradation, steady-state water flow, and chemical release into atmosphere through a stagnant air boundary layer. The solution includes water-phase advection and diffusion and gas-phase diffusion. Shoemaker et al. [1990] extended the solution given by Jury et al. [1983] to one- and two-dimensional analytical solutions considering gas-phase sorption as well as water-phase sorption. Gas-phase sorption (direct partitioning of a contaminant from gas phase to solid phase) significantly retarded the propagation of a

contamination front under very dry soil conditions. Shan and Stephens [1995] developed an one-dimensional analytical solution to investigate the density effect of a contaminated gas mixture on vertical transport of VOCs in the unsaturated zone. In the analytical solution, the gas velocity is proportional to total contaminant concentration in the mixture and molecular weights of contaminants. Therefore, density-driven advection of gas mixture generates fast transport of contaminants when the concentrations are relatively high and the contaminants have high molecular weights like TCE and PCE.

One of the earlier numerical studies considering an advective gas flow were done by Weeks et al. [1982]. They used a one-dimensional finite difference model to simulate transport of two atmospheric fluorocarbons from the atmosphere into the very thick unsaturated zone. The model included diffusion, convection associated with a decline in the water table, and partitioning processes. Among the three processes, gas diffusion was the primary mechanism causing downward migration of the fluorocarbons in the undisturbed unsaturated zone with small groundwater discharge. Using a two-dimensional finite element model, Metcalfe and Farquhar [1987] investigated advective transport due to the change in gas density in simulating the migration of carbon dioxide and methane from waste disposal sites. In the simulation, density and viscosity of gas mixture were evaluated as a function of contaminant concentrations.

Falta et al. [1989] investigated density-driven gas flow in the unsaturated zone by analytical and numerical methods. Analytically, they estimated maximum velocities of various gas mixtures, which are generated by the change in gas density due to vaporization of contaminants. They reported that transport of halogenated contaminants, such as TCE and chloroform, is highly affected by density-driven flow of gas phase, and

that the flow is significant in a relatively permeable zone. Using the modified TOUGH, a three dimensional numerical code with the finite difference method, Falta et al. [1989] numerically analyzed the density-driven migration of toluene and carbon tetrachloride in the unsaturated zone; at 25 ^{o}C, 1 atm, approximate maximum density of gas mixture is 1.27 kg/m^3 for toluene + air and 1.93 kg/m^3 for carbon tetrachloride + air while pure air is about 1.17 kg/m^3. Their numerical analysis showed that the density-driven flow of gas was large and noticeable for carbon tetrachloride while the flow was small for toluene.

Mendoza and Frind [1990a; 1990b] developed a two-dimensional model to investigate main transport mechanisms, such as diffusion, density-driven advection, and advection due to vaporization at sources, in the unsaturated zone. The model was validated through a comparison of simulation results and experimental data. Based on the results of various simulations, they also pointed out the importance of density-driven advection of gas phase on contaminant transport, and reported that soil-surface boundary plays a very important role in releasing contaminants from the subsurface into the atmosphere. Open soil-surface much reduced the development of contaminant vapor plume relative to the closed soil-surface boundary. They also noted that higher moisture content can increase the contaminant concentration in water phase, thus more contaminant can be transported into the saturated zone.

In the unsaturated zone, water phase constantly interacts with gas phase, and the two phases simultaneously flow through porous media as a multiphase flow. In unsaturated zone, the numerical works done by Metcalfe and Farquhar [1987], Falta et al. [1989], and Mendoza and Frind [1990a; 1990b] neglected water flow and contaminant transport in water phase under the assumptions of a local equilibrium between gas and

water phases. Sleep and Sykes [1989] developed a two-dimensional model that included the movements of water and gas in simulating contaminant transport in variably saturated media. Under the assumption that the capillary effect between gas and water phases is negligible, the model linked water phase flow and gas phase flow in terms of their saturation levels. The density was treated as a function of contaminant concentrations without any effect of gas compression. Sleep and Sykes [1989] showed that: (i) contaminant transport due to the density-dependent gas flow caused greater spreading of TCE in gas phase in the unsaturated zone; (ii) a combined effect of density-dependent advection of gas phase and contaminant partitioning between water-air phases increased pollution of groundwater in the saturated zone; and, (iii) an in-situ gas venting, in which a vacuum is applied below a source zone of immobilized TCE, was very effective in removing TCE vapor.

Mendoza and McAlary [1990] simulated vapor transport of TCE from its residual source in a two-dimensional domain, and investigated potential of groundwater contamination due to dissolution of TCE. Their simulation results suggested that, regardless of ground surface boundary conditions, groundwater can be significantly polluted by TCE, and infiltration will accelerate the development of contaminated groundwater plumes. Since Mendoza and McAlary [1990] handled the unsaturated zone and the saturated zone as separate domains, direct mass transfer of TCE at the interface between the two zones was not achieved.

Thomson et al. [1997] developed a two-dimensional finite-element-based model to simulate flow of gas and water phases and TCE transport in the phases. In estimating the density of gas mixture, the model included both gas phase compressibility and TCE

concentration in the mixture. Water and gas flow equations are coupled through the gas-water capillary pressure and saturation degrees in the presence of an immobile NAPL source. The model excluded sorption and potential biological transformation while including the first-order relationship for mass transfer between phases, i.e., NAPL/water, NAPL/gas, and water/gas. The numerical simulations done by Thomson et al. [1997] showed that: (i) fluctuations in the water table largely contribute to the transport of VOCs from the contaminated saturated zone through the unsaturated zone and into the atmosphere; (ii) the density-driven advection of gas phase increases groundwater contamination and dissolution of contaminants from an immobile NAPL source; and, (iii) high infiltration makes groundwater contamination by VOCs worse since the infiltration develops the downward movement of water and blocks contaminant transport into the atmosphere.

As discussed above, density-driven advection of gas phase plays an important role in spreading VOCs, especially chlorinated solvents such as TCE, in the unsaturated zone and in transporting them into the groundwater in the saturated zone. A variety of experiments and numerical works have demonstrated the effect of density-driven advection on contaminant transport. However, the numerical modeling efforts discussed earlier have been conducted under limited conditions. For example, Mendoza and Frind [1990a; 1990b] considered only gas phase while excluding water flow and Thomson et al. [1997] neglected contaminant sorption onto soil and biological transformations while considering advection, dispersion, and diffusion in water and gas phases. In a review of available public-domain models, Karapanagioti et al. [2003] pointed out that gas advection has not been much considered for transport modeling in the unsaturated zone.

A few of the models included gas advection and none of the models accounted for both gas advection and biological processes at the same time. In this thesis, contaminant transport in both water and gas phases is considered with multiphase flow. Since the unsaturated and saturated zones are treated in a single domain, the transport of contaminants into the atmosphere or into the groundwater in the saturated zone is effectively estimated with density-driven advection of gas, mass transfer between water-gas phases, sorption of dissolved contaminants into soil and biological transformations.

2.2 Biological Transformation and Transport of Contaminants in Subsurface Systems

VOCs released in the unsaturated zone may contact with indigenous microorganisms, which can biologically transform the compounds [Vogel et al., 1987]. Among VOCs, due to the frequent appearance of chlorinated hydrocarbons in groundwater contamination and their toxicity, dehalogenation processes of VOCs have been extensively studied [Vogel and McCarty, 1985; Freedman and Gossett, 1989; Maymo-Gatell et al., 1997; Wu et al., 1998; Pavlostathis and Prytula, 2000; Hendrickson et al., 2002; Dyer, 2003; He et al., 2003].

Biological transformations of chlorinated hydrocarbons are very complicated processes and depend on contaminant chemical properties, concentration, and subsurface environment parameters, such as oxygen, microorganism, oxidation-reduction potential, and temperature. For example, under anaerobic conditions, TCE can be transformed to dichloroethylenes (DCEs), vinyl chloride (VC) [Vogel and McCarty, 1985], and ethylene [Freedman and Gossett, 1989]. In Figure 2.1, among three DCE isomers produced theoretically, *cis*-1,2-DCE (cDCE) is the most common byproduct, and 1,1-DCE is the least prevalent one [Wiedemeier, 1998]. Thus, cDCE has been often used as a representative among DCE isomers in sequential-bioreaction modeling [Clement et al., 2000]. The transformations of TCE and DCEs requires a low oxidation-reduction potential [Vogel et al., 1987; Freedman and Gossett, 1989]. When TCE is dechlorinated under methanogenic conditions, competition between methanogenesis and dechlorination of TCE for electron donors occurs [Wu et al., 1998]. In Equations (2.1) and (2.2), molecular hydrogen is used as an electron donor for both reactions.

$$\text{Methanogenesis: } 4H_2 + CO_2 \rightarrow CH_4 + 2H_2O \qquad (2.1)$$

TCE dechlorination: $3H_2 + C_2HCl_3 \rightarrow C_2H_4 + 3HCl$ (2.2)

During reductive dechlorination of TCE shown in Figure 2.1, the chlorinated hydrocarbons are used as electron acceptors, not as sources of carbon, and a chlorine atom is removed and replaced with an hydrogen atom [Wiedemeier, 1998]. Wu et al. [1998] studied the effect of different organic materials as a substrate or an electron donor on dechlorination of TCE under methanogenic conditions. They reported that the fraction of a substrate used for dechlorination may increase when the substrate is slowly biodegraded. Davis et al. [2002] investigated rate coefficients and associated half-lives for biodegradation of TCE, DCEs, and VC. In their studies, the higher concentration of halogenated compounds showed the lower degradation rate and the longer half-life. Davis et al. [2002] found diverse group of microorganisms including iron reducers and anaerobic heterotrophs in the anaerobic zone where reductive dechlorination of TCE occurred. In field studies for contaminated sites, Dyer [2003] found TCE, DCEs and VC in both the unsaturated and the saturated zones.

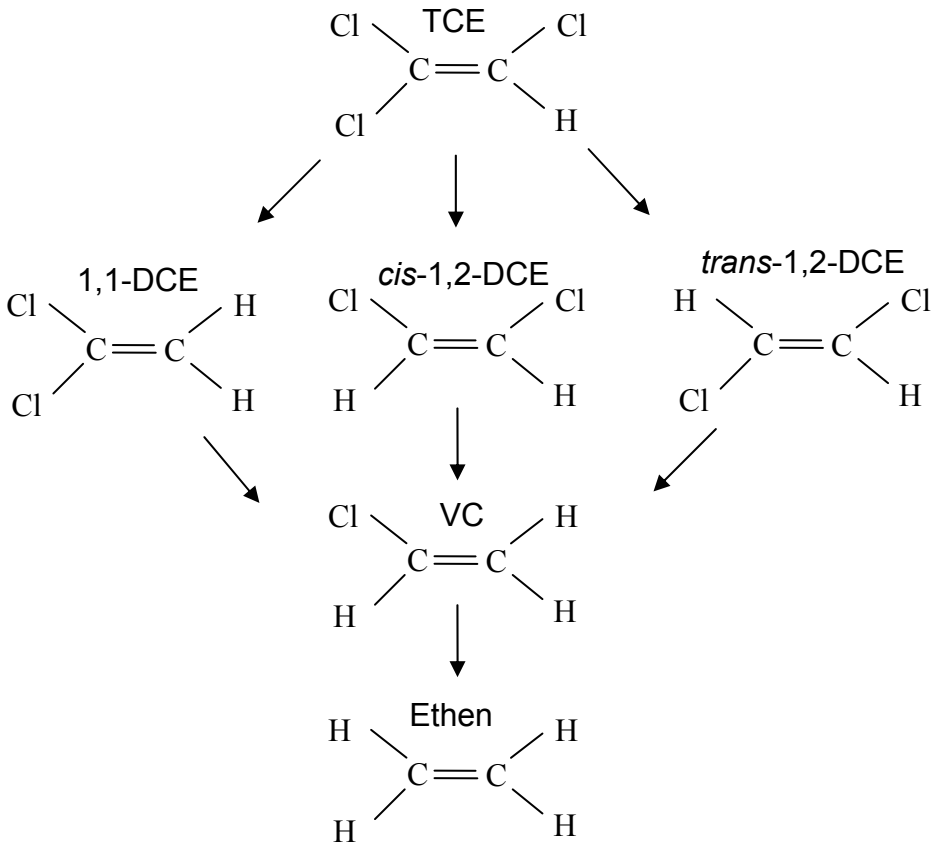

Figure 2.1 Reductive dehalogenation of TCE [Lorah, 1997]

A wide range of chlorinated hydrocarbons can be microbially degraded under aerobic conditions via cometabolism [Smith and McCarty, 1997; Wiedemeier, 1998; Verce and Freedman, 2000; Verce et al., 2002]. The degradation is catalyzed by microbial enzymes, such as methane monooxygenase (MMO) in methanotrophic bacteria, and the enzymes may oxidize TCE to TCE epoxide, which is subsequently mineralized [Smith and McCarty, 1997; Johan et al., 2001]. Because cometabolism yields no carbon or energy benefits to microbial cells [Alvarez-Cohen and Speitel, 2001], microorganisms use other substrates to grow new cells and to meet their energy

requirements. In order to raise methane-oxidizing bacteria, which transform TCE, Smith and McCarty [1997] provided methane gas as an energy source for the bacteria. The methane showed two functions: an energy source for cell growth and a competitive inhibitor of TCE cometabolism. The inhibition kinetics by methane varied with TCE concentration: Methane addition inhibited TCE cometabolism at low TCE concentrations, however, it enhanced TCE cometabolism at high TCE concentrations.

DCEs and VC can be detoxified by aerobic and anaerobic microorganisms, generating the benign products such as ethylene, inorganic chloride, and carbon dioxide [Vogel and McCarty, 1985; Freedman and Gossett, 1989; Coleman et al., 2002; He et al., 2003]. Under aerobic conditions, cDCE can not be used as a source of energy and carbon while VC can be used as a primary substrate for microbial growth [Verce et al., 2002; Singh et al., 2004]. Verce et al. [2002] reported that cDCE is biodegraded by aerobic cultures grown on VC, which can be generated by dehalogenation of DCEs under anaerobic conditions. Cometabolism may occur relatively slowly in comparison to metabolism of growth substrate [Alexander, 1994].

Biological degradation kinetics of contaminants under anaerobic or aerobic conditions are very important in designing in-situ bioremediation system, and they are also required as components of fate and transport models [Alvarez-Cohen and Speitel, 2001]. Biological processes of contaminants in the subsurface are highly complex and are combined with a variety of biochemical and environmental factors such as competition, product toxicity (inhibition), energy and carbon source, and heterogeneity of subsurface systems [Vogel et al., 1987; Murphy et al., 1997; Murphy and Ginn, 2000; Alvarez-Cohen and Speitel, 2001; Cupples et al., 2004; Yu et al., 2005]. Therefore, it may be

almost impossible to entirely understand and express all biological reaction kinetics. In applications, Michaelis-Menten (or Monod) and pseudo-first-order kinetics maybe used to express reductive dechlorination and cometabolic biodegradation reactions of chlorinated hydrocarbons [Smith et al., 1997; Clement et al., 2000; Pavlostathis and Prytula, 2000; Alvarez-Cohen and Speitel, 2001]. Michaelis-Menten model are [Pavlostathis and Prytula, 2000]:

$$r_b = -\frac{k^{'} S}{K_S + S} \tag{2.3}$$

where r_b is the rate of bioreactions ($ML^{-3}T^{-1}$); $k^{'} = kX$ is the maximum bioreaction rate (MT^{-1}) for a constant biomass concentration; k is the maximum specific rate of substrate degradation ($M_{substrate}\ M^{-1}{}_{cell}\ T^{-1}$); S is the substrate (contaminant) concentration (ML^{-3}); X is the active microbial concentration (ML^{-3}); K_S is the half-saturation constant for the substrate of the bioreaction (ML^{-3}). Pseudo-first-order model is a simplification of Michaelis-Menten model on the assumption that substrate concentrations (S) are significantly lower than half-saturation constants (K_S) and can be written as [Pavlostathis and Prytula, 2000]:

$$r_b = -k_1 S \tag{2.4}$$

where k_1 is the pseudo-first-order reaction coefficient (T^{-1}). Based on experimental studies on sequential reductive dechlorination of chlorinated benzene congeners (CBs), Pavlostathis and Prytula [2000] recommended Michaelis-Menten model over pseudo-first-order model for the modeling of CBs transformation. In experimental studies of biological reduction of PCE and TCE, Haston and McCarty [1999] reported that Michaelis-Menten kinetics is the best approach in modeling chlorinated aliphatic

hydrocarbons (CAH). The kinetic parameters for CAH have been investigated through various laboratory experiments [Barrio-Lage et al., 1987; Fennell and Gossett, 1998; Haston and McCarty, 1999; Cupples et al., 2004; Yu et al., 2005]. For field-scale applications, Clement et al. [2000] used first-order models to represent sequential biotransformations of perchloroethylene (PCE) and TCE in the saturated zone. The use of Michaelis-Menten and pseudo-first-order kinetics, given in Equations (2.3) and (2.4) respectively, would be appropriate when the bioreaction rate is primarily a function of contaminant concentration under nearly constant microbial mass over time. If active bioremediation techniques such as bioaugmentation and biosimulation cause to highly increase microorganism mass at target sites, the effect of the mass change on degradation rates needs to be considered. The first-order model is reasonable for most natural attenuation modeling [Wiedemeier, 1998] and for biodegradation at low-pollutant concentration in the groundwater flow [Schmidt et al., 1985]. Weber and DiGiano [1996] suggested that first-order equations are widely applicable for description of various environmental reactions such as mass transfer between phases. In addition to reaction kinetics, their reaction rates may spatially vary over contaminated zones. The rates depend on the type and amount of bacteria present in the aquifer and the availability of electron donors and carbon source. To delineate the spatial variations in reaction patterns (aerobic or anaerobic reactions) and reaction rates, Clement et al. [2000] divided a contaminated area into a few reaction zones based on field-monitoring data, and assigned different coefficients for sequential biotransformations to each zone in order to match numerical results with field data.

Most of transport modeling of reactive contaminants, including physicochemical and biological transformation processes, has been conducted only in the fully saturated zones [Yeh and Tripathi, 1991; Schaerlaekens et al., 1999; Clement et al., 2000; Fang et al., 2003]. A three-dimensional finite-element-based hydrogeochemical transport model, HYDROGEOCHEM [Yeh and Tripathi, 1991], was developed, and used to simulate the transport of reactive multiple species with various chemical processes such as precipitation-dissolution, sorption, ion exchange, and oxidation-reduction [Tripathi and Yeh, 1993]. In addition to such physicochemical reactions, Fang et al. [2003] considered biological processes in BIOGEOCHEM to simulate complicated microbiological and chemical reactions of multicomponents in the groundwater. Rifai et al. [2000] developed a two-dimensional finite difference model, BIOPLUME III, to investigate the natural attenuation of organic contaminants in the groundwater. The model, which includes both pseudo-first-order and Monod kinetics for biodegrdation, was used to evaluate the impact of anaerobic processes on the fate and transport of benzene, toluene, ethylbenzene, and xylene (BTEX) at Patrick Air Force Base (AFB) in Florida. Essaid et al [1995] developed a two-dimensional transport model with sequential biological processes, known as BIOMOC, to predict biodegradation of contaminants such as benzene and toluene at a crude oil spill site. The model uses Monod kinetics for biodegradation processes. Clement [1997] developed a three-dimensional transport of reactive multicompounds in the groundwater, RT3D, which includes sequential biodegradation reactions of contaminants such as PCE and TCE. RT3D was applied to analyze multicomponent transport and biotransformation of PCE via sequential dechlorination processes

(PCE→TCE→cDCE→VC→Ethene) within the fully saturated zone at the Area-6 site in Dover Air Force Base, Delaware.

Biological processes within water phase in the unsaturated zone constantly occur, and a parent contaminant and its daughter contaminants exist in water and gas phases through partitioning processes [Borch et al., 2003]. Biological processes in the unsaturated zone have not considered in transport modeling even though they play important roles in generating toxic intermediates, spreading them in the unsaturated zone, and transporting them into the saturated zone. To investigate the effect of biological processes in the unsaturated zone on contaminant transport and groundwater pollution, this study takes account of sequential dehalogenations of TCE, e.g., TCE→cDCE→VC, under anaerobic conditions and cometabolism of TCE under aerobic conditions within water phase in the unsaturated or saturated zone. Michaelis-Menten (or Monod) and pseudo-first-order equations are used to express bioreaction kinetics of contaminants in multicomponent transport modeling.

Transport models of reactive multispecies are described by a set of partial differential equations, and, due to the change in fluid properties and reactions between chemicals, the equations may become highly nonlinear. In formulating a system of nonlinear equations, three approaches are used: (i) a mixed differential and algebraic equation (DAE) approach; (ii) a direct substitution approach (DSA); and, (iii) a sequential iteration approach (SIA). DAE and DSA require extremely large computer resources in terms of central processing unit (CPU) memory and CPU time since they solve all variables simultaneously while SIA needs the fewest resources since it solves variables sequentially and iteratively [Yeh and Tripathi, 1989]. Through the comparison

of the three approaches, Yeh [1989] recommended SIA for practicality and flexibility in simulating multispecies transport with complex reactions in two- or three-dimensional domains. In this study, TechFlow^{MP} employs SIA to handle nonlinear equations for multispecies and multiphase. To improve the convergence of SIA and to reduce computational burdens of DAE in very complicated reaction systems, Molins et al [2004] and Fang et al. [2003] proposed methods that decouple or decompose reactions processes into a few groups of processes.

In cases of flow and transport modeling in three-dimensional domains, high computation capacity is often required due to the complexity of the modeling and the large CPU needs [Gwo and Yeh, 1996]. Gwo [2001] developed a high-performance computer model, HBGC123D, to simulate heat transfer, reactive solute transport, and hydrogeological and biological processes in groundwater systems. HBGC123D is a shared-memory parallel code that utilizes the OpenMP directives as a parallel computation scheme, which is also implemented to TechFlow^{MP} in this study.

2.3 In-situ Air Sparging

In-situ air sparging (IAS) is a remediation technology used for subsurface removal of dissolved VOCs and NAPL [Thomson and Johnson, 2000]. Air sparging injects clean, pressurized air into the subsurface below the water table. The air rises due to the forces of buoyancy and capillary, and it contacts with dissolved or NAPL contaminants, which are partitioned into the air. The air containing the contaminants is carried to the unsaturated zone, where the air is typically withdrawn by a soil vapor extraction (SVE) system. IAS is readily used for contaminants with high Henry's law

constants, boiling points less than 250 to 300 ^{o}C, or vapor pressures greater than 0.5 mmHg, which include benzene, xylene, toluene, and TCE [EPA, 2004]. IAS works best in uniform coarse-grained soils such as sand and gravel, and it is effective when intrinsic permeability is equal to or greater than 10^{-9} cm^2 [Sellers, 1999; EPA, 2004]. The applicability and performance of IAS are determined by a variety of factors, such as geological and hydrogeological conditions, contaminant properties, and contaminant distribution at sites [Wilson, 1995]. Geological and hydrogeological conditions include aquifer depth, soil texture, porosity, permeability, heterogeneity, and stratigraphy; contaminant properties include vapor pressure, solubility, and biodegradability; contaminant distribution includes its horizontal and vertical extents.

The use of IAS technology is growing more rapidly than the theoretical and design knowledge associated with the technique, and mathematical models of air sparging are in the early stages of development [McCray, 2000]. Published air-sparging models became available in the early to mid-1990s. The first conceptualizations of air flow during air sparging were of bubbles rising in the saturated zone. It is generally accepted that airflow occurs in discrete air channels for most porous media, including gravel or well-sorted coarse sands. Many laboratory experiments demonstrated airflow as discrete bubbles or channels in coarse porous media [Ji et al., 1993; Chen et al., 1996; Plummer et al., 1997; Burns and Zhang, 1999; Peterson et al., 1999; Peterson et al., 2000; Reddy and Adams, 2001]. Corapcioglu et al. [2004] theoretically estimated the rise velocity of air bubbles based on the macroscopic balance equations for forces acting on the bubbles, such as inertia force, mass force, buoyant force, surface tension, and drag force. The theoretical velocity showed good agreement with laboratory-measured

velocity by Roosevelt and Corapcioglu [1998]. Air channeling is ubiquitous at the pore scale and occurs at various scales during IAS [Clayton, 1999]. Heterogeneities of capillarity and relative-permeability appear to be the primary cause of air channels at macroscopic and large scales [Ji et al., 1993; Ahlfeld et al., 1994]. At smaller scales, air channels may be closely spaced relative to the representative elementary volume of a typical model, and air-water flow can be assumed to be a continuum within relatively homogeneous porous media [McCray, 2000]. Air-water flow as a continuum is applied for multiphase flow models.

Generally, air-sparging models are divided into two groups [McCray, 2000]: (i) compartmentalized, lumped-parameter models; and, (ii) multiphase fluid-flow models. In compartmentalized air-sparging models, fluid phases and biophysicochemical processes are separated into compartments: For an example, a three-compartment model may consist of water compartment, gas compartment, and mass-transfer compartment for sorption. Gas compartment usually used to represent air-channels in porous media. The primary purpose of compartment models is to address mass-transfer limiting diffusion of dissolved contaminants, and/or nonequilibrium mass transfer across air-water or NAPL-water phases [McCray, 2000]. Compartment models are useful to address the effect of air channeling on contaminant removal. Wilson [1992] used a well-mixed two-compartment (a water compartment and a reaction compartment between water and gas) model to develop simple analytical air-sparging models that were used to estimate the removal of a dissolved contaminant under steady- or unsteady-states. Local equilibrium between water and gas phases was assumed in the analytical models. Wilson et al. [1994] developed a numerical model to simulate VOC transport into sparged air by dispersion and air-

induced circulation of the water in the vicinity of a sparging well. In the model, the air was assumed to flow through discrete, persistent channels in the aquifer. By simplifying air-sparging systems into a few compartments and considering discrete fluid flows without any interaction between fluids, compartmentalized, lumped-parameter models have advantages to represent many complex mass-transfer processes in a bulk volume of porous media. However, the models cannot describe dynamic behavior of injected air and groundwater, the temporal- and spatial-distribution of the air, and physicochemical processes associated with the dynamic behavior [McCray, 2000].

Under the assumption that air-water fluid is a continuum, multiphase fluid-flow models are often used to describe a simultaneous flow of water and air, which occurs during IAS. When immiscible multiple fluids move through porous media, the interfacial tension between the fluids is nonzero, and a distinct fluid-fluid interface separates the fluids within each pore [Bear, 1972]. The existence of fluid-fluid interfaces makes multiphase flow problems much more difficult to analyze and model than single-phase flow such as the saturated groundwater flow [Celia et al., 1995]. The ability of an interface to carry a nonzero stress is quantified by the interfacial tension for the fluid-fluid pair, and the pressure difference across an interface between fluids is called capillary pressure. For gas-water systems, the capillary pressure, P_c, can be written as,

$$P_c = P_g - P_w \tag{2.5}$$

where P_g and P_w are gas and water pressure, respectively.

A major difficulty in modeling multiphase flow comes from the constitutive relationships governing multiphase movement [Parker et al., 1987]. The relationships are expressed as functional relationships of capillary pressures (P_c), saturations (s), and

relative permeabilities (k_r) of coexisting phases. The relationships and their dependence on porous media and fluid characteristics have been widely studied [Brooks and Corey, 1964; Stone, 1970; Mualem, 1976; van Genuchten, 1980; Parker et al., 1987; Demond and Roberts, 1991; Miller et al., 1998; Ataie-Ashtiani et al., 2002]. Capillary pressure-saturation equations such as Brook-Corey equation [Brooks and Corey, 1964] and van Genuchten equation [van Genuchten, 1980] are widely used to describe the relationship between capillary pressure and effective saturation of a wetting fluid for multiphase flow [Leij et al., 1997]. In air-water systems, since the contact angle between a water-air interface and solid soil is less than 90^o at water-phase, water is a wetting fluid, which will preferentially wet the solid, and air becomes a nonwetting fluid [Bear, 1972]. The effective saturation of a wetting fluid (water) is defined by

$$s_{we} = \frac{s_w - s_{wr}}{1 - s_{wr}} \tag{2.6}$$

where s_{we}, s_w, and s_{wr} are the effective water saturation, real water saturation, and irreducible water saturation, respectively. The Brook-Corey equation can be written as,

$$s_{we} = \begin{cases} 1 & P_c \le P_d \\ \left(P_d / P_c\right)^{\lambda} & P_c > P_d \end{cases} \tag{2.7}$$

where P_d is the displacement pressure and λ is a fitted parameter. The van Genuchten equation can be expressed as,

$$s_{we} = \begin{cases} 1 & P_c \le 0 \\ \left[1 + \left(\alpha P_c\right)^n\right]^{-m} & P_c > 0 \end{cases} \tag{2.8}$$

where α, m, and n are empirical parameters that effect the slope or location of the inflection point of a capillary pressure-saturation curve.

In multiphase flow, each fluid is regarded as a continuum in a porous medium, and each fluid has its own flow pathway according to its saturation level. The permeability of each fluid within a porous medium is affected by the presence of the other phase. The Darcy law, originally describing the flow of a single-phase fluid completely saturating a porous medium, may be extended to describe multiphase flow [Bear, 1972]. Under the extension of Darcy's law, the permeability of each fluid is called an effective permeability. The ratio of the effective permeability of each fluid to the permeability of a single-phase fluid is defined as relative permeability. Relative permeability is generally expressed as a function of fluid saturation. In water-gas fluid systems, Brooks and Corey parametric model yields the relative permeabilities of water and gas phase as follows [Brooks and Corey, 1964],

$$k_{rw} = s_{we}^{(2+3\lambda)/\lambda} \tag{2.9}$$

$$k_{rg} = c_k \left(1 - s_{we}\right)^2 \left[1 - s_{we}^{(2+\lambda)/\lambda}\right] \tag{2.10}$$

and the van Genuchten model gives [van Genuchten, 1980]

$$k_{rw} = s_{we}^{1/2} \left[1 - \left(1 - s_{we}^{1/m}\right)^m\right]^2 \tag{2.11}$$

$$k_{rg} = c_k \left(1 - s_{we}\right)^{1/2} \left(1 - s_{we}^{1/m}\right)^{2m} \tag{2.12}$$

where k_{rw} and k_{rg} are relative permeabilities of water and gas phases, respectively, and c_k is the Klinkenberg factor, which accounts for the air slippage in air-water flow systems [Bear, 1972]. Parker et al. [1987] extended van Genuchten model to three fluid phases and suggested closed-form expressions for capillary pressure-saturation ($P_c - s$) and saturation-relative permeability relationships ($s - k_r$) in two- and three-fluid phase porous media systems.

$P_c - s$ and $s - k_r$ relationships may be different when a fluid-fluid interface is advancing or receding on a solid surface [Bear, 1972]. The phenomena are called hysteresis, produced by pore scale effects associated with the difference in a contact angle between fluids and a solid and nonwetting fluid entrapment during saturation path reversals [Lenhard et al., 1989]. Typically, the relationships are highly nonlinear, and their experimental measurements are often a difficult task. Ataie-Ashtiani et al. [2002] reported that the task can be more difficult in the presence of microheterogeneities which generate complex functional dependencies in $P_c - s - k_r$ relationships. In both environmental remediation and petroleum reservoir engineering, nonhysteretic $P_c - s$ and $s - k_r$ relationships are usually accepted in multiphase flow modeling because the relationships are less computationally demanding and require fewer data [Miller et al., 1998]. This study also uses nonhysteretic relationships to estimate fluid saturation and relative permeability in multiphase flow modeling.

Multiphase flow equations are complex and highly nonlinear because of capillary pressure and relative permeability relationships incorporated into the equations. Most of modelings for multiphase flow have been done by numerical methods [Mohtar et al., 1994; van Dijke et al., 1995; McCray and Falta, 1996, 1997; Marulanda et al., 2000; Mei et al., 2002], and a few investigators developed analytical solutions [van Dijke et al., 1995; Philip, 1998; van Dijke and van der Zee, 1998]. Due to the nonlinearity of multiphase flow equations, analytical solutions are derived based on simplifying assumptions, such as steady-stage air flow, incompressible air, constant air velocity, and stagnant water. Relationships for relative permeability or capillary pressure were also simplified for the solutions. van Dijke et al. [1995] developed an analytical solution to

estimate air saturation levels and the radius of influence of IAS in a steady state situation with a point source injection. The analytical solution showed good agreement with IAS simulation results. The analytical solution is a steady boundary-layer solution that neglects air flow due to vertical capillary pressure gradients. Philip [1998] presented a full air-flow solution that allows vertical downward flow below an air-sparging point. The solution was given in terms of two dimensionless numbers; Kirchhoff potential that increases monotonically with capillary pressure and air saturation and Stokes stream function that maps the pattern of air flow.

Numerical analysis on multiphase flow have significantly contributed to the understanding of the theoretical aspects of IAS and to the design of IAS system [McCray, 2000]. Mohtar et al. [1994] developed a two-dimensional steady-state model, SPARG, to simulate air sparging in porous media. The model, based on finite element method, was used to predict the distribution of capillary pressure during air sparging. Using a three-dimensional multiphase flow model developed by Huyakorn et al. [1994], Panday et al. [1994] depicted the distribution of steady-state gas pressure in the vicinity of a sparging well and the profiles of air velocity along a vertical cross-section and a horizontal plane. Transient air flows in a homogenous axially symmetric porous medium were simulated by van Dijke and van der Zee [1995], who developed nondimensionalized flow equations for water and gas based on the mixed form of the Richard equation. Their simulation results showed that injected air induced groundwater table mounding at the injection well, and that dynamic movements of air and water were stabilized within 2 hours, leading nearly steady-state air flow in static water pressure. The groundwater table mounding was also reported by Lundegard and Andersen [1996].

Using a vacuum extraction with IAS, Unger et al. [1995] investigated controlling mechanisms in removing TCE as DNAPL above and below the groundwater table. At early times, TCE in the unsaturated zone was mainly removed by rapid mass transfer from NAPL to gas phase. At later times, remediation was controlled by mass transfer between NAPL and water phase in the saturated zone. In IAS modeling, Unger et al. [1995] used CompFlow model developed by Forsyth and Shao [1991], and employed two horizontal sparging wells to yield good contact between injected air and DNAPL. The importance of the contact time was also pointed out by Bass et al. [2000], who reviewed many field and experimental cases and provided predictive indicators for successful application of IAS.

Radius of influence (ROI) of sparging wells, generally defined by arbitrary gas-phase saturation, is one of most important parameters in design of IAS system. McCray and Falta [1996; 1997] proposed that the accurate estimation of ROI can be obtained from gas-phase pressures measured in monitoring probes at contaminated sites. In IAS simulations using T2VOC code, Falta et al. [1995] showed that anisotropy of soil matrix has great importance in determining ROI, and heterogeneities of soil media also play an important role in airflow pathways; For example, a less permeable horizontal disc (such as a clay lens) as the heterogeneity in a permeable porous medium contributes to lateral movement of air injected below the disc. The effect of low-permeable layers was demonstrated through experiments [Ji et al., 1993] and numerical studies [McCray and Falta, 1996; van Dijke and van der Zee, 1998]. Benner et al. [2000] used IAS to remediate sandy soils and shallow groundwater contaminated with LNAPL at a drum storage site, and they used BIOVENTING^{plus} to simulate the site. Toluene, ethylbenzene,

and total xylene were dominant among the NAPL contaminants. The simulation results showed that biodegradation was the most important mechanism in total contaminant removal at the site. Comparison of continuous sparging versus pulse sparging suggested that the former is better than the latter if mass-transfer constraints is very small and contaminants are readily biodegraded. Mei et al. [2002] used a pseudo-transient method to investigate steady-state air flow by air venting and sparging in an axisymmetric domain. They pointed out that the compressibility of gas has significant effects on determining capillary pressure, the vertical velocity of gas, and ROI at some regions during IAS. Philip [1998] and Mei et al. [2002] showed that the ROI in a finer soil was larger than that in a coarse soil because of a stronger capillarity in the finer soil. Through air injection and extraction tests at a site contaminated mainly with toluene, ethylbenzene, and xylene, Lee et al. [2002] evaluated ROI using two indicators: (i) the temporal variation of gas-phase pressure and (ii) the propagation of dissolved oxygen concentrations in the groundwater. In their study, a pressure-based ROI was estimated with locations in which gas-phase pressure is greater than or equal to 2.5 mmH_2O [USACE, 1995] while oxygen-based ROI was evaluated with locations in which dissolved oxygen concentration need to be greater than or equal to 5 % to enhance biodegradation of contaminants [EPA, 1995a]. The pressure-based ROI estimated ranged 3.3 m to 10.5 m, and the ROI showed similar magnitude with oxygen-based ROI.

IAS is usually used in conjunction with SVE that remove gas mixture containing VOCs from the unsaturated zone with high permeability in a relative short time [Johnson et al., 1993; Nyer and Suthersan, 1993]. In SVE, pneumatic pressure gradients induced by vacuum pumps create a gas flow in the subsurface. IAS with SVE have been successfully

applied to many sites contaminated with gasoline and chlorinated solvents [Brockman et al., 1995; Aelion et al., 1997; Hughes and Dacyk, 1998; Kerfoot et al., 1998; Rabideau et al., 1999; Murray et al., 2000; Kirtland et al., 2001]. Bass et al. [2000] summarized 44 air sparging cases, consisting of 8 sites for chlorinated solvents such as PCE and TCE and 39 sites for petroleum hydrocarbons; IAS was more successful at chlorinated solvent sites than at petroleum sites because of the rebound of concentrations at the petroleum sites; Absorbed contaminants at the petroleum sites caused concentration rebound after IAS ends and thus decreased IAS performance. Through two-dimensional laboratory experiments, Bruce et al. [1998] reported that approximately 85% of methyl tert-butyl ether (MTBE) as NAPL was removed by volatilization during air sparging.

In IAS, injected air enhances biological processes of contaminants [Aelion et al., 1997; Travis and Rosenberg, 1997; Aelion and Kirtland, 2000; Bass et al., 2000; Kirtland et al., 2001; Lee et al., 2002], and nutrient injections can accelerate the processes [Brockman et al., 1995; Pfiffner et al., 1997; Blount et al., 2002]. Brockman et al. [1995] investigated the effect of nutrients (nitrogen and phosphorus in gas phase) on in-situ bioremediation of a TCE-contaminated site through three experiment stages; At the first stage as a control experiment, only air is injected; at the second stage, 1-4% methane (by volume) with air was injected; and at the last stage, 4 % methane with additional nitrous oxide (0.07% by volume) and triethyl phosphate (0.007 % by volume) are injected. As compared to the control experiment, the methane injection at the second stage showed a rapid and large increase in the density of methanotrophic microorganisms. At the third stage, the addition of nitrogen and phosphorus increased the frequency of TCE biodegradative potential by approximate three orders of magnitude.

In IAS with SVE, nonequilibrium effects are associated with diffusion- and dispersion-limited mass transfer of VOCs between phases. Rate-limited mass transfer has great effect on the efficiency of IAS. A first-order mass transfer equation has been often used to nonequilibrium mass transfer of VOCs in porous media [Sleep and Sykes, 1989; Braida and Ong, 2000]. By implementing a dual-permeability approach used in fractured porous media, Falta [2000] developed a dual-media formulation to simulate the effect of local gas channels that form during IAS. The final equation of the formulation becomes same formulation as a general first-order equation, and the formulation can be used to estimate the coefficient of the first-order equation. Biodegradation plays also important role in air sparging efficiency [Aelion et al., 1997; Aelion and Kirtland, 2000], however the process was not much considered in air-sparging models [McCray, 2000]. In this study on IAS, aerobic biodegradation processes as well as nonequilibrium mass transfer between phases in contaminant transport are taken into consideration with multiphase flow modeling, which can elucidate a simultaneous flow of air and water phase during IAS.

2.4 Thermal-enhanced Venting

Thermal-enhanced venting (TEV) is a heat-based in-situ remediation technique to enhance removal or recovery of medium- to low-volatile residual hydrocarbon contaminants in the unsaturated zone. TEV is different to traditional soil venting because heated air instead of air at ambient conditions is applied to contaminated zones. TEV can be used in many places where excavation is not possible, such as under and around surface structures, and around empty underground tanks and utilities [EPA, 1995b].

The rise in temperature changes physical and chemical properties of an organic chemical; In general, its density and adsorption onto solid phase (or into soil organic matter) decrease; however, its vapor pressure and molecular diffusion in the aqueous and gaseous phases increase [Davis, 1997; Werth and Reinhard, 1997]. For less-volatile contaminants, gas-phase concentrations increase by three- or five-fold when temperature increases by 20-30°C [Kaluarachchi and Islam, 1995]. Typically, the viscosity of a liquid decreases as the temperature increases, but the viscosity of gases increases with temperature.

Application of heat to the unsaturated zone can be done by injection of hot gases (steam or air) or direct application of electrical heat energy into the ground. Through numerical modelings in one- and two-dimensional unsaturated domains, Islam and Kaluarachchi [1995] examined the effect of hot air (from 20 ^{o}C to 90 ^{o}C) on the recovery of hydrocarbons; Hot-air injection highly increased the recovery of medium- to low-volatile compounds such as n-dodecane, naphthalene, and n-hexylbenzene while the injection showed negligible effect on the removal of highly volatile hydrocarbons such as benzene. Steam injection is used to increase the transfer of heat to soils; The heat capacity of steam is approximately four times that of air (approximately 1 kJ/kg ^{o}C), and heat of evaporation (more than 2000 kJ/kg ^{o}C) is effective to heat soils [Davis, 1997]. Steam injection has been investigated to remove NAPL contaminants in the variably saturated zone [Falta et al., 1992; Kaslusky and Udell, 2002; Schmidt et al., 2002; Gudbjerg et al., 2004]. Due to the condensation of water, steam injection can leave behind water saturation, and contaminants may remain at high concentration in the residual [Kaluarachchi and Islam, 1995; Davis, 1997]. Steam injection may cause the

downward migration of DNAPL to a location below the steam zone [She and Sleep, 1999]. The migration occurs when DNAPL that is evaporated in the steam zone, condenses and is accumulated in the cooler soils at the edge of the heated region. To avoid the migration, the injection of mixtures of steam and air instead of pure steam has been proposed to remove DNAPL with the air at the edge [Kaslusky and Udell, 2002; Schmidt et al., 2002]. The condensation of steam can also reduce gas permeability in porous media [Kaluarachchi and Islam, 1995].

Electrical energy can be applied directly into the ground to heat soil and injected air. For soil venting experiments, Lingineni and Dhir [1992] used a resistance heater at the inlet of one-dimensional column to heat both soil and air. They presented the propagation of evaporation fronts (location of minimum temperature due to volatilization) and thermal fronts (location that soil temperature increases mainly due to heat conduction) during experimental periods. Lingineni and Dhir [1992] suggested that thermal venting is highly effective when thermal fronts move faster than evaporation fronts do; The rate of thermal-front movement depends mostly on the ratio of energy contents of air and soil and air flow rate; and the rate of evaporation-front movement depends on residual saturation level, air flow rate, and the volatility of contaminants. Due to enthalpy for NAPL vaporization, sharp temperature drop occurred around the evaporation front.

Electrical heating has been proven effective in sandy media, and it also has a greater potential than steam to be effective in less permeable media such as clays [Davis, 1997]. Gauglitz et al. [1994] conducted field tests of six-phase soil heating with venting to remove TCE and PCE in clay soils. In the tests, electrical resistive heating effectively

heated a clay zone and maintained at about 100^{o}C. As venting removes vaporized soil water, air permeability increased. During heating, off-gas concentrations of TCE and PCE showed little change, but comparison of contaminant concentrations in soil samples between pre- and post-tests indicated substantial soil remediation. Through two-dimensional laboratory experiments, Heron et al. [1998] showed that resistive heating and SVE is very effective in removing dissolved TCE. No temperature drop was detected because of no NAPL. In a review of rate-limited mechanisms, they pointed out that the major effect of heating on TCE removal was on the increase in volatility of TCE. Fotinich et al. [1999] examined the effect of hot air on the removal of diesel at two different flow rates and inlet temperatures (60 and 90^{o}C) in a soil-venting system. Their column experiments showed that constant supply of hot air lead a steady increase in temperature without any significant temperature drop due to evaporation of diesel components. They suggested that temperature may have greater effect on determining total cleanup time than injection/extraction rate. The increase in temperature from 60 to 90 ^{o}C reduced the cleanup time by a factor of 4.5 while the threefold increase in air flow rate (from 2.9 cm/s to 8.7 cm/s in a superficial velocity) reduced the time by a factor of 3.75.

TEV system involves a variety of parameters because of the change in physical and chemical properties with temperature. The applicability and performance could be predicted on the basis of site-specific hydro-geological conditions and the properties of target contaminants. To obtain an optimized design of thermal venting for a contaminated site, we need to understand the behavior of fluid and contaminants in subsurface systems. Several options of TEV under given situations could be set and their performance will be

evaluated to choose a final option. The TEV study in this thesis investigates fluid flow and contaminant transport under nonisothermal conditions. The transport of heat and its effect on TCE removal are also examined.

CHAPTER III

DENSITY-DRIVEN TRANSPORT OF CONTAMINANTS IN A VARIABLY SATURATED ZONE

As discussed in Chapter II, density gradients in gas phase generate gas flow in a variably saturated zone, and the gas flow constantly interacts with water flow, becoming a multiphase flow. Thus, contaminants will migrate in the multiphase flow. In this chapter, four main topics are addressed: (i) governing equations for a multiphase flow and contaminant transport in each phase; (ii) numerical schemes to solve the equations; (iii) verification of TechFlow^{MP} model developed here using numerical and experimental data published in literature; and, (iv) investigation of the effect of important parameters on density-driven transport of contaminants. The effect of the density-driven transport on dissolved contaminant plume development in the saturated zone is examined through various applications, and a multiphase flow in the unsaturated zone is also addressed.

3.1 Governing Equations

Contaminant transport in a multiphase flow can be expressed in terms of three fundamental equations: (i) flow equations for gas and water phases; (ii) momentum equation; and, (iii) contaminant transport equations. These equations are highly coupled: For example, flow equations are linked by capillary pressures and saturation levels of each phase. Momentum equation, expressed as Darcy's law equation, depends on phase saturation levels and contaminant concentrations that may change density and viscosity of fluid. Contaminant transport equations are connected to each other through mass

transfer processes. Flow and transport equations are linked in terms of mass transfer and concentration. Subsurface environments consist of four phases (water, gas, NAPL, and solid soil). Among these phases, water and gas phases are mobile, and saturation levels of NAPL at source zones change due to mass transfer between phases (water-NAPL and/or gas-NAPL).

Density and viscosity of gas phase are defined as a function of contaminant concentrations and/or gas pressure. Mass transfer between phases occurs through dissolution and volatilization of NAPL, water-gas partitioning, and sorption. These processes are frequently simplified by local equilibrium assumptions, but the local equilibrium status between mobile phases is rarely achieved in field applications [Mackay et al., 1991; Thomson et al., 1997]. Non-equilibrium processes are hard to describe in a convenient mathematical form [Miller et al., 1990; Powers et al., 1991; Wilkins et al., 1995], so a first-order relationship is commonly adapted to express mass transfer between phases [Sleep and Sykes, 1989; Thomson et al., 1997]. In this study, a first-order relationship is also used to describe dissolution, volatilization, and water-gas partitioning of organic compounds in porous media. Biological transformations of organic contaminants, discussed in the next Chapter IV, are expressed as a first-order relationship or Michaelis-Menten equation.

3.1.1 Multiphase Flow Equations

From mass conservation equation and Darcy's law, the governing equation of a multiphase flow can be derived [Sleep and Sykes, 1989; Thomson et al., 1997]

$$\frac{\partial\left(\phi s_f \rho_f\right)}{\partial t} = \nabla \cdot \left[\frac{\rho_f k_m k_{rf}}{\mu_f}\left(\nabla P_f + \rho_f g \nabla z\right)\right] + Q_f^{'} \tag{3.1}$$

where subscript *f* represents mobile fluids, ϕ is porosity, *s* is fluid saturation, ρ is fluid density (ML^{-3}), μ is dynamic viscosity ($ML^{-1}T^{-1}$), k_r is relative permeability, k_m is intrinsic permeability tensor for soil media (L^2), P is fluid pressure ($ML^{-1}T^{-2}$), g is the gravitational constant (LT^{-2}), z is elevation (L), and $Q_f^{'}$ represents the strength of sources/sinks of mass ($ML^{-3}T^{-1}$). Flow equations are linked by capillary pressures at an interface between phases [Parker et al., 1987; Thomson et al., 1997]

$$P_{cgw} = P_g - P_w \tag{3.2}$$

$$P_{cnw} = P_n - P_w \tag{3.3}$$

where P_{cgw}, P_{cnw}, P_g, P_w, P_n are gas-water capillary pressure, NAPL-water capillary pressure, gas pressure, water pressure, and NAPL pressure ($ML^{-1}T^{-2}$), respectively. The sum of saturation of three phases (water, gas, and NAPL) is

$$s_w + s_g + s_n = 1 \tag{3.4}$$

In this study, since a NAPL is considered as an immobile residual, the change in NAPL saturation occurs only due to vaporization and/or dissolution. The saturation of NAPL, s_n, can be nonzero only in NAPL source zones, and its saturation levels will be assigned as initial conditions. Also, if the saturation level of an immobile NAPL is small relative to that of water or gas and the pressures of gas and water phases are independent on the pressure of immobile NAPL, the presence of NAPL can be disregarded in solving water and gas flow equations [Sleep and Sykes, 1989; Thomson et al., 1997]. Under this condition, water and gas flow equations are solely linked by Equation (3.2) while

Equation (3.3) can be excluded from fluid flow computations. In this study, two nonlinear flow equations for water and gas phases are considered to be coupled by Equations (3.2) and (3.4).

Water Flow Equation

Since both saturation and pressure of water phase vary with depth in the unsaturated zone, from Equation (3.1), water flow equation for a variably saturated zone can be expanded as follows [Bear and Bachmat, 1990; Diersch and Perrochet, 1999]:

$$s_w S_s \frac{\partial \psi_w}{\partial t} + \phi \frac{\partial s_w}{\partial t} = \nabla \cdot \left[\frac{\rho_w k_m k_{rw} g}{\mu_w} \left(\nabla \psi_w + \nabla z \right) \right] + Q_w \tag{3.5}$$

where subscript w represents water phase, $S_s = \left[(1-\phi)\alpha + \phi \beta_w \right] \rho_w g$ is a specific volumetric storativity (L^{-1}), $\psi_w = P_w / \rho_w g$ is water-equivalent pressure head of water phase (L), $\beta_w = (1/\rho_w)(d\rho_w / dP_w)$ is the compressibility of water under an isothermal condition (LT^2M^{-1}), $\alpha = (1/V_t)(dV_t / dP_w)$ is soil matrix compressibility (LT^2M^{-1}), V_t is a bulk volume of porous media element (L^3), and $Q_w = Q_w^{'} / \rho_w$ is the strength of sources/sinks of water phase (L^{-1}). In Equation (3.5), the effect of dissolved contaminants on water density is assumed to be negligible. Thus, water density is set to be constant under an isothermal condition.

For a gas-water system, in which the two phases are mobile, the relationship between effective water saturation and gas-water capillary pressure is given in Equations (2.6)-(2.8), and, as given in Equations (2.9) and (2.11), relative permeability of water phase can be written in terms of effective water saturation. In this study, van Genuchten model given by van Genuchten [1980] and Parker et al. [1987] is used to define closed-

form expressions for capillary pressure-saturation and saturation-relative permeability relationships.

Boundary conditions (B.C.) for Equation (3.5) are written as

Dirichlet (type 1) B.C. $$\psi_w = \psi_{w\Gamma} \tag{3.6}$$

Newman (type 2) B.C. $$\frac{\partial \psi_w}{\partial \vec{n}} = f_w \tag{3.7}$$

where $\psi_{w\Gamma}$ is water pressure head on a boundary (L), f_w is a value of water pressure head gradient, and $\vec{n}$ is a unit vector normal to a boundary (L).

Gas Flow Equation

From multiphase flow Equation (3.1), as density and saturation of gas phase vary in the unsaturated zone, gas flow equation can be written as follows:

$$\phi s_g \frac{\partial \rho_g}{\partial t} + \phi \rho_g \frac{\partial s_g}{\partial t} = \nabla \cdot \left[\frac{\rho_g k_m k_{rg}}{\mu_g} \rho_w g \left(\nabla \psi_g + \frac{\rho_g}{\rho_w} \nabla z \right) \right] + I_g + Q_g \tag{3.8}$$

where subscript g represents gas phase, $\psi_g = P_g / \rho_w g$ is water-equivalent pressure head of gas phase (L), and I_g indicates mass transfer of contaminants due to partitioning processes of contaminants between phases ($ML^{-3}T^{-1}$).

Under an isothermal condition, the density of a gas mixture in Equation (3.8) is a function of gas pressure and concentration of contaminants. The density of a gas mixture containing vapors of multi-species can be expressed as [Thomson et al., 1997]:

$$\rho_g(P_g, C) = \rho_{air} + \gamma_g \psi_g + \sum_{i=1}^{N} C_g^i \left(1 - \frac{\rho_{air}}{\rho_v^i} \right) \tag{3.9}$$

where ρ_{air} is pure air density (ML^{-3}), N is the number of contaminants, γ_g is the compressibility of gas phase (T^2L^{-2}), ρ_v^i is density of pure vapor of i^{th} contaminant

(ML^{-3}), C_g^i is the concentration of i^{th} contaminant in the gas phase (ML^{-3}). Assuming that a gas mixture obey the ideal gas law, the compressibility, γ_g, can be determined by,

$$\gamma_g = \frac{d\rho_g}{d\psi_g} = \frac{M_g}{RT} \tag{3.10}$$

where M_g is an averaged molecular weight of the gas mixture. Substituting Equations (3.9) and (3.10) into the time derivative of gas density at the first term on the left-hand side of Equation (3.8) yields

$$\frac{\partial \rho_g}{\partial t} = \frac{M_g}{RT}\frac{\partial \psi_g}{\partial t} + \sum_{i=1}^{N}\left(1 - \frac{\rho_{air}}{\rho_v^i}\right)\frac{\partial C_g^i}{\partial t} \tag{3.11}$$

Volatilization of immobile NAPL and gas-water partitioning of multispecies can be significant sources or sinks and should be considered [Sleep and Sykes, 1989; Thomson et al., 1997]. By applying a first-order relationship for the mass transfer processes, we obtain

$$I_g = \sum_{i=1}^{N} \phi s_g \left[\lambda_V^i \left(C_{ge}^i - C_g^i\right) + \lambda_H^i \left(HC_w^i - C_g^i\right)\right] \tag{3.12}$$

where λ_V^i and λ_H^i are the first-order mass transfer coefficients (T^{-1}) of i^{th} contaminant for NAPL/gas and water/gas, respectively, C_{ge}^i is the maximum concentration of i^{th} contaminant in gas phase, C_w^i is the concentration of i^{th} contaminant in water phase, and H is a dimensionless Henry's law coefficient. Substituting Equations (3.11) and (3.12) into Equation (3.8) yields,

$$\phi s_g\left(\frac{M_g}{RT}\frac{\partial \psi_g}{\partial t}+\sum_{i=1}^{N}\left(1-\frac{\rho_{air}}{\rho_v^i}\right)\frac{\partial C_g^i}{\partial t}\right)+\phi\rho_g\frac{\partial s_g}{\partial t}$$
$$=\nabla\left[\frac{\rho_g k_m k_{rg}}{\mu_g}\rho_w g\left(\nabla\psi_g+\frac{\rho_g}{\rho_w}\nabla z\right)\right]+\sum_{i=1}^{N}\phi s_g\left[\lambda_V^i\left(C_{ge}^i-C_g^i\right)+\lambda_H^i\left(HC_w^i-C_g^i\right)\right]+Q_g \tag{3.13}$$

In Equation (3.13), relative permeability of gas phase is written in terms of effective water pressure [Parker et al., 1987], and the permeability can be estimated by van Genuchten model shown in Equation (2.12). Viscosity of low-pressure multicomponent gas mixture is estimated by Wilke's semi-empirical method [Reid et al., 1987],

$$\mu_g=\sum_{i=1}^{N}\frac{x_i\mu_i}{\sum_{j=1}^{N}x_j\Phi_{ij}} \tag{3.14}$$

with

$$\Phi_{ij}=\frac{1}{\sqrt{8}}\left(1+\frac{M_i}{M_j}\right)^{-1/2}\left[1+\left(\frac{\mu_i}{\mu_j}\right)^{1/2}\left(\frac{M_j}{M_i}\right)^{1/4}\right]^2 \tag{3.15}$$

where μ_g, μ_i, and μ_j are viscosities of gas mixture and pure vapors of i^{th} and j^{th} species, respectively, x_i is a fractional molar concentration of i^{th} species, and M_i and M_i are molecular weights of i^{th} and j^{th} species, respectively.

Boundary conditions for Equation (3.13) are:

$$\text{Dirichlet (type I) B.C. } \psi_g=\psi_{g\Gamma} \tag{3.16}$$

$$\text{Newman (type II) B.C. } \frac{\partial\psi_g}{\partial\vec{n}}=f_g \tag{3.17}$$

where $\psi_{g\Gamma}$ and f_g are a gas pressure head and a gas-pressure-head gradient in a boundary, respectively, and $\vec{n}$ is a unit vector normal to a boundary.

3.1.2 NAPL Equation

The change in saturation of immobile NAPL occurs as a result of its vaporization into gas phase and/or dissolution into water phase, and the change can be expressed using first-order relationships as follows:

$$\frac{\partial}{\partial t}\left(\rho_n \phi s_n\right) = \sum_{i=1}^{N}\left[-\phi s_w \lambda_D^i \left(C_{we}^i - C_w^i\right) - \phi s_g \lambda_V^i \left(C_{ge}^i - C_g^i\right)\right] \tag{3.18}$$

where ρ_n is NAPL density (ML^{-3}), λ_D^i is a first-order coefficient for dissolution of i^{th} contaminant (T^{-1}), and C_{we}^i is the maximum concentration (solubility) of i^{th} contaminant in water phase (ML^{-3}).

3.1.3 Mass Continuity Equation

The equation for advective-dispersive transport of i^{th} species in mobile phases (water (w) and gas (g)) will be written as

$$\frac{\partial\left(\phi s_f C_f^i\right)}{\partial t} = \nabla\left(\phi s_f D_f^i \nabla C_f^i\right) - \nabla\left(q_f C_f^i\right) + I_f^i + Q_f C_f^{*i} \tag{3.19}$$

where superscript i and subscript f represent indexes of contaminants and fluid phases, respectively; C is a concentration of contaminants (ML^{-3}); D and q are a dispersion tensor (L^2T^{-1}) and Darcy flux (LT^{-1}), respectively; I indicates inter-phase mass transfers and biological reactions of contaminants ($ML^{-3}T^{-1}$); C^* is specified concentrations of contaminants at a source/sink; and, Q is a strength of sources/sinks (T^{-1}). Darcy velocity for each fluid flow through porous media, estimated by Darcy's law, can be written as

$$q_f = -\frac{k_m k_{rf}}{\mu_f} \rho_w g \left(\nabla \psi_f + \frac{\rho_f}{\rho_w} \nabla z \right) \tag{3.20}$$

The dispersion tensor of i^{th} species in mobile phase *f*, D_f^i, is defined by [Bear, 1972]

$$D_{f,mn}^i = \alpha_T \left| v_f \right| \delta_{mn} + (\alpha_L - \alpha_T) \frac{v_{f,m} v_{f,n}}{\left| v_n \right|} + \tau_f D_f^{*i} \delta_{mn} \qquad m,n = x,y,z \tag{3.21}$$

where α_L and α_T are longitudinal and transversal dispersivity of soil media, respectively, $v_f = q_f / \phi s_f$ is pore velocity of a specified phase, τ is tortuosity, D^* is a molecular diffusion coefficient, and δ_{mn} is the Kronecker delta. The empirical equation for the tortuosity of fluids, developed by Millington and Quirk [1961], can be used in porous media [Weeks et al., 1982; Mendoza and Frind, 1990a; Thomson et al., 1997],

$$\tau_f = (\phi s_f)^{7/3} / \phi^2 \tag{3.22}$$

By applying a first-order relationship to dissolution, volatilization and water-gas partitioning processes of contaminants in porous media, mass transfers for water and gas phases can be written as,

$$\left[\phi s_w \frac{dC_w^i}{dt} \right]_{MassTransfer} = \phi s_w \lambda_D^i \left(C_{we}^i - C_w^i \right) + \phi s_g \lambda_H^i \left(C_g^i - H^i C_w^i \right) \tag{3.23}$$

$$\left[\phi s_g \frac{dC_g^i}{dt} \right]_{MassTransfer} = \phi s_g \lambda_V^i \left(C_{ge}^i - C_g^i \right) - \phi s_g \lambda_H^i \left(C_g^i - H^i C_w^i \right) \tag{3.24}$$

where superscript *i* represents an index of contaminants.

Biological transformations of organic compounds depend on properties of chemical compounds and various parameters of subsurface environments, and, as discussed earlier in Chapter II, biotransformation processes are very complicated and

site-specific. To simplify the kinetics of biotransformation of chlorinated compounds, Michaelis-Menten model [Haston and McCarty, 1999; Pavlostathis and Prytula, 2000; Yu et al., 2005] or a first-order relationship [Schmidt et al., 1985; Clement et al., 2000; Dinicola et al., 2002], shown in Equations (2.3) and (2.4), respectively, have been often used, and are also implemented herein to express sequential bioreactions of contaminants. In sequential bioreactions of compounds in water phase, the reduction in a parent compound through a biotransformation means the increase in its daughter compound. In terms of the daughter compound, biotransformation processes can be written as follows:

For a first-order relationship,

$$\left[\phi s_w \frac{\partial C_w^i}{\partial t}\right]_{biorxn} = \phi s_w \lambda_B^{i-1} C_w^{i-1} - \phi s_w \lambda_B^i C_w^i \tag{3.25}$$

or for Michaelis-Menten model,

$$\left[\phi s_w \frac{\partial C_w^i}{\partial t}\right]_{biorxn} = \phi s_w \frac{k_B^{i-1} C_w^{i-1}}{K_S^{i-1} + C_w^{i-1}} - \phi s_w \frac{k_B^i C_w^i}{K_S^i + C_w^i} \tag{3.26}$$

where superscript *i-1* and *i* represent parent and daughter compounds, respectively, λ_B is a first-order biological transformation coefficient (T^{-1}), k_B is a maximum bioreaction rate ($ML^{-3}T^{-1}$), and K_S is a half-saturation constant for a bioreaction (ML^{-3}). In this study, biological reactions are considered to be occurred only in water phase because most microorganisms for biological reactions exist in water phase.

Sorption of dissolved contaminants on soil particles retards the transport of contaminants, and the sorption capacity depends on physical and chemical properties of soil media. Due to the hydrophobic effect of VOCs, sorption of dissolved VOCs onto soil particles are much faster than the partitioning process between gas and water phase, so a

linear sorption equilibrium can be used. Under such equilibrium status, the change in the concentration of a sorbed contaminant onto soil particles is directly proportional to that of the dissolved contaminant. The relationship is expressed as

$$\left[\frac{\partial\left(\rho_b C_s^i\right)}{\partial t}\right]_{sorption} = -\rho_b K_D^i \frac{\partial C_w^i}{\partial t} \tag{3.27}$$

where superscript *i* represents a target compound, C_s^i is the concentration of sorbed contaminant in soil phase ($M_{compound} M_{soil}^{-1}$), ρ_b is a bulk density of the soil phase ($M_{soil} L^{-3}$), K_D^i is a sorption coefficient ($L^3 M_{soil}^{-1}$). As all surface of soil particles are covered preferentially by water, sorption of dissolved contaminants onto solid soil phase is considered while direct sorption of vaporized contaminants onto dry soil surface is excluded in this study. From Equations (3.23) through (3.27), the inter-phase mass transfer, I_f^i, for water (*w*) and gas (*g*) phases in Equation (3.19) will be written as

$$I_w^i = \left[\phi s_w \frac{dC_w^i}{dt}\right]_M + \left[\phi s_w \frac{\partial C_w^i}{\partial t}\right]_{biorxn} + \left[\frac{\partial\left(\rho_b C_s^i\right)}{\partial t}\right]_{sorption} \tag{3.28}$$

$$I_g^i = \left[\phi s_g \frac{dC_g^i}{dt}\right]_M \tag{3.29}$$

Substitution of Equations (3.28) and (3.29) into Equation (3.19) yields transport equations of sequentially-bioreactive contaminants in water and gas phases as follows:

For water phase, in a case of first-order bioreactions

$$\begin{aligned}\left(\phi s_w + \rho_b K_D^i\right)\frac{\partial C_w^i}{\partial t} &= \nabla\left(\phi s_w D_w^i \nabla C_w^i\right) - \nabla\left(q_w C_w^i\right) + \phi s_w \lambda_D^i \left(C_{we}^i - C_w^i\right) \\ &+ \phi s_g \lambda_H^i \left(C_g^i - H^i C_w^i\right) + \phi s_w \lambda_B^{i-1} C_w^{i-1} - \phi s_w \lambda_B^i C_w^i + Q_f' C_f^{i*}\end{aligned} \tag{3.30}$$

,or in a case of Michaelis-Menten-type bioreactions

$$\left(\phi s_w + \rho_b K_D^i\right)\frac{\partial C_w^i}{\partial t} = \nabla\left(\phi s_w D_w^i \nabla C_w^i\right) - \nabla(q_w C_w^i) + \phi\, s_w \lambda_D^i \left(C_{we}^i - C_w^i\right)$$
$$+ \phi\, s_g \lambda_H^i \left(C_g^i - H^i C_w^i\right) + \phi s_w \frac{k_B^{i-1} C_w^{i-1}}{K_S^{i-1} + C_w^{i-1}} - \phi s_w \frac{k_B^i C_w^i}{K_S^i + C_w^i} + Q_f^{'} C_f^{i*} \tag{3.31}$$

and for gas phase

$$\phi s_g \frac{\partial C_g^i}{\partial t} = \nabla\left(\phi s_g D_g^i \nabla C_g^i\right) - \nabla(q_g C_g^i) + \phi\, s_g \lambda_V^i \left(C_{ge}^i - C_g^i\right)$$
$$- \phi\, s_g \lambda_H^i \left(C_g^i - H^i C_w^i\right) + Q_f C_f^{i*} \tag{3.32}$$

Four types of boundary conditions can be considered for Equations (3.30)-(3.32) as follows [Frind, 1982; Sleep and Sykes, 1989; Mendoza and Frind, 1990a]:

(i) Dirichlet (type I) conditions are

$$C_w^i = C_{wo}^i \tag{3.33}$$

$$C_g^i = C_{go}^i \tag{3.34}$$

where C_{wo} and C_{go} are specified values of contaminant concentrations in water and gas phases on boundaries, respectively.

(ii) Neuman (type II) conditions are

$$\phi s_w D_w^i \frac{\partial C_w^i}{\partial n} = b_{wo}^i \tag{3.35}$$

$$\phi s_g D_g^i \frac{\partial C_g^i}{\partial n} = b_{go}^i \tag{3.36}$$

where b_{wo} and b_{go} are specified dispersive fluxes of contaminants in water and gas phases on boundaries, respectively.

(iii) Cauchy (type III) conditions are

$$\left(-\phi s_w D_w^i \nabla C_w^i + q_w C_w^i\right)\vec{n} = q_{wn} C_{wo}^i \tag{3.37}$$

$$\left(-\phi s_g D_g^i \nabla C_g^i + q_g C_g^i\right)\vec{n} = q_{gn} C_{go}^i \tag{3.38}$$

where q_{wn} and q_{gn} are Darcy fluxes of water and gas on boundaries, respectively, and $\vec{n}$ is unit vectors normal to the boundaries.

(iv) Free exit boundary can be used in cases that contaminants reach an exit boundary, in which boundary values can not be specified [Frind, 1988; Thomson et al., 1997]. In the boundary, the natural boundary term, $\phi s_w D_w \partial C_w / \partial n$, containing unknown boundary values, will remain unchanged.

For contaminant transport in gas phase, the ground surface can be treated as a stagnant boundary layer due to vegetation and surface roughness. The flux across the boundary layer can be represented as [Thibodeaux, 1981; Mendoza and Mcalary, 1990]

$$b_{go} = \frac{D_g^i}{\delta_g}(C_{gs}^i - C_{atm}^i) \tag{3.39}$$

where b_{go} is a contaminant flux, δ_g is the thickness of a stagnant boundary layer of gas phase at the ground surface, C_{gs} is a contaminant concentration in soil gas phase at the ground surface, and C_{atm} is a contaminant concentration at the top of the layer. The C_{atm} is usually set to zero for the atmosphere. This approach can be applied to a groundwater table boundary, which is usually assumed to be impermeable to gas phase. A contaminant flux across the layer of the table boundary can be expressed as [Mendoza and Frind, 1990a; Mendoza and Mcalary, 1990]

$$b_{wo} = \frac{D_w^*}{\delta_w}(C_{wt}^i - C_{wb}^i) \tag{3.40}$$

where b_{wo} is a contaminant flux across a groundwater table boundary, D_w^* is an effective aqueous dispersion coefficient, δ_w is the thickness of the groundwater table boundary layer, and C_{wt} and C_{wb} are contaminant concentrations in water phase at the top and bottom of the boundary layer, respectively. Equations (3.39) and (3.40) imply a linear approximation of contaminant dispersion through stagnant boundary layers in gas and water phases, respectively.

3.2 Numerical Solution

Using Galerkin finite-element technique [Huyakorn and Pinder, 1983], a three-dimensional numerical model, TechFlow^{MP}, was developed to solve coupled equations for multiphase flow and multispecies transport. The model uses three-dimensional isoparametric rectangular prism element and a linear interpolation function, which are described in detail in Appendix A.

Water flow equation shown in Equation (3.5) can be solved as water pressure-head (ψ_w)-form, water saturation (s_w)-form, or mixed ($\psi_w - s_w$)-form. The water saturation-based equation (s_w-form) is mass conservative [Celia et al., 1990; Diersch and Perrochet, 1999], but the equation can be applied only to the unsaturated zone because water saturation is not a variable in the saturated zone. Since water pressure-head is continuous and unique in the saturated and unsaturated zones, it has been widely applied to both zones. However, water pressure-head form produces significant global mass balance errors, which come from the time derivative term of water pressure head [Celia et al., 1990]. To overcome these errors, Celia et al. [1990] introduced a modified Picard

method, which uses the mixed form. They showed that the mixed form produces accurate mass conservative solutions, and it can be used for both the unsaturated and saturated zones. The mixed form has been successfully applied by Rathfelder and Abriola [1994] and Lehmann and Ackerer [1998]. The modified Picard method for the mixed form solely uses pressure head as a primary variable. To solve water flow equation in a single-phase system, Diersch and Perrochet [1999] introduced a primary variable switching scheme, which selectively uses water pressure head or water saturation as a primary variable in the mixed form according to water saturation level of each element. The scheme takes advantage of s_w-form and ψ_w-from by separately handling the unsaturated and saturated zones, but it brings great complexity in applying to a multiphase system. In this study, since modeling domains are highly coupled multiphase and multicomponent systems and the modified Picard method has been successfully applied in the unsaturated and saturated zone, the method is used in modeling density-driven transport of contaminants. Thus, pressure heads of gas and water phases are selected as primary variables. A detailed description of numerical method for the modified Picard method is given in Appendix B.

Flow velocities of gas and water phases, shown in Equation (3.20), are required for the solution of transport equations. In a density-driven flow in gas or water phases, the velocity of each phase plays an important role in contaminant transport, and has been widely discussed [Yeh, 1981; Diersch and Kolditz, 2002]. When the velocity is estimated locally at every element, discontinuity problems arise [Yeh, 1981]. To improve accuracy and overcome the discontinuity problem, Yeh [1981] proposed a method for globally continuous Darcy velocity, in which a finite element technique is applied to Equation

(3.20), and the method has been used to successfully solve transport problems in a variably saturated zone [Srivastava and Yeh, 1992; Yeh et al., 1993]. In this study, the continuous velocity approximation is employed to correctly simulate the density-driven advection of gas phase. The approximation method used here is summarized in Appendix C.

The time derivatives in flow and transport equations (Equations (3.5), (3.13), and (3.30)-(3.32)) are approximated by a finite difference technique. This technique commonly uses the ε-family of approximation, in which a weighted average of the time derivatives is estimated at two consecutive time steps [Reddy, 1993] (See Appendix D for details). The backward difference technique (fully implicit method, ε=1.0), which requires the least computational effort, is generally acceptable for flow equations [Frind, 1982]. However, since transport equations are more sensitive to the ε values, the equations are usually solved by semi-implicit Crank-Nicolson technique (ε=0.5) with a second-order accuracy in time. The technique reduces the smearing effects [Mendoza and Frind, 1990a]. All simulations in this study used ε=1.0 for flow equations and ε=0.5 for transport equations in each phase.

Mass lumping of time-derivative mass matrices is used to improve the stability of the solution of nonlinear flow equations because mass lumping eliminates all convergence difficulties produced in consistent forms of the matrices [Frind, 1982; Celia et al., 1990; Rathfelder and Abriola, 1994]. Mass lumping process implies that each node in an element has an equal portion of total mass stored in the element. To show the effect of mass lumping on numerical oscillations, Celia et al. [1990] compared the finite element approximation with the finite difference approach, and they concluded that

modeling the unsaturated flow, especially for infiltration into dry soils, should use a lumping procedure for time matrices. They also suggested that the modified Picard scheme with mass lumping is very reliable and robust in unsaturated flow problems. However, for a one-dimensional linear advection-dispersion transport problem, Daus et al. [1985] showed that the consistent finite element formulation produces more accurate results than the lumped formulation. For non-linear density-dependent transport problems, Frind [1982] applied mass lumping procedures to flow and transport equations, producing more stable results. In this study, we used mass lumping procedures to effectively handle non-linear problems.

Multiphase flow and transport equations are fully coupled and nonlinear. To reduce numerical difficulty due to the coupling and non-linearity, in this study, a sequentially-iterative scheme is used. This iterative scheme solves a set of decoupled system equations [Diersch and Kolditz, 2002]: water and gas flow equations, Darcy velocity equation, and transport equations are consecutively solved, and the solution procedures are repeated until all solutions are converged below specified tolerance levels. This sequential-iterative scheme has been commonly used in solving multiphase multicomponent transport simulations [Sleep and Sykes, 1989; Mendoza and Frind, 1990a; Thomson et al., 1997]. The criteria used herein for convergence of general or modified Picard scheme are [Lehmann and Ackerer, 1998]

$$\max\left|\psi^{t+1,m+1}-\psi^{t+1,m}\right| \le \varepsilon_{a,\psi}+\varepsilon_{r,\psi}\left|\psi^{t+1,m+1}\right| \qquad \text{for flow equations} \tag{3.41}$$

$$\max\left|C^{t+1,m+1}-C^{t+1,m}\right| \le \varepsilon_{a,C}+\varepsilon_{a,C}\left|C^{t+1,m+1}\right| \qquad \text{for transport equations} \tag{3.42}$$

where ε_a and ε_r are absolute and relative errors, respectively.

The length of time steps was automatically adjusted by the number of iterations done for flow and transport equations at the previous time step. The minimum and maximum time steps are set at the beginning of each simulation.

Nonlinear transport equations do not have discrete criteria for accuracy and stability. As criteria for one-dimensional linear advection-dispersion problems, Daus et al. [1985] proposed the grid Peclet number, $Pe = v\Delta l / D \le 2$, and Courant number, $Cr = v\Delta t / \Delta l \le Pe / 2$ where $v = q / \phi$ is an averaged pore water velocity, D is a dispersion coefficient, and Δl is a grid spacing or a characteristic element length. As an approximate guide, Mendoza and Frind [1990a; 1990b] used these numbers in solving two-dimensional density-driven gas flow and contaminant transport problems. In this study, we checked these two dimensionless numbers while modeling, and adjusted time steps and/or grid spacings to follow the criteria ($Pe \le 2$ and $Cr \le Pe / 2$) for these numbers.

Mass balance calculation is used to determine the fate and transport of contaminant mass in each phase over time and to verify mass conservation during simulations. The calculation scheme was well described by Huyakorn and Pinder [1983], and was used by Mendoza and Frind [1990a]. The details of the method used for mass balance calculation are given in Appendix E.

3.3 Model Verification

3.3.1 Infiltration into a Homogeneous Soil Column

Water infiltration into a homogeneous medium having very low initial content of water is simulated in this problem. The infiltration occurs due to constant water pressure head at the top of a soil column. The problem has been widely tested in previous works [Celia et al., 1990; El-kadi and Ling, 1993; Li, 1993; Rathfelder and Abriola, 1994; Lehmann and Ackerer, 1998; Diersch and Perrochet, 1999]. The profile of a soil column used by the previous studies are as follows (Figure 3.1): the length of column = 30 cm; the intrinsic permeability of soil medium = 9.35247×10^{-12} m^2, which is equivalent to hydraulic conductivity = 9.22×10^{-5} m/s with $\rho_w = 998.2$ kg/m^3 (20^oC), $g = 9.807$ m/s^2, and $\mu_w = 993\times10^{-6}$ kg/m s; $\phi = 0.368$; the residual saturation of water $s_m = 0.277$; and $n = 2$ and $\alpha_{gw} = 3.35$ m^{-1}, which are used to estimate relative permeability and saturation of water phase. The initial and boundary conditions are: initial water-equivalent pressure head $\psi_{wo} = -10\,m$, constant pressure head $\psi_w = -0.75\,m$ at the top of the column, and $\psi_w = -10\,m$ at the bottom as boundary conditions. Constant atmospheric pressure head $\psi_g = 0$ m and a specific volumetric storativity $S_s = 0$ were set throughout the column. A uniform mesh was used where $\Delta z = 0.25$ cm. The simulation time is 6 hours with various time-steps being used in time integration, dt =10-40 sec. The convergence criteria, $\varepsilon_{a,\psi}$ and $\varepsilon_{r,\psi}$, were 1.0*e*-5. The water flow equation, Equation (3.5), was solved to investigate the change in water saturation, which is determined by gas-water capillary pressure head. The simulation results are presented in Figure 3.2 (a) and (b) as profiles of water pressure

head and water saturation with depth, respectively. In Figure 3.2 (a), the results of water pressure head of this study at t = 6 hrs show very good agreement with the Philip semianalytical solution and other numerical results given by Lehmann and Ackerer [1998].

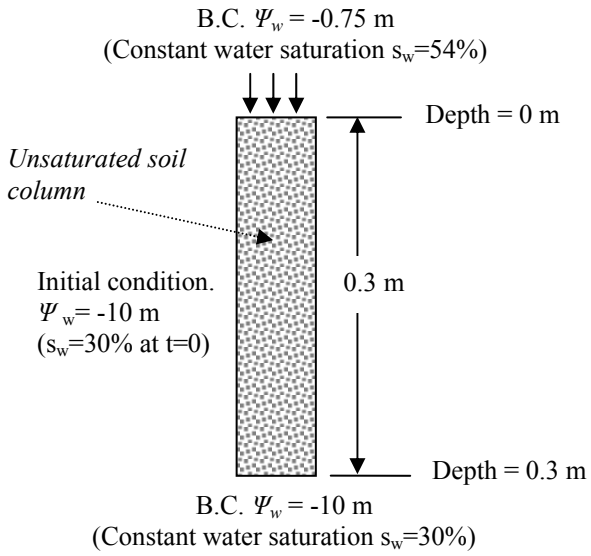

Figure 3.1 Diagram for infiltration into a homogenous medium column

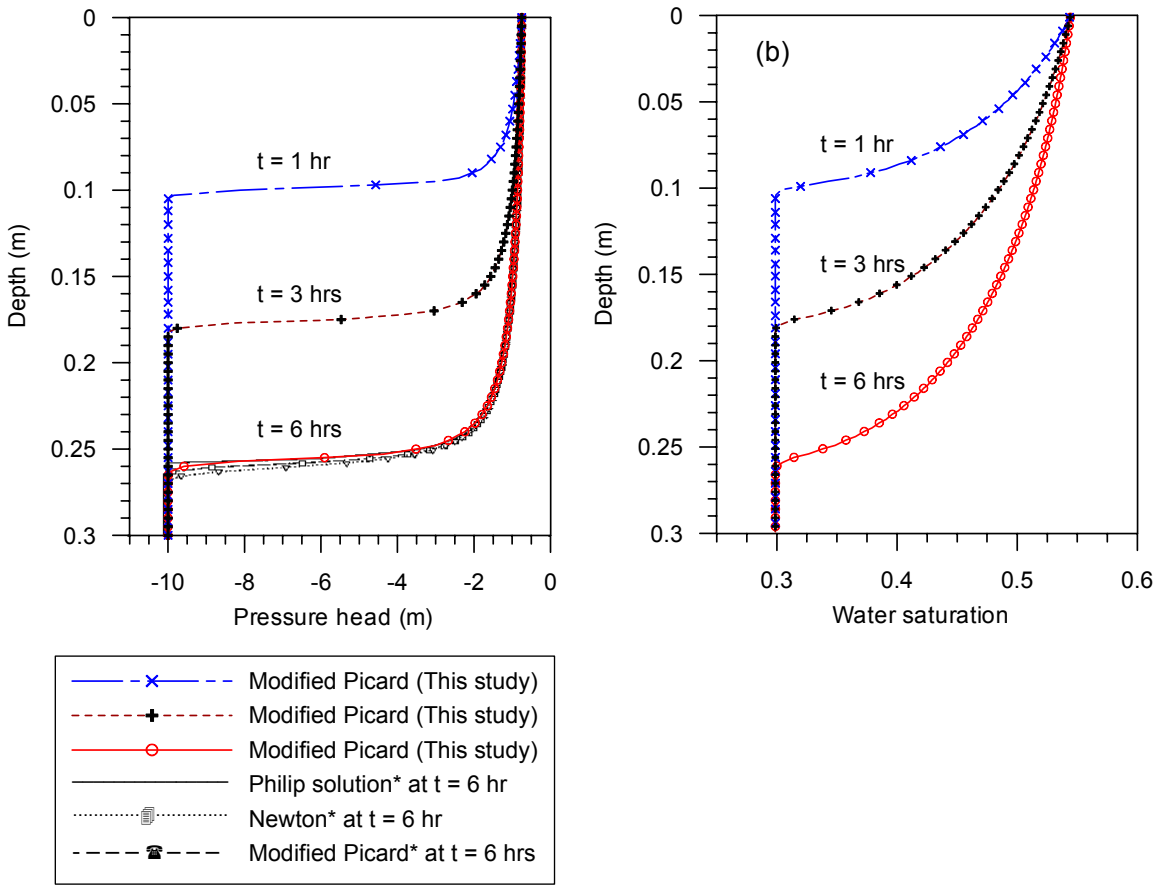

Figure 3.2 Temporal variations of water pressures and water saturation levels. (a) The changes in water pressure head distribution and (b) water saturation level with time. The * in (a) indicates previous results given by Lehmann and Ackerer [1998].

3.3.2 Advective-dispersive Transport of Chlorinated Solvent Vapor in the Unsaturated Zone

Mendoza and Frind [1990b] examined the effect of the density-driven advection of gas phase in a two-dimensional unsaturated zone. In this problem, flow of gas phase and transport of a conservative volatile organic compound are simulated in a cross-sectional plane, shown in Figure 3.3.

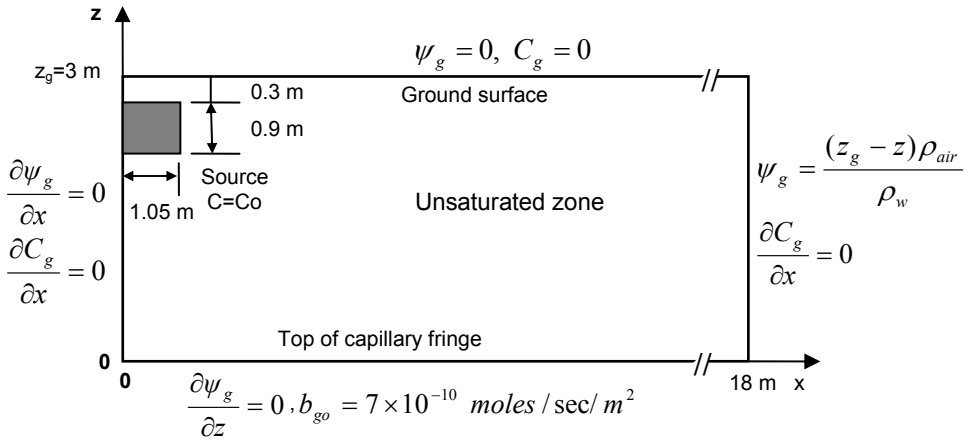

Figure 3.3 A simulation domain, a source zone, and boundary conditions

To illustrate the effect of the advective transport in gas phase, high porosity, ϕ = 0.4, and intrinsic permeability, $k = 1 \times 10^{-10}\,\mathrm{m}^2$, which favor density-driven advective transport, are used (Table 3.1). The properties of the soil medium correspond to those of coarse sand. The medium has uniform water saturation level of 20 % with a vertically 30-cm linear transition zone from z = 0.3 m to 0 m. It is assumed that water-phase is motionless with constant water-saturation levels and that local equilibrium of contaminant partitioning is achieved between water and gas phases. At the source zone, the concentration of a target contaminant, which has a molecular weight of 3.5 times that

of air, is 1.0 g/L. A variable mesh grid is used in the idealization of the problem domain, which has five spaces of 20 cm, four spaces of 5 cm, and 84 spaces of 20 cm grid in *x*-direction and uniform grid spacing of 10 cm in *z*-direction. Since TechFlow^{MP} of this study uses three-dimensional Cartesian coordinates, a layer of 10 cm thickness in *y*-direction was used to emulate a two-dimensional plane. The solution domain consists of 2790 rectangular prism elements and 5828 nodes. The run time is 4 days with a 0.1-1 hour-long time steps.

Table 3.1 Properties of a soil medium, a contaminant, and air for simulation[1)]

Parameters	*Values*
Soil medium	
Permeability, k_m	1.0×10^{-10} m^2
Porosity, ϕ	40 %
Water saturation, s_w[2)]	20 %
Residual water saturation, s_m	20 %
Pore-size index, λ	1.65 g/cm^3
Longitudinal dispersivity, α_L	0.15 m
Transverse dispersivity, α_T	0.0075 m
Temperature, T	20 °C
Generic VOC	
Molecular weight, M_C	100.625 g/mol
Molecular diffusion coefficient, D^*	9.0×10^{-6} m^2/s
Vapor viscosity, μ_C	1.0×10^{-5} Pa s
Henry's constant, H	0.17

[1)] Values are given by Mendoza and Frind [1990b].
[2)] Thirty-centimeter linear transition to full saturation at top of capillary fringe.

In Figure 3.4, the contaminant plumes for two cases are shown: diffusion-only transport and advection-dispersion transport. Values of concentration in Figure 3.4 (a) and (b) are 0.001, 0.01, and 0.1 to 1.0 at intervals of 0.1. The results of this study agree well with those given by Mendoza and Frind [1990b], and show distinct effect of density-

dependent transport of the contaminant: the plume development of contaminated gas is much larger at density-dependent transport than at diffusion-only transport. Near the source zone, advective flows are generated by the increase in density of gas mixture, and the magnitude of gas velocity depends on contaminant concentration gradients (Figure 3.4 (c)).

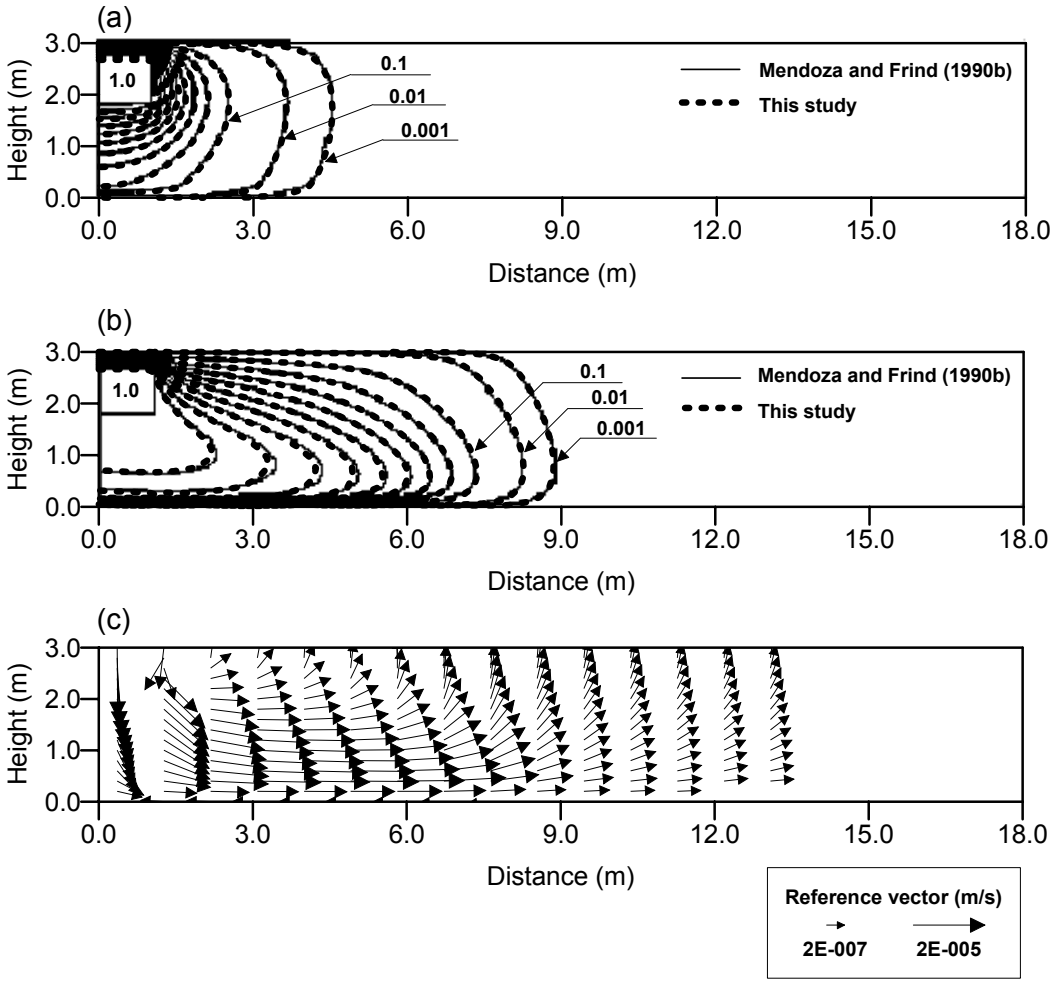

Figure 3.4 Concentration profiles and Darcy velocity at 4 days: (a) contaminant transport by diffusion only, (b) contaminant transport by diffusion, mechanical dispersion, and density-driven advection, and (c) Darcy velocity distribution in the case of the density-driven transport in gas phase

3.3.3 Laboratory Experiment of Transport of TCE Vapor in the Unsaturated Zone

A large-scale laboratory experiment was performed to simulate the transport of TCE vapor (R. L. Johnson, unpublished data, 1988), and the experimental data are used by Mendoza and Frind [1990a] in their numerical modeling. The data and a description of experimental setup are based on the paper written by Mendoza and Frind [1990a]. A large square column (10 m × 10 m) and 3 m deep, was filled with washed soil media, and one liter of TCE was introduced into 0.3-m square area at 0.45 m below the top of the column. At the top, air was continuously ventilated to remove TCE in the atmosphere, so TCE concentration on the ground surface was assumed to be zero. The concentrations of TCE at sampling points, shown in Figure 3.5 (a), are measured for three days.

To model the transport of vaporized TCE in the experiment, Mendoza and Frind [1990a] used a two-dimensional rectangular domain in axisymmetric coordinates, but, since the model developed in this study uses Cartesian coordinates and rectangular prism elements, one-eighth of a rectangular column (the experiment box) with depth 3 m is used as our domain as illustrated in Figure 3.5 (b). The domain in this study consists of 5418 nodes and 4300 rectangular prism elements. The nodal grid is composed of a space of 15 cm, four spaces of 7.5 cm, seven spaces of 15 cm, and ten spaces of 30 cm in x- and y-directions, and, from the bottom in z-direction, two spaces of 28 cm, eleven spaces of 15.25 cm, four spaces of 7.625 cm, and three spaces of 15.25 cm.

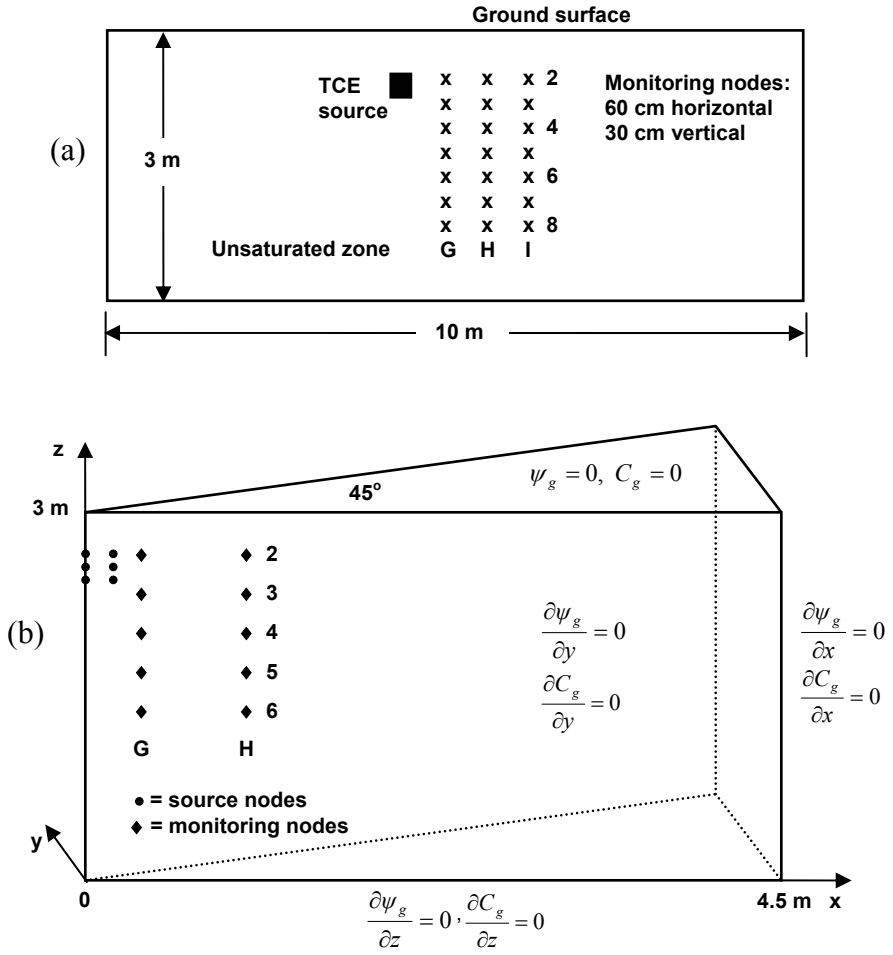

Figure 3.5 (a) Laboratory experiment setup and (b) a modeling domain for this study.

The properties of soil media used in the experiment, air, and TCE are given in Table 3.2. This study used same values of parameters for model settings reported by Mendoza and Frind [1990a]: A longitudinal dispersivity, α_L, was set to one half of the radius, up to maximum of 1.0 m, and a transverse dispersivity, α_T, was ignored. The concentration at top nodes (x = 0-0.15 m, z = 2.55 m) of a source zone was set to 75 % of the saturated vapor concentration of TCE, and that at other nodes of the source zone (x = 0-0.15 m, z = 2.39-2.47 m) was set to the saturated vapor concentration.

Table 3.2 Simulation parameters for the experiment and numerical model[1)]

Parameters	*Values*
Porous medium	
Permeability, k	5.0×10^{-11} m^2
Porosity, ϕ	35 %
Water saturation, s_w	31.43 %
Residual water saturation, s_m	31.43 %
Bulk density, ρ_b	1.65 g/cm^3
Temperature, T	10 °C
Trichloroethylene	
Molecular weight, M_{TCE}	131.4 g/mol
Saturated vapor concentration, C_{ge}	0.264 g/L
Molecular diffusion coefficient, D^*	7.6×10^{-6} m^2/s
Vapor viscosity, μ_{TCE}	0.95×10^{-5} Pa s
Henry's constant, H	0.17
Sorption coefficient, K_D	2.5×10^{-5} L/g
Air	
Molecular weight, M_{air}	28.75 g/mol
Viscosity, μ_{air}	1.80×10^{-5} Pa s
Density, ρ_{air}	1.25 g/L

[1)] Values are given by Mendoza and Frind [1990a] except air density.

A comparison of experimental breakthrough curves, previous results of an advection-dispersion simulation by Mendoza and Frind [1990a], and results of this study is shown in Figure 3.6. At three points (G3, G4, and G5), the concentration profiles

obtained from this study are slightly lower than the experimental data, but most breakthrough curves of this study show good agreement with the experimental data and the best fit curves given by Mendoza and Frind [1990a]. In Figure 3.7, concentration profiles for two cases (diffusion-only transport and density-driven transport) are given to show the effect of density-driven advection on the transport of TCE in this experiment.

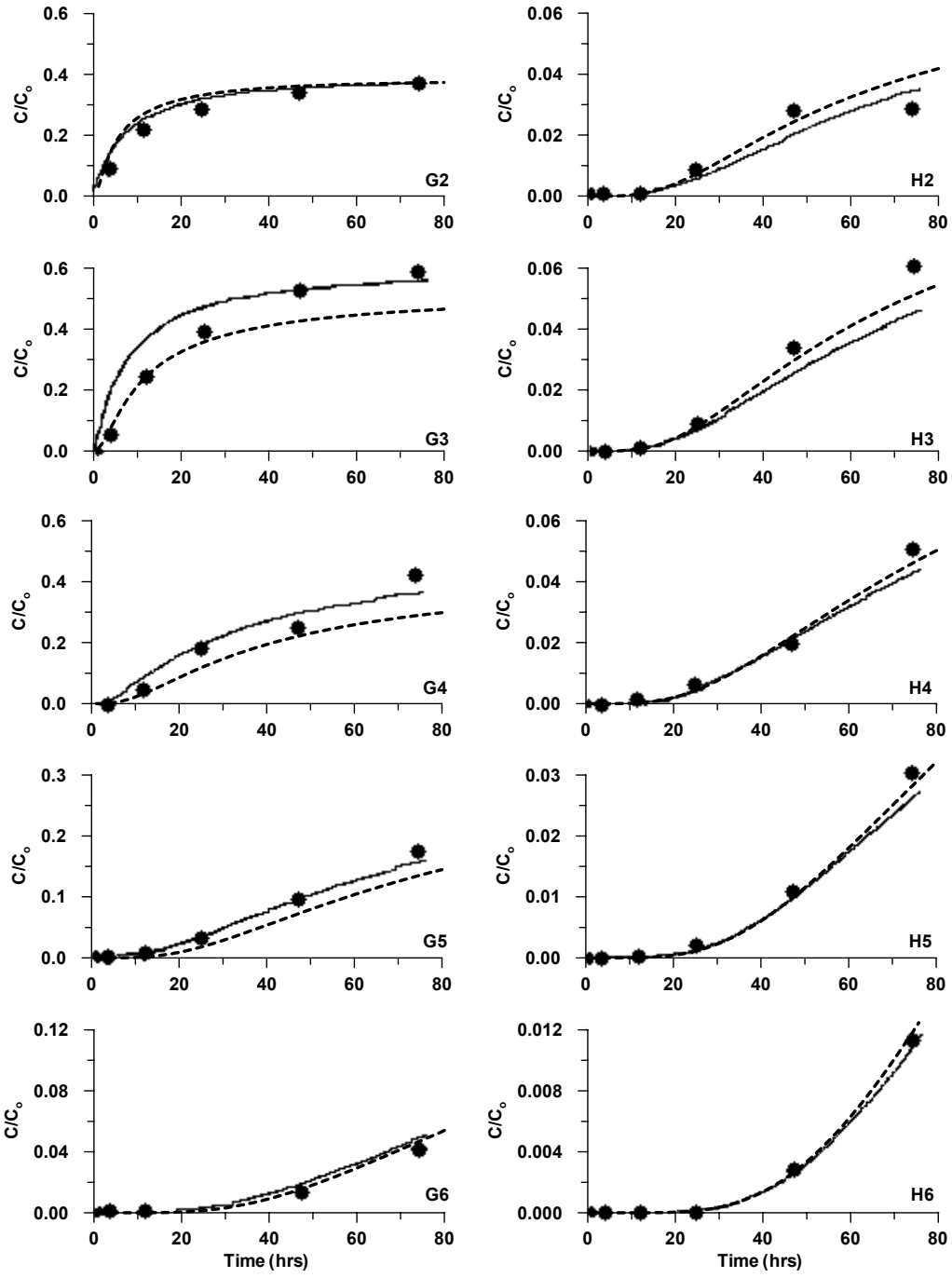

Figure 3.6 Breakthrough curves at monitoring points of experiment units: experiment data (solid circles), previous simulation results done by Mendoza and Frind [1990a] (solid lines), and simulation results of this study (dashed lines).

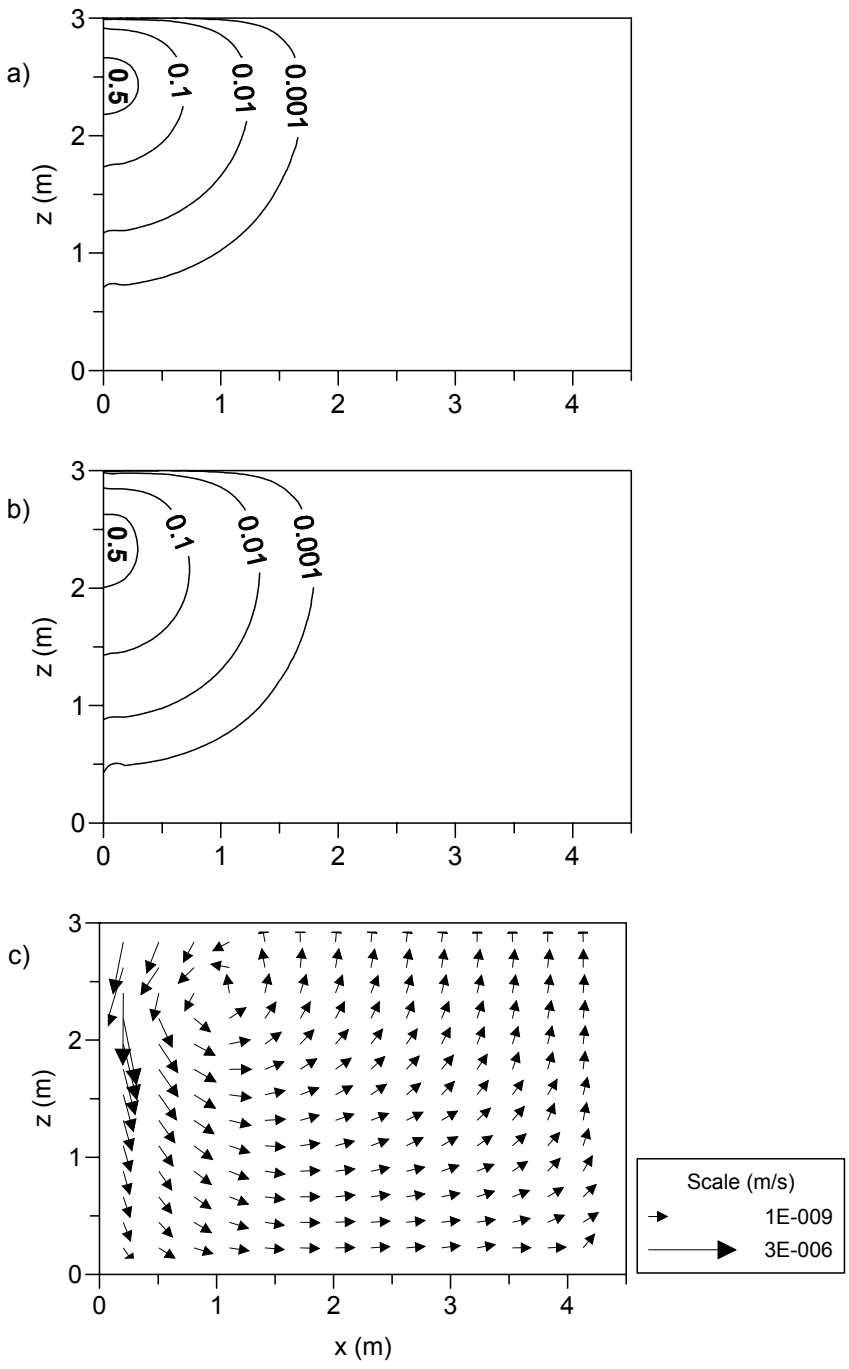

Figure 3.7 Relative concentration profiles (C/Co) and Darcy velocity at 80 hours: (a) a diffusion-only transport simulation, (b) an advective-dispersive transport simulation, and (c) Darcy velocity of gas phase in (b).

3.4 Application of Density-driven Transport of a Conservative Contaminant in a Two-dimensional Domain

3.4.1 Modeling Domain and Parameters

A two-dimensional unconfined sandy aquifer with dimensions of (200 m × 16 m) in (x, y) directions was used to simulate the density-driven transport of TCE. The domain extends from the ground surface to the fully saturated aquifer (Figure 3.8). As shown in Figure 3.8, TCE in the form of NAPL is introduced to the unsaturated zone and resides in pore spaces as an immobilized contaminant source. From the immobile source, TCE will vaporize into soil gas and dissolve into water phase, then will migrate along with the flow of gas and water phases. In this chapter, TCE is assumed to be conservative to examine solely the density-driven transport of TCE, and the biological transformations of TCE into DCEs and VC are discussed in the next Chapter IV.

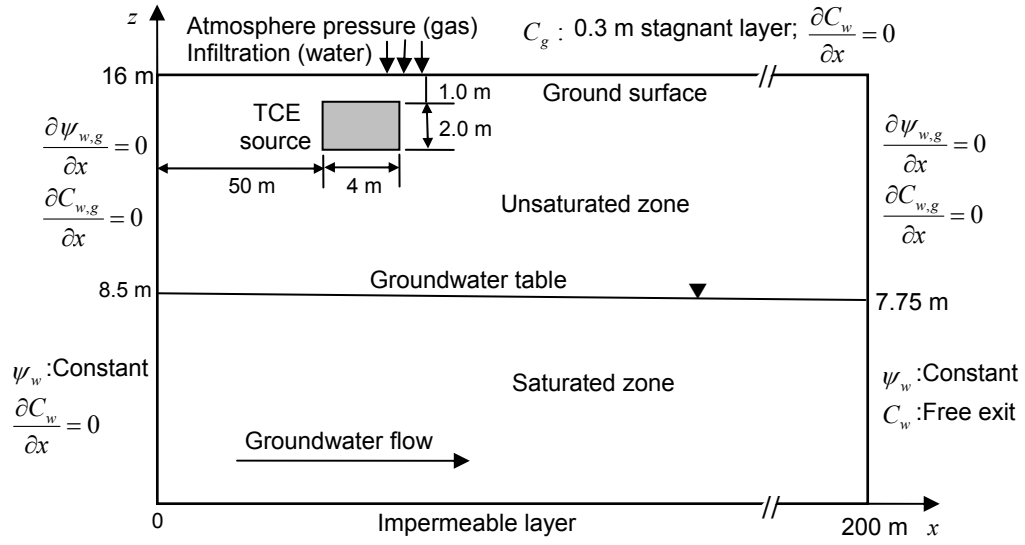

Figure 3.8 A schematic diagram of a modeling domain and site conditions

In Figure 3.8, an immobile TCE residual is set to its NAPL saturation of 5 % at distance x = 50-54 m and elevation z = 13-15 m. Initial concentrations of TCE in gas, water, and solid phases, are set to zero within the domain. As boundary conditions at the ground surface, the recharge for infiltration is 30 cm per year for water phase, and constant atmospheric pressure is applied for gas phase. For contaminant transport in gas phase, the ground surface is set to a stagnant boundary layer of 0.3 m thickness. The parameters of a soil medium, water, and gas phases used here are given in Table 3.3, and properties for TCE are listed in Table 3.4. Three different values of intrinsic permeability for soil medium are used to investigate the influence of soil permeability on contaminant transport, and one value is 1.0×10^{-10} m^2 that is equivalent to an aqueous hydraulic conductivity of 1.0×10^{-3} m s^{-1}. The water table elevation ranges from 8.5 m on the left boundary to 7.75 m on the right. First-order rate coefficients for dissolution, water-gas partitioning, and volatilization (λ_D, λ_H, and λ_V) are 1.0 d^{-1}, which were used by Thomson et al. [1997]. The model domain grid consists of 16,884 nodes and 8,200 elements, which was discretized with uniform grid spacing of 1 m in x-direction and variable grid spacing of 0.125-0.5 m in z-direction: from the bottom in z-direction, fourteen spaces of 0.5 m, three spaces of 0.25 m, six spaces of 0.125 m, six spaces of 0.25 m, and twelve spaces of 0.5 m. The run time is up to 300 days with the length of time steps ranging between initial 1 hour and 2 days, which was adjusted according to an automatic time-stepping scheme.

Mass balance calculations are performed to determine the fate and transport of contaminants in the system (details are presented in Appendix E). In the calculations, TCE mass emitted into the atmosphere or remained in the domain is estimated, and the

changes in TCE mass within each phase and within the unsaturated/saturated zones are investigated.

In order to investigate the effects of the density-driven advection in gas phase, infiltration, and permeability on contaminant transports in gas and water phases, six scenarios are studied as shown in Table 3.5. Based on the simulation results, fate and transport of TCE are analyzed: Especially, temporal and spatial distribution of TCE in the domain and TCE transfer into the groundwater in the saturated zone are examined and are compared for each case.

Table 3.3 Simulation parameters

Parameters	Values
Porous medium	
Permeability*, k	1.0×10^{-10} m^2
	7.07×10^{-11} m^2
	5.0×10^{-11} m^2
Porosity, ϕ	0.35
Residual water saturation, s_m	0.
Bulk density, ρ_b	1600 kg/m^3
Temperature, T	15 °C
Longitudinal dispersivity, α_L	1.0 m
Transverse dispersivity, α_T	0.01 m
Soil organic content, f_{oc}	2.5×10^{-5}
Parameters for the unsaturated zone	
n	2.0
α_{gw}	5.0 m^{-1}
Water	
Water molecular weight, M_w	18
Water density, ρ_w	997.3 kg/m^3
Water dynamic viscosity, μ_w	1.0×10^{-3} Pa s
Air	
Molecular weight, M_{air}	28.75
Density, ρ_{air}	1.23 kg/m^3
Viscosity, μ_{air}	1.8×10^{-5} Pa s

* Three values of soil permeability are used for six different scenarios

Table 3.4 Properties of TCE at 15°C

Parameters	Values
[a] Molecular weight	131.39
[b] Vapor density, kg/m^3	5.56
[c] Vapor dynamic viscosity, Pa s	9.38×10^{-6}
[d] Henry constant, dimensionless	0.227
[e] Molecular diffusion in air, m^2/s	7.87×10^{-6}
[f] Molecular diffusion in water, m^2/s	8.206×10^{-10}
[g] Sorption coefficient, K_{oc}, L/kg	100
[h] Vapor pressure, mmHg	41.27
[i] max. C_g, kg/m^3	0.302
[j] max. C_w, kg/m^3	1.33

[a] Montgomery [2000].
[b] Calculated by the ideal gas law.
[c] Calculated Thodos and coworkers' equation [Perry et al., 1984] based on data from Reid et al. [1987].
[d] Calculated from regression data [Gossett, 1987]:.
[e] Calculated from the Fuller, Schettler, and Giddings relation [Perry et al., 1984].
[f] Calculated by the Wilke-Chang method [Perry et al., 1984].
[g] Values from Mackay et al. [1992].
[h] Calculated using regression equation (1) on page 657 [Reid et al., 1987].
[i] Calculated from Vapor pressure by the ideal gas law.
[j] Calculated from Henry constant, $C_g = H \times C_w$.

Table 3.5 Scenarios used in simulations

Case No.	Transport mechanism in gas phase	Infiltration	Permeability
1	Diffusion-only	No	1.0×10^{-10} m^2
2	Density-driven advection + Dispersion	No	1.0×10^{-10} m^2
3	Diffusion-only	Yes	1.0×10^{-10} m^2
4	Density-driven advection + Dispersion	Yes	1.0×10^{-10} m^2
5	Density-driven advection + Dispersion	Yes	7.07×10^{-11} m^2
6	Density-driven advection + Dispersion	Yes	5.0×10^{-11} m^2

3.4.2 Effect of Density-driven Transport of TCE in Gas Phase

Through Case 1 and 2 simulations, the effects of two transport mechanisms (diffusion-only transport and density-driven transport) on TCE plume developments within water and gas phases in a variably saturated zone are compared in Figures 3.9 through 3.11. The studies on the two mechanisms for VOCs in the unsaturated zone were carried out by Mendoza and Frind [1990b] and Falta et al. [1989].

In Case 1, gas phase is assumed to be stagnant, and water flow in the unsaturated zone will be negligible without infiltration. Therefore, TCE transport in the unsaturated zone will occur mostly by molecular diffusion due to concentration gradients of TCE within water and gas phases. In fact, because TCE diffusivity in gas phase is larger by 3-orders of magnitude than that in water phase, TCE diffusion in gas phase will become a dominant mechanism to spread TCE in the unsaturated zone.

In Case 2, the change in the density of gas mixture is considered. For the conditions identified in Table 3.3, TCE has a molecular weight of 4.57 times that of air, and the density of gas mixture containing saturated TCE vapor will be about 1.47 times that of pure air. The increase in gas density due to the vaporization of TCE at the source will cause instability in gas phase and will generate an advective movement of gas. The dynamic viscosity of air is greater than that of TCE (Table 3.3), so that of a gas mixture containing TCE vapor reduces as the increase in TCE concentration within the gas mixture. In the saturated vapor pressure of TCE, the viscosity of the gas mixture decreased by about 7 % of air viscosity.

The transport of vaporized TCE for Case 1 and 2 is illustrated in Figure 3.9. In relatively high concentration zone (>10 mg/L) near the source, Case 2 has greater lateral

and vertical migration of TCE than Case 1 does. In Figure 3.9 (b) and (d), TCE concentration contours (≥100 mg/L) show downward curvatures that are mainly generated by density-driven flow of gas. In Case 2, wide high-concentration zones are located above the groundwater table, which may accelerate TCE transfer into the groundwater.

In Figure 3.9 (e), velocity profiles of gas flow show the direction and magnitude of gas flow derived by the density increase of gas phase in Case 2: After gas phase moved downward up to the groundwater table, the gas flow had lateral movement (into left or into right). The velocity profiles show significant vertical and horizontal gas flow near the source, which accelerates TCE transfer to the groundwater in the saturated zone. Reference vectors are used to represent the magnitude of each velocity and the maximum. The maximum velocity in the domain occurs as a downward velocity through the source, in which high density-gradients are expected, and the magnitude of gas velocities reduces with distance from the source. Mendoza and Frind [1990b] pointed out that the strength of density-driven transport depends on the relatively high velocities through a source zone. The dissipation of gas velocities means the decreased density effect at lower vapor concentrations. At a low concentration of TCE (1.0 mg/L), the density increase of a gas mixture due to TCE vapor is very small, approximately 0.06 % of air density. Therefore, as TCE vapor concentration becomes low, the density effects diminish, and diffusion in gas phase becomes dominant as a transport mechanism

Near the source in the unsaturated zone (for instance, approximately x = 15-90 m in Figure 3.9 (d)), diffusion and/or density-driven advection of gas phase is the main driving force to spread TCE in the unsaturated zone. The development of TCE plumes in

gas and water phases will happen mostly as follows: At first, TCE at the source vaporizes into gas phase, and the vaporized TCE is transported within gas phase. At the same time, the vaporized TCE is partitioned into water phase, generating dissolved TCE. Direct dissolution of TCE from the source also occurs, but this showed little influence on migration of the TCE plume in the unsaturated zone.

In far down-gradient zones (for instance, approximately $x > 90$ m in Figure 3.9 (d)), long extended plumes of vaporized TCE may come from contaminated groundwater in the saturated zone: After dissolved TCE in the saturates zone migrated along with the groundwater flow from the high concentration zone (almost directly below the sources) to the down-gradient zones, the TCE is partitioned into gas phase in the unsaturated zone. In the saturated zone, the groundwater flow, shown in Figure 3.9 (f), is a primary mechanism for migration of TCE. The spreading of dissolved TCE in the domain is presented in Figures 3.10 for Case 1 and 2. The groundwater flow in the saturated zone contributes to the expansion of TCE plume in the saturated zone as well as into the unsaturated zone in the down-gradient area. In multiphase flows of gas and water in the domain, as each phase constantly interacts with the other in terms of fluid flow and mass transfer, pollution of one phase will result in pollution of the other phase.

In Figure 3.9 and 3.10, Case 1 and 2 shows different spreading patterns of TCE between down-gradient areas with relatively low concentrations (TCE ≤ approximately 1 mg/L) and up-gradient areas with high concentrations (TCE > approximately 100 mg/L): At the up-gradient areas, the development of dissolved and vaporized TCE plumes is greater in Case 2 than in Case 1, however, at the down-gradient areas, Case 1 shows larger spreading of TCE in the down gradient area than Case 2 does. These phenomena in

TCE spreading in gas and water phases result from the density-driven advection of gas phase, shown in Figure 3.9 (e). In Case 2, the advection of gas phase not only contributes to the spreading of vaporized TCE near the source but also accelerates the release of vaporized TCE into the atmosphere in the down-gradient areas. As shown in velocity profiles at $x > 100$ m in Figure 3.9 (e), the outgoing gas flow to the ground surface will help decrease TCE concentration in the unsaturated zone by prompting the release of vaporized TCE into the atmosphere. The release of vaporized TCE accelerates mass transfer of dissolved TCE in the saturated zone into gas phase, and helps to retard the development of dissolved TCE plume in the saturated zone. Many research works in the literature indicated that loss of contaminant mass to the atmosphere through the ground surface plays an import role in reducing the spreading of contaminant plumes in the subsurface [Sleep and Sykes, 1989; Mendoza and Frind, 1990b; Thomson et al., 1997]. Through a large-scale experiment, Jellai et al. [2003] reported mass transfer of TCE to the atmosphere that reached nearly 95 % of initial TCE volume. They also indicated that the transfer process is essentially governed by molecular diffusion and significantly reduces the potential for groundwater pollution.

a) TCE concentration in gas phase at t = 100 days, Case 1

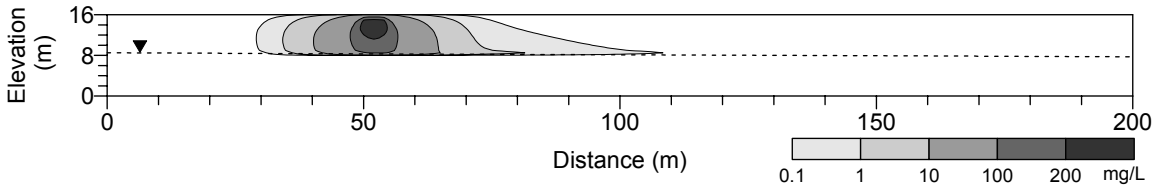

b) TCE concentration in gas phase at t = 100 days, Case 2

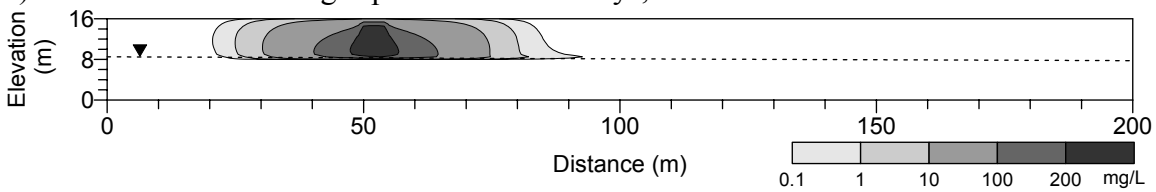

c) TCE concentration in gas phase at t = 200 days, Case 1

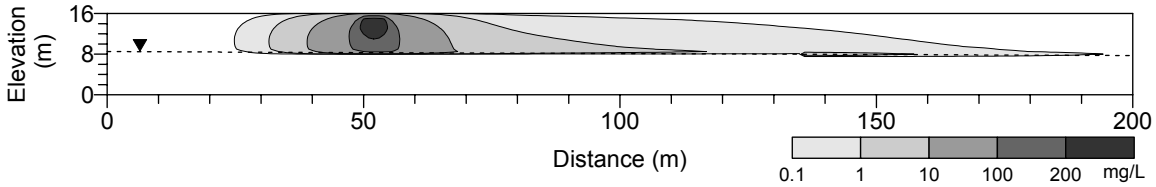

d) TCE concentration in gas phase at t = 200 days, Case 2

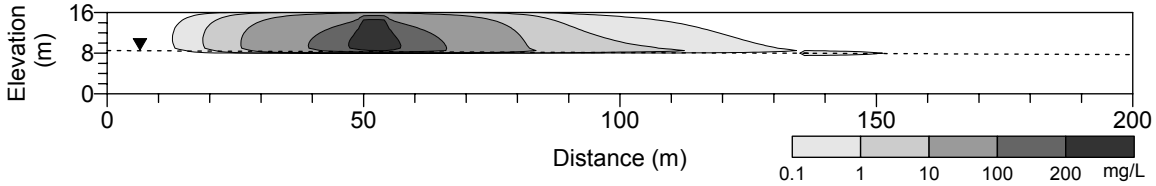

e) Darcy velocity of gas phase at t = 200 days, Case 2

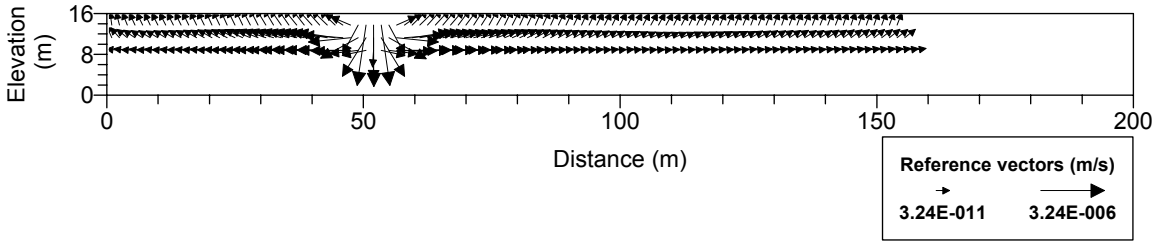

f) Darcy velocity of water phase at t = 200 days, Case 2

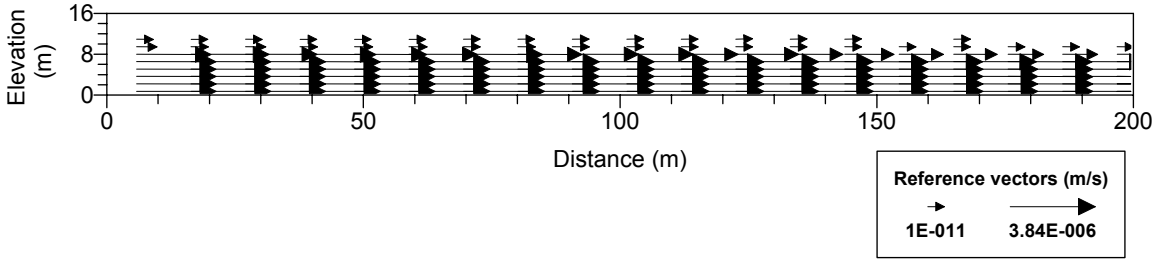

Figure 3.9 Vaporized TCE concentration profiles in gas phase for Cases 1 (diffusion-only transport) and 2 (density-driven transport) and Darcy velocities of gas and water phases at Case 2.

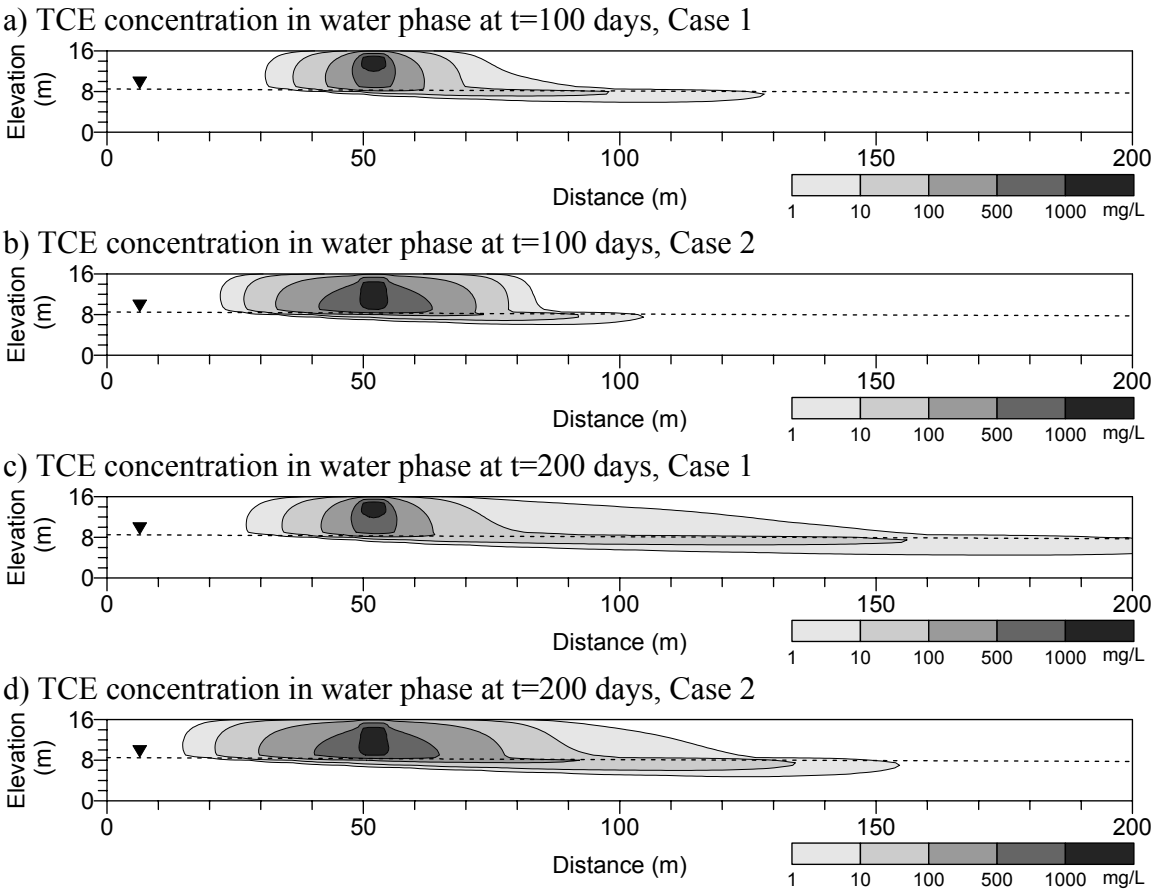

Figure 3.10 Dissolved TCE concentration profiles in water phase for Cases 1 (diffusion-only transport) and 2 (density-driven transport).

To investigate fate of TCE in the domain, we carried out mass balance calculations every time step. These methods are described in Appendix E. The mass balance calculations showed good accuracy for the simulations: The accumulated mass-balance error up to 300 days and the mass-balance error at every time step was less than 1.7 % and 0.03 %, respectively.

In Figure 3.11, the evolution of TCE mass in gas or water phases and release of TCE to the atmosphere are illustrated. Figures 3.11 (a) and (b) show that mobilized TCE mass (dissolved or vaporized TCE from the source) is much greater at Case 2 than at Case 1: At 200 days, vaporized TCE mass of Case 2 in gas phase is approximate twice that of Case 1. In Figure 3.11 (a) and (b), vaporized TCE mass in the unsaturated zone shows sharp increases at an initial stage (up to approximately 50 days in Case 1 and 100 days in Case 2), and over time TCE spread seems to approach stabilized conditions. Dissolved TCE mass in the saturated zone, however, shows steady increases after a period of lag time, around 40 days, which is the transport time for TCE from the source area to the saturated zone. TCE mass transported into the groundwater in the saturated zone is much greater in the density-driven transport of TCE (Figure 3.11 (b)) than in diffusion-only transport (Figure 3.11 (a)). This implies that the former has greater potential of groundwater pollution than the latter has. As mentioned earlier in Figure 3.10, however, we need to note that the development of low concentration of dissolved TCE plume at down-gradient areas is greater in Case 1 than Case 2. For the two cases, daily release rate and total TCE mass that is released to the atmosphere are given in Figure 3.11 (c) and (d), respectively. Case 2 also shows higher daily and total release rates than Case 1 does. It is noted that the greater mass of mobilized TCE (vaporized

TCE + dissolved TCE at the source) results in the greater mass reduction of TCE at the source. In Figure 3.12, the density-driven advection at Case 2 contributes to fast mass reduction of TCE as NAPL at the source.

From Cases 1 and 2, we may conclude that the density-driven advection of gas phase becomes a strong driving force to transfer TCE from NAPL phase to other phases (gas, water, and solid soil) as well as to the atmosphere.

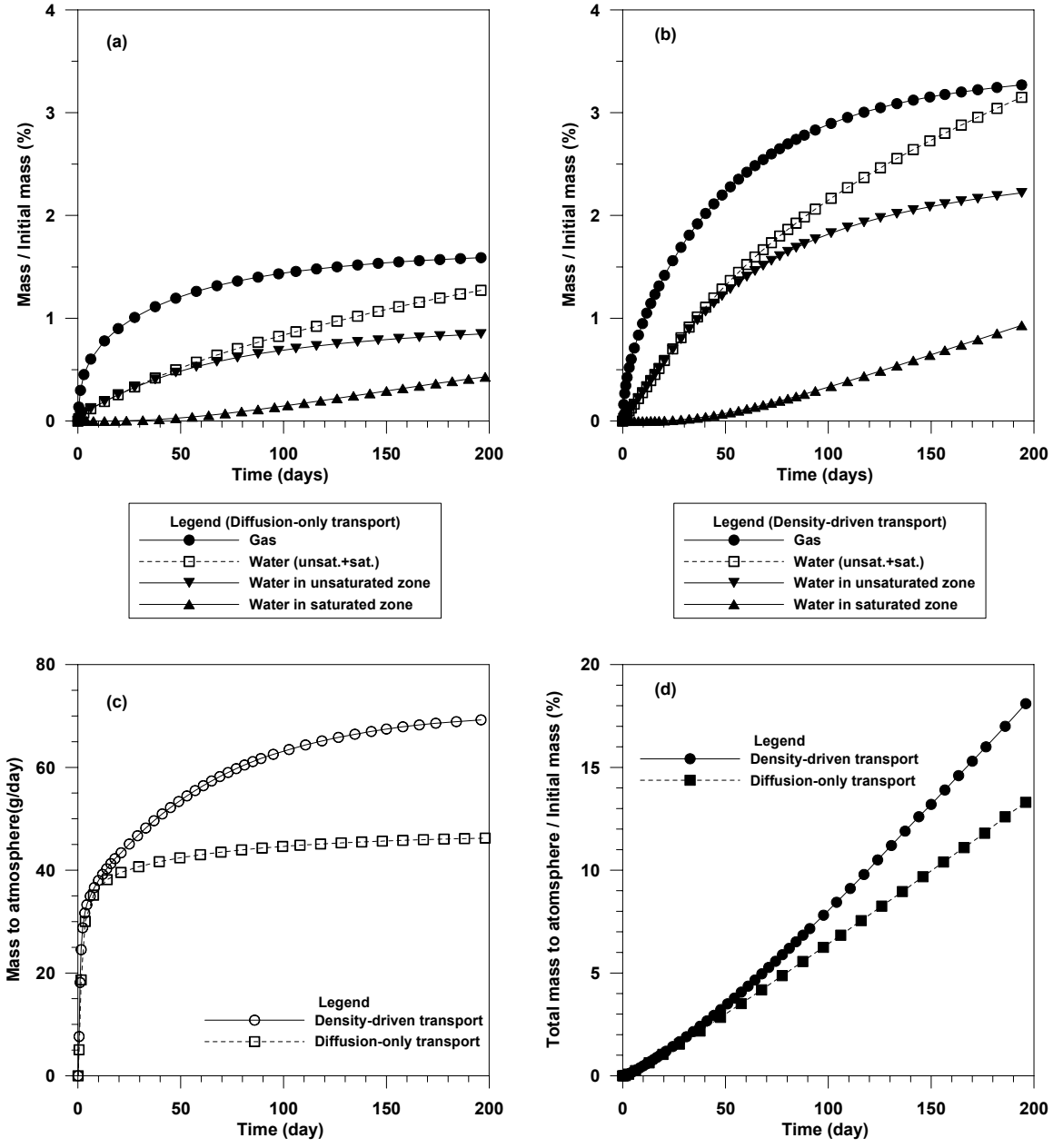

Figure 3.11 TCE distributions in the system: (a) Case 1 (diffusion-only transport) and (b) Case 2 (density-driven transport), and TCE release to the atmosphere: (c) daily release rate and (d) total released mass of TCE

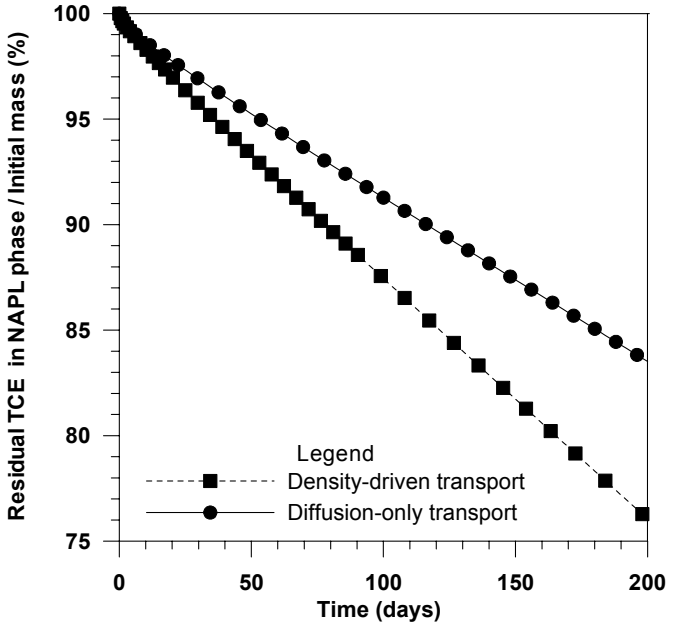

Figure 3.12 TCE mass reduction at the source for Cases 1 (diffusion-only transport) and 2 (density-driven transport)

3.4.3 Effect of Infiltration on TCE Transport

In Cases 3 and 4, uniform infiltration (water recharge at the ground surface) of 30 cm/yr is applied to investigate its effect on fate and transport of TCE in subsurface environments. The results of Cases 3 and 4 are compared with no infiltration cases (Case 1 and 2). As shown in Figure 3.13, the infiltration increased water saturation in the unsaturated zone, and generated nearly uniform water content at z = 11-16 m. In Case 4, the infiltration induced a downward water flow in the unsaturated zone (Figure 3.14 (f)), and raised the groundwater velocity in the saturated zone: The horizontal velocities of the groundwater for Case 2 (No infiltration, Figure 3.9 (f)) and Case 4 (Infiltration, Figure 3.14 (f)) in the saturated zone are 3.84×10^{-6} and 3.98×10^{-6} m/s, respectively. In Equation (3.4), if NAPL saturation doesn't change, an increase in water saturation implies a reduction in gas saturation. The decrease in gas saturation reduces the relative permeability of gas phase according to van Genuchten model for a saturation-relative permeability relationship, given in Equation (2.12). The infiltration in Cases 3 and 4 decreased density-driven advection of gas phase around the source: Maximum Darcy velocities of gas phase at Case 2 (Figure 3.9 (e)) and Case 4 (Figure 3.14 (e)) are 3.24×10^{-6} and 3.18×10^{-6} m/s, respectively, indicating approximately 2 % reduction in maximum gas velocity due to the infiltration.

In Figure 3.14 (a)-(d), the effects of the uniform infiltration on contaminant plume development in water and gas phases are illustrated by comparing two cases: Case 2 (density-driven transport without infiltration) and Case 4 (density-driven transport with infiltration). In Figure 3.14, TCE concentration contours for Cases 2 and 4 indicate that infiltration slightly increases the spreading of dissolved and vaporized TCE in the

variably saturated zones. Furthermore, the concentration contours suggest that infiltration has greater influence on higher concentration regions near the source. Since dissolved TCE concentrations around the groundwater table vary over a distance, downward mass flux of dissolved TCE will be much greater at the high concentration regions (near the source) than at low concentration regions.

Infiltration has a significant effect on the distribution of TCE (Figure 3.15). In Figure 3.11 (b) for Case 2 (No infiltration), the mass of TCE in gas phase is greater than that in water phase (both the unsaturated and saturated zones) until 200 days. The difference in relative mass percentages of between vaporized TCE and dissolved TCE in the unsaturated zone is more than 1 % at 200 days. In Case 4, infiltration significantly increases dissolved TCE mass in the unsaturated zone as water content rises, so the difference in relative mass percentages between vaporized TCE and dissolved TCE in the unsaturated zone reduced to less than 0.4 % at 200 days (Figure 3.15). After 95 days, total dissolved TCE mass exceeds vaporized TCE mass.

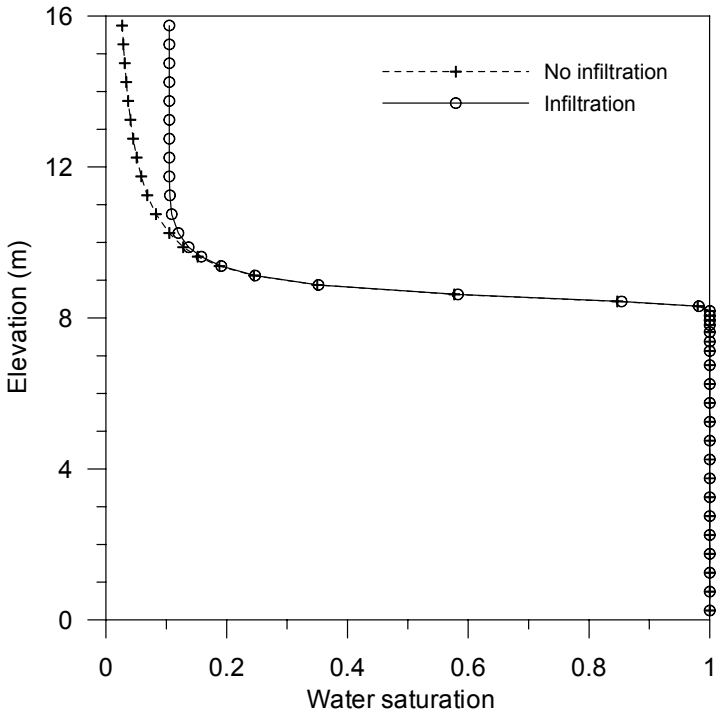

Figure 3.13 Water saturation with infiltration or without infiltration at x = 50 m: the groundwater table is located at around z = 8.3 m.

a) TCE concentration in water phase at t=250 days, Case 2

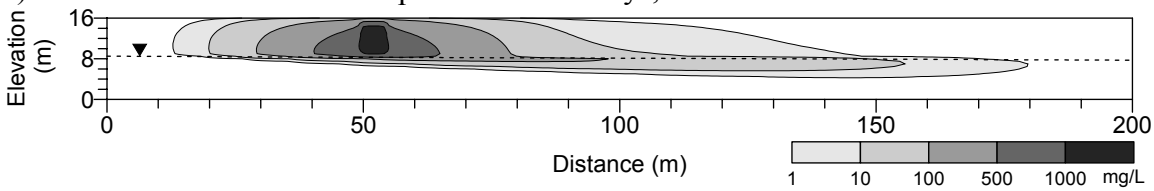

b) TCE concentration in water phase at t=250 days, Case 4

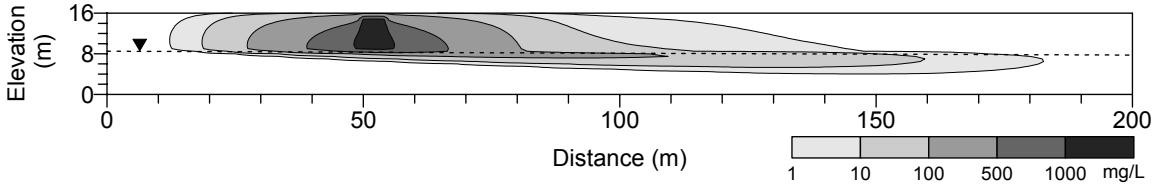

c) TCE concentration in gas phase at t=250 days, Case 2

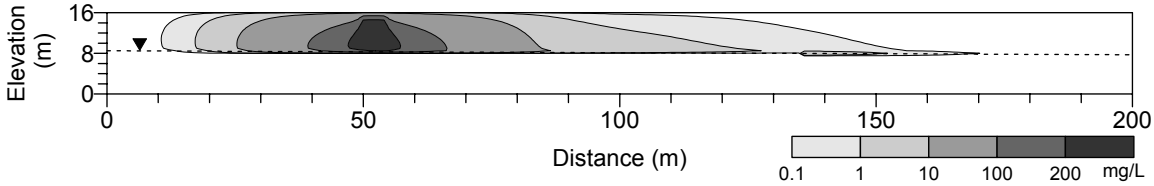

d) TCE concentration in gas phase at t=250 days, Case 4

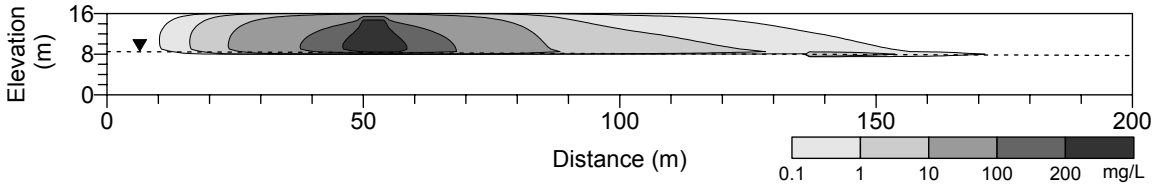

e) Darcy velocity of gas phase at t=200, Case 4

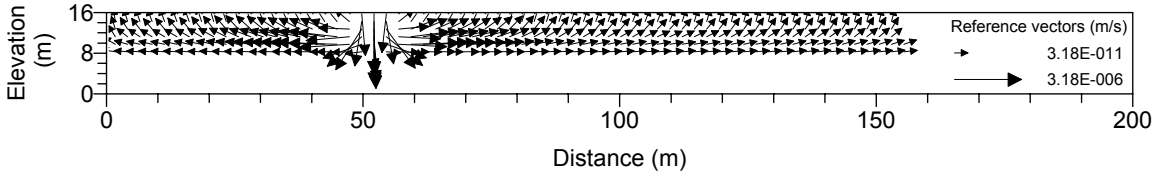

f) Darcy velocity of water phase at t=200, Case 4

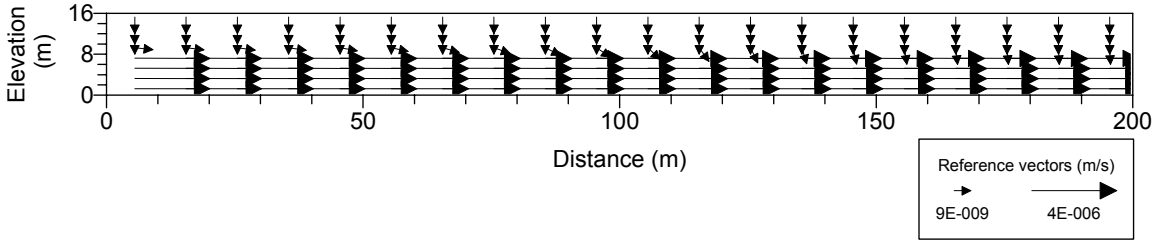

Figure 3.14 Effect of infiltration on TCE transport

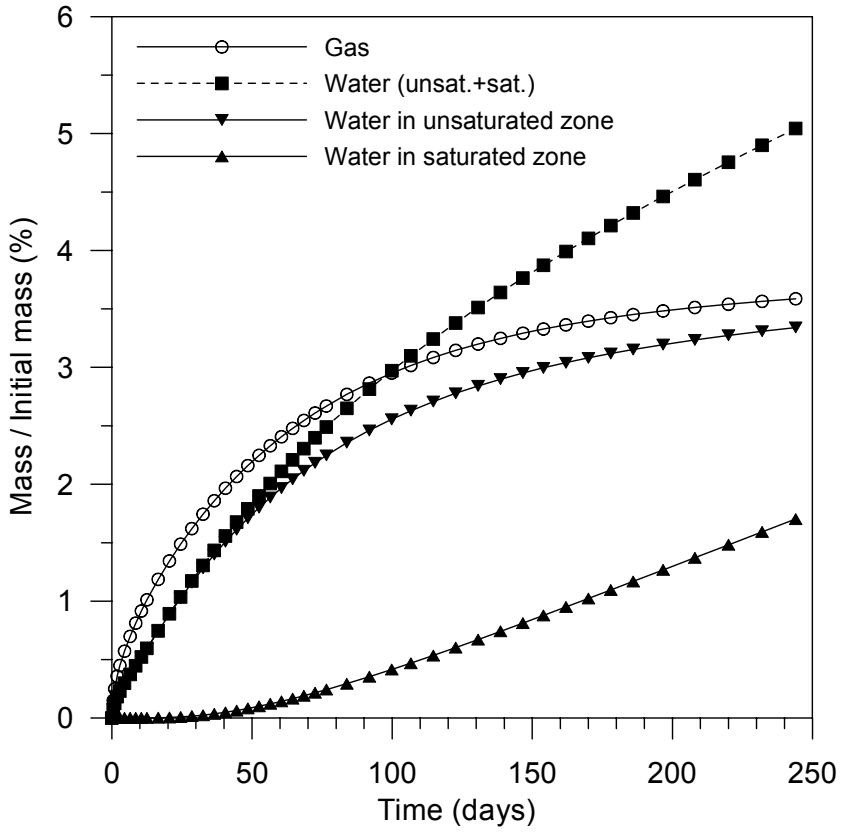

Figure 3.15 Distribution of TCE in gas and water phases, Case 4

Mass transfer rates of dissolved TCE from the unsaturated zone to the saturated zone are compared to evaluate the potential of groundwater pollution for four cases (Cases 1, 2, 3, and 4) in Figure 3.16. Both density-driven transport and uniform infiltration applied at the ground surface increase the transfer rates. The effect of the infiltration is represented by the differences in TCE transfer rates between Case 1 and 3 or between 2 and 4 (dashed arrows in Figure 3.16) while the effect of the density-driven transport is expressed by the differences of TCE transfer rates between Case 1 and 2 or between Cases 3 and 4 (solid arrows in Figure 3.16). The effect of the density-driven transport on the TCE transfer rates appears to be greater than that of the infiltration under simulation conditions used here. For example, in the comparison of Cases 2 and 4, infiltration raises TCE transport to the saturated zone by approximately 39 % (from 4.1 g/d in Case 2 to 5.7 g/d in Case 4) at 150 days. In the comparison of Cases 3 and 4, however, density-driven transport in gas phase raises the transport of TCE mass to the saturated zone by approximately 204 % (from 2.8 g/d in Case 3 to 5.7 g/d in Case 4). These results suggest that the density-driven transport of TCE in gas phase has greater potential on groundwater pollution than the infiltration under the conditions applied to Cases 1 through 4.

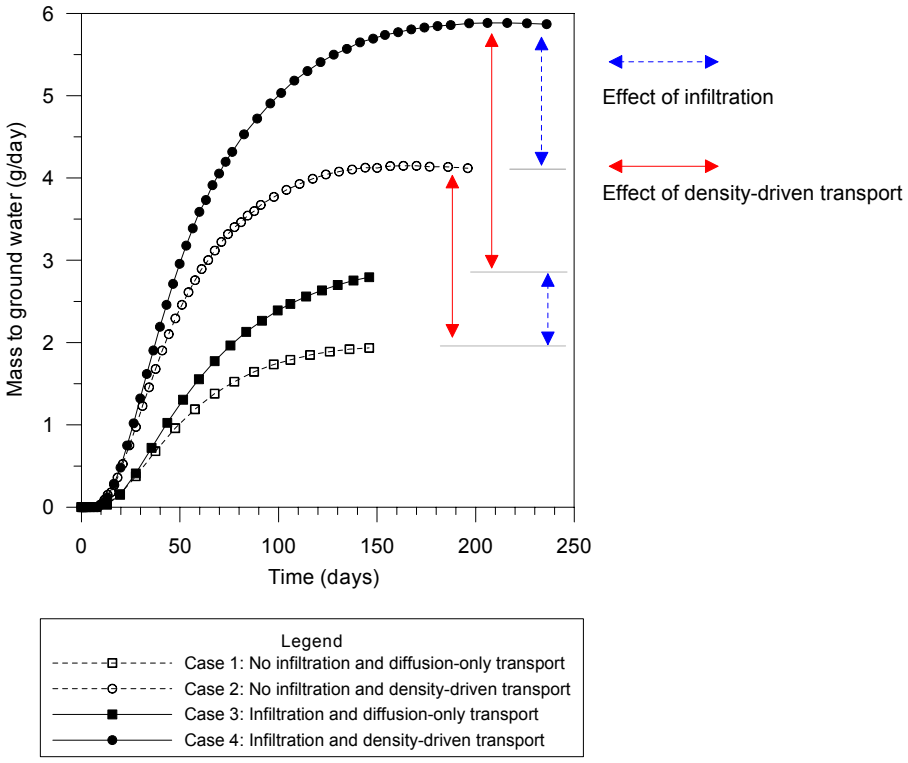

Figure 3.16 Mass transfer rates of dissolved TCE from the unsaturated zone to the saturated zone for four cases (Cases 1, 2, 3, and 4)

3.4.4 Effect of Permeability on TCE Transport

As seen in Darcy's law equation (Equation (3.20)), the permeability of porous media is a key parameter to determine Darcy velocity of water and gas phases in the media. Therefore, the permeability plays an important role in contaminant transport including density-driven transport in gas phase in a variably saturated zone [Mendoza and Frind, 1990b]. The effect of permeability of porous soil matrix on density-driven transport is examined through simulations under three different permeabilities: 1.0×10^{-10} m^2 for Case 4, 7.07×10^{-11} m^2 for Case 5, and 5.0×10^{-11} m^2 for Case 6.

In Figures 3.17 and 3.18, the spreading of TCE plume is proportional to the magnitude of permeabilities of porous media: the greatest permeability in Case 4 shows the widest spreading of TCE plumes in the unsaturated and saturated zone. Among three cases (Cases 4, 5, and 6), Case 6 shows the least spreading of TCE plume in the unsaturated zone, however, the spreading by density-driven advection of gas phase in Case 6 is still significant below the source when it is compared with the spreading by diffusion-only transport of Case 1.

The velocity profiles of gas phase for the three cases are presented in Figure 3.17 (d)-(f). The velocities near the source zone depend on the magnitude of permeabilities. The reduction in permeability of porous media implies a decrease in the velocity of the groundwater, and this results in slow development of contaminant plumes. The maximum Darcy velocities of gas phase are 3.14×10^{-6}, 2.39×10^{-6}, and 1.8×10^{-6} m/s for the permeability of 1.0×10^{-10}, 7.07×10^{-11} and 5.0×10^{-11} m^2, respectively. Mendoza and Frind [1990b] stated that, as soil permeability decreases, advection becomes less important.

Thus, contaminant transport mechanism will transit from an advection-dominated to a diffusion-dominated process.

a) TCE concentration in gas phase at t = 300 days, Case 4 (Permeability = 1.0×10^{-10} m^2)

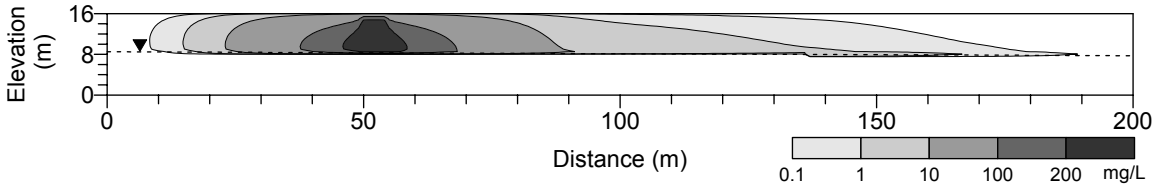

b) TCE concentration in gas phase at t = 300 days, Case 5 (Permeability = 7.07×10^{-10} m^2)

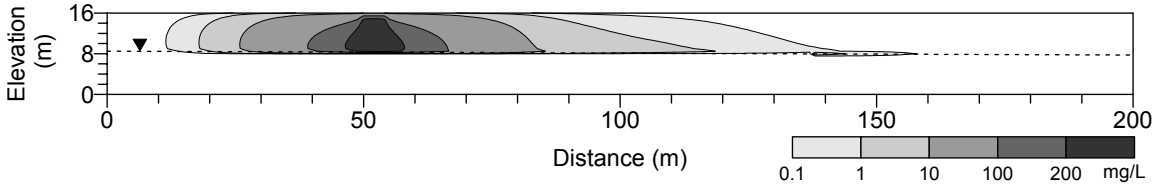

c) TCE concentration in gas phase at t = 300 days, Case 6 (Permeability = 5.0×10^{-10} m^2)

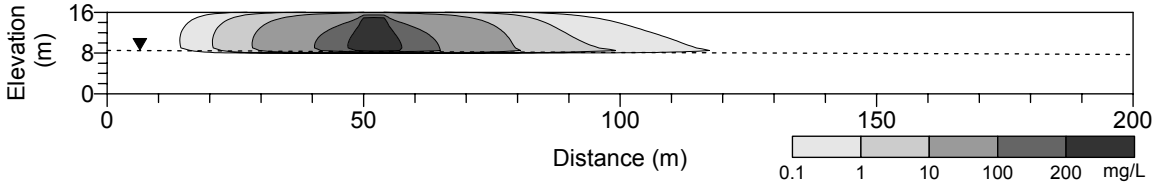

d) Darcy velocity of gas phase at t = 300 days, Case 4 (Permeability = 1.0×10^{-10} m^2)

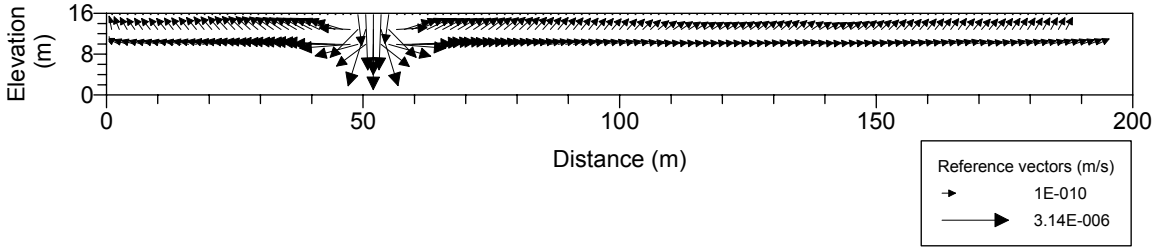

e) Darcy velocity of gas phase at t = 300 days, Case 5 (Permeability = 7.07×10^{-10} m^2)

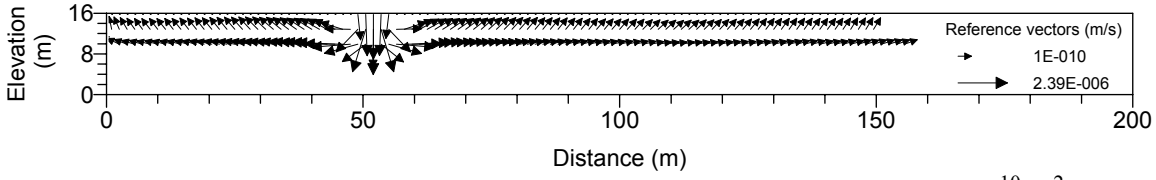

f) Darcy velocity of gas phase at t = 300 days, Case 6 (Permeability = 5.0×10^{-10} m^2)

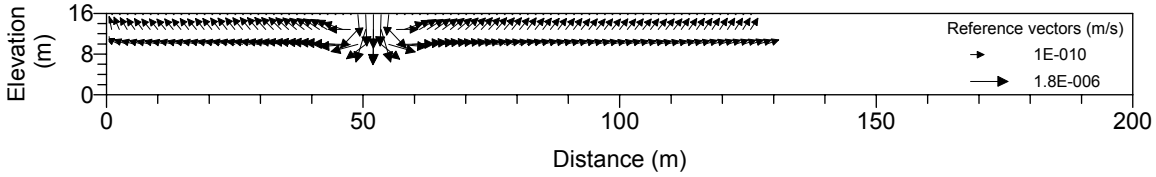

Figure 3.17 Effect of intrinsic permeability of soil on transport of vaporized TCE in the unsaturated zone and Darcy velocity of gas phase at three different permeabilities of soil (Cases 4, 5, and 6)

a) TCE concentration in water phase at t = 300 days, Case 4 (Permeability = 1.0×10^{-10} m^2)

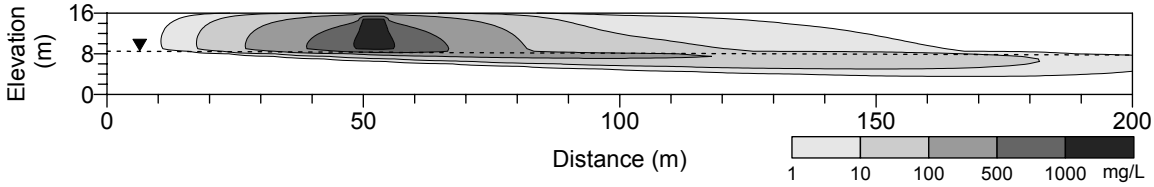

b) TCE concentration in water phase at t = 300 days, Case 5 (Permeability = 7.07×10^{-10} m^2)

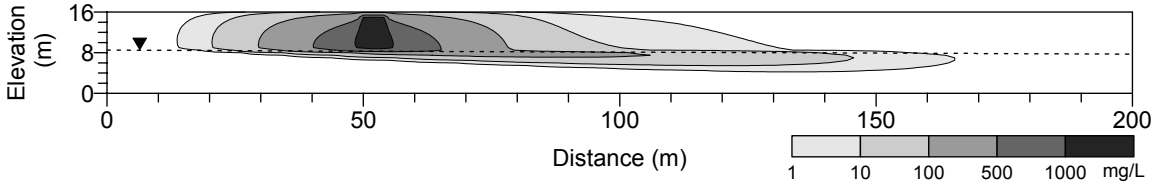

c) TCE concentration in water phase at t = 300 days, Case 6 (Permeability = 5.0×10^{-10} m^2)

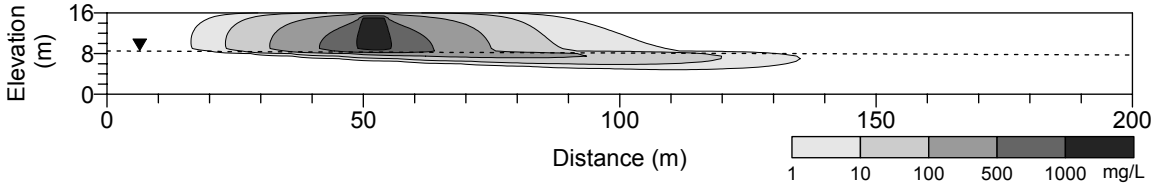

Figure 3.18 Effect of intrinsic permeability of soil on transport of dissolved TCE in the unsaturated and saturated zones (Cases 4, 5, and 6)

Mass transfer of TCE to the groundwater and to the atmosphere is shown in Figures 3.19 and 3.20, respectively. Among simulations for the three different permeabilities, the highest permeability (Case 4) generates the highest mass transfer rate of TCE to the atmosphere and to the groundwater. This results in the fast reduction of TCE mass in the source (Figure 3.21).

The location of a contaminant source is an important factor to determine its fate and distribution in subsurface environments [Jellali et al., 2003]. Thomson et al. [1997] reported that, as a contaminant source becomes closer to the groundwater table, the dissolution rate increases and groundwater contamination becomes worse. Under the simulation conditions in which the NAPL source is close to the ground surface, large portion of mobilized TCE is released into the atmosphere: In Case 4 at 250 days, the average transfer rate of TCE into the atmosphere (Figure 3.19 (a)) is greater than ten times that dissolved into the groundwater (Figure 3.20 (a)). In Figure 3.19, for Case 4 at 250 days, the portion of total dissolved TCE was 5.1 % of initial TCE mass in the domain, and about 1.8 % of the initial mass was transferred to the groundwater. In terms of mobilized TCE mass (sum of dissolved and vaporized TCE from the source), for Case 4 at 250 days, 17 % of the total mobilized TCE is dissolved TCE, and about 6 % of the total mobilized TCE was transferred to the groundwater in the saturated zone.

Mendoza and Frind [1990a] reported that, even though small portion of TCE in the source zone is transported to the groundwater in the saturated zone, dissolved TCE concentration in the groundwater may be still high and can exceed its drinking water standard (Maximum contaminant level of TCE: 0.005 mg/L) listed on the National Primary Drinking Water Regulations [EPA, 2000] in the down gradient area. In this

study, regardless of the magnitude of the permeabilities for Case 4, 5, and 6, relatively high concentrations of dissolved TCE in the saturated zone were predicted in the simulations (Figure 3.17), and showed high potentials for groundwater pollution.

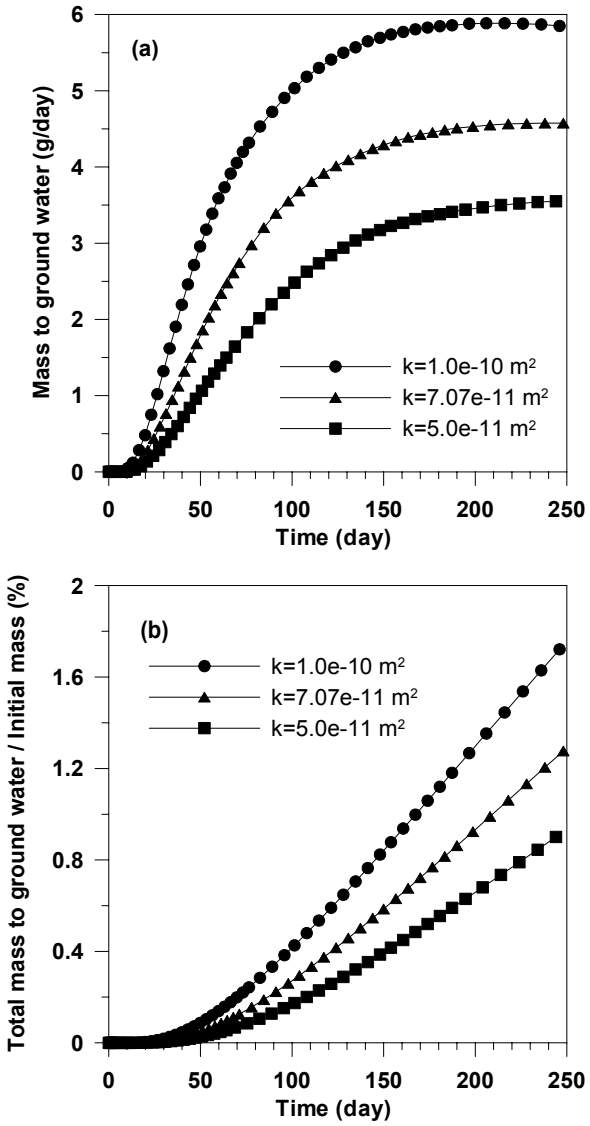

Figure 3.19 TCE transfer to the groundwater over time for three different permeabilities (1.0×10-10 m2 for Case 4, 7.07×10-11 m2 for Case 5, and 5.0×10-11 m2 for Case 6): (a) Daily TCE transfer rates and (b) total TCE ratio transferred to the groundwater in the saturated zone

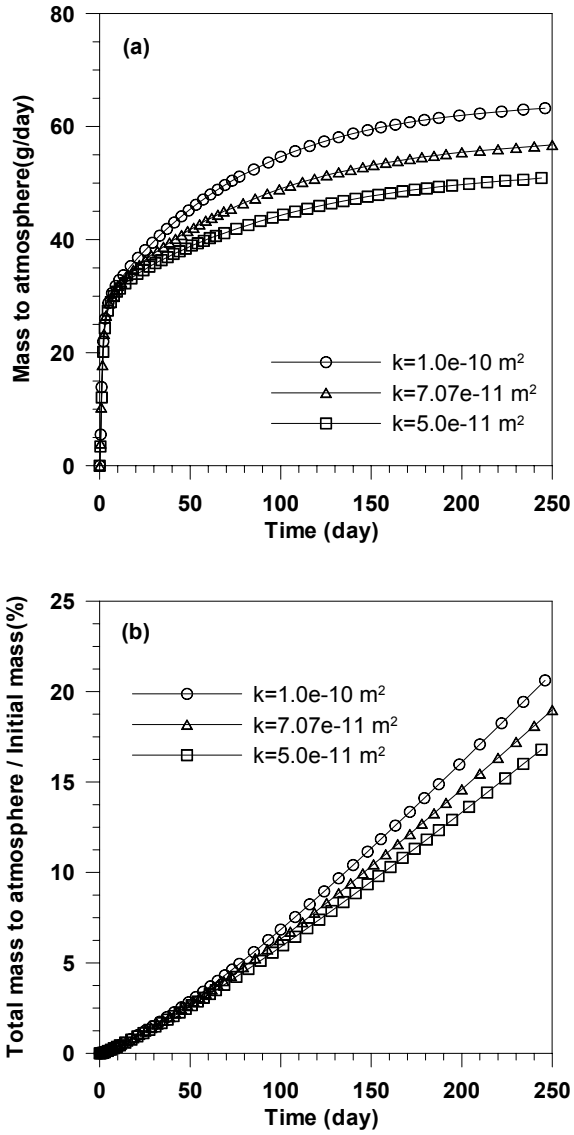

Figure 3.20 TCE transfer to the atmosphere over time for three different permeabilities (1.0×10-10 m2 for Case 4, 7.07×10-11 m2 for Case 5, and 5.0×10-11 m2 for Case 6): (a) Daily TCE transfer rates and (b) total TCE ratio transferred to the atmosphere

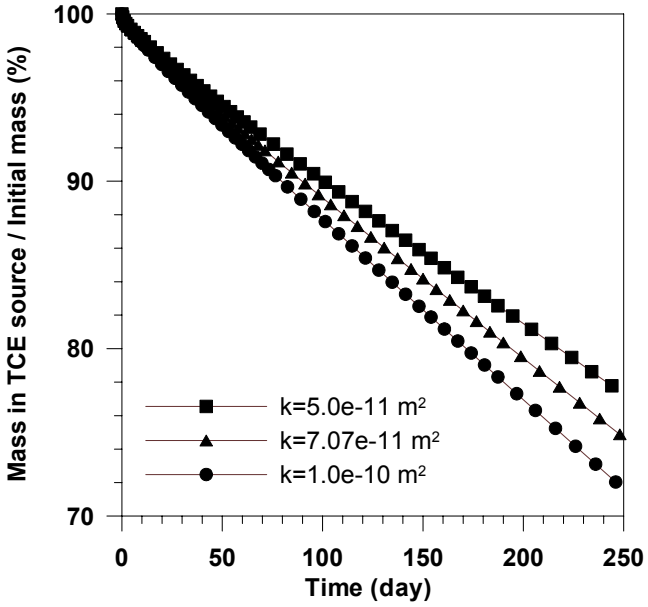

Figure 3.21 The reduction in TCE mass as NAPL at the source over time for three different permeabilities (1.0×10^{-10} m^2 for Case 4, 7.07×10^{-11} m^2 for Case 5, and 5.0×10^{-11} m^2 for Case 6)

3.5 Application of Density-driven Transport of a Conservative Contaminant in a Three-dimensional Domain

3.5.1 Modeling Domain

The density-driven advection of gas phase in a three-dimensional domain is needed for simulations in more realistic scenarios. The two-dimensional (2D) domain shown in Figure 3.8 is extended to a three-dimensional (3D) domain with dimensions (200 m x 50 m x 16 m) in (x, y, z) directions, respectively (Figure 3.22). Similarly as mentioned in section 3.4, TCE in the form of NAPL is introduced to the unsaturated zone and resides in pore spaces as an immobilized contaminant source (5 m × 5 m × 2 m).

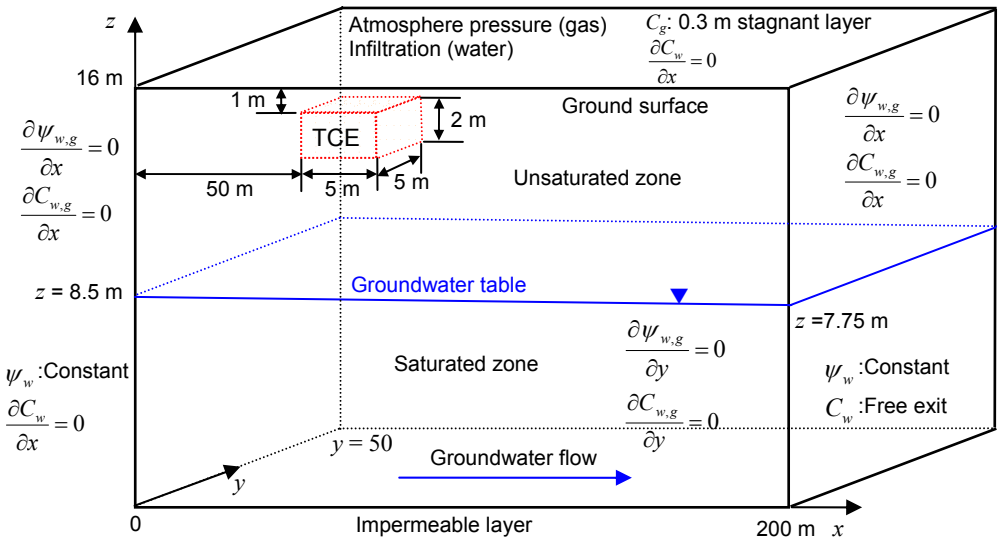

Figure 3.22 A schematic diagram of a modeling domain and site conditions in a 3D domain

At the source, the saturation of an immobile TCE residual is 5 %. Initial concentrations of TCE in gas, water, and solid phases are set to zero within the domain.

Same initial and boundary conditions used in section 3.4 are applied here: As boundary conditions at the ground surface, the recharge for infiltration is 30 cm per year for water phase, and constant atmospheric pressure is applied for gas phase. For gas phase, no flow condition is applied to all boundaries except the boundary for the ground surface. Intrinsic permeability for soil medium is 1.0×10^{-10} m^2, and other properties of a soil medium, water, and gas phases used here are given in Table 3.3.

The model domain grid consists of 19,880 nodes and 17,290 elements, which was discretized as follows: In x-direction, Δx = 2.5 m at x = 0-150 m and Δx = 5 m at x = 150-200 m; In y-direction, Δy = 2.5 m at y = 0-15 m and Δy = 5 m at y = 15-50 m; and, In z-direction, Δz = 1 m at z = 0-7 m and z = 9-15 m, and Δz = 0.5 m at z = 7-9 m and z = 15-16 m. The run time was up to 300 days with the length of time steps ranging between initial 1 hour and 2 days, which was adjusted according to an automatic time-stepping scheme.

3.5.2. Results of TCE Transport in the 3D Domain

Transport of dissolved and vaporized TCE in the variably saturated 3D domain considering a density-driven advection in gas phase is illustrated in Figure 3.23 and 3.24, respectively. As seen in Figure 3.22, when a contaminant source in a 3D domain is finite in y-direction, the contaminant migration in y-direction is additionally considered as well as its migration in x- and z-direction. The contaminant transport in y-direction reduced the transport of TCE in x-direction. In Figure 3.23 (b) for the 3D domain, the front of the dissolved TCE plume with a concentration of 1 mg/L reached around 170 m in x-direction at 300 days while, in Figure 3.18 (a) for the 2D domain, the dissolved TCE

plume migrated more than 200 m in the *x*-direction during the same period. Since the density-driven advection is accounted into all directions, its strength in any single direction is reduced. However, the effect of density-driven advection in gas phase on TCE transport is observed near the source (Figures 3.23 and 3.24). At high concentration areas, dissolved and vaporized TCE concentration profiles on *x*-*z* plane at $y = 0$ m in Figures 3.23 and 3.24 show graphically similar patterns as seen in Figures 3.17 and 3.18.

Fate of TCE over time is given in Figure 3.25, which indicates that the release of TCE to the atmosphere will also play a key role in reducing TCE at the source in a 3D domain: About 58 % of mobilized TCE mass was released to the atmosphere. The portion of TCE dissolved in the saturated zone increases continuously with time, and it will accelerate groundwater pollution.

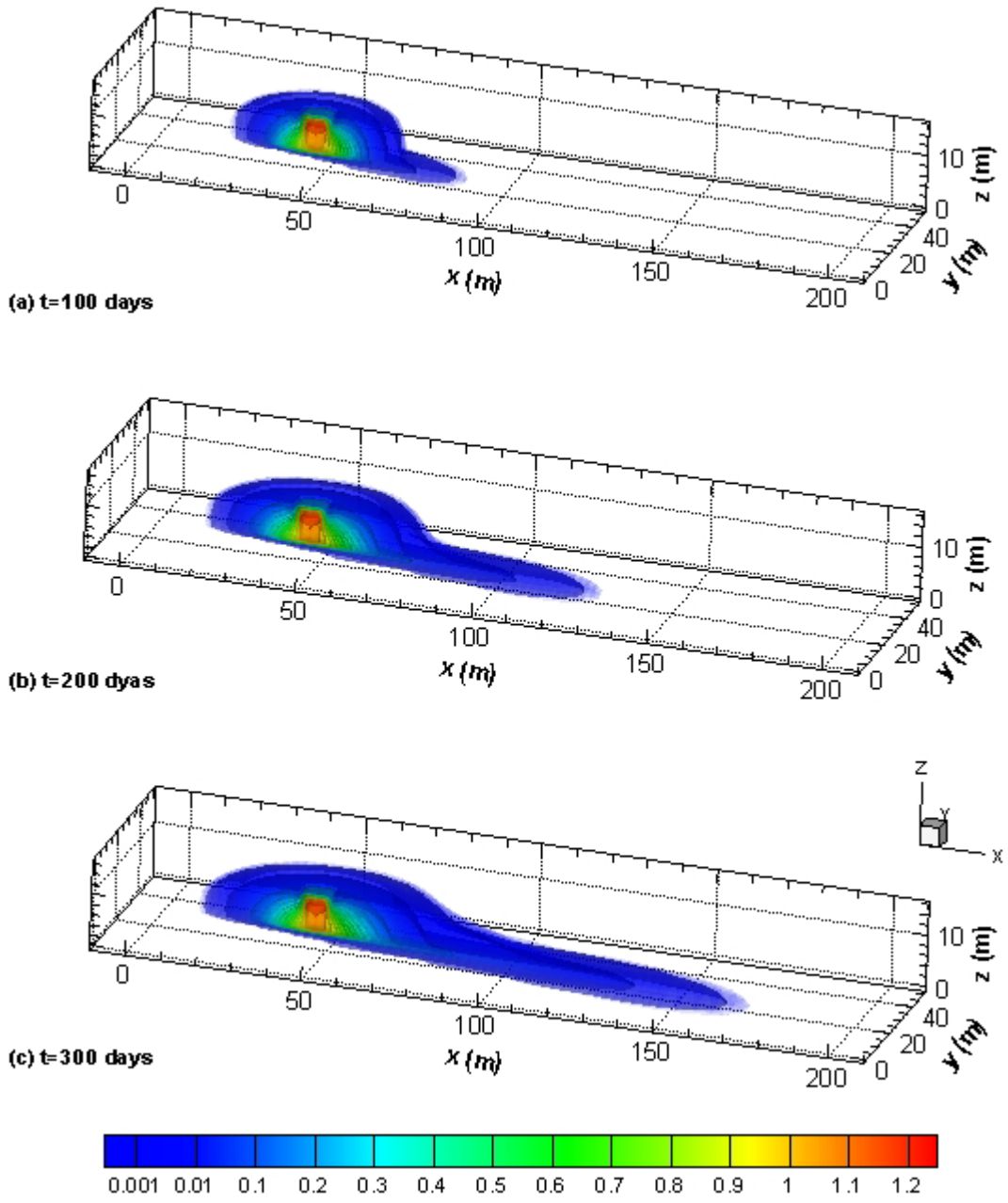

Figure 3.23 Transport of dissolved TCE in the 3D domain. The unit of concentrations is g/L.

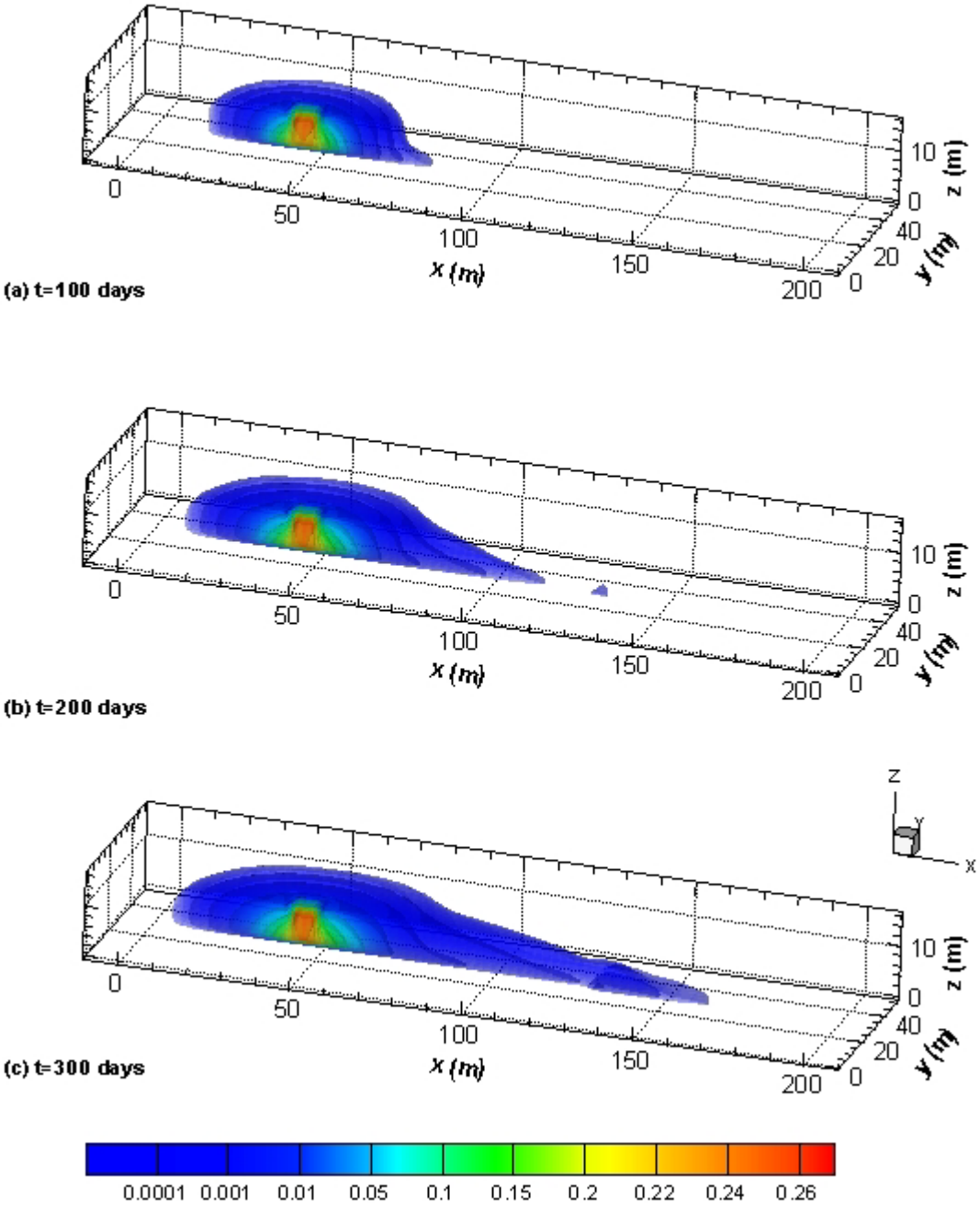

Figure 3.24 Transport of vaporized TCE in the 3D domain. The unit of concentration is g/L.

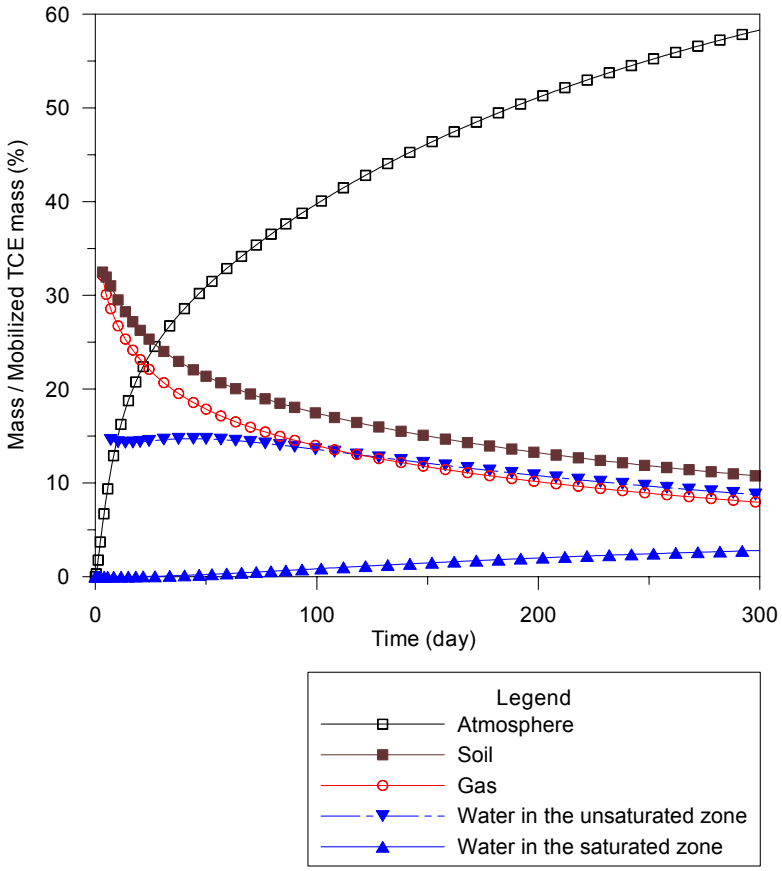

Figure 3.25 Fate of TCE in the domain. The mobilized TCE mass indicates the sum of dissolved and vaporized TCE mass from the source.

3.6 Summary

In this chapter, the governing equations for multiphase flow and contaminant transport are formulated. These equations are solved using Galerkin finite element method. The model developed here was verified using numerical and experimental data available in the literature, and it was used to investigate the effect of density-driven advection of gas phase, infiltration, and permeability on fate and transport of TCE in a variably saturated zone. From the results of simulations in the two-dimensional and three-dimensional domains, the following conclusions can be deduced;

(i) Density-driven advection of gas phase occurs near a contaminant source, and plays a dominant role in the spreading of TCE in the unsaturated zone and in its transport to the groundwater in the saturated zone. Due to the density-driven transport of TCE, groundwater plumes with high concentrations of TCE were developed in the saturated zone near the source zone, and mass transfer rates of TCE to the groundwater increased.

(ii) The density-driven advection also increased the release of TCE into the atmosphere, and, especially, it helped to retard the migration of dissolved TCE in the far down-gradient saturated zone by accelerating the release of TCE vaporized from the contaminated groundwater to the atmosphere. In this study, since NAPL source is close to the ground surface, TCE mass released into the atmosphere was much greater than that dissolved into the groundwater in the saturated zone.

(iii) Infiltration at the ground surface raised water saturation in the unsaturated zone and the downward water velocity in the unsaturated zone. The increase in water saturation had significant effects on contaminant distribution: Dissolved TCE in the unsaturated zone has been largely increased, so, after a period of lag time, dissolved TCE mass exceeded vaporized TCE mass. Infiltration results in the increase in the mass flux of dissolved TCE to the saturated zone.

(iv) Permeability was an important factor to determine the strength of the density-driven transport of TCE and overall contaminant transport in subsurface systems because the permeability is directly related with fluid velocities. As the permeability of porous soil media becomes smaller, the effect of the density-driven advection of gas phase on contaminant spreading reduces. However, the advection was still an important mechanism to transport the contaminant to the saturated zone.

(v) In a three-dimensional domain, the density-driven advection of gas phase on TCE transport increased the migration of TCE in all directions. The transport of TCE in the three-dimension domain alleviated the density-gradient of gas phase when it is compared with the transport in a two-dimensional domain, thus the strength of the density-driven advection in x-direction decreased and TCE plume development in the x-direction was retarded.

CHAPTER IV

BIOLOGICAL TRANSFORMATION OF CONTAMINANTS

In Chapter III contaminants considered were assumed to be conservative. At contaminated sites, biological processes may occur in the subsurface system even though the reaction rates are highly variable. In this chapter, biological processes are considered as a component of biologically reactive contaminant migration. TechFlow^{MP} computer model developed in this study is verified using one- and three-dimensional analytical solutions with sequential bioreactions. Then, several simulations for biologically reactive contaminants are conducted to examine the effect of biological processes on fate and transport of the multispecies transport in groundwater systems.

4.1 Introduction

Volatile organic compounds (VOCs) in water phase can be utilized and transformed into other chemicals by various microorganisms in subsurface environments. The transformation of VOCs usually occurs as the result of complex biological processes, which have been extensively studied [Vogel and McCarty, 1985; Vogel et al., 1987; Freedman and Gossett, 1989; Wu et al., 1998; Schafer et al., 2003]. Biological reactions play an important role in the transport of VOCs in groundwater systems since the processes can convert toxic contaminants into benign substances or may introduce new toxic intermediates. Also, the interactions between VOCs and organic/inorganic materials in gas, water, and solid phases can cause the changes in chemical properties of the compounds or of fluid phases [Yaron et al., 1984].

Trichloroethylene (TCE), which is widely used as an industrial solvent, is one of the most frequently detected contaminants in the subsurface [Wu and Schaum, 2001]. TCE can be transformed to dichloroethylenes (DCEs) and then to vinyl chloride (VC) through reductive dehalogenations under anaerobic environments [Vogel and McCarty, 1985]. The two intermediates are also toxic, and these have been detected with TCE in the unsaturated and saturated zones at contaminated sites [Dyer, 2003]. In the unsaturated zone, DCEs and VC exist in both water and gas phases through partitioning processes [Borch et al., 2003]. Since TCE, DCEs and VC have different physical and chemical properties such as density, vapor pressure, solubility, and diffusivity, they may have distinct transport patterns in subsurface systems.

In this chapter, reductive dechlorination of TCE under anaerobic conditions is used to examine biological transformations of VOCs and transport of parent and daughter contaminants in groundwater systems. As seen in Figure 2.1, the dechlorination of TCE produces three DCE isomers. As cis-1,2-DCE (cDCE) is the most common byproduct among the isomers, cDCE is employed to express the sequential biological processes of the dechlorination of TCE (TCE$\rightarrow$cDCE$\rightarrow$VC) in subsurface environments.

Biological transformations of VOCs depend on various parameters, such as chemical properties, concentration, and environmental conditions. The kinetics of biological processes is very complex. As discussed in Chapter 2.2, Michaelis-Menten (or Monod) and pseudo-first-order kinetics are often used to express biological processes [Smith et al., 1997; Clement et al., 2000; Pavlostathis and Prytula, 2000; Alvarez-Cohen and Speitel, 2001]. In this study, these two kinetic models are also employed to express reductive dechlorination of TCE, cDCE, and VC.

The focus of the discussion presented in this chapter is on: (i) fate and transport of TCE, cDCE, and VC with biological transformations; (ii) the effect of bioreaction rates on the transformations; and, (iii) the comparison of the effect of two kinetic models on generation and transport of the contaminants.

Density-driven advection of gas phase due to multispecies (TCE, DCEs, and VC) in the variably saturated zone is also considered at all simulations. TechFlow^{MP} is verified using analytical solutions for contaminant transport with first-order sequential bioreactions available in the literature.

4.2 Model Verification

4.2.1 Reactive Multi-species Transport in One-dimensional Uniform Flow

Chemical and biological transformations of contaminants are important factors in determining their fate and transport. Analytical solutions for transport of multiple contaminants with sequential bioreactions in a uniform groundwater flow are available in the literature, the solutions can be used to verify numerical models. Consider sequential reactions of three contaminants with first-order relationships:

$$C_1 \xrightarrow{k_1} C_2 \xrightarrow{k_2} C_3 \xrightarrow{k_3} \text{Benign byproducts} \tag{4.1}$$

where C_1, C_2, and C_3 are concentrations of the first, second, and third chemicals (ML^{-3}), respectively; and, k_1, k_2, and k_3 are first-order biological reaction coefficients for the first, second, and third chemicals (T^{-1}), respectively.

In a uniform groundwater flow, transport equations of chemical species 1, 2, and 3 can be expressed:

$$(1+K_D)\frac{\partial C_1}{\partial t} = D\frac{\partial^2 C_1}{\partial x^2} - v\frac{\partial C_1}{\partial x} - k_1 C_1 \tag{4.2}$$

$$\frac{\partial C_2}{\partial t} = D\frac{\partial^2 C_2}{\partial x^2} - v\frac{\partial C_2}{\partial x} - k_2 C_2 + k_1 C_1 \tag{4.3}$$

$$\frac{\partial C_3}{\partial t} = D\frac{\partial^2 C_3}{\partial x^2} - v\frac{\partial C_3}{\partial x} - k_3 C_3 + k_2 C_2 \tag{4.4}$$

where K_D is a constant adsorption coefficient of chemical species 1, x, y, and z are distance (L), t is time (T), D is a constant hydrodynamic dispersion coefficient (L^2T^{-1}), and v is a constant groundwater flow velocity (LT^{-1}). In Equations (4.2)-(4.4), sorption isotherm of species 1 on solid phase is assumed to be an equilibrium reaction, and species 2 and 3 do not have a sorption process. Dividing Equation (4.2) by $(1+K_D)$ yields

$$\frac{\partial C_1}{\partial t} = D^*\frac{\partial^2 C_1}{\partial x^2} - v^*\frac{\partial C_1}{\partial x} - k_1^* C_1 \tag{4.5}$$

where superscript * denotes division by $1+K_D$. The initial and boundary conditions can be given as,

$$C_1 = 0,\ C_2 = 0,\ C_3 = 0 \text{ for } x > 0,\ t = 0 \tag{4.6}$$

$$C_1 = C_1^o,\ C_2 = C_2^o,\ C_3 = C_3^o \text{ for } x = 0,\ t \geq 0 \tag{4.7}$$

where C_i^o is constant concentration of species i (i = 1, 2 , 3) at the boundary $x = 0$.

By using a Fourier sine transformation method, analytical solutions for the system of Equations (4.2)-(4.7) are obtained as [Lunn et al., 1996]:

$$C_1(x,t) = C_1^o P_1 \tag{4.8}$$

$$C_2(x,t) = C_2^o P_2 + \frac{k_1 C_1^o}{k_2 - k_1}\left\{P_1 - P_2 + \exp\left(\frac{k_2 - k_1}{K_d}t\right)\left[P\left(D, \frac{\mu_2 - \mu^*}{D - D^*}\right) - P\left(D^*, \frac{\mu_2 - \mu^*}{D - D^*}\right)\right]\right\} \tag{4.9}$$

$$
\begin{aligned}
C_3(x,t) = {} & C_3^o P_3 + \frac{k_2 C_2^o}{k_3 - k_2}\left(P_2 - P_3\right) \\
& + \frac{k_1 k_2 C_2^o}{\left(k_2 - k_1\right)\left(k_3 - k_1\right)\left(k_3 - k_2\right)}\left\{\left(k_2 - k_1\right)P_3 + \left(k_1 - k_3\right)P_2 + \left(k_3 - k_2\right)P_1\right\} \\
& + \frac{k_1 k_2 C_1^o}{\left(k_2 - k_1\right)\left(k_3 - k_2\right)}\exp\left(\frac{\left(k_2 - k_1\right)}{K_d}t\right)\left[P\left(D, \frac{\mu_2 - \mu^*}{D - D^*}\right) - P\left(D^*, \frac{\mu_2 - \mu^*}{D - D^*}\right)\right] \\
& - \frac{k_1 k_2 C_1^o}{\left(k_3 - k_1\right)\left(k_3 - k_2\right)}\exp\left(\frac{\left(k_3 - k_1\right)}{K_d}t\right)\left[P\left(D, \frac{\mu_3 - \mu^*}{D - D^*}\right) - P\left(D^*, \frac{\mu_3 - \mu^*}{D - D^*}\right)\right]
\end{aligned}
\tag{4.10}
$$

where

$$\mu_i = v^2 / 4D + k_i, \;\; i=1, 2, 3 \tag{4.11}$$

$$\mu^* = \mu_1 / \left(1 + K_D\right) \tag{4.12}$$

$$P_1 = P\left(D^*, \frac{\mu^*}{D^*}\right) \tag{4.13}$$

$$P_{i=2\ or\ 3} = P\left(D, \frac{\mu_i}{D}\right) \tag{4.14}$$

$$
\begin{aligned}
P(A,\lambda) = \frac{1}{2}\Bigg\{ & \exp\left(\frac{vx}{2D} - x\sqrt{\lambda}\right) erfc\left(\frac{x}{\sqrt{4At}} - \sqrt{4\lambda t}\right) \\
& + \exp\left(\frac{vx}{2D} + x\sqrt{\lambda}\right) erfc\left(\frac{x}{\sqrt{4At}} + \sqrt{4\lambda t}\right)\Bigg\}
\end{aligned}
\tag{4.15}
$$

To numerically simulate the transport of these three reactive contaminants, a one-dimensional problem is defined as follows: the length of domain is 2 m in *x*-direction with $\Delta x = 1\,\text{cm}$, and C_1^o, C_2^o, and C_3^o are 1, 0, and 0, at *x*=0 m respectively. Other simulation parameters, such as flow velocity and reaction rates, are given in Table 4.1.

Table 4.1 Simulation parameters*

Parameter	Value
Dispersion coefficient, D	0.18 cm^2 /hr
Velocity, v	0.2 cm/hr
Decay rate of species 1, k_1	0.05 hr^{-1}
Decay rate of species 2, k_2	0.03 hr^{-1}
Decay rate of species 3, k_3	0.02 hr^{-1}
Retardation factor, R_f	1.
Run time, t	400 hrs

*Parameters given by Sun et al. [1999a]

In this simulation, three transport equations are coupled by sequential degradation processes and are solved using the Crank-Nicolson scheme ($\alpha = 0.5$) with variable time steps of 10-3600 sec. In Figure 4.1, the simulation results are compared with analytical solutions, which are calculated using MAPLE 7.0 program using Equations (4.8)-(4.15). The numerical results obtained show very good agreement with the analytical solutions.

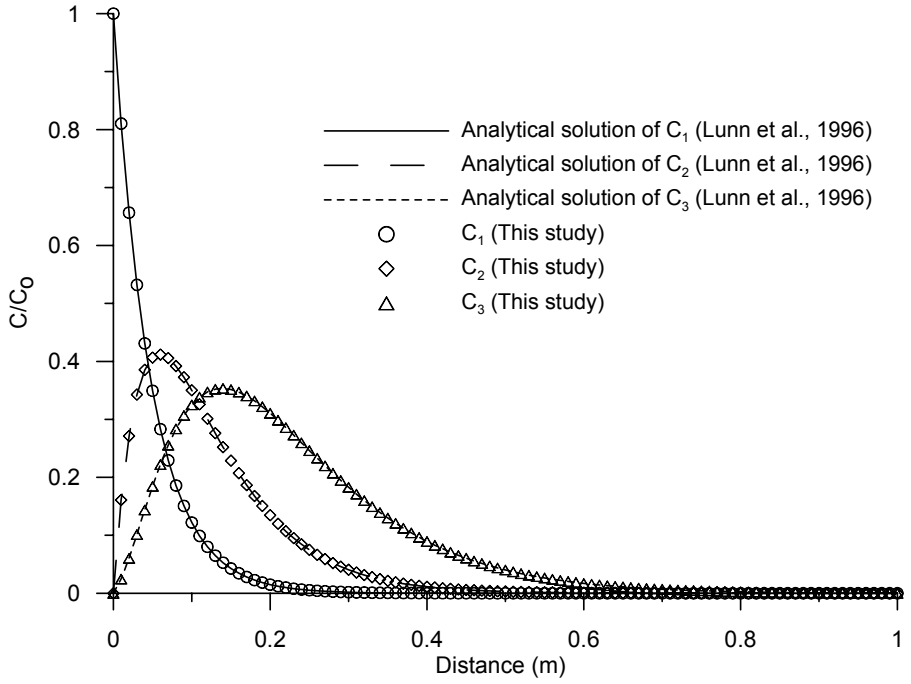

Figure 4.1 Comparison of concentration profiles of three species at t = 400 hrs: numerical results (symbols) and analytical solutions (lines).

4.2.2 Reactive Multispecies Transport in a Three-dimensional Uniform Flow Field

The fate and transport equation for single species contaminant undergoing a first-order reaction in a three-dimensional uniform flow field can be given as [Bear, 1979],

$$\frac{\partial C}{\partial t} - D_x \frac{\partial^2 C}{\partial x^2} - D_y \frac{\partial^2 C}{\partial y^2} - D_z \frac{\partial^2 C}{\partial z^2} + v \frac{\partial C}{\partial x} = -kC \tag{4.16}$$

where C are the concentration of the species (ML^{-3}), D_x, D_y, and D_z are the dispersion coefficients (L^2T^{-1}) in *x*-, *y*-, and *z*-direction, respectively, *v* is a constant groundwater flow velocity (LT^{-1}) in *x*-direction, and k is a first-order reaction coefficient (T^{-1}). As seen in Equation (4.1), a sequential reaction chain of each species, degraded with a first-order relationship, can be expressed as [Sun et al., 1999a; Sun et al., 1999b; Wiedemeier, 1999; Clement et al., 2000]

$$C_1 \xrightarrow{k_1} \cdots C_{i-1} \xrightarrow{k_{i-1}} C_i \xrightarrow{k_i} \cdots \xrightarrow{k_{n-1}} C_n \tag{4.17}$$

where subscript *i* indicates a species, C_i and C_{i-1} are concentration of target species and its parent species, respectively. Further, k_i and k_{i-1} are first-order reaction coefficients of target species and its parent species, respectively, and *n* is the total number of species.

The transport system of reactive contaminants with irreversible sequential first-order reactions in a three-dimensional uniform flow field can be expressed [Sun et al., 1999a]

$$\frac{\partial C_i}{\partial t} - D_x \frac{\partial^2 C_i}{\partial x^2} - D_y \frac{\partial^2 C_i}{\partial y^2} - D_z \frac{\partial^2 C_i}{\partial z^2} + v \frac{\partial C_i}{\partial x} = y_i k_{i-1} C_{i-1} - k_i C_i, \; i = 1,2,...,n \tag{4.18}$$

where y_i is a stoicheometric yield factor that describes the production of target species from its parent species. The values of C_{i-1} and k_{i-1} are assumed to be zero at $i = 1$. To

develop an analytical solution of Equation (4.18), Sun et al. [1999a] defined an auxiliary variable, a_i, for species 2 to *n*:

$$a_i = C_i + \sum_{j=1}^{i-1} \prod_{l=j}^{i-1} \frac{y_{l+1} k_l}{k_l - k_i} C_j \ , \ i = 2,3,...,n \tag{4.19}$$

Differentiating Equation (4.19) with respect to time and substituting it into Equation (4.18) yield new transport equations in terms of the auxiliary variable, a_i, for species 2 to *n* as follows:

$$\frac{\partial a_i}{\partial t} - D_x \frac{\partial^2 a_i}{\partial x^2} - D_y \frac{\partial^2 a_i}{\partial y^2} - D_z \frac{\partial^2 a_i}{\partial z^2} + v \frac{\partial a_i}{\partial x} = -k_i a_i \ , \ i = 2,3,...,n \tag{4.20}$$

with

$$a_{io} = C_{io} + \sum_{j=1}^{i-1} \prod_{l=j}^{i-1} \frac{y_{l+1} k_l}{k_l - k_i} C_{jo} \tag{4.21}$$

where a_{io} and a_{ib} are initial and boundary conditions of species *i* in the transformed system, respectively. Equation (4.20) is in the same form as Equation (4.16), so any previously-derived analytical solution for single-species transport in a three-dimensional uniform flow can be applied to Equation (4.20) [Sun et al., 1999a]. After obtaining the a_i solution of Equation (4.20) by the analytical solution, the concentration of target species *i* in the untransformed Equation (4.18) will be calculated by [Sun et al., 1999a]

$$C_i = a_i - \sum_{j=1}^{i-1} \prod_{l=j}^{i-1} \frac{y_{l+1} k_l}{k_l - k_i} C_j \ , \ i = 2,3,...,n \tag{4.22}$$

Analytical solutions for transport of reactive single-species in a three-dimensional uniform flow were developed by Domenico [1987], Wexler [1992], and Park and Zhan [2001]. Wexler [1992] derived the following solution for contaminant transport with a first-order reaction in a three-dimensional domain with infinite width and height as:

$$C(x,y,z,t) = \frac{C_o x \exp\left(\frac{vx}{2D_x}\right)}{8\sqrt{\pi D_x}} \int_0^t \tau^{-\frac{3}{2}} \exp\left[-\left(\frac{v^2}{4D_x}+k\right)\tau - \frac{x^2}{4D_x\tau}\right] \bullet \left\{erfc\left[\frac{Y_1-y}{2\sqrt{D_y\tau}}\right] - erfc\left[\frac{Y_2-y}{2\sqrt{D_y\tau}}\right]\right\} \bullet \left\{erfc\left[\frac{Z_1-z}{2\sqrt{D_z\tau}}\right] - erfc\left[\frac{Z_2-z}{2\sqrt{D_z\tau}}\right]\right\} d\tau \quad (4.23)$$

with

Initial condition (I.C.):

$$C = 0,\ 0 < x < \infty,\ -\infty < y < +\infty, \text{ and } -\infty < z < +\infty \text{ at t=0} \quad (4.24)$$

Boundary conditions (B.C.):

$$C = C_o,\ x = 0,\ Y_1 < y < Y_2, \text{ and } Z_1 < z < Z_2 \quad (4.25a)$$

$$C = 0,\ x = 0,\ y < Y_1 \ or\ y > Y_2, \text{ and } z < Z_1 \ or\ z > Z_2 \quad (4.25b)$$

$$\frac{\partial C}{\partial x} = 0,\ x = \infty \quad (4.25c)$$

$$\frac{\partial C}{\partial y} = 0,\ y = \pm\infty \quad (4.25d)$$

$$\frac{\partial C}{\partial z} = 0,\ z = \pm\infty \quad (4.25e)$$

where Y_1 and Y_2 are the lower and upper limits of a contaminant source zone in y-direction, respectively, Z_1 and Z_2 are the lower and upper limits of the zone in z-direction, respectively, and τ is a dummy variable of integration for time integral.

To demonstrate the transport of sequentially reactive contaminants in a three-dimensional domain, we set up the following problem (Figure 4.2): the size of domain is (40 m × 24m × 24 m) in (x, y, z) directions, v = 0.2 m/d, $D_x = 0.3$ m^2/d, $D_y = 0.3 D_x$, $D_z = 0.1 D_x$, k_1 = 0.05 d^{-1}, k_2 = 0.02 d^{-1}, and k_3 = 0.01 d^{-1}.

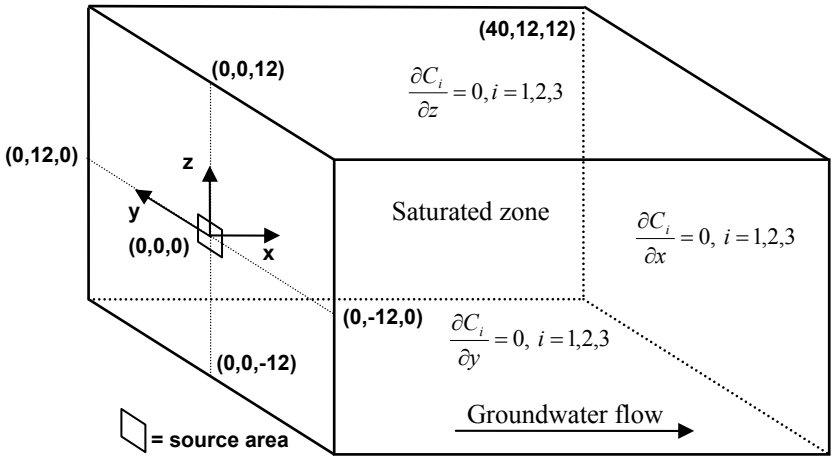

Figure 4.2 Schematic of a three-dimensional domain for transport of three reactive contaminants

Initial and boundary conditions are:

I.C.

$$C_i(x, y, z, t = 0) = 0\,,\ i = 1,\ 2,\ 3 \tag{4.26}$$

B.C.

All boundaries are no flux (type II) condition,

$$\frac{\partial C_i}{\partial x} = \frac{\partial C_i}{\partial y} = \frac{\partial C_i}{\partial z} = 0,\ i = 1,\ 2,\ 3 \tag{4.27}$$

except the followings:

$$\text{Type I. } C_1 = 1 \text{ at } x = 0,\ -0.5 \le y \le 0.5,\ -0.5 \le z \le 0.5,\ t > 0. \tag{4.28a}$$

$$\text{Type I. } C_2 = 0 \text{ at } x = 0,\ y = all,\ z = all,\ t > 0 \tag{4.28b}$$

$$\text{Type I. } C_3 = 0 \text{ at } x = 0,\ y = all,\ z = all,\ t > 0 \tag{4.28c}$$

The domain consists of 45,056 rectangular prism elements and 49,005 nodes. The discretization of the domain are: In x-direction, $\Delta x = 0.25$ at x = 0-1 m, $\Delta x = 0.5$ at x = 1-2

m, Δx = 1.0 at x = 2-40 m; and, in y- and z-direction, Δy and Δz = 0.25 at y and z= 0-±1 m, Δy and Δz = 0.5 at y and z = ±1-±2 m, and Δy and Δz = 1.0 at y and z = ±2-±12 m.

In Figure 4.3, comparisons of the concentration profiles of analytical solutions, which are calculated by MAPLE 7.0 program, and numerical results of this study at time 100 days are given. The profiles are illustrated at two planes: x-y plane at z = 0 and x-z plane at y = 0. The greater dispersion coefficient in y-direction than in z-direction causes the development of the wider contaminant plume on x-y plane than on y-z plane. Due to biotransformations of species 1, the byproducts (species 2 and 3) may be more important than species 1 down-gradient from the source: for example, at a point (30 m, 0, 0), the concentrations of species 2 and 3 are higher than those of species 1.

In Figure 4.4, concentration evolutions of contaminants over time at several locations are shown. Under the simulation conditions used here, the stabilized concentrations of species 1 and 2 decrease with distance in x-direction while the stabilized concentration of species 3 increases with distance in x-direction up to x=10 m. In Figure 4.3, the highest concentration zone of species 3 is located at around x=10 m. In Figure 4.4 (a), as the mesh grid becomes dense, the numerical solutions at point (5,0,0) show more accurate results.

The numerical results in Figures 4.3 and 4.4 show very good agreement with the analytical results.

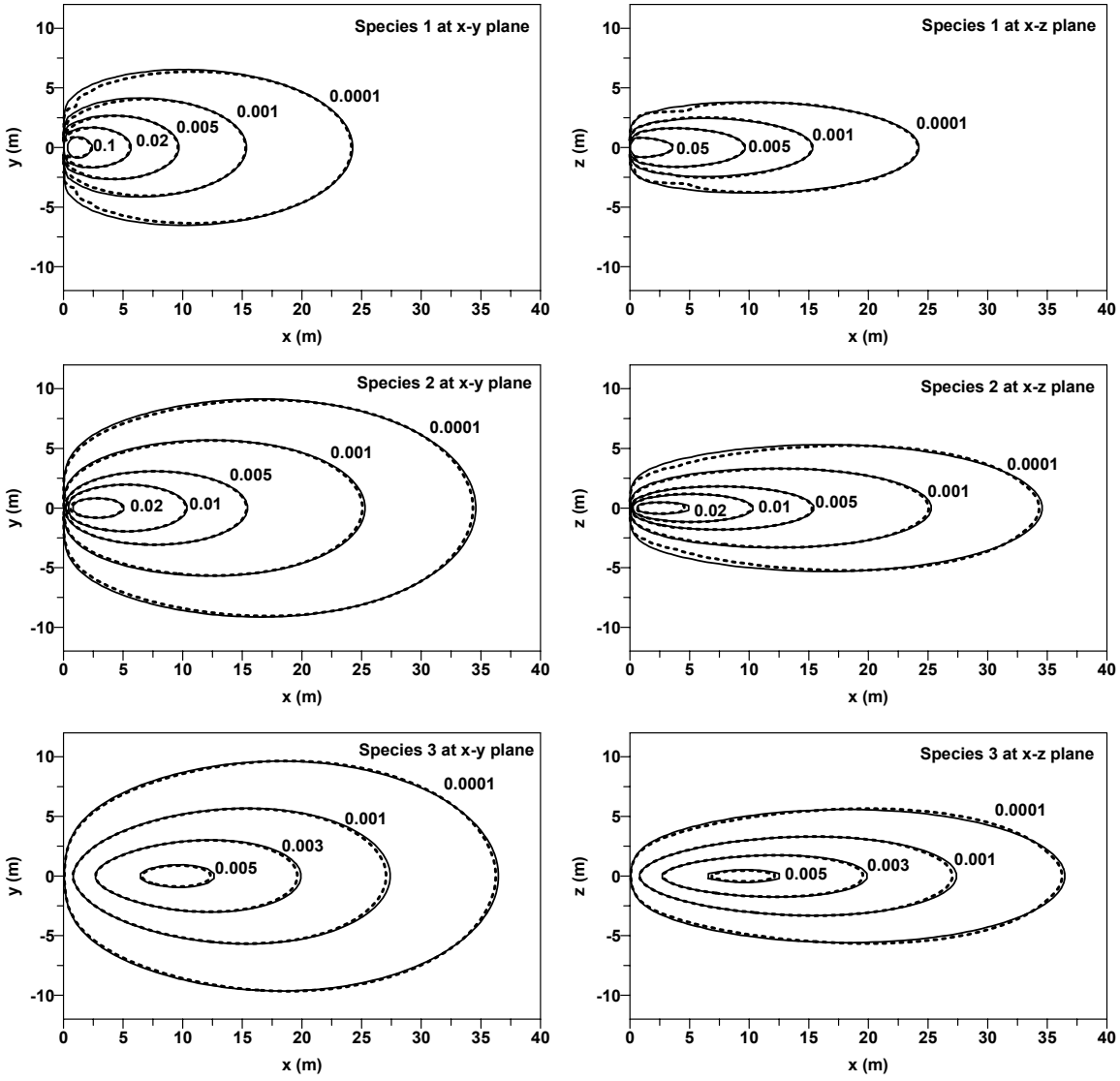

Figure 4.3 Concentration of three species on *x*-*y* plane at $z = 0$ and *x*-*z* plane at $y = 0$ at $t =$ 100 days: analytical solutions (solid lines) and dashed lines (numerical results of this study).

(a) Species 1

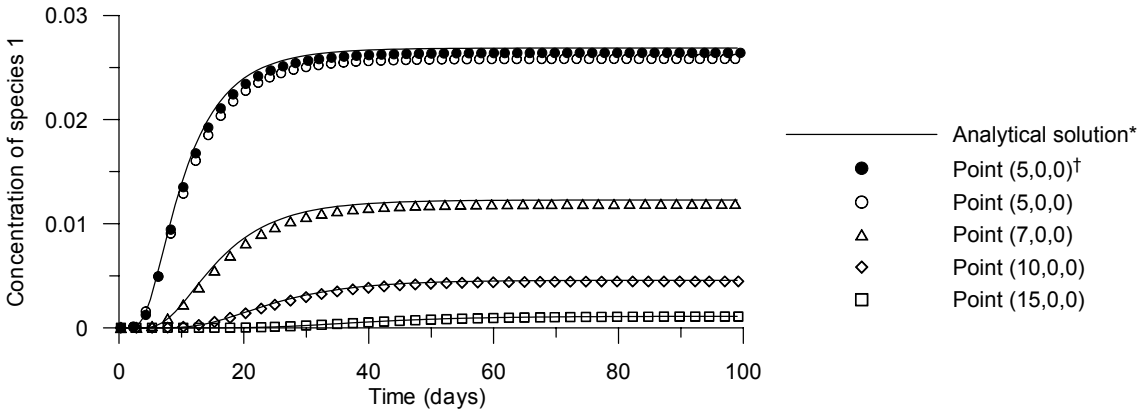

(b) Species 2

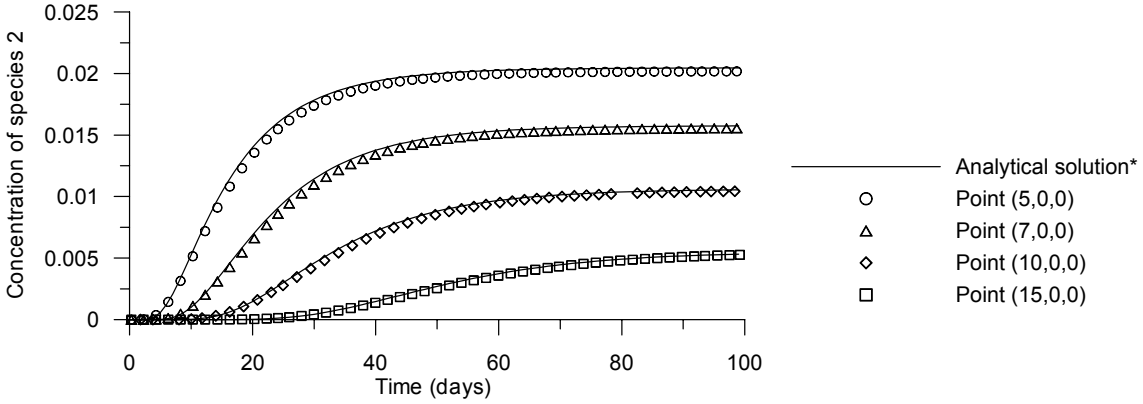

(c) Species 3

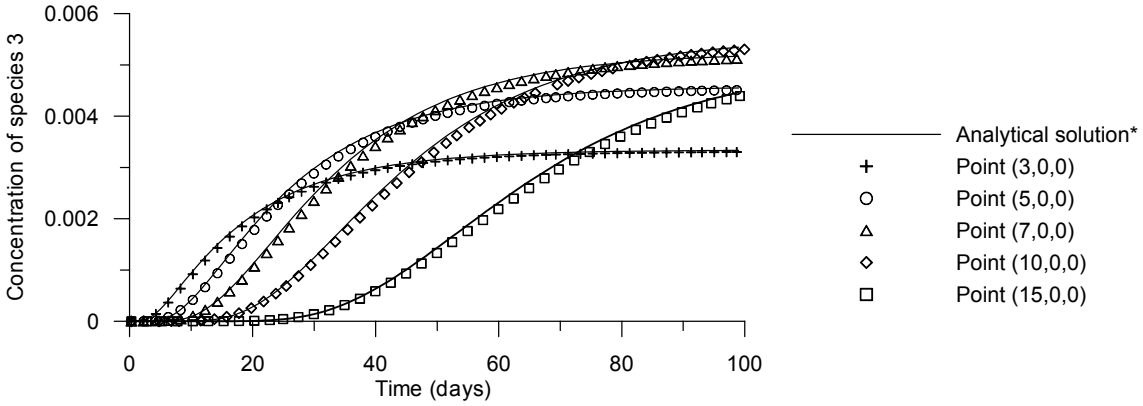

Figure 4.4 Concentration evolutions of three species at specified locations over time: *Analytical solutions (lines) and numerical results (symbols). † used a dense mesh (Δx = 0.25 at x = 0-6 m and the other grids are same). The unit of distance in point (x, y, z) is a meter.

4.3 Application of Transport of Biologically Reactive Contaminants

4.3.1 Modeling Domain and Parameters

As shown in Figure 3.7, the two-dimensional unconfined sandy aquifer with a dimension of (200 m × 16 m) in (x,y) directions is used to simulate transport of multi-species (TCE, cDCE, and VC) with biological transformations. The concentrations of all species are used in determining density-driven advection of gas phase, addressed in Chapter III.

For flow equations, the same initial and boundary conditions used in section 3.4 of Chapter III are applied here (Figure 4.5). For transport equations, the same boundary conditions used for TCE in section 3.4 of Chapter III are employed here for TCE, cDCE, and VC. As the contaminant source, an immobile TCE residual is set to its NAPL saturation of 5 % at distance x = 50-54 m and elevation z = 13-15 m. Initial concentrations of TCE, cDCE, and VC in gas, water, and solid phases, are set to zero within the domain. As boundary conditions at the ground surface, the recharge for infiltration is 30 cm per year for water phase, and constant atmospheric pressure is applied for gas phase. For transport equations for all contaminants in gas phase, the ground surface is set to a stagnant boundary layer of 0.3 m thickness, and left- and right-hand side boundaries are set to no flux condition.

Since three contaminants in water and gas phases are considered due to biological transformations, computational burden would be more than three times that for single contaminant in section 3.4 of Chapter III. Based on experience gained on simulations done in Chapter III, coarse mesh grids are used in diffusion-dominated zones and low concentration zones far away from the TCE source to reduce computational burden. The

domain idealization grid used here consists of 8,190 nodes and 3,952 elements. The domain is discretized as follows: In x-direction, Δx = 2.5 m at x = 0-40 and 80-200 m, and Δx = 1.0 m at x = 40-80 m; in z-direction, Δz = 0.5 m at z = 0-6.5 and 9.5-16 m, and Δz = 0.25 m at z = 6.5-9.5 m.

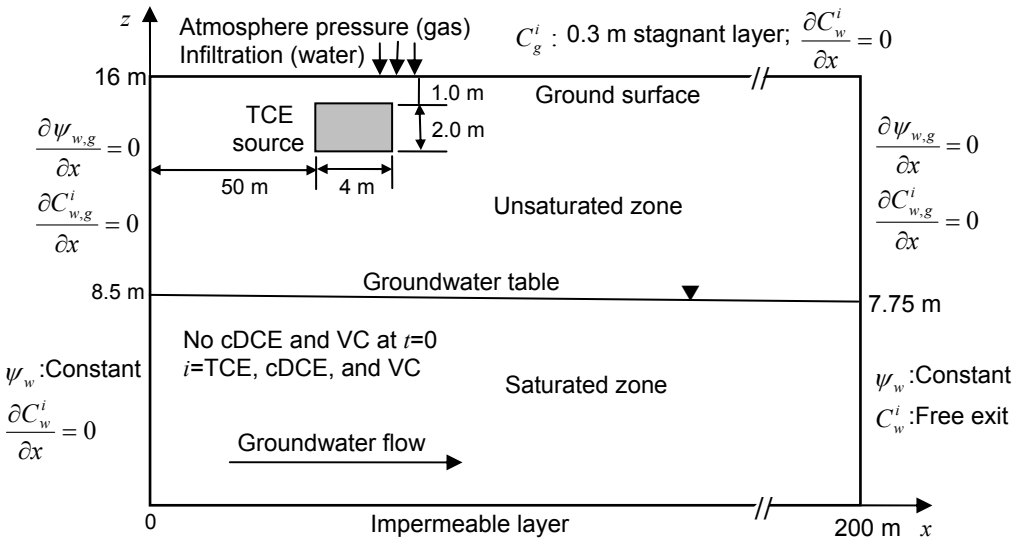

Figure 4.5 A schematic diagram of a modeling domain

The properties of the soil medium, water, and gas used in this application are given in Table 4.2. The intrinsic permeability of the soil medium, 1.0×10^{-10} m^2, is equivalent to an aqueous hydraulic conductivity of 1.0×10^{-3} m s^{-1}. The physical and chemical properties of three contaminants (TCE, cDCE, and VC) used herein are given in Table 4.3. The properties of TCE are already mentioned in Table 3.4. Estimated retardation coefficients of TCE and cDCE due to sorption are approximately 1.2 and 1.1, respectively, which correspond to field data reported by Witt et al. [2002]. The

retardation coefficient of dissolved VC is nearly 1.0, implying that its retardation effect is negligible. Biological transformations of multispecies (TCE, cDCE, and VC) are expressed by first-order relations or Michaelis-Menten kinetics. However, dissolution, water-gas partitioning, and volatilization for the species are represented by first-order relationships, and their rate coefficients (λ_D, λ_H, and λ_V) are set to 1.0 d^{-1}, which were used by Thomson et al. [1997]. The conversion coefficients for TCE to cDCE and cDCE to VC are $Y_{DCE/TCE} = 0.738$ and $Y_{VC/DCE} = 0.645$, respectively, which are calculated by dividing a molecular weight of a daughter contaminant by that of a parent contaminant.

Table 4.2 Properties of soil, water, and air

Parameters	Values
Porous medium	
Permeability, k	1.0×10^{-10} m^2
Porosity, ϕ	0.35
Residual water saturation, s_m	0.
Bulk density, ρ_b	1600 kg/m^3
Temperature, T	15 °C
Longitudinal dispersivity, α_L	1.0 m
Transverse dispersivity, α_T	0.01 m
Soil organic content, f_{oc}	0.0005
Parameters for the unsaturated zone	
n	2.0
α_{gw}	5.0 m^{-1}
Water	
Water molecular weight, M_w	18
Water density, ρ_w	997.3 kg/m^3
Water dynamic viscosity, μ_w	1.0×10^{-3} Pa s
Air	
Molecular weight, M_{air}	28.75
Density, ρ_{air}	1.23 kg/m^3
Viscosity, μ_{air}	1.8×10^{-5} Pa s

All simulations were carried out up to 400 days with variable time steps ranging from 1 to 24 hours, which were adjusted according to an automatic time-stepping scheme. Mass balance calculations are performed to determine the fate and transport of all contaminants, especially the biological transformation of each species in the system. In the calculations, mass transfer of each species to the atmosphere and to the groundwater in the saturated zone was separately calculated, and mass conservation for biotransformation processes was checked. Numerical results obtained for case studies are given in the following sections.

Table 4.3 Properties of three contaminants at 15°C

Parameters	TCE	cDCE	VC
[a] Molecular weight	131.39	96.94	62.50
[b] Vapor density, kg/m^3	5.56	4.10	2.64
[c] Vapor dynamic viscosity, Pa s × 10^6	9.38	9.29	9.27
[d] Henry constant, dimensionless	0.227	0.097	0.756
[e] Molecular diffusion in air, m^2/s × 10^6	7.87	8.84	10.42
[f] Molecular diffusion in water, m^2/s × 10^{10}	8.206	8.711	10.65
[g] Sorption coefficient, K_{oc}, L/g	0.1	0.049	0.003
[h] Vapor pressure, mmHg	41.27	129.2	2136.30
[i] max. C_g, kg/m^3	0.302	0.697	7.434
[j] max. C_w, kg/m^3	1.33	7.19	9.83

[a] Montgomery [2000].
[b] Calculated by the ideal gas law.
[c] Calculated Thodos and coworkers' equation [Perry et al., 1984] based on data from Reid et al. [1987].
[d] Calculated from regression data [Gossett, 1987]:.
[e] Calculated from the Fuller, Schettler, and Giddings relation [Perry et al., 1984].
[f] Calculated by the Wilke-Chang method [Perry et al., 1984].
[g] Values from Mackay et al. [1992].
[h] Calculated using regression equation (1) on page 657 [Reid et al., 1987].
[i] Calculated from Vapor pressure by the ideal gas law.
[j] Calculated from Henry constant, $C_g = H \times C_w$.

4.3.2 Transport and Biotransformation of Contaminants with First-order Relationships

Biotransformation rates of TCE, cDCE and VC, depend on various environmental factors such as population of microorganism, temperature, reduction potential, and contaminant concentration. The bioreaction processes and kinetics have been studied extensively and reported in the literature [Wiedemeier, 1998; Pavlostathis and Prytula, 2000; Cupples et al., 2004; Yu et al., 2005]. Biotransformation rates of each species are an important factor in determining the generation of daughter contaminants and the development of contaminated plume for parent and daughter contaminants.

Since contaminated environments are highly site-specific, it is hard to describe representative values of the bioreaction rates for every site. For first-order relationships of biotransformations of TCE, cDCE, and VC, three cases with different reaction coefficients are defined to simulate the bioreaction effect of multispecies transport of contaminants in the system (Table 4.4). The bioreaction rate data for the three contaminants are obtained from the literature [Clement et al., 2000; Suna et al., 2001] and are used for the cases. Among the cases, Case F-1 has the highest biodegradation coefficients for TCE, cDCE, and VC, which are reported by Suna et al. [2001], and Case F-3 has the lowest reaction coefficients, which were calculated from field monitoring data by Clement et al. [2000]. The coefficients for Case F-2 are set to be approximately half of the coefficients for Case F-1. In addition, a no-bioreaction case is simulated to show TCE transport without any biotransformation.

Transport of TCE in gas and water phases is shown in Figure 4.6 and 4.7, respectively. As discussed in Chapter III, TCE transport in the unsaturated zone near the

source occurs mainly due to density-driven advection. The magnitude of the advection in gas phase is illustrated in Figure 4.6 (e): Through the source zone, strong downward movement of gas phase is observed.

Table 4.4 Biotransformation scenarios for first-order relationships

First-order coefficient, day^{-1}	TCE	cDCE***	VC
Case F-1*	3.0×10^{-3}	2.5×10^{-3}	3.8×10^{-3}
Case F-2	1.5×10^{-3}	1.25×10^{-3}	1.9×10^{-3}
Case F-3**	1.1×10^{-4}	1.6×10^{-4}	1.0×10^{-4}

*data from Suna et al. [2001]
**data from Clement et al. [2000]
***cDCE is used as a representative daughter product of TCE among DCEs

Since the biotransformations of contaminants are assumed to occur only in the water phase, bioreaction rates of contaminants are determined mostly by their dissolved concentration, the magnitude of bioreaction coefficients, and water content in the system. The vertical profiles of water contents were already shown in Figure 3.11. As the density-driven advection of gas phase increases the spreading of vaporized contaminants and mass transfer of contaminants into water phase, the advection will also enhance the biotransformation of TCE.

Biotransformation of dissolved TCE implies the reduction in dissolved TCE mass in water phase and in the domain. In terms of TCE mass, the greater reaction coefficient causes the faster mass reduction, retarding the development of TCE plume in the system. To demonstrate the biotransformation effect on TCE transport, the transport profiles of four cases (no bioreaction, Case F-1, F-2, and F-3) are compared in Figures 4.6 and 4.7: Among the cases, Case F-1 (the greatest bioreaction coefficients) shows the least

development in dissolved and vaporized TCE plumes. Due to mass transfer of TCE between water and gas phases, the effect of the biotransformation of dissolved TCE on its transport occurs in both phases. Graphically, the difference in the size of the high concentration zone of dissolved TCE (≥ 1000 mg/L) between no-bioreaction case and Case F-1 is small, and the difference in the front of dissolved TCE plume (0.1 mg/L) between the two cases is less than 5 m down-gradient in Figure 4.7. The profiles of daily biotransformed TCE mass are shown in Figure 4.8 (a). Biotransformed TCE mass continuously increases over time even though the temporal increment of the TCE mass decreases. The increase in biotransformed TCE mass results from the increase in total mass of dissolved TCE in the system. Daily biotransformed TCE mass is proportional to the magnitude of first-order rate coefficients for biotransformation of TCE: At 400 days, the biotransformed TCE mass for Cases F-1, F-2, and F-3 is approximately 8.56, 4.78, and 0.39 g/day, which correspond to 0.3, 0.15, and 0.011 % of dissolved TCE mass, respectively.

Since dissolved TCE is transformed solely to cDCE, the generation rates of cDCE can be estimated from TCE biotransformation rates in Figure 4.8 (a) and a yield coefficient between TCE and cDCE, $Y_{DCE/TCE} = 0.738$. The evolution of total cDCE mass generated from TCE is presented in Figure 4.8 (b). As the increment of total mass of generated cDCE is determined mainly by dissolved TCE mass and water saturation level, the generated cDCE mass will rise with the increase in dissolved TCE mass.

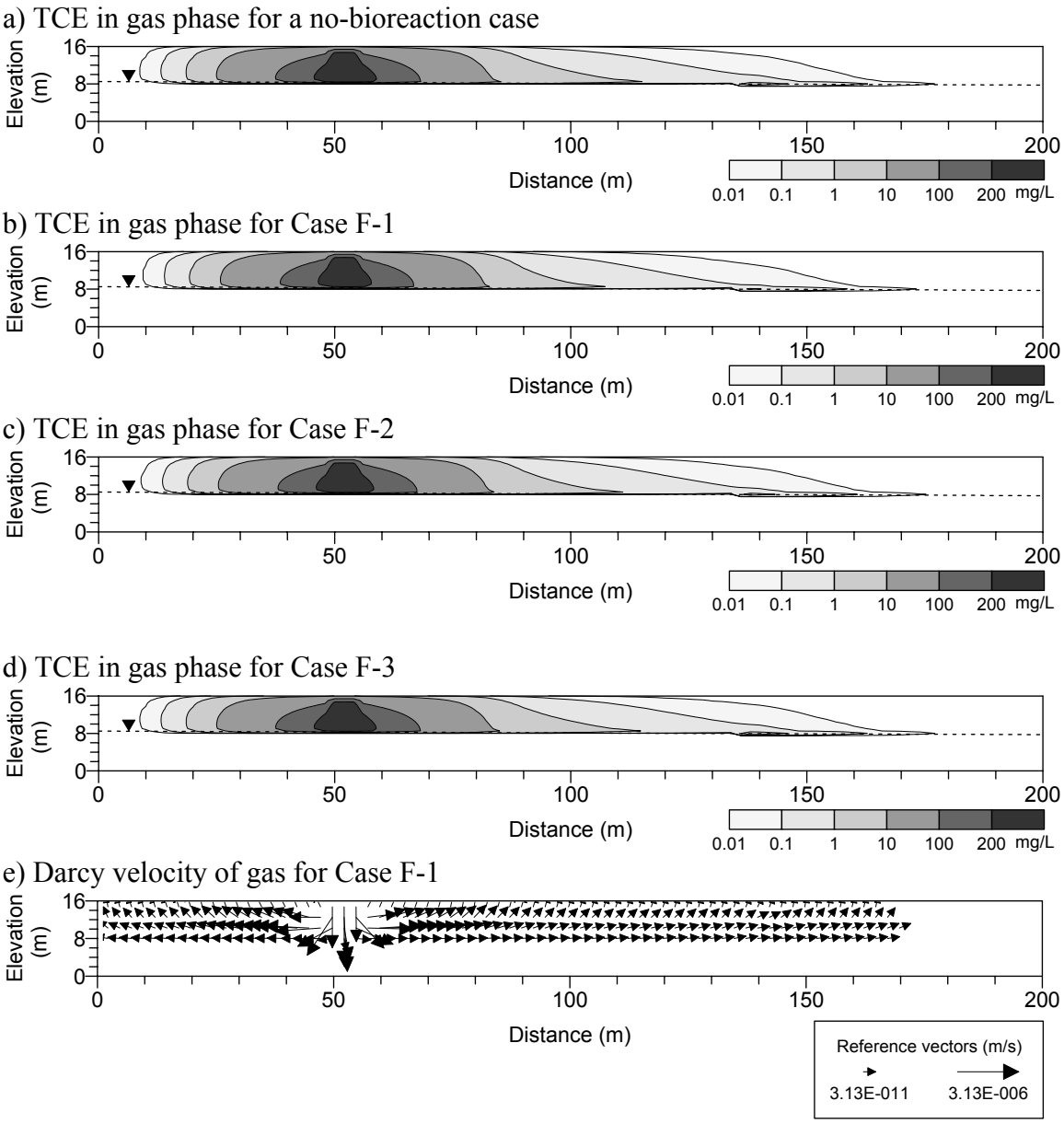

Figure 4.6 TCE concentration in gas phase for four cases(No-bioreaction, Case F-1, F-2, and F-3) and Darcy velocity of gas for Case F-1 at t=300 days

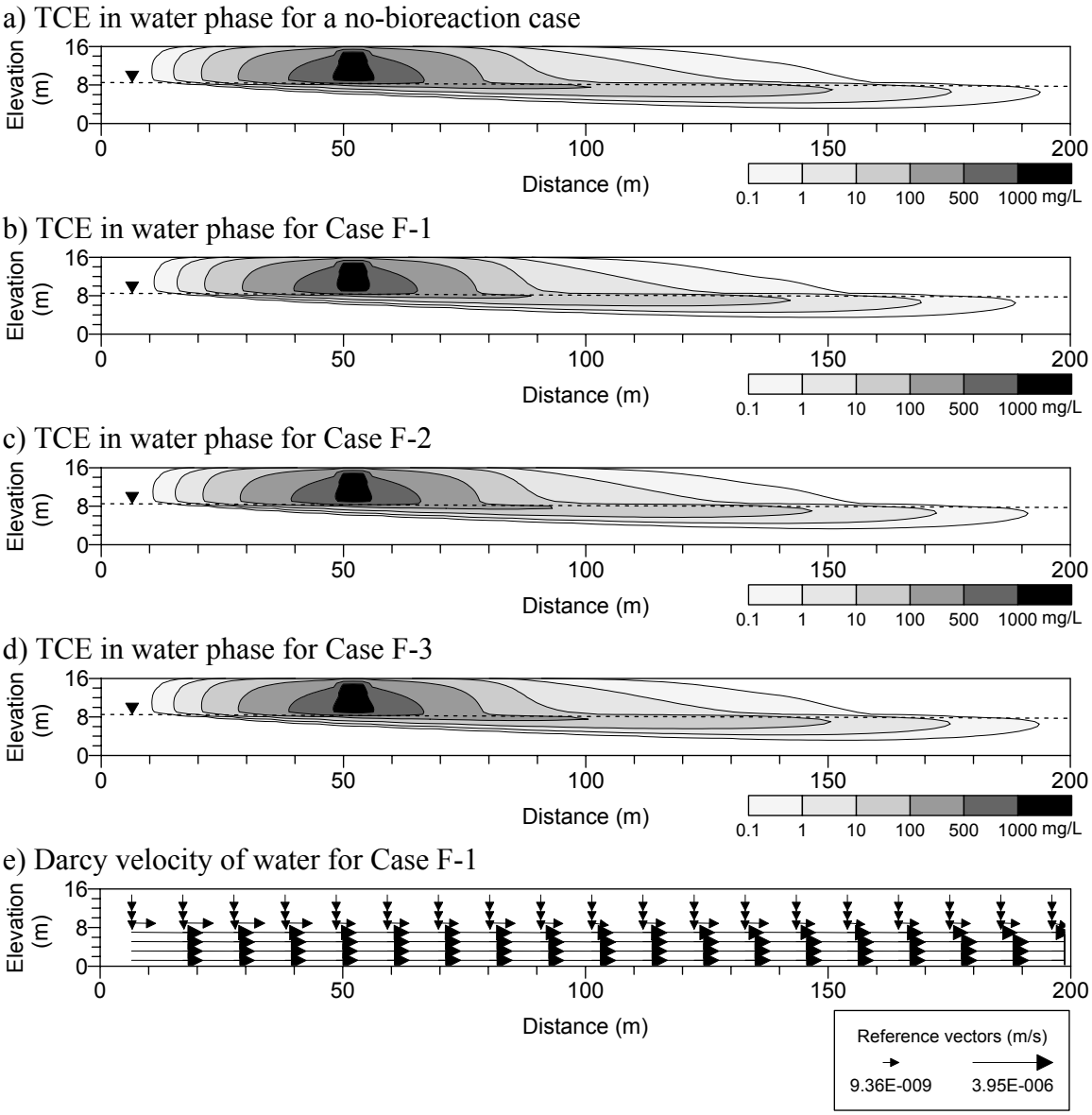

Figure 4.7 TCE concentration in water phase for four cases(No-bioreaction, Case F-1, F-2, and F-3) and Darcy velocity of water phase for Case F-1 at t=300 days

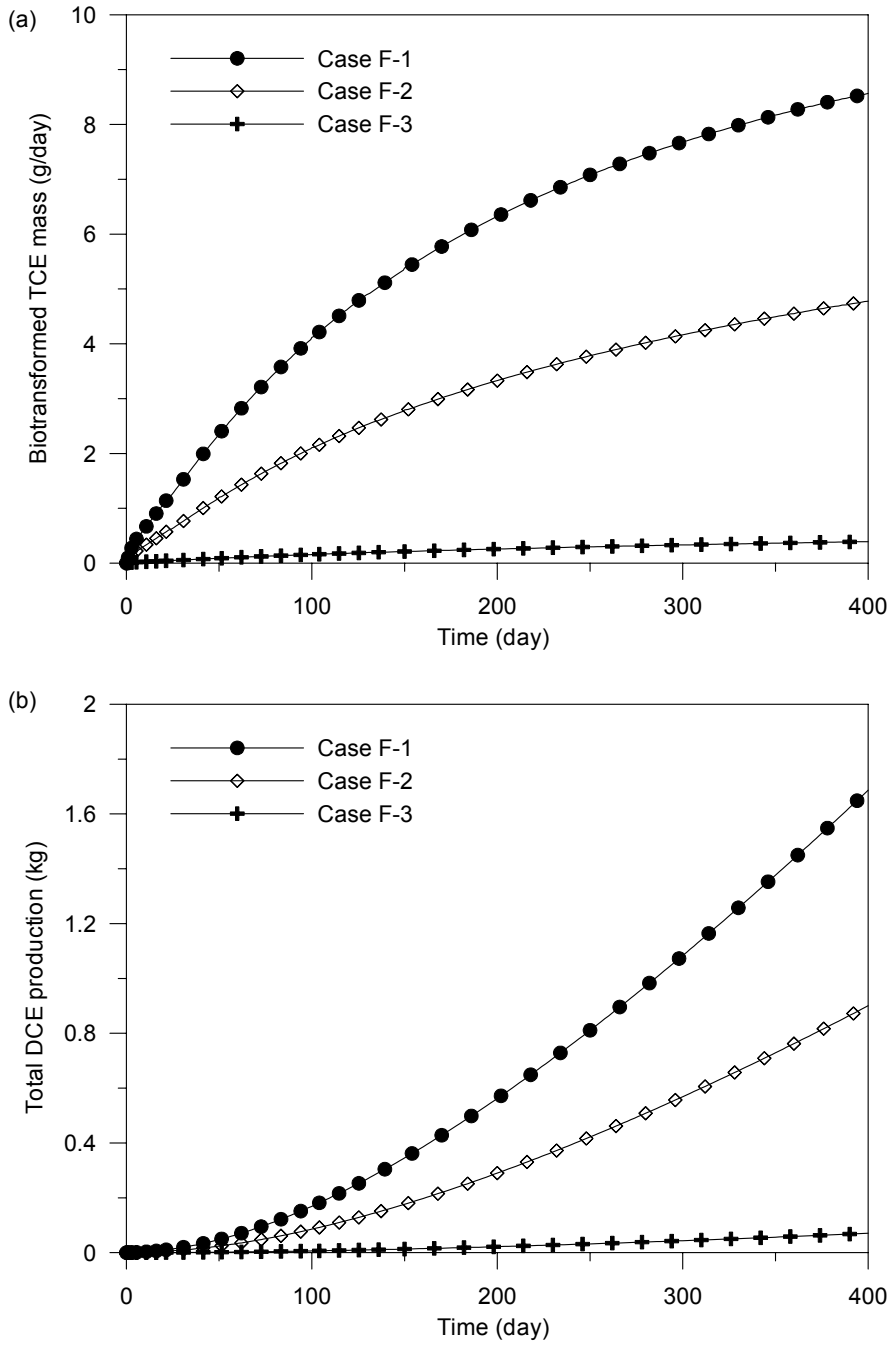

Figure 4.8 Biotransformation of TCE and production of cDCE. (a) Daily biotransformed TCE mass and (b) Total cDCE mass generated over time for three cases: Case F-1, F-2, and F-3.

For three cases (Case F-1, F-2, and F-3), the concentration profiles of cDCE, which is generated from dissolved TCE and a new contaminant in the system, is given in Figure 4.9: (a)-(c) for dissolved cDCE concentration profiles and (d)-(f) for vaporized cDCE concentration profiles. For all three cases, the high concentration zones of cDCE are located just above the groundwater table. Two zones of the highest concentration of cDCE are observed on left-side and right-side positions from the zone directly below the TCE source. The two zones are generated by three main factors: the density-driven transport in gas phase, the release of cDCE to the atmosphere, and the downward groundwater flow in the unsaturated zone. As discussed in section 3.4 of Chapter III, due to high density of gas mixture containing vaporized TCE around the source (x = 50-55m and z = 13-15 m), the flow of contaminated gas moves downward from the source, and then the flow splits into two directions (into left or right) just above the groundwater table (Figure 4.6(e)). While TCE vapor in gas phase migrates in high water content area above the groundwater table, vaporized TCE partitions into water phase, and then some portion of the dissolved TCE will be degraded into cDCE. The two-directional gas flow will contribute in transporting the generated cDCE into left- or right-side. The release of cDCE to the atmosphere decreases its concentration near the ground surface: Atmospheric loss of contaminants including cDCE plays an important role in reducing contaminant mass in the systems (Figure 4.13). The downward movement of water will enhance the downward migration of dissolved cDCE in the unsaturated zone and its transport to the saturated zone. The air inlet from the ground surface above the source may contribute to the dilution of cDCE concentration near the source.

While cDCE in water phase moves downward in the unsaturated zone, some portion of dissolved cDCE will vaporize into gas phase, which may also cause the change in the density of gas mixture. The concentration contours of vaporized cDCE are illustrated in Figure 4.9 (d)-(f). The highest concentration zones of vaporized cDCE agree with those of dissolved cDCE shown in Figure 4.9 (a)-(c).

For the three cases (Case F-1, F-2, and F-3), the concentration distribution of dissolved and vaporized cDCE shows similar trends for three phases. The values of cDCE concentrations, however, shows distinct difference according to the magnitude of bioreaction coefficients: For Case F-1, the highest biotransformation rate of TCE results in the highest concentration profiles of its daughter contaminant cDCE and the widest plume development in both gas and water phases.

In Figure 4.10, daily biotransformation rates of cDCE and total mass of VC produced by the biotransformation are given. The bioreaction coefficients of both TCE and cDCE play an important role in determining VC production: Since the concentration of cDCE depends on the biotransformation coefficient for TCE and the concentration of cDCE is linked with the generation of VC, the VC production depends on the biotransformation of both TCE and cDCE. Relative difference in total VC production between Cases F-1 and F-2 becomes larger than that in total cDCE production between the two cases: For example, at t=400 days, total cDCE production of Case F-1 is less than two times that of Case F-2, however, total VC production of Case F-1 is greater than three times that of Case F-2.

a) DCE in water phase for Case F-1

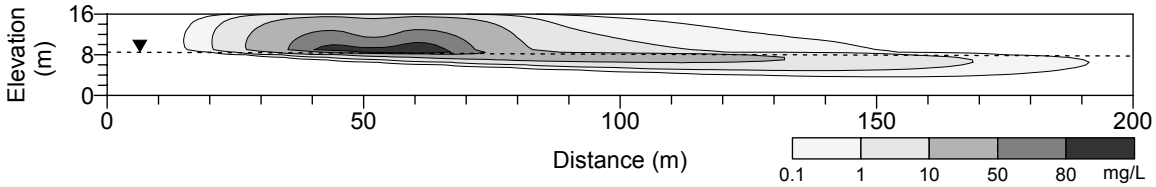

b) DCE in water phase for Case F-2

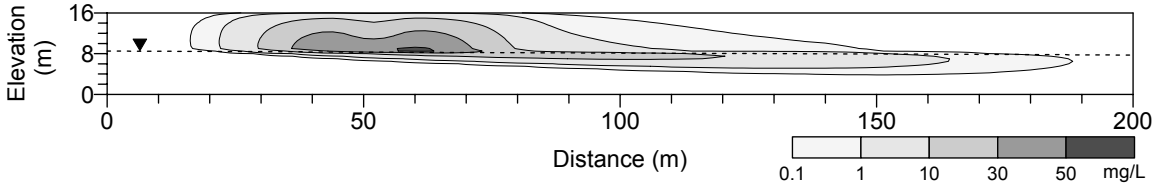

c) DCE in water phase for Case F-3

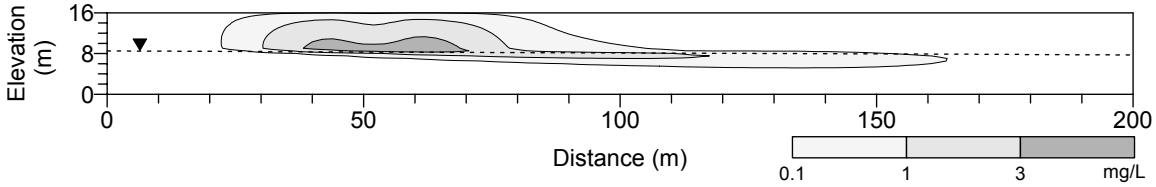

d) DCE in gas phase for Case F-1

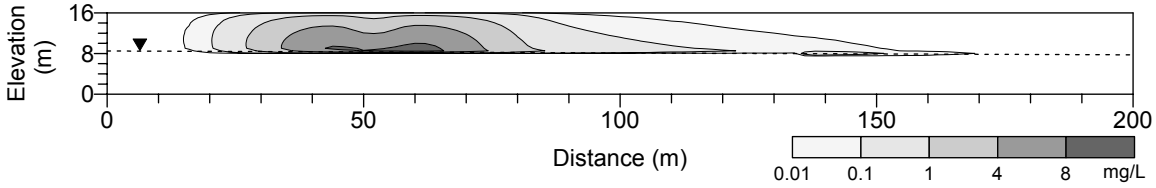

e) DCE in gas phase for Case F-2

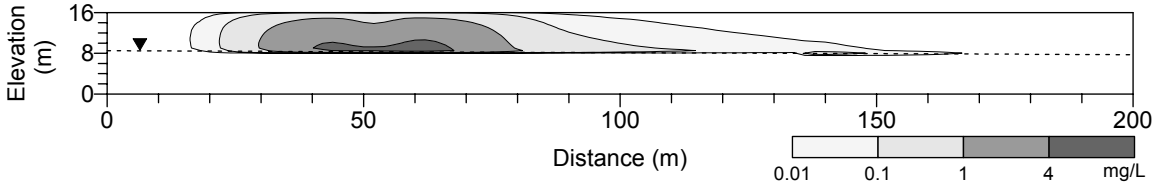

f) DCE in gas phase for Case F-3

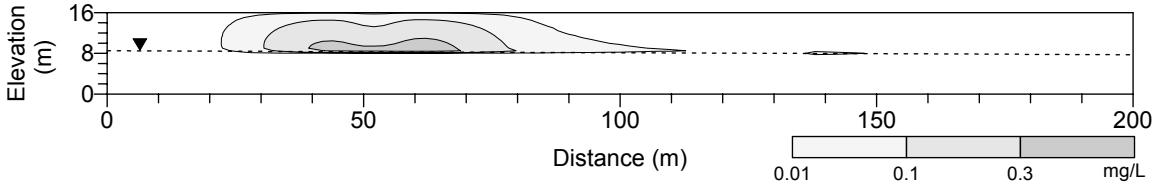

Figure 4.9 DCE concentration in water and gas phases for three cases: Case F-1, F-2, and F-3 at t=300 days

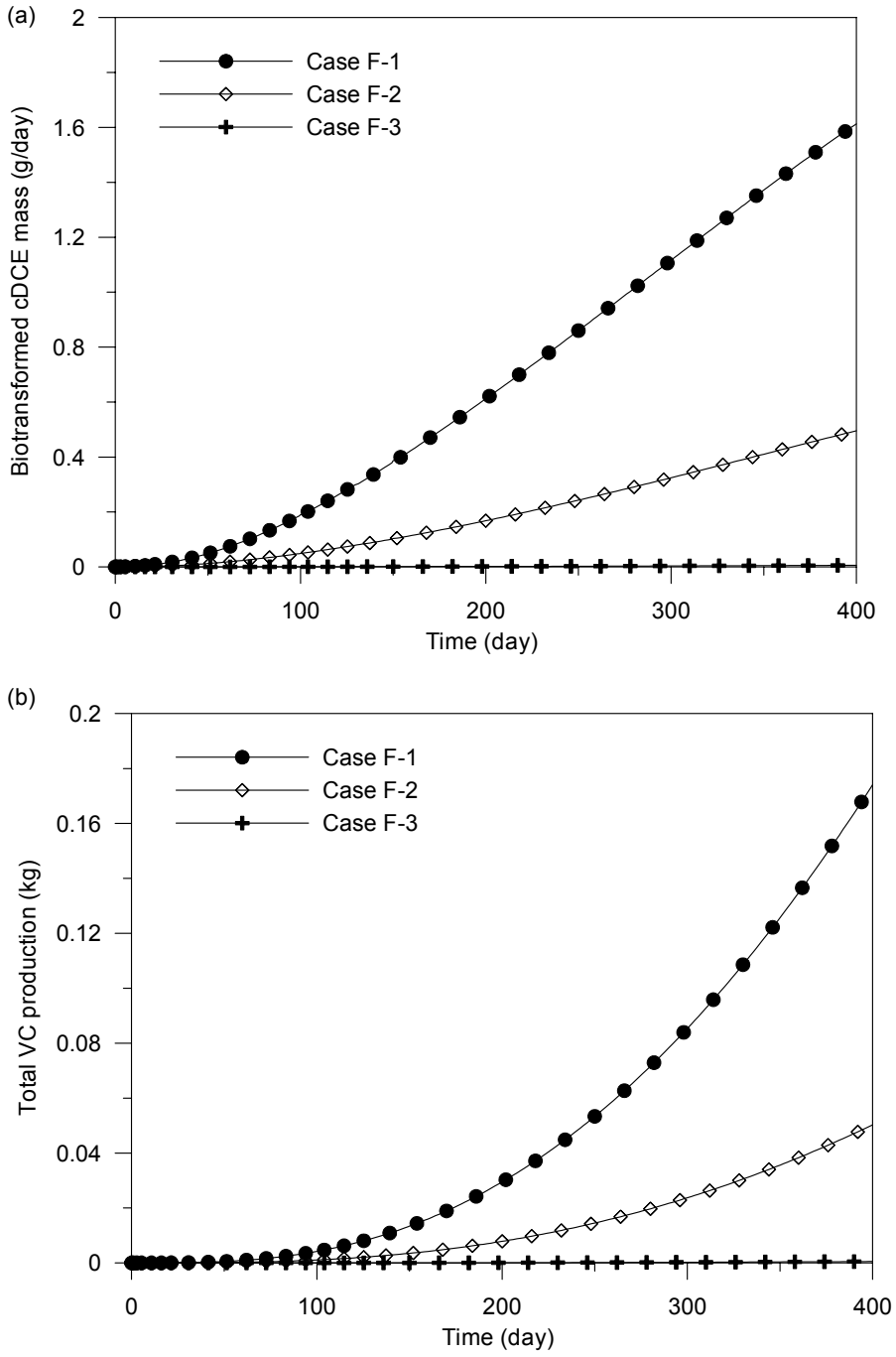

Figure 4.10 Biotransformed cDCE mass and production of VC. (a) Daily biotransformed cDCE mass and (b) Total VC mass generated over time for three cases: Case F-1, F-2, and F-3

VC is generated by biotransformation of cDCE in water phase, and it partitions into gas phase. The concentration distribution of VC in water and gas phases is given in Figure 4.11. The highest concentration zones of dissolved VC are detected in the down gradient saturated zone while the highest concentration zones of vaporized VC correspond roughly to those of vaporized cDCE shown in Figure 4.9.

The concentration profiles of dissolved VC reflects the concentration profiles of dissolved cDCE and characteristics of sequential biotransformations: since VC is generated mostly around the groundwater table, the VC will be easily transferred to the saturated zone, and then will migrate in the relatively fast ground water flow. Since VC is generated after its parent contaminant cDCE is produced and accumulated, a time lag between the appearances of cDCE and VC may contribute to the down gradient movement of the high concentration zones of dissolved VC in Figure 4.11.

In Figure 4.11, among three cases (Cases F-1, F-2, and F-3), Case F-1 shows highest concentration profiles of dissolved and vaporized VC. In each case, the concentration of dissolved VC (Figure 4.11) is much lower than that of dissolved cDCE (Figure 4.9). For Cases F-1 and F-2, even though the concentration of dissolved VC is very low, however, in wide areas, the concentration exceeds its drinking water standard (Maximum contaminant level of VC: 0.002 mg/L) listed on the National Primary Drinking Water Regulations [EPA, 2000].

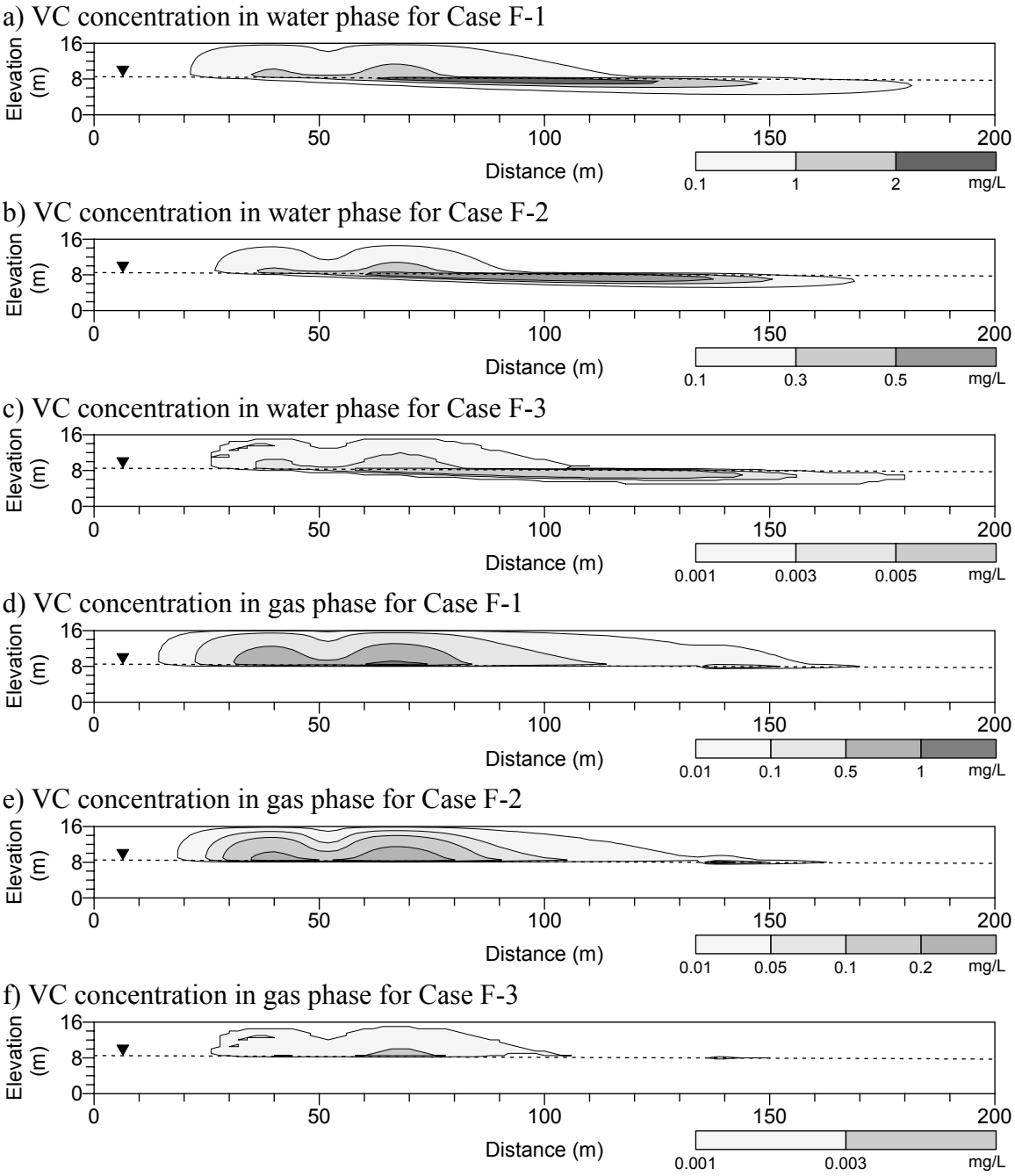

Figure 4.11 VC concentration in water and gas phases for Cases F-1, F-2, and F-3 at t=300 days

In Figures 4.7, 4.9, and 4.11, the highest concentration zones of TCE, cDCE, and VC in water phase appeared at different locations due to gas and water flow, sequential bioreactions, and non-equilibrium mass transfer between phases. Due to the interactions between the complex processes, the generation and distribution of intermediate contaminants (cDCE and VC) can not be simply predicted, but these will be determined by coupled and nonlinear relationships of the processes.

The distribution of contaminants depends on various factors such as physical and chemical properties of substances and environmental conditions. For Case F-1, the evolution of mass distribution of TCE, cDCE, and VC is illustrated in Figure 4.12. The temporal changes in the distribution of TCE in the domain show similar trends with those shown in section 3.4 of Chapter III (for a no bioreaction case): TCE mass within gas and water phase in the unsaturated zone increases over time while its increment decreases over time. Dissolved TCE in the saturated zone, however, increases almost linearly after a period of time lag, which is traveling time for TCE to reach the saturated zone from the source. After about 150 days, dissolved TCE mass is greater than vaporized TCE mass in the domain.

The distribution of cDCE, which is generated by the biotransformation of dissolved TCE, is given in Figure 4.12 (b). Total dissolved cDCE mass is much greater than total vaporized cDCE mass. This distribution of cDCE in water or gas phases is related with the generation of cDCE only in water phase and chemical properties of cDCE. The vaporized cDCE comes from water phase through a non-equilibrium partitioning process. As seen in Table 4.3, the solubility of cDCE is approximately 5.4 times that of TCE while the saturated vapor concentration of cDCE is about 2.3 times that

of TCE. The evolution of dissolved cDCE mass in the unsaturated and in the saturated zone suggests that, at the beginning of Case F-1 simulation, cDCE is generated mostly in the unsaturated zone, so dissolved cDCE mass in the unsaturated zone is greater than that in the saturated zone until 350 days. However, as TCE transfers into the groundwater in the saturated zone, dissolved cDCE mass in the saturated zone increases faster than that in the unsaturated zone from about 150 days, and, after 350 days, dissolved cDCE mass in the saturated zone exceeds that in the unsaturated zone.

In Figure 4.12 (c), the distribution of VC is shown: Dissolved VC in the saturated zone has sharp increase after 150 days, and becomes a dominant portion of VC distribution. The factor that dissolved VC in the saturated zone is much greater than that in the unsaturated zone is related to one that the existence of the highest concentration zone of dissolved VC in the saturated zone seen in Figure 4.11. In the unsaturated zone, due to high vapor pressure of VC, its mass in gas phase is greater than dissolved VC.

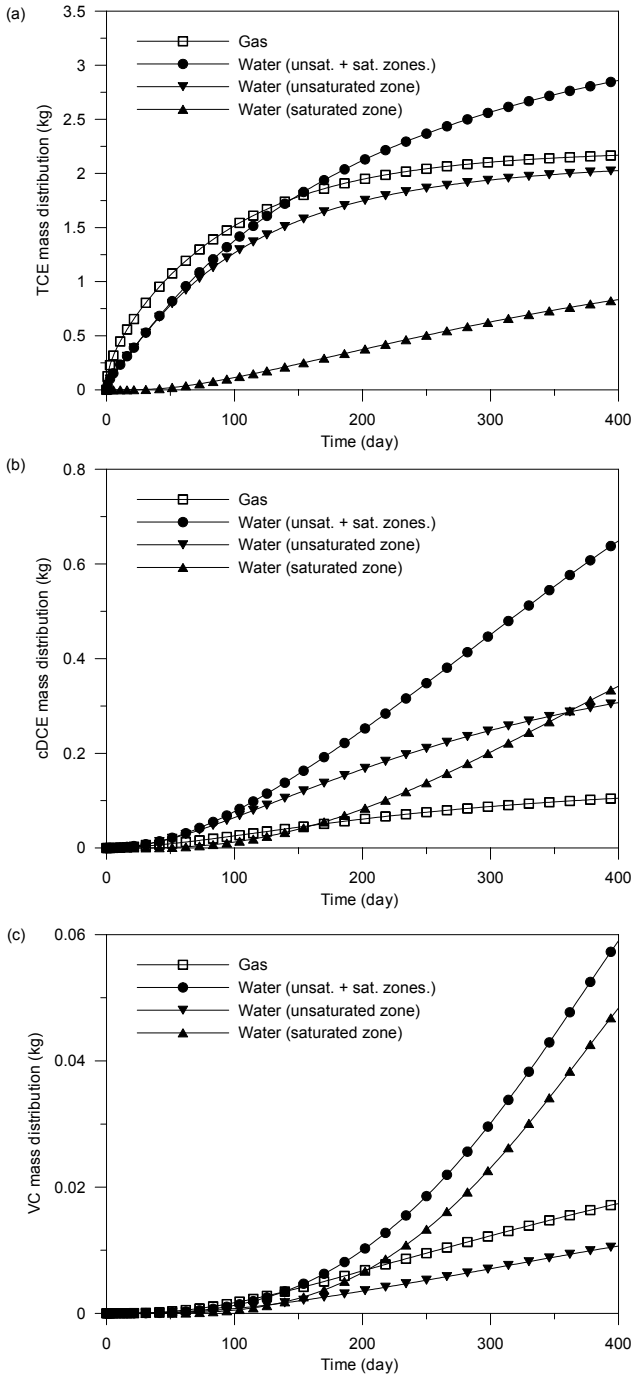

Figure 4.12 Distribution of TCE, cDCE, and VC in the domain for Case F-1

Through mass balance calculations in the domain and at boundaries, the fate of TCE, cDCE, and VC is investigated and is presented in Figure 4.13. At 400 days, the release of TCE to the atmosphere, adsorbed TCE to soil medium, dissolved TCE, and vaporized TCE, and biotransformed TCE mass are approximately 33, 4.5, 4.5, 3.4, and 3.6 % of initial TCE mass at the source, respectively. Since the source is close to the ground surface, TCE release to the atmosphere dominates the fate of TCE. In Figure 4.13 (b), as TCE mass in water phase increase with time, the portion of bioreaction shows fast increase. After 200 days, TCE mass in gas phase reaches almost stabilized conditions: It may imply a dynamic equilibrium condition in which TCE mass vaporized from the source almost balances the sum of vaporized TCE mass for atmospheric loss and mass transfer into the water phase. Sorption plays an important role to determine the fate of TCE. The sorption will help to retard the development of TCE plume.

In Figure 4.13 (c) and (d), relative portions of cDCE and VC mass in gas phases decrease over time. Dissolved cDCE has the largest portion among the distributions of generated cDCE. In Figure 4.13 (d), the ratio of dissolved VC mass to total generated VC ranges from 27 and 37 %. For cDCE and VC, the ratios of biotransformed mass to total generated mass steadily increase over time. This implies that the role of contaminant biotransformation on determining fate of contaminants will become larger over time. Therefore, for long term simulations of TCE transport in subsurface systems, biotransformation should be taken into consideration.

Of course, total biotransformation mass depends on the magnitude of bioreaction coefficients. As expected from retardation factors of cDCE and VC, sorption of VC is minimal while that of cDCE has more than ten percent of total cDCE mass generated

during simulations. The atmospheric loss of cDCE and VC has significant effects on fate of the contaminants even though those are generated in water phase and VC comes mainly from the saturated zone: The loss of cDCE to the atmosphere increases continuously with time, and, since 200 days, the loss of VC to the atmosphere exceeds dissolved VC mass in the systems. It indicates that mass release to the atmosphere should be included in modeling fate and transport of volatile organic compounds as long as contaminant plume is connected with open ground surface through the unsaturated zone.

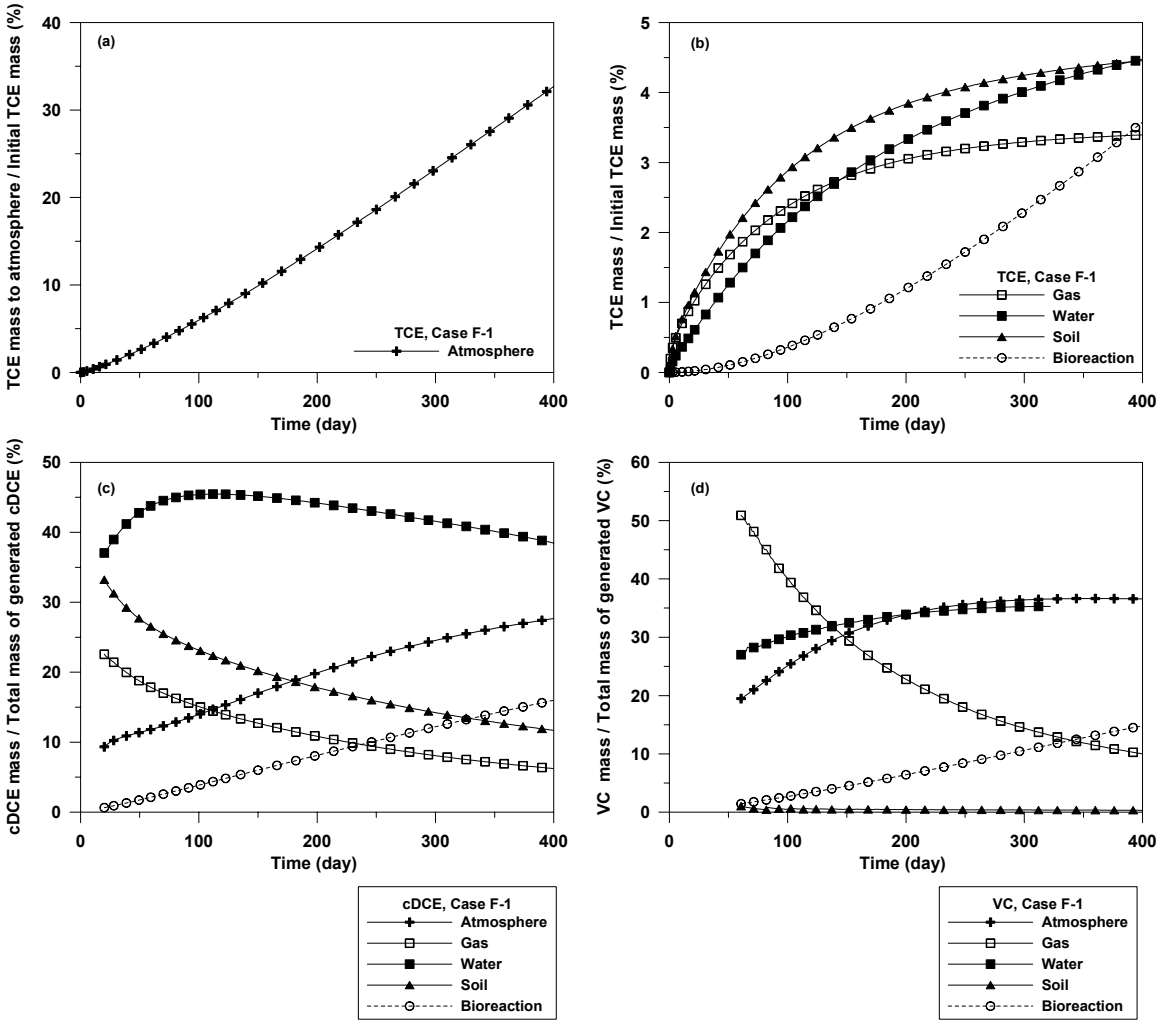

Figure 4.13 Fate of TCE, cDCE, and VC for Case F-1

4.3.3 Transport and Biotransformation of Contaminants with Michaelis-Menten Kinetics

Michaelis-Menten kinetics has been often used to represent sequential dechlorination of chlorinated hydrocarbons [Barrio-Lage et al., 1987; Haston and McCarty, 1999; Pavlostathis and Prytula, 2000; Yu et al., 2005]. Michaelis-Menten kinetics is more complicated than a first-order relationship: As mentioned in Equation (2.3) in Chapter II, when the half-saturation constant is much greater than contaminant concentration, Michaelis-Menten kinetics becomes a first-order relationship while, on the contrary, when the former is much less than the latter, the kinetics becomes a zero-order model.

In the previous section 4.3.2, the study on multispecies biotransformation with first-order relationships showed that concentration profiles of the compounds highly depend on the values of bioreaction rates. First-order coefficients for biological transformations of chlorinated hydrocarbons have been estimated through laboratory and field work by many researchers, and published data were used in the previous section. Parameters of Michaelis-Menten kinetics for TCE, cDCE, and VC have been often estimated only through various laboratory works, which are conducted under well controlled conditions [Cupples et al., 2004; Yu et al., 2005]. Due to lack of field data for the parameters, three different experimental data are used to simulate the sequential biotransformations of TCE, cDCE, and VC, which are listed in Table 4.5.

In Michaelis-Menten kinetics, the concentration of microorganism plays an important role in determining maximum bioreaction rates. However, the field measurement of dechlorination microorganisms, such as *Dehalococcoides* group

organisms, is a difficult task, and, even though dechlorination microorganisms have been detected in contaminated zones and the microbial biomass has been measured through special laboratory procedures, the measurement data are very limited at specified locations [Davis et al., 2002; Lendvay et al., 2003]. The distribution of microorganisms may also vary over locations and subsurface environments. In this study, to overcome complicated biological situations and lack of field data, dechlorination microorganisms are assumed to be distributed uniformly at a biomass concentration of 5 μg/L in contaminated areas, which is chosen based on laboratory and field data (Table 4.5). In this section, the effect of Michaelis-Menten-kinetics biotransformations of multispecies on their fate and transport are examined under conditions given in Tables 4.2, 4.3, and 4.5.

Table 4.5 Biotransformation scenarios for Michaelis-Menten kinetics

Scenarios	TCE		cDCE		VC	
	k_B [d)] (μM/d)	K_s (μM)	k_B [d)] (μM/d)	K_s (μM)	k_B [d)] (μM/d)	K_s (μM)
Case MM-1 [a)]	0.62	2.8	0.11	1.9	0.012	602
Case MM-2 [b)]	0.008	1.4	0.00185	3.3	0.0017	2.6
Case MM-3 [c)]	0.36	0.54	0.36	0.54	0.36	290

[a)] data from Yu et al. [2005].
[b)] data from Haston and McCarty [1999].
[c)] data from Fennel and Gossett [1998].
[d)] k_B is calculated with a biomass concentration (protein or volatile suspended solid) of 5 μg/L.

The concentration profiles of multispecies (TCE, cDCE, and VC) for the three cases are illustrated in Figures 4.14-16. In terms of concentration, its profiles for dissolved and vaporized TCE with Michaelis-Menten kinetics show similar trends with

those with first-order kinetics shown in Figures 4.6 and 4.7, respectively. However, the concentration profiles of dissolved cDCE show distinct difference between Michaelis-Menten kinetics and first-order kinetics: The highest concentration zones at Michaelis-Menten kinetics have been moved to far down gradient zones near the front of dissolved cDCE plume (for instance, Figure 4.14 (b)) while the highest concentration zones at first-order kinetics are located above the groundwater table around the source (for instance, Figure 4.9 (a)). The difference between cDCE concentration profiles of the two kinetics comes from the characteristics of each kinetics: In cases of first-order kinetics, the generation of cDCE is linearly proportional to dissolved TCE concentration, however, in cases of Michaelis-Menten kinetics, if dissolved TCE concentration is much higher than the half-saturation constant, K_s, in Equation (2.3), the kinetics become zero-order, and thus the generation of cDCE is nearly independent on TCE concentration. For example, in first-order kinetics, the generation rate of cDCE at dissolved TCE of 100 mg/L is ten times that at dissolved TCE of 10 mg/L. In the contrary, for Case MM-1 in which the values of K_s for TCE is 2.8 μM (0.37 mg/L), the difference in the generation rates of cDCE under 10 and 100 mg/L of dissolved TCE would be less than 5 %. This suggests that the generation of cDCE in the relatively high concentration zones (≥ 10 mg/L) in Figure 4.14 (a) will be almost same. Under such circumstances, dilution due to advection (groundwater flow in the saturated zone) and dispersion will play an important role to determine the concentration of dissolved cDCE in the saturated zone. The inflow of clean groundwater from the left-end boundary to the highly contaminated zone (especially x = 30-80 m) will reduce the concentration of cDCE in the groundwater due to dilution processes, and, as the groundwater becomes polluted over distance, the dilution effect

will decrease. High concentrations of VC also appear in the down gradient saturated zone near the front of dissolved VC plume.

In Case MM-1, the biotransformation coefficient of TCE is relatively large: The coefficients at 0.1 and 1.0 mg/L of dissolved TCE concentration correspond to approximately 0.17 and 0.06 d^{-1} as first-order coefficients. The high biodegradation of TCE retards the development of its plume in the saturated zone (Figure 4.14 (a)). VC has the lowest bioreactivity, so its dissolved plume is widely developed as shown in Figure 4.14 (c). Due to the generation of VC in the saturated zone, vaporized VC is also present in wide regions, which is partitioned from dissolved VC into gas phase.

Case MM-2 has the least bioreaction coefficients for TCE among the three cases in Table 4.5. The development of TCE in the unsaturated zone is much larger in Case MM-2 than in Case MM-1. Dissolved cDCE and VE also have low concentrations in the domain in Figure 4.15, and vaporized VC concentration in the domain was less than 1 μg/L.

The concentration profiles of daughter contaminants (cDCE and VC) are related to bioreaction parameters in a complicated manner (maximum bioreaction rates and half-saturation constants) of both a parent and the daughter contaminants. In Case MM-3, TCE, cDCE, and VC have the same maximum bioreaction coefficient and the same half-saturation constant. The development of dissolved TCE plume in Case MM-3 is much smaller than that in Case MM-2. Among the three cases, the development of dissolved cDCE plume is least in Case MM-2 and is greatest in Case MM-1. The phenomena come from the difference of bioreactivity of TCE and cDCE: For Case MM-1, TCE and cDCE

are readily dechlorinated, but, for Case MM-2, the dechlorination of cDCE is very low while TCE is readily transformed to cDCE.

Figure 4.16 (c) and (f) draw our attention: The concentration of dissolved VC is greater than that of dissolved cDCE. This phenomenon results from low bioreactivity of VC due to higher half-saturation coefficient of VC than that of cDCE. For instance, the biotransformation coefficient of dissolved cDCE at 0.5 mg/L corresponds to approximately 0.063 d^{-1} as a first-order coefficient, however the coefficient of dissolved VC at 0.5 mg/L does to 0.0014 d^{-1} as a first-order coefficient. This implies that, as the production of VC from cDCE is greater than the biotransformation of VC, VC is accumulated in the domain, raising VC concentration. During reductive dechlorination processes of multiple chlorinated hydrocarbons such as PCE, TCE, DCEs, and VC, due to competition for electron donors, VC is the least susceptible to the processes since it is least oxidized among these compounds [Wiedemeier, 1998]. So the rate of dechlorination reaction decreases with the decrease in the degree of chlorination of the compounds [Vogel and McCarty, 1985]. Under such environmental conditions, VC may be accumulated in multispecies-mixed plume [Murray and Richardson, 1993].

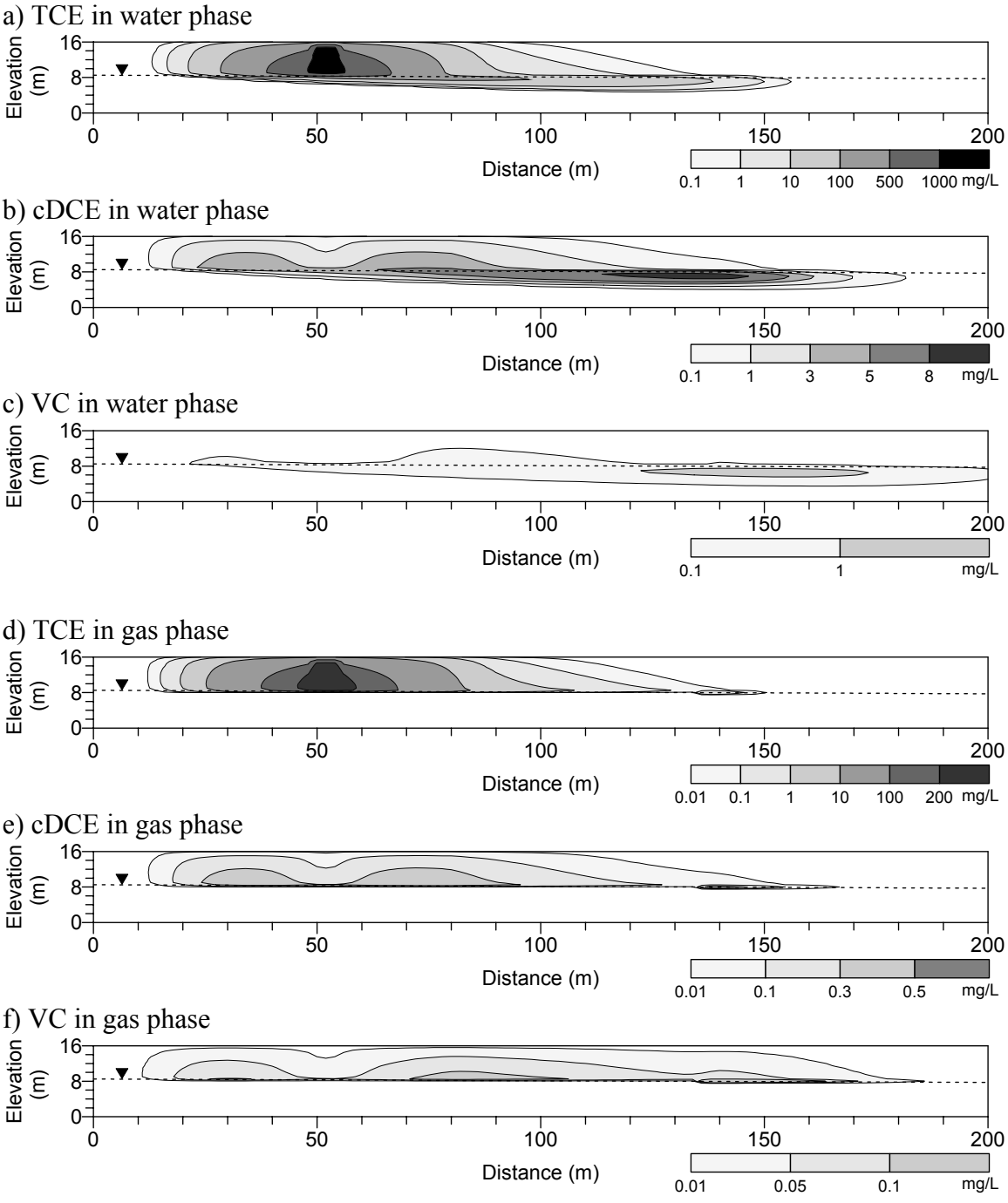

Figure 4.14 Concentration profiles of dissolved or vaporized contaminants (TCE, cDCE, and VC) at t=300 days, Case MM-1

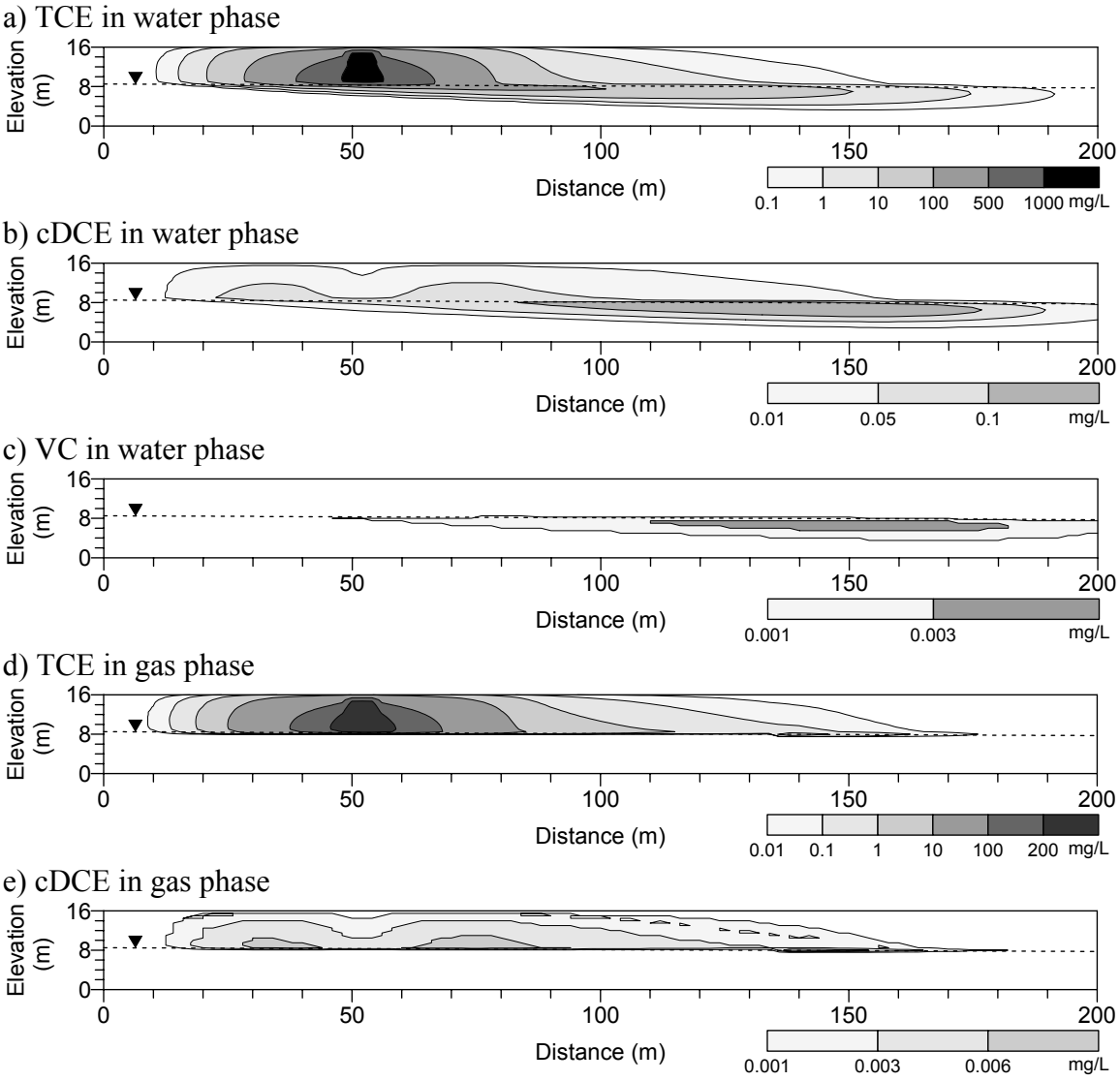

Figure 4.15 Concentration profiles of dissolved or vaporized contaminants (TCE, cDCE, and VC) at t=300 days, Case MM-2

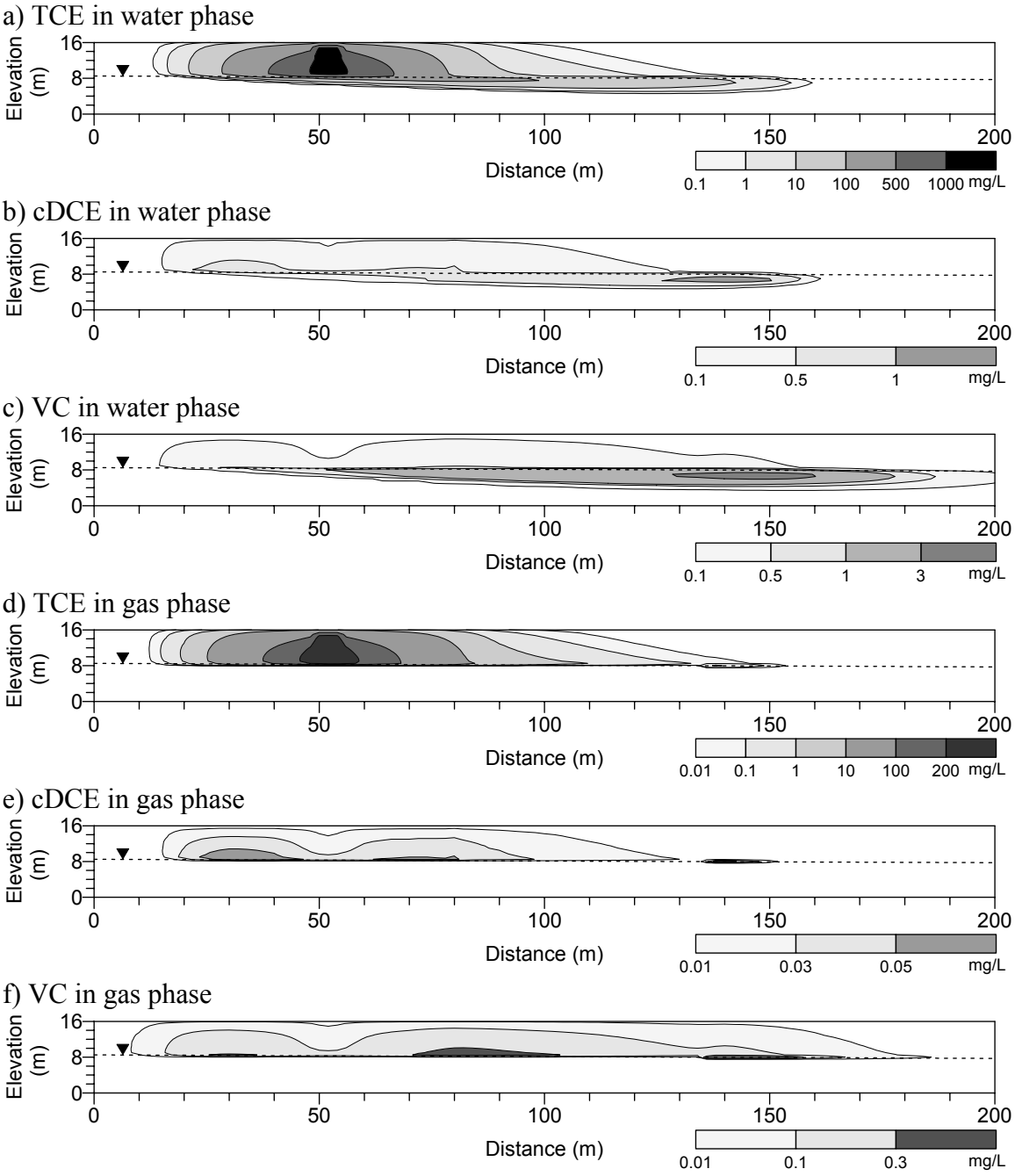

Figure 4.16 Concentration profiles of dissolved or vaporized contaminants (TCE, cDCE, and VC) at t=300 days, Case MM-3

The changes in total mass of cDCE and VC, generated by biotransformation of TCE and cDCE, respectively, are presented in Figure 4.17. As mentioned earlier, Case MM-1 has the highest cDCE production, and Case MM-3 has the highest VC production over time. Case MM-2 has very small biotransformation in the production of cDCE and VC.

For Case MM-1, the variations in distribution of TCE, cDCE, and VC are shown in Figure 4.18. The variations in TCE distribution in Figure 4.18 (a) are similar with those of TCE seen in Figure 4.12 (a). As the highest-concentration zones for cDCE appears in the saturated zone (Figure 4.14 (b)), dissolved cDCE in the saturated zone has fast increase over time. In Figure 4.18 (c), dissolved VC mass in the saturated zone dominates in the distribution of VC.

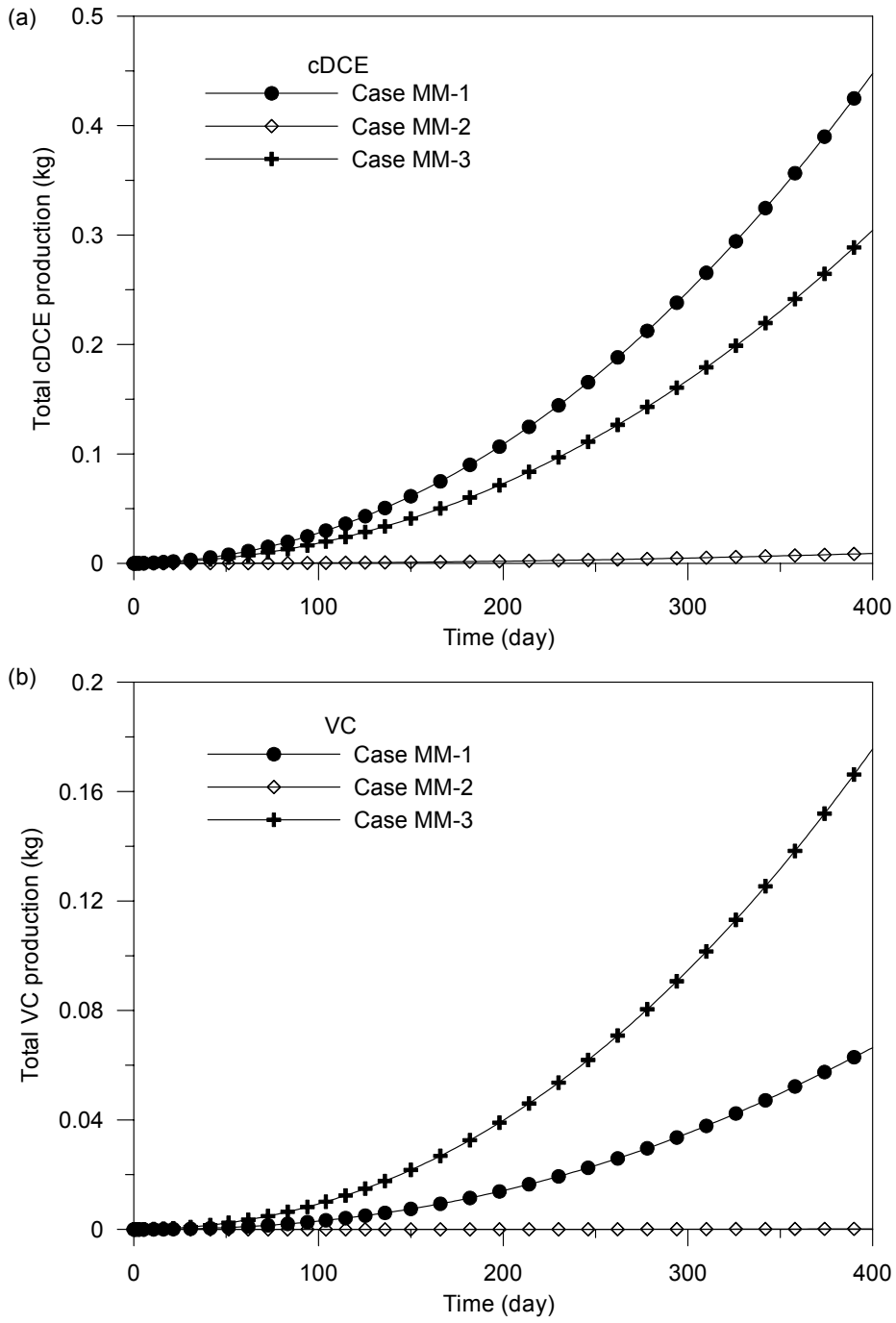

Figure 4.17 Total productions of cDCE and VC for Cases MM-1, MM-2, and MM-3

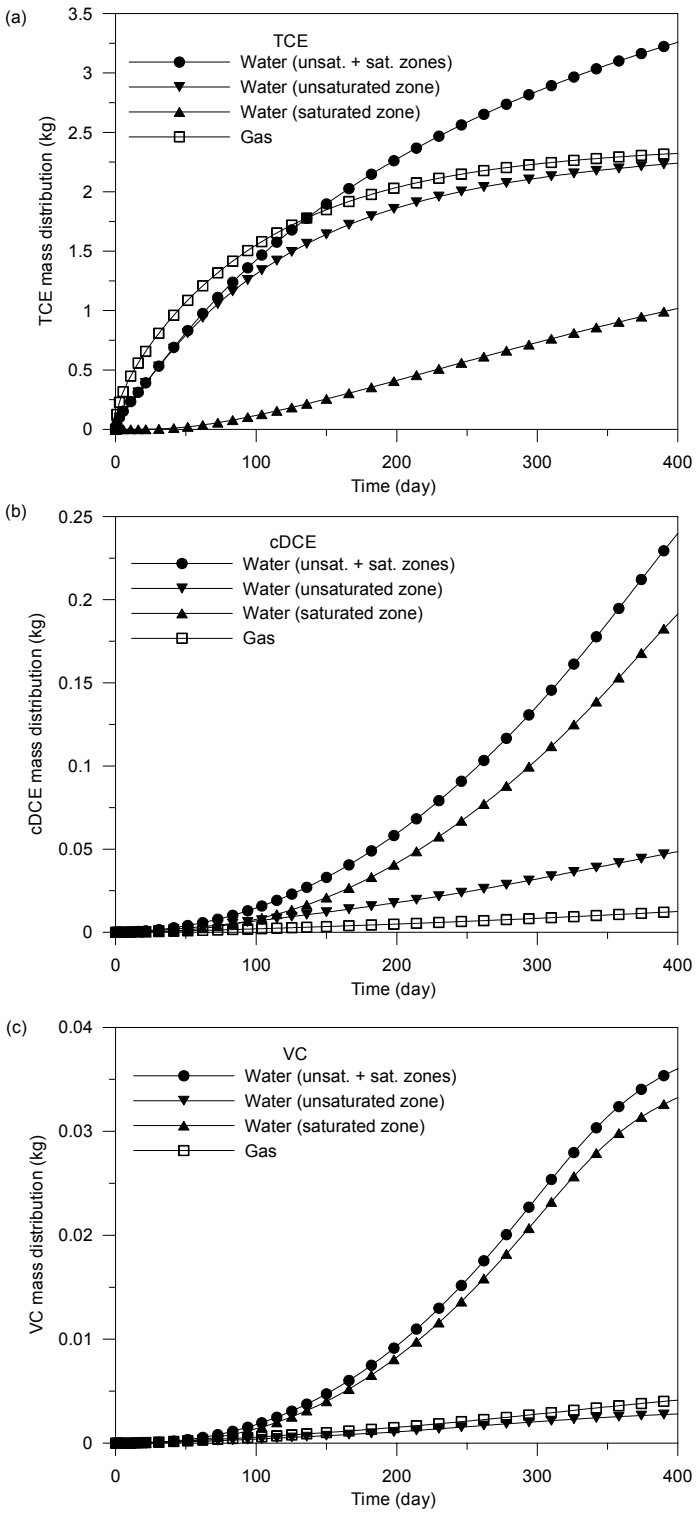

Figure 4.18 Temporal variations in mass distribution of TCE, cDCE, and VC for Case MM-1

4.4 Summary

In this chapter, the effect of biological transformations on fate and transport of multispecies are analyzed. To represent biological reactions of chlorinated solvents in the groundwater system, sequential bioreactions of TCE to cDCE, and to VCE are used. TechFlow^{MP} model developed here was successfully verified for sequential bioreactions using one- and three-dimensional transport problems. As kinetics of reductive dechlorination for TCE, cDCE, and VC for total six simulations, first-order and Michaelis-Menten kinetics are employed with three different reaction cases for each kinetics. The parameters are chosen from field tests or laboratory experimental data. Density-driven advection of gas phase, discussed in Chapter III, was also considered in all simulations. From the results of simulations for two sets of three scenarios of first-order relationships and Michaelis-Menten kinetics, the followings can be summarized:

(i) Biotransformation of dissolved TCE reduced the development of TCE plume in both the unsaturated and unsaturated zones and produces daughter contaminants, which become new contaminants in water and gas phases. The degree of the reduction depended on the magnitude of biotransformation coefficients for TCE. For three cases using first-order relationships, the concentration profiles of TCE in water and gas phases showed similar results. For three cases using Michaelis-Menten kinetics, the biotransformation of TCE has significant effect on the spreading of TCE plume in water and gas phases.

(ii) Density-driven advection of gas phase had influence on the distribution of cDCE in the domain, especially in the unsaturated zone. Due to density-driven gas flow in the unsaturated zone, for simulation cases with first-order kinetics, the highest concentration zones of cDCE occurred on the left-side and right-side positions from the zone directly below TCE source. Since biotransformations occurs sequentially, there was a time lag between the increase in cDCE concentration and the increase in VC concentration.

(iii) In cases that first-order relationships are used for biotransformation of contaminants, since bioreaction coefficients are independent on contaminant concentration, the generation of a daughter contaminant was proportional to the concentration of a parent contaminant dissolved in water phase. For Michaelis-Menten kinetics, however, the biotransformation rates are determined by the concentration of a parent contaminant and two parameters (maximum bioreaction rate and half-saturation constant), the kinetics for the production of a daughter contaminant becomes complicated. In simulations with Michaelis-Menten kinetics, the highest concentration zones for dissolved cDCE were located at the down gradient saturated zone. The locations and the peak concentrations depended on kinetic parameters.

(iv) High concentration zones of dissolved VC were shown in the saturated zone just below the groundwater table, and high concentration zones of vaporized VC in the unsaturated zone showed similar patterns with high concentration zones of

vaporized cDCE. In a case with Michaelis-Menten kinetics (Case MM-3), the accumulation of VC mass in the domain was observed due to fast biotransformation of cDCE and slow bioreaction of VC. Such circumstances may happen due to competition between multispecies for reductive dechlorination.

(v) Atmospheric loss of TCE was a dominant mechanism to reduce the contaminant in the domain. For cDCE and VC, dissolved components became significant over time. The importance of dissolved contaminants was emphasized for cases with Michaelis-Menten kinetics. As mass of dissolved contaminants increases with time, biotransformation of the contaminants continuously increased. This suggests that biological transformations for dissolved volatile organic compounds should be considered in long-term simulations to accurately predict fate of the contaminants.

CHAPTER V

IN SITU AIR SPARGING

In situ air sparging (IAS) is an effective remediation technique to clean up soil and groundwater contaminated with volatile organic compounds (VOC) in relatively permeable subsurface environments. In this chapter, multiphase flow in subsurface systems and contaminant removal by IAS application are investigated. For IAS simulations, TechFlow^{MP} is tested with gas injection/extraction applications in the subsurface. For verification purposes the results obtained are compared with previous numerical works for air sparging reported by van Dijke et al. [1995]. Then, various cases are investigated for IAS applications to analyze the effects of aquifer and other parameters of IAS systems on the remediation efficiency of this remedial procedure. The parameters investigated include flow rate of air injection, depth of injection wells, injection method, and the distance between injection wells.

5.1 Introduction

The application of IAS requires knowledge on two main processes: The first is the dynamic movement of liquid and gas flows as a multiphase flow through porous media, and the second is the chemical and biological reactions such as mass transfer between phases and biotransformations of contaminants. A schematic of an IAS operation is shown in Figure 5.1. The analysis on multiphase flow may allow us to understand: (i) flow path and velocity of gas phase in the unsaturated and saturated zones; (ii) the change in flow path and velocity of the groundwater due to IAS; and, (iii) the distribution of gas

saturation levels. In determining multiphase flow, one of the key parameters is $P_c - s - k_r$ (capillary pressure-saturation-relative permeability) relationships, which was discussed in Chapter II. These relationships are very complicated and site-specific for subsurface systems. In this study, van Genuchten models [van Genuchten, 1980; Parker et al., 1987] are used to describe these relationships. These models have been often applied to IAS problems as reported in the literature [van Dijke et al., 1995; Mei et al., 2002]. In calculating a relative permeability of gas phase (Equation (2.12)), Klinkenberg factor is set to 1, indicating that air slippage in air-water flow systems is not considered here.

Knowledge on mass transfer of contaminants between phases and biological reactions of contaminants in water phase is required in estimating the removal of contaminants in various flow scenarios. Since mass transfer and bioreactions are complicated and highly heterogeneous in groundwater systems, it may be impossible to describe every aspect of the processes. Thus, simplified but representative reaction kinetics is usually applied to contaminant transport computations. In this study, in modeling IAS systems, a first-order relationship is used to express mass transfer of contaminants between phases, and Michaelis-Menten kinetics is employed to describe biological transformation of contaminants.

The purpose of this chapter is two folds. The first one is to enhance our understanding of multiphase flow in porous media by investigating the behavior of gas and liquid (i.e., the contaminated groundwater) as immiscible fluids. The movement of gas phase is more dynamic than that of the groundwater, and gas phase plays an important role in carrying vaporized contaminants from the saturated zone into the

unsaturated zone above the groundwater table. In IAS operations, since the degree of contact between gas phase and contaminated groundwater is one of the important factors determining mass transfer rates of contaminants from water phase to gas phase, the distribution of gas flow has significant influence on the remediation efficiency of IAS systems. In this study, a multiphase flow in IAS operations is examined in terms of saturation levels and fluid velocity profiles of each phase in a three-dimensional domain.

The second one is to evaluate the removal efficiency of contaminants by IAS operations. Based on the results of various simulations for IAS systems conducted here, the purpose is to provide design parameters for optimized IAS systems for contaminated sites. Since the number of simulation run is limited, the solutions for the parameters may not be fully optimized, but these will help to enhance our understanding of design parameters of IAS remediation systems.

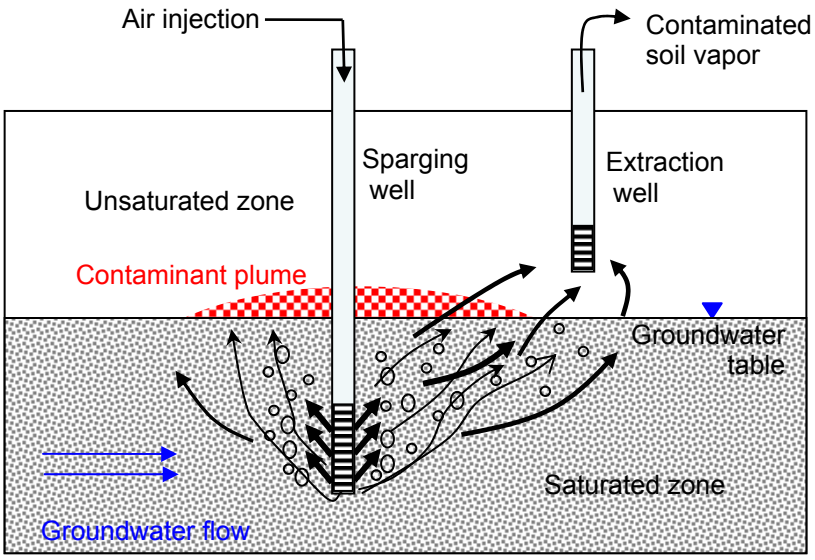

Figure 5.1 A schematic of an in-situ air sparging operation

5.2 Model Verification

5.2.1 Unsteady Radial Flow of Gas in the Unsaturated Zone

Unsteady radial gas flow due to gas injection or soil vapor extraction (SVE) at a single well in a confined unsaturated zone is simulated to verify TechFlow^{MP} model. Abriola et al. [1997] used these injection/extraction problems used here to test their two-dimensional numerical model, called MISER, which was applied to simulate SVE and bioventing of organic chemicals in the unsaturated zone.

The modeling domain used here consists of a one layer confined unsaturated zone as shown in Figure 5.2. Gas is injected or extracted through a fully penetrating well. The soil in the confined unsaturated zone is homogenous and isotropic. The soil properties used in this application are given in Table 5.2. Water saturation level in the unsaturated zone is uniform at an immobile residual level of 0.12. Nitrogen gas, which was applied by MISER model, is also used to represent the gas phase in the unsaturated zone.

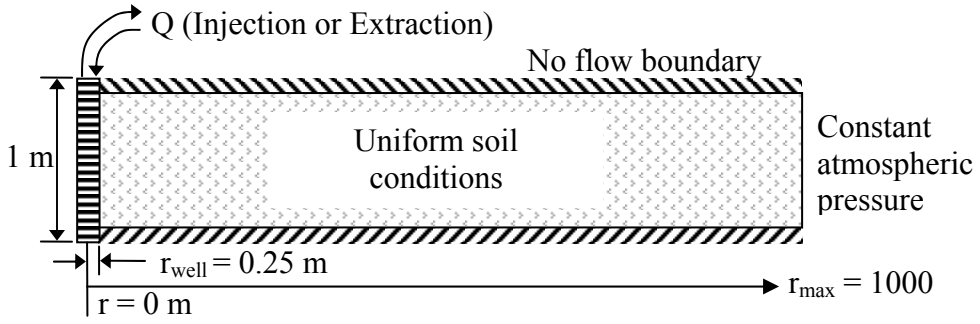

Figure 5.2 A schematic of a modeling domain

Since TechFlow^{MP} uses a Cartesian coordinate system, an arc-shape domain with one layer homogeneous unsaturated zone is used to simulate gas injection/extraction

through a single well in a two-dimensional radial coordinate. The angle of the arc on *x*-*y* plane is approximately 10°. The domain grid consists of 11,214 nodes and 5,377 elements, which was discretized as follows: in *x*-direction, 10 spaces of 0.83 m, 25 spaces of 1.67 m, 30 spaces of 5 m, 75 spaces of 10 m, and 10 spaces of 5 m; in *y*-direction, 2 spaces of 0.52 m, 15 spaces of 1.04 m, 32 spaces of 2.07 m, and 20 spaces of 4.04 m; and, in *z*-direction, one space of 1 m.

Table 5.1 Soil properties for the unsaturated zone

Parameter	Values*
Porosity	0.33
Permeability	1×10^{-11} m^2
Residual water saturation	0.12
Coefficients for $P_c - s - k_r$ relationships	
n	7.0
α_{gw}	0.002 Pa^{-1}

* Values were given by Abriola et al. [1997]

Two cases were simulated: One is a gas extraction test case with a flow rate of 10 ft^3/min (17 m^3/hr), and the other is a gas injection test case with a flow rate of 1 ft^3/min (1.7 m^3/hr). The run time is up to ten days with a 10-1000 second variable time steps.

In Figure 5.3, the simulation results of the two cases used in this study are compared to the quasi-analytical solutions developed by McWhorter [1990] and MISER model output reported by Abriola et al. [1997]. For both gas injection and extraction problems, the results of this study show good agreement with the other results as given in Figure 5.3.

(a) Soil vapor extraction test

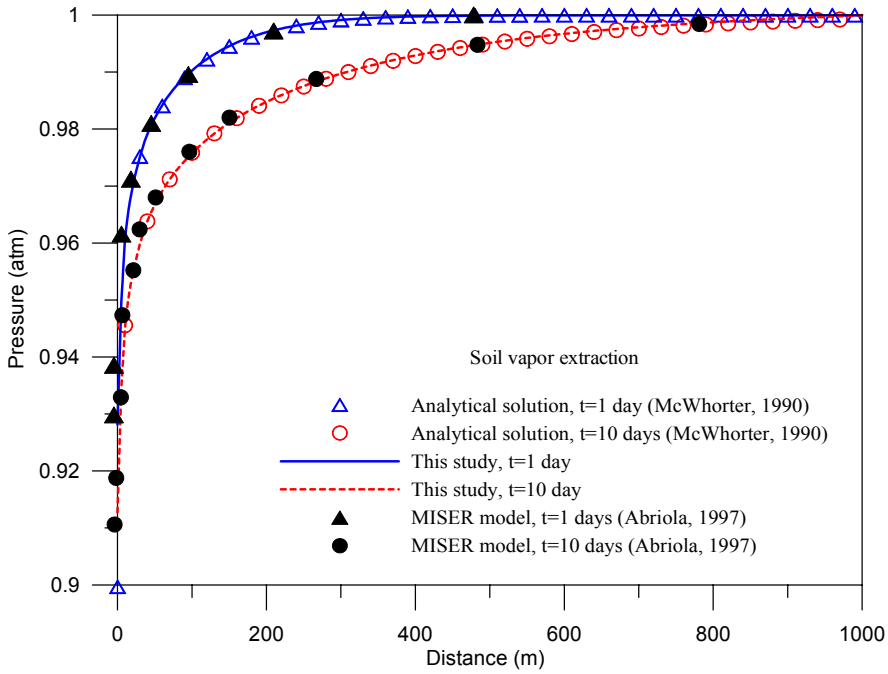

(b) Gas injection test

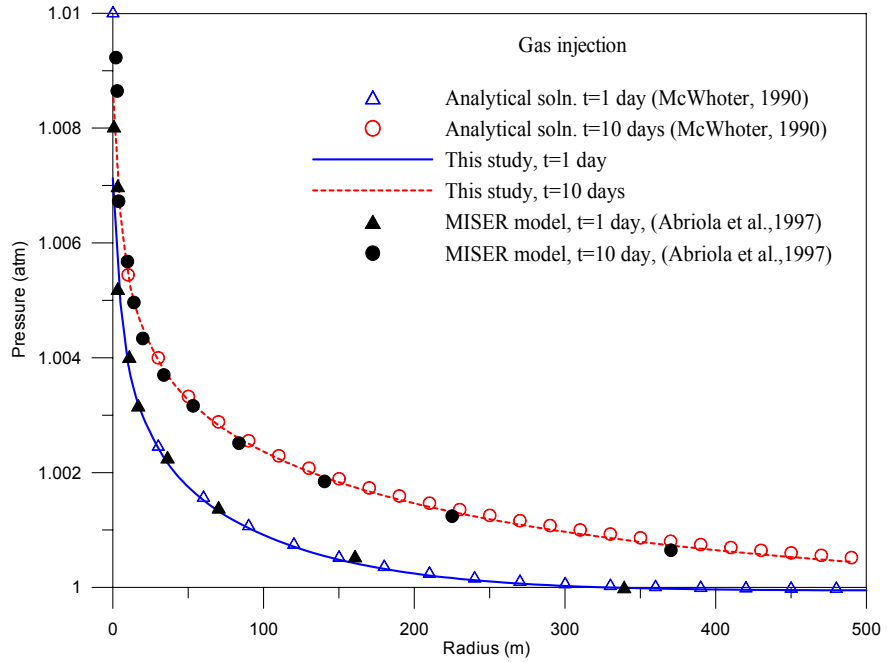

Figure 5.3 Comparisons of analytical solutions and numerical results of two models (MISER and TechFlow^{MP}) at gas extraction/injection tests

5.2.2 Air Sparging in a Homogenous Axially Symmetric Porous Medium

van Dijke et al. [1995] investigated multiphase flow in air sparging operations in a two-dimensional axially symmetric domain. In this application, the axi-symmetric domain is converted to a three-dimensional domain for TechFlow^{MP} that uses Cartesian coordinates (Figure 5.4). In the study conducted by van Dijke et al. [1995], water and air were considered as two immiscible incompressible continuous phases because gas compressibility is expected to play a minor role under steady-state conditions in which continuous channels to the vadose zone exist. van Dijke et al. [1995] used the mixed from of the Richards equations for both water and air to describe an interactive movement of the two fluids in a porous medium. In addition, for numerical computations, the equations were non-dimensionalized in terms of dimensionless numbers such as the mobility ratio (the ratio of the viscosity of water to that of air), the gravity related dimensionless numbers for water and air, and the capillary number. Simulation results are presented in terms of the changes in gas saturation levels and air volume that is stored in the domain.

The properties of a soil medium and fluids (water and gas) are given in Table 5.2. van Genuchten models [van Genuchten, 1980; Parker et al., 1987] are used to express $P_c - s - k_r$ relationships between water and gas phases.

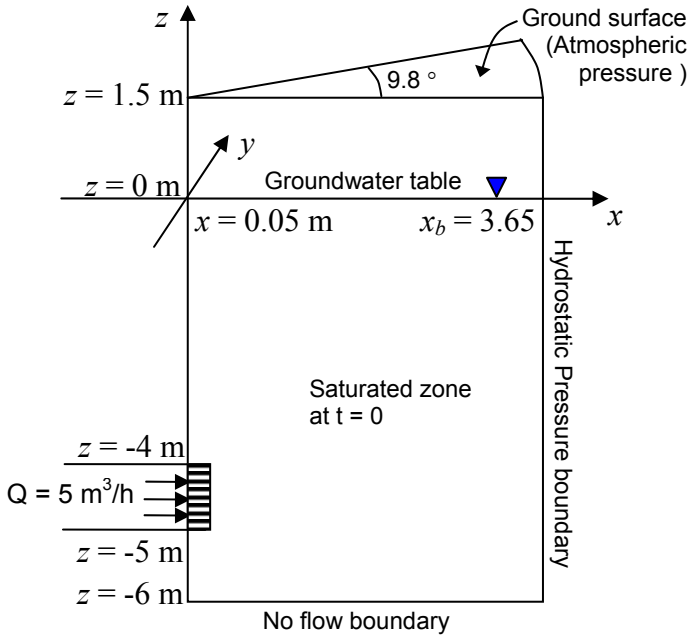

Figure 5.4 A schematic of a model domain for air sparging

Table 5.2 Soil and fluid properties for air sparging

Parameter	Values*
Permeability	5.3×10^{-11} m^2
Porosity	0.39
Residual water saturation	0.01
Coefficients for $P_c - s - k_r$ relationships	
n	3
α_{gw}	2 m^{-1}
ρ_{gas}	1.24 kg/m^3
μ_{gas}	1.77×10^{-5} Pa s
ρ_{water}	1000 kg/m^3
μ_{water}	1.30×10^{-3} Pa s

*Values were given by van Dijke et al. [1995]

van Dijke et al. [1995] used linear triangular finite elements in two dimensions to discretize a two-dimensional axially symmetric domain, however, in this study, the domain shown in Figure 5.4 is discretized using rectangular prism elements. In general,

the use of a Cartesian coordinate is more complicated than that of a two-dimensional radial coordinate system, but the former coordinate system can readily employed in more complex groundwater flow in subsurface systems, while the latter coordinate system can be used under restricted groundwater conditions such as no groundwater movement. In this problem, water in the saturated zone is assumed to be initially stationary without water flow in or out of the domain. In Figure 5.4, the domain idealization grid consists of 36,005 elements and 42,528 nodes, and is discretized with variable sizes of meshes: In x-direction, Δx = 0.02-0.24 m (the width of an element is 1.08 times the width of the previous element) at x = 0.05 to 3.1 m, Δx = 0.13 m at x = 3.1 to 3.37 m, and Δx = 0.14 m at x = 3.37 to 3.65 m; in y- direction, Δy = 0.013 m at y = 0 to 0.013 m, Δy = 0.006 m at y = 0.013 to 0.025 m, Δy = 0.008 m at y = 0.025 to 0.125 m, and Δy = 0.013 m at y = 0.125 to 0.25 m; and, in z- direction, Δz=0.05 m at z= -3.5 to -5.5 m, and Δz=0.1 m at z= +1.5 to -3.5 and -5.5 to -6 m. The simulation ran up to two hours with time steps ranging from 0.01 to 15 seconds.

In terms of air saturation contour plots in Figure 5.5, the results of this study are compared to the gas saturation profiles given by van Dijke et al. [1995]. Since gas saturation is determined by capillary pressure between water and gas phases as seen in Equation (2.8), the gas saturation distribution implies the profiles of gas pressure above the hydrostatic pressure of water phase. For instance, in Figure 5.5, the gas saturations of 0.08 and 0.04 represent the gas pressure of approximately 0.24 and 0.18 mH_2O above the water pressure, respectively. The zero gas saturation indicates that the gas pressure is equal or less than the water pressure. In IAS, the degree of gas saturation has important meanings: (i) Gas saturation level is one of the key factors in determining remedial

performance of IAS. Gas saturation should be greater than zero to remediate polluted groundwater by mass transfer of contaminants from water phase to gas phase; and, (ii) the degree of gas saturation determines the relative permeability of soil matrix, which has a significant impact on Darcy velocity of gas flow below the initial groundwater table.

In air sparging simulations conducted here, after some short periods of the expansion of the air zone (the zone that gas saturation is greater than zero below the initial water table) in all directions (upward, downward, and lateral), the upward growth of the air zone due to buoyancy dominated the flow system, although some lateral expansion of the air zone also continued. In this problem, the air zone reached the groundwater table approximately 5.5 minutes after beginning of air injection, and air volume stored in the initially saturated zone increased sharply until around 8 minutes. After that sharp increase, the air volume increased very slowly, and gas flow through the porous medium in the initially saturated zone became stabilized over time. The time required for hydrostatic conditions to be reached is about two hours, and, after that time, the air saturation became almost a steady state. Under such conditions, the steady-state airflow can be treated as a single-phase flow [van Dijke et al., 1995].

The gas saturation distributions at t = 8.2 min and 1.71 hrs are given in Figure 5.5 (a) and (b), respectively. The air-saturation contours of two studies (the results of this study and the published data of van Dijke et al. [1995]) show better agreement at the more stabilized gas flow phase (t=1.71 hrs) in Figure 5.5 (b) as opposed to an initial stage (t=8.2 min) in Figure 5.5 (a). In Figure 5.5 (b), the results of the two studies show the different profiles of gas saturation of 0.04 and 0.08 at $-1 \le z \le 0$ m (near the groundwater table). Except that difference, in Figure 5.5 (b), the difference between gas saturation

profiles of the two studies is greater in the vicinity of the injection points than at locations away for the points: i.e. the difference is greater at approximately $z \leq -3$ m than at $-3 \leq z \leq -1$ m. That may be due to the difference in mesh discretization methods and coordinate systems used in this study and van Dijke et al.'s study [1995]. As discussed earlier, a Cartesian coordinate system is used in this study while a two-dimensional radial coordinate system is used in the study of van Dijke et al. [1995]. Rectangular prism elements in a Cartesian coordinate system used here might have difficulty in describing the vicinity of gas injection/extraction wells in circular-arc-shape column domains like the domain shown in Figure 5.4 unless highly dense grid meshes are used in the domain.

Generally, in IAS, since air injection points are located much deeper than contaminated groundwater plumes, gas saturation distribution in the vicinity of the injection points may not have a significant impact on contaminant removal by IAS. On the contrary, gas saturation at mixing zones, in which injected air contacts with contaminated groundwater far above air injection points, will be more important than gas saturation near air injection points. The minimum distances between contaminant plumes and air injection points are discussed later.

Overall, the results of this study show good agreement with the data published by van Dijke et al. [1995]. Based on the results of this study for IAS, we can expect that, in Cartesian coordinate systems, TechFlow^{MP} model can be used to accurately simulate gas saturation distributions below the groundwater table under IAS. The accurate calculation of gas saturation profiles implies that TechFlow^{MP} model is capable to simulate the multiphase flow (interactive movement of gas phase and groundwater) below the groundwater table under IAS operations.

van Dijke et al. [1995] ignored air-phase compressibility to simplify air sparging modeling: Air density was assumed to be constant. In IAS, air pressure at injection points should be greater than the hydrostatic pressure to release air into the saturated zone. In the results of this study under constant gas density, air injection pressure at an injection point of z=-4.5 m was approximately 4.8 mH_2O, which is about 0.3 mH_2O above the hydrostatic pressure at that point. That air injection pressure is equivalent to 0.46 atmospheric pressure, which may cause approximately 30 % increase in gas density compared to air density at the ground surface. In IAS, air injection pressure depends on injection-point depths below the groundwater table and properties of soil media: Air injection pressure rises with the increase in injection-point depths. In air sparging at deep injection points, the variation in gas density could be an important factor to determine gas flow below the groundwater table, thus in all IAS simulations discussed in the following sections, the change in gas density due to gas pressure variations is considered.

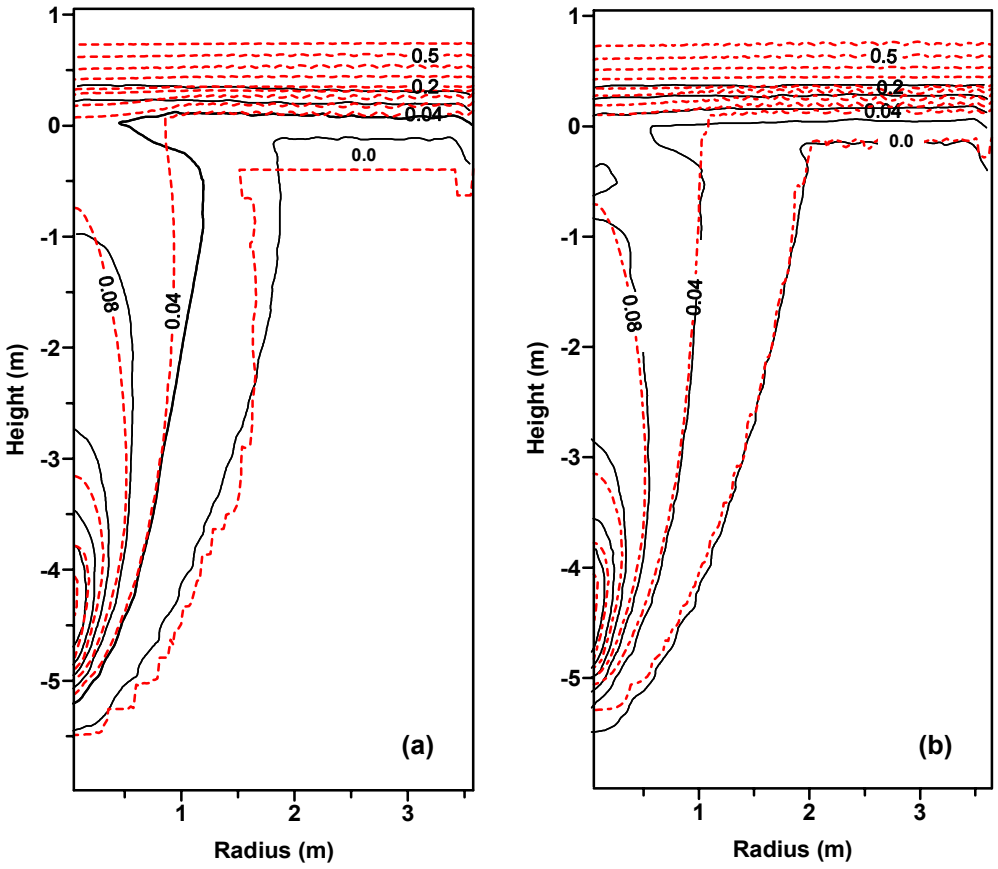

Figure 5.5 Air saturation contour plots at (a) t=8.2 minutes and (b) t=1.71 hours for the results of this study (dashed lines) and numerical output done by van Dijke et al. [1995] (solid lines). A radius indicates the distance from *z*-axis to a data point on *x*-*y* plane.

5.3 Application of In-situ Air Sparging

5.3.1 Modeling Domain and Parameters

In this section, IAS is simulated in a three-dimensional unconfined aquifer to investigate multiphase flow (liquid and gas phases) and contaminant removal by IAS. As IAS is commonly combined with SVE, IAS systems in this study consist of injection and extraction wells. In this application two types of wells (Vertical and horizontal wells) are used. For vertical well systems, single and multiple wells are employed for injection/extraction units, and, for horizontal well systems, single well is used for injection and extraction. Thus, an IAS system has at least two wells (one injection well and one extraction well). In this application, to reduce the computational burden of IAS modeling in a three-dimensional domain, we have used two three-dimensional domains to represent the modeled region. For IAS with two wells, a smaller domain is used with dimensions of (40m × 20m × 15m) in (x,y,z) directions respectively. For IAS with six wells, a larger domain is used with dimensions of (40m × 30m × 15m) in (x,y,z) directions respectively. The large domain is shown in Figure 5.6, which includes vertical and horizontal wells for gas injection/extraction. The parameters of a soil medium, water, and gas as used in this application are given in Table 5.3.

In IAS modeling, trichloroethylene (TCE) is a target contaminant, and a cometabolic process of TCE under aerobic conditions is considered as a biological reaction. To set up initial conditions for a contaminated zone, a contaminant transport simulation was conducted under the conditions that a TCE source is present at the groundwater table. Initial dissolved and vaporized TCE concentration profiles in the

domain are given in Figure 5.7, and these profiles are used through all simulations for IAS systems in this chapter. Initially TCE is present with gas, water, and soil solid phases in the unsaturated and saturated zones. The properties for TCE are already given in Table 3.4.

For flow equations of gas phase, all boundaries are assigned as no flow condition except that a constant atmospheric pressure is applied at the ground surface. For water flow equations, the boundaries of the saturated zone at the left- and right-hand side boundaries (on *y*-*z* planes at *x*=0 and 40 m) in Figure 5.6 are set to constant hydraulic head representing groundwater flow in increasing x-direction, and the other boundaries are set to no flow condition. For contaminant transport in gas phase, the ground surface is set to a stagnant boundary layer of 0.3 m thickness, and, for contaminant transport in water phase, the boundary of the saturated zone at the right-hand side boundary (on *y*-*z* plane and at *x*=40 m) is set to a free exit condition. The elevation of the groundwater table ranges from 9.65 m at the left-hand side boundary (*x*=0 m) to 9.5 m at the right-hand side boundary (*x*=40 m).

Under IAS operations, air injection derives dynamic movement of gas phase, and the velocity of gas phase relative to water phase is variable within the influence zone of IAS. Under such conditions, mass transfer characteristic of chemical species between gas and water phase may depend on the relative velocity between the two phases [Hecht et al., 1995; Jang and Aral, 2003]. Hecht et al. [1995] investigated volume-related mass transfer coefficients for TCE in a column experiment for cometabolic degradation of TCE. In the range of superficial gas velocities up to 0.04 m/s, the mean mass transfer

coefficient of TCE between water and gas phases is suggested as follows [Hecht et al., 1995]:

$$k_{TCE} = 0.45\, q_{gas} \tag{5.1}$$

where q_{gas} denotes superficial gas velocities of gas phase (m/s) and corresponds to Darcy velocity of gas phase in a porous medium.

In IAS model of this study, gas injection/extraction wells are located at the middle of *y*-direction (at $y = 0$ m) in the smaller and larger domains mentioned earlier, and, in the larger domain, additional injection/extraction wells are installed at the mirror locations across the *x*-*z* plane at $y = 0$ m. Since soil media in the domain are homogeneous and the locations and injection/extraction rates at wells are set to be symmetric across the *x*-*z* plane at $y = 0$ m, the smaller and larger domains including IAS systems with injection/ extraction wells will be symmetric across the *x*-*z* plane at $y = 0$ m. Thus, the half of each domain in *y*-direction ($y \geq 0$ m) is used in numerical simulations in this study. For all flow and transport equations, no flux symmetry boundary condition is assigned to the *x*-*z* plane at $y = 0$ m, which becomes a boundary because the half of total domains is used for IAS modeling.

The numerical domain ranges $x = 0$-40 m, $y = 0$-10 (a small domain) or $y = 0$-15 m (a large domain), and $z = 0$-15 m. The small domain grid consists of 35,112 nodes and 31,590 elements, and the large domain grid 48,048 nodes and 43,875 elements. The two domains are discretized: in *x*-direction, $\Delta x = 1.0$ m at $x = 0$-10 and 35-40 m, and $\Delta x = 0.5$ m at $x = 10$-35 m; in *z*-direction, $\Delta z = 1.0$ m at $z = 0$-1 and 13-15 m, and $\Delta z = 0.5$ m at $z =$ 1-13 m. In *y*-direction, for the small domain, $\Delta y = 0.5$ m at $y = 0$-8 m, and $\Delta y = 1$ m at $y =$ 8-10 m; for the large domain, $\Delta y = 0.5$ m at $y = 0$-10 m, and $\Delta y = 1$ m at $y = 10$-15 m.

All simulations for IAS operations were carried out up to 60 days with variable time steps ranging from 1 sec to 2 hrs. Mass balance calculations were done every time step to trace the removal efficiency of contaminants. Since the highest concentration zones are located on *x*-*z* plane at $y = 0$ m and *x*-*y* plane at $z = 9$ m, concentration contour plots of dissolved TCE are presented on these two planes herein. Concentration profiles of the contaminant on other planes in *x*-, *y*-, and *z*-directions are also checked but are not presented here. In this study, a target concentration of dissolved TCE is selected as 0.001 g/L in cleaning up the contaminated groundwater by the IAS system.

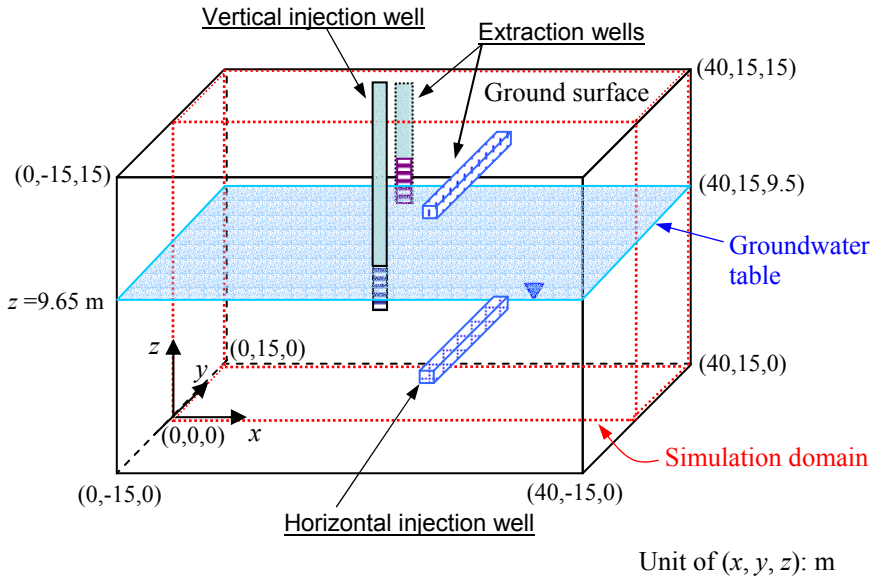

Figure 5.6 Schematic of in situ air sparging

Table 5.3 Properties of soil, water, and air

Parameters	Values
Porous medium	
Permeability, $k_{xx}=k_{yy}$	1.0×10^{-10} m^2
Permeability, k_{zz}	5.0×10^{-11} m^2
Porosity, ϕ	0.35
Residual water saturation, s_m	0.01
Bulk density, ρ_b	1600 kg/m^3
Temperature, T	15 °C
Longitudinal dispersivity, α_L	1.0 m
Transverse dispersivity, α_T	0.1 m
Soil organic content, f_{oc}	0.0005
Parameters for the unsaturated zone	
n	3
α_{gw}	2 m^{-1}
Water	
Water molecular weight, M_w	18
Water density, ρ_w	997.3 kg/m^3
Water dynamic viscosity, μ_w	1.0×10^{-3} Pa s
Air	
Molecular weight, M_{air}	28.75
Density, ρ_{air}	1.23 kg/m^3
Viscosity, μ_{air}	1.8×10^{-5} Pa s

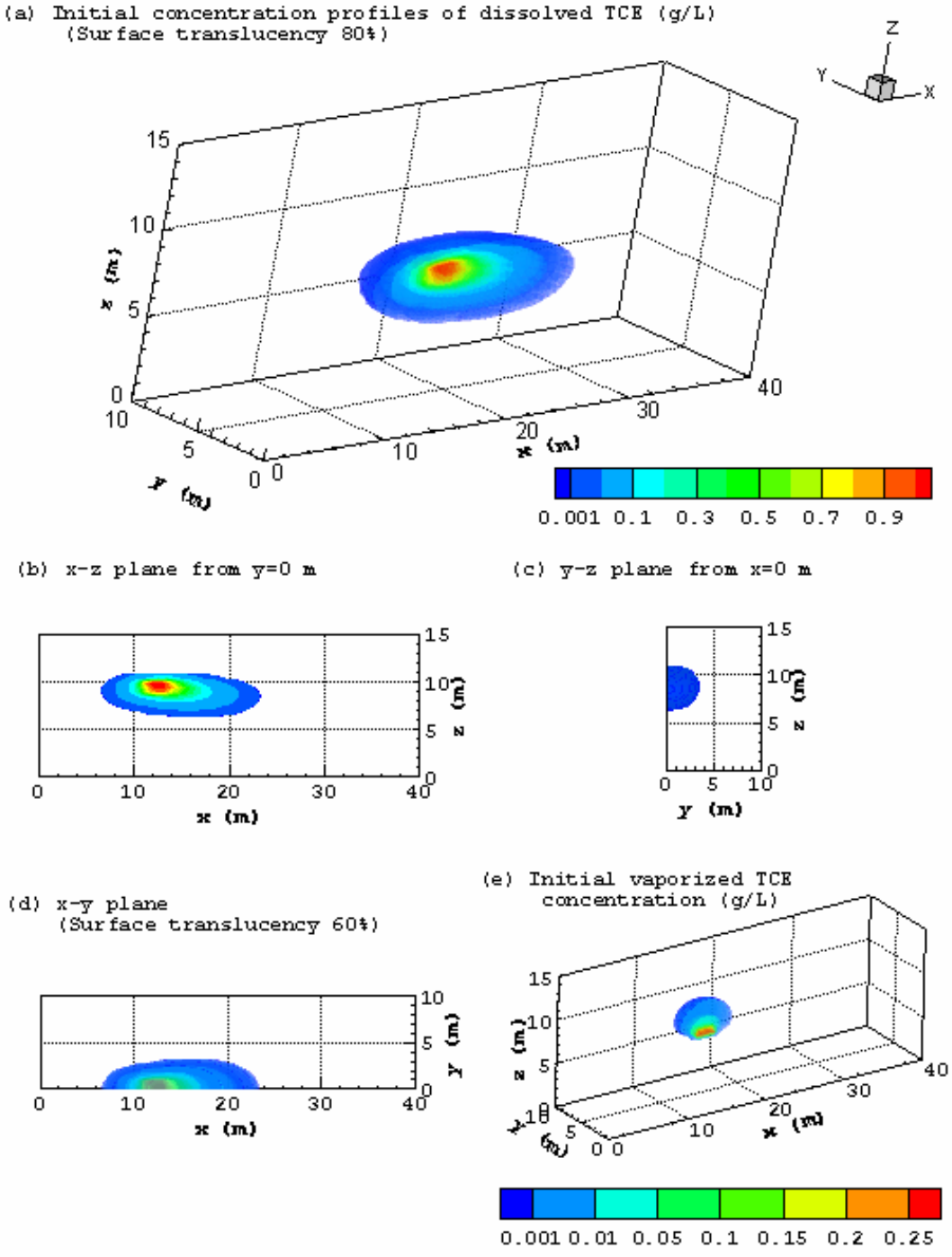

Figure 5.7 Initial concentration profiles of dissolved TCE (a, b, c, and d) and vaporized TCE (e).

5.3.2 Multiphase Flow and Contaminant Removal under IAS with One Vertical Injection Well

Injection flow rates of IAS are highly variable and site-specific. In the literature [Marley et al., 1992; Johnson et al., 1993; Benner et al., 2000; Benner et al., 2002; Lee et al., 2002], the flow rates used ranges from 2 to 460 m^3/hr. During pilot-scale IAS/SVE evaluations, several injection rates are usually tested to find out optimal values [Marley et al., 1992; Lee et al., 2002].

In this study, for IAS systems with two vertical wells (one for injection and one for extraction), five scenarios with different flow rates have been simulated to investigate the effect of flow rates on flow of air and water phase and removal efficiency of TCE. Flow rates for each scenario are shown in Table 5.4. Typically, extraction rates in the unsaturated zone are larger than injection rates to capture all injected air. In these simulations, the extraction rates are selected as twice the injection rates.

Table 5.4 Scenarios for IAS with one vertical injection well

Case No.	Flow rates (m^3/hr)		Well screen location
	Injection	Extraction	
V-1	5	10	Injection well: x=25-25.5, y=0, z=2-3 m Extraction well: x=25-25.5, y=0, z=11-12 m
V-2	10	20	
V-3	30	60	
V-4	50	100	
V-5	60	120	

Injection rates are one of the important factors in determining the performance of IAS. These rates have influence on the following parameters: (i) gas saturation levels in

the saturated zone; (ii) the radius of influence (ROI) of injection well; (iii) flow of groundwater and gas; and, (iv) mass transfer of dissolved contaminants into gas phase.

In Figure 5.8, the distributions of gas saturation in IAS at two different injection flow rates (10 m^3/hr for Case V-2 and 60 m^3/hr for Case V-5) are given. Based on these distributions, the cone of IAS influence, which implies a mixing zone where injected air contacts with the groundwater, can be estimated. Since contaminant removal in IAS primarily depends on mass transfer of contaminants from water phase to gas phase, the size of the mixing zone should be large enough to cover target contaminant plumes. The mixing zone can increase by (i) raising gas injection rates at a well; (ii) installing additional wells (multiple injection wells); and/or, (iii) using horizontal wells. The first option is discussed in this section, and the other two options are addressed in the following sections. In Figure 5.8, the increase in air injection rate at one well from 10 to 60 m^3/hr results in the expansion of IAS influence zone and the increase in gas saturation levels in the vicinity of sparging wells: For example, gas saturation levels around the sparging well increase from approximately 30 to more than 50 %. Considering the distribution of dissolved TCE in Figure 5.7, the expansion of IAS influence zone in Figure 5.8 implies the injection well can cover wider contaminant plumes. Nyer and Suthersan [1993] pointed out that maximum dimension of IAS cone could be obtained by injecting as little as 30 % of soil pore volume for finer sediments and 50 % for coarse sediments. The increase in gas saturation below the groundwater table has significant impacts on both multiphase flow (groundwater and gas flow) and contaminant removal by mass transfer from water phase to gas phase. Regarding a multiphase flow, gas saturation determines relative permeabilities of gas and water phase. The increase in gas

saturation in soil matrix implies the increase in relative permeability of gas phase and inversely the reduction in that of water phase. Regarding contaminant removal, the increase in gas saturation will raise the vaporization of dissolved contaminants since the increase in vaporized contaminants is linearly proportional to gas saturation as seen in Equation (3.24). Furthermore, as a mass transfer coefficient becomes larger due to the increase in the gas flow velocity, contaminant transfer between phases will be accelerated. On the contrary, the increase in gas saturation below the groundwater table can generate unfavorable situations on contaminant removal: Due to the increase in gas saturation, the velocity of groundwater flow will decrease, and thus contaminated groundwater plumes may have difficulty entering the mixing zones generated by IAS and some portion of the plumes may be diverted around the mixing zones (Figure 5.11).

Gas flow patterns (the shape of IAS influence zone) highly depend on subsurface conditions such as heterogeneity of soil media. In the laboratory experiments for the visualization of air flow in air sparging, Ji et al. [1993] reported that air sparging into a experimental tank filled with uniform beads produced a roughly parabolic shape of air plume and the larger air injection into the tank contributed to the increase in the size of the air plume. In IAS modeling of this study, as soil media is homogeneous, the cone of IAS influence (or the distribution of gas saturation) is nearly axi-symmetric even though the cone is not exactly symmetric due to the groundwater flow in the increasing x-direction. Ji et al. [1993] reported that air flow is very sensitive to heterogeneity of porous media: Heterogeneity in porous media results in highly distorted air flow patterns, far different from parabolic air plumes. Low-permeable layers (stratified media) can increase the lateral movement of injected air and may generate preferential flow channels

in high permeable areas [Ji et al., 1993; McCray and Falta, 1996]. Heterogeneity in soil media can reduce contact between injected air and contaminant plumes surrounded by low permeable media. If air injection pressure is high enough, horizontal low-permeable layers can be ruptured and penetrated by injected air [Ji et al., 1993]. The distribution of gas saturation is an outcome of complicated relationships of relevant parameters such as air injection rates and heterogeneous geological conditions of the subsurface systems. The gas saturation distribution will become an important factor to determine the remedial performance of IAS. In IAS application, minimum gas saturation levels required to successfully remediate contaminated groundwater can be estimated through field experiments and/or numerical modeling and may vary over locations at contaminated sites. Also, required gas saturation levels will be site-specific and depend on remediation goals (i.e., remedial concentrations of contaminants) at polluted sites. Based on information about required minimum gas saturation levels and contaminated groundwater plumes at target sites, air injection rates as a design parameter for IAS systems can be determined.

(a) Air injection rate Q = 10 m^3/hr

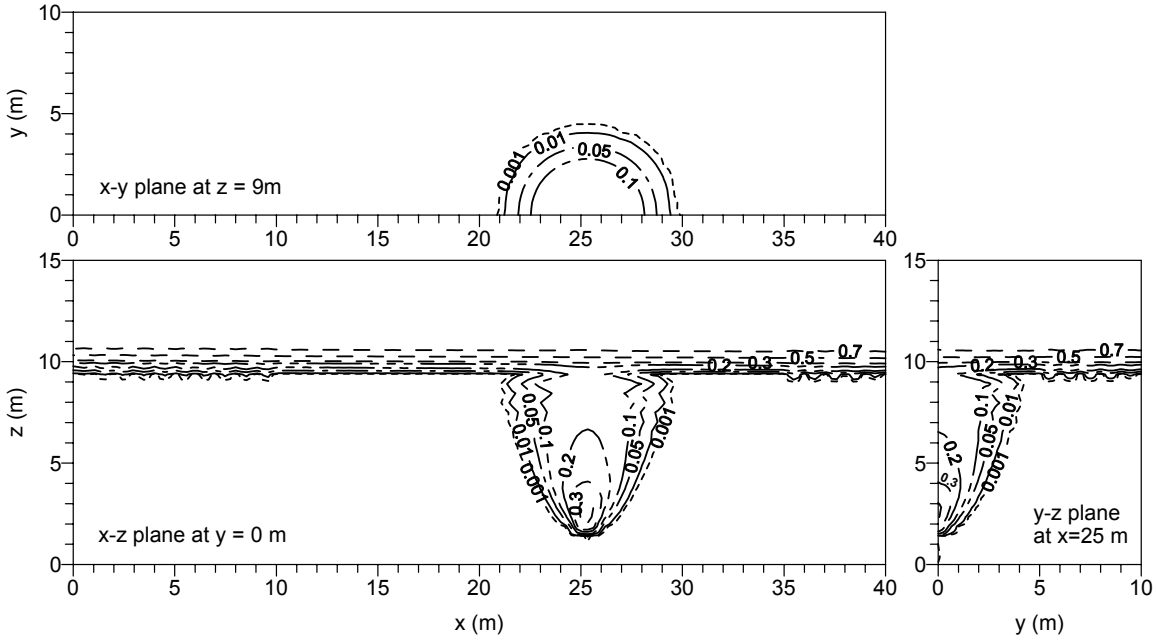

(b) Air injection rate Q = 60 m^3/hr

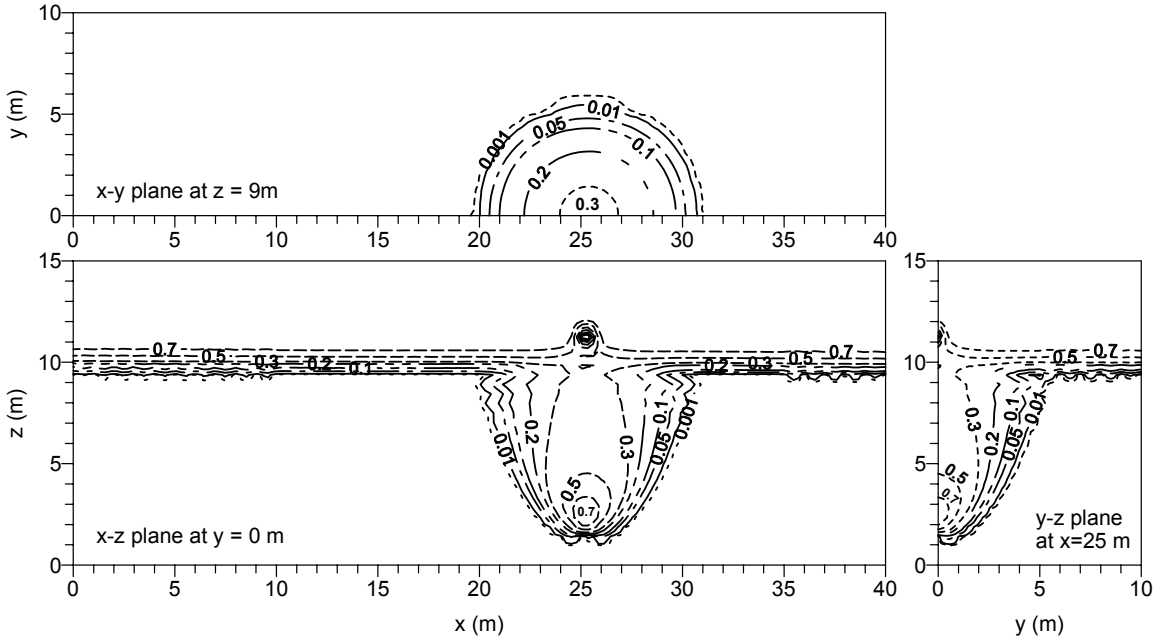

Figure 5.8 Air saturation under two air injection rates (Q = 10 and 60 m^3/hr) at one vertical well.

As seen in Figure 5.8, as the increase in injection rates expands the size of IAS influence zone and raises gas saturation levels around the injection points, the injection-rate increase will result in raising the volume of air displaced soil pore water below the groundwater table. In Figure 5.9 (a), temporal variations in gas volume stored in the sparging zones are presented for five different injection flow rates listed in Table 5.4. Regardless of air injection rates, the nearly-linear sharp increase in air volume stored in the sparging zones occurs for approximately 15 minutes after the start of injection, and then the air volume reaches a stabilized maximum values. The maximum air volume proportionally increases with air injection rates. The temporal variations of the air volume shown in Figure 5.9 (a) agree with the temporal air-volume change in the numerical results for air sparging reported by van Dijke et al. [1995]. The temporal variation of the air volume in the sparging zones can be used as a reference in monitoring the change in gas-water capillary pressure in the subsurface systems at contaminated. Based on that temporal variation, we may estimate an operation time to stabilize multiphase flow (gas and groundwater) in the subsurface during the operation of IAS. In Figure 5.9 (a), the temporal variations of the air volume suggest that air injection rates will have minor effects on the time required for gas flow stabilization in this study, but the gas-flow stabilization time may depend on the depth of injection points below the groundwater table and geological conditions such as intrinsic permeability and soil texture properties.

Some air sparging simulation cases conducted by van Dijke et al. [1995] showed the fluctuation in the stored air volumes when injected air reaches the groundwater table and leaves the saturated zone. In this study, however, that fluctuation does not occur.

Radius of influence (ROI) can be defined as a maximum radius from an injection well to a location at which remedial effects due to injected air at the well are observed or as a radius from an injection well to a location at which the change in gas pressure in the subsurface due to air sparging is detected. In this study, since the main purpose of IAS application is the remediation of contaminated groundwater, ROI is used to indicate the maximum radius within which remedial processes happen due to injected air. ROI is one of the key factors in designing IAS systems. ROI can be used to determine air injection rates and a distance between injection wells. At contaminated sites, ROI can be estimated as an arbitrary gas saturation levels, gas pressures, or gas-species concentrations based on site conditions because remedial processes are contaminant-dependent and site-specific [McCray and Falta, 1996; Lee et al., 2002]. The most common method to estimate ROI is to use gas-phase saturation profiles. This method is accurate and is easily applicable since gas saturation can be calculated using water and gas pressures measured at contaminated sites [McCray and Falta, 1996].

ROI for the five cases listed in Table 5.4 is estimated in terms of four different levels of gas saturation and is presented in Figure 5.9 (b). ROI and injection rates are non-dimensionalized using two dimensionless variables (Dimensionless radius and gravity number for gas phase) introduced by van Dijke et al. [1995; 1998] in air sparging modeling. The dimensionless radius (r') is:

$$r' = \frac{r}{H_c} \tag{5.2}$$

where r is a radius (a distance from an injection well to a certain location), and H_c is the depth of injection screen center as a characteristic length. The dimensionless gravity

number of gas phase (N_g), which implies the importance of gravity forces (or buoyancy forces) relative to viscous forces, is:

$$N_g = \frac{k_m \Delta\rho\, g}{\mu_g \left(Q_g / A\right)} \tag{5.3}$$

where k_m is an intrinsic permeability of soil porous media, $\Delta\rho = \rho_w - \rho_g$, Q_g is an air injection rate, and A is total surface areas of air injection screens. In this study, the lateral intrinsic permeability shown in Table 5.3 is used for k_m in Equation (5.3).

Using the distributions of gas saturation on the x-y plane at z = 9 m below the groundwater table (for example, gas saturation profiles at the plane in Figure 5.8), the ROI shown in Figure 5.9 (b) is estimated as a maximum radius of each gas saturation level (0.1, 1, 5, and 10 %). ROI may have different values according to depth (z-values below the groundwater table) because the distributions of gas saturation on the x-z plane at y = 0 m show parabolic shapes. In this study, since air plumes are fully expanded at z = 9 m (approximately 0.5 m below the groundwater table) as seen in Figure 5.8, the ROI at z = 9 m is selected a representative value for each injection well after gas flow is stabilized (after 2 hours for each simulation). In Figure 5.9 (b), at an injection rate Q=30 m^3/hr ($1/N_g = 0.31$ for Case V-3), ROI for gas saturation of 0.1 and 10 % is approximately 5.2 ($r' = 0.74$) and 3.6 m ($r' = 0.51$), respectively. When injection rates rises from 5 ($1/N_g = 0.05$) to 60 m^3/hr ($1/N_g = 0.61$), ROI for gas saturation of 1 % increases from about 3.6 ($r' = 0.51$) to 5.3 m ($r' = 0.75$).

As discussed earlier, the degree of gas saturation plays an important role in contaminant removal. Since contaminant concentrations in the groundwater vary over time and location, it is difficult to predict exact remedial performance of each gas

saturation level. The values of ROI at different saturation levels and inject rates shown in Figure 5.9 (b) can be used to predict approximate remediation zones and evaluate a remedial performance at each injection rate listed in Table 5.4.

(a) Air volume changes

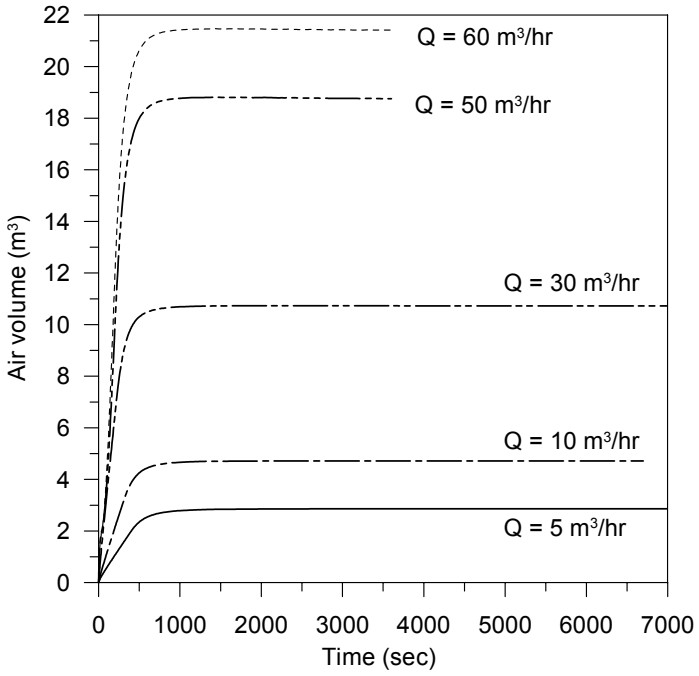

(b) Radius of influence

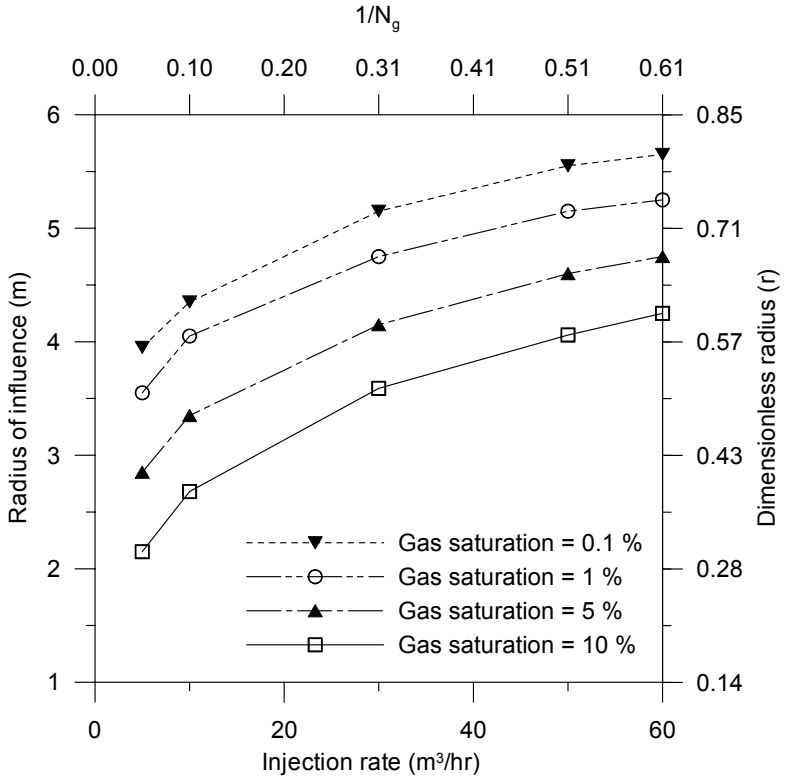

Figure 5.9 Air volumes stored in air sparging zones and radius of influence at z = 9 m.

Gas flow patterns at two different injection rates are given in Figure 5.10. In IAS, injected gas constantly interacts with the groundwater as a multiphase flow while both fluids flow through porous soil media, and gas flow patterns are determined by the relationships of groundwater and gas pressures. In Figure 5.10, around the injection points, gas flow shows some lateral movement, but overall, its upward movement is dominant below the initial groundwater table. In the case of air injection rate of 60 m^3/hr in Figure 5.10 (b), some downward velocity profiles are observed. After air is released at very high velocities from the injection points, as air plumes expand with its upward movement, air velocity reduces. In Figure 5.10, around injection points, maximum Darcy velocities of gas phase for Cases V-2 and V-5 are about 1.0 and 4.0 cm/s, respectively. The increase in air injection rates leads to raise gas saturation around the injection points as seen in Figure 5.8 and to increase gas flow velocities in the cone of IAS influence. In Figure 5.10, Darcy velocities of gas phase at a point of (x = 25, y = 0, z = 9 m) for Cases V-2 and V-5 are 0.15 and 0.54 cm/s, respectively, which imply that, according to Equation (5.1), the mass transfer coefficient of Case V-5 at that point is approximately 3.5 times that of Case V-2. In Figure 5.10, gas velocities within the cone of IAS influence increase as a location approaches an injection well on y-z planes at z=25 m: For example, on the y-z plane at z = 25 m in Figure 5.10 (b), Darcy velocities of gas phase at y=0 and 4 m are approximately 0.54 and 0.1 cm/s, respectively. In this study, these velocity profiles will be favorable in the application of IAS to clean up a contaminated site with the initial contaminant concentration profiles shown in Figure 5.7 because remedial loads (dissolved TCE concentrations) increase in the decreasing y-direction at y = 0-10 m. In

Figure 5.7 (d), the highest contaminant loads are located in the middle of the dissolved TCE plumes (at $y = 0$ m) in y-direction.

As seen in Table 5.4, the extraction points are located at the same location on x-y planes with different elevations in z-direction. In Figure 5.10, extraction rates are twice injection rates to provide extraction capacities enough to capture all injected air. For both Cases V-2 and V-5, gas flows by vapor extraction in the unsaturated zone appear to cover ROI of injection wells.

(a) Darcy velocity of gas phase at air injection rate, 10 m^3/hr

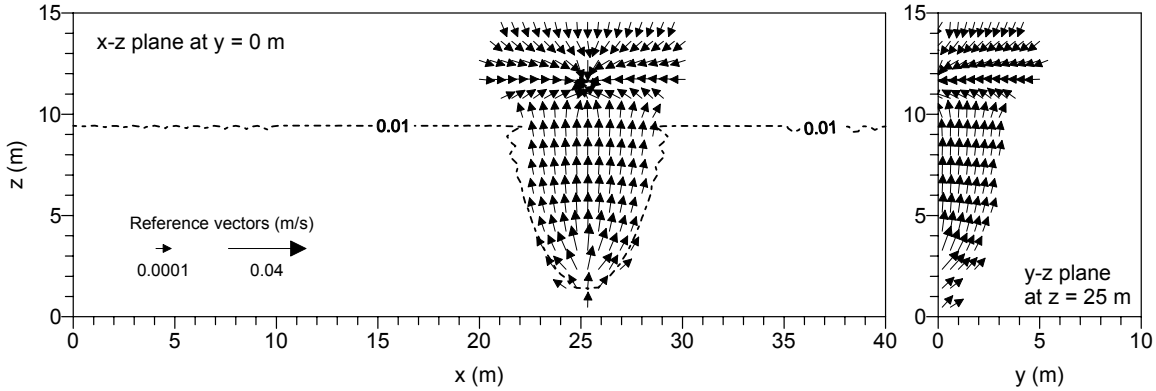

(b) Darcy velocity of gas phase at air injection rate, 60 m^3/hr

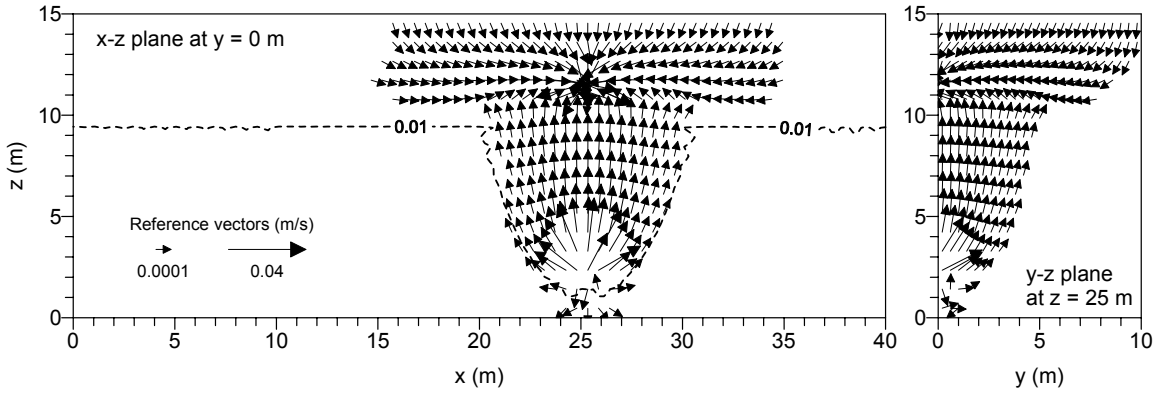

Figure 5.10 Darcy velocity of gas phase at two air injection rates (10 and 60 m^3/hr) for Case V-2 and V-5. Dashed lines indicate gas saturation level of 0.01.

Up to now, in published numerical works for air sparging [Panday et al., 1994; van Dijke et al., 1995; Lundegard and Andersen, 1996; McCray and Falta, 1996, 1997; van Dijke and van der Zee, 1998; Marulanda et al., 2000; Mei et al., 2002], gas flow in homogeneous or heterogeneous media has been well studied. However, the groundwater flow in IAS are not much considered even though the gas and groundwater flows are inter-linked and dissolved contaminants migrate along with the groundwater flow. The effect of air sparging on the groundwater flow has been discussed conceptually: As injected air replaces pore water in the saturated zone, the air will cause to reduce the groundwater flow and divert a portion of groundwater flow around the cone of IAS influence [Johnson et al., 1993; Nyer and Suthersan, 1993]. To investigate the effect of IAS on the groundwater flow, a study on a multiphase flow (gas and groundwater flows) in a three-dimensional domain should be conducted. Using TechFlow^{MP} model developed in this study, the changes in flow path and velocity of the groundwater due to air sparging are investigated in the three-dimensional domain shown in Figure 5.6. In Figure 5.11, after injected air flow is stabilized, the groundwater flow patterns in the domain are given. In addition to velocity profiles of the groundwater in Figure 5.11, a gas saturation of 0.01 is included to indicate the cone of IAS influence.

Regarding the groundwater flow, one of the most important things in IAS is the mixing between injected air and contaminated groundwater. In IAS, contaminated groundwater should enter into the cone of IAS influence to contact with injected air. If the cone of IAS influence (or ROI) is smaller than contaminant plumes or contaminated groundwater plumes diverts around the IAS influence zones, remedial actions by IAS may be not sufficient to meet a remediation goal. In Figure 5.11, the change in the

groundwater flow velocity within the zone of IAS influence depends on air injection rates. For Cases V-2 and V-5, the groundwater velocities show significant reduction within the cone of IAS influence compared to the background groundwater velocity near x=0 m: In Figure 5.11 (a), at three different elevations z=3, 5, and 9 m of the injection well location (x=25 and y=0 m), groundwater flow velocities for Case V-2 are 4.98×10^{-7}, 1.49×10^{-6}, and 1.96×10^{-6} m/s, respectively, which corresponds to approximately 13, 38, and 50 % of the background groundwater velocity (3.9×10^{-6} m/s) far away from the injection well, respectively. In Figure 5.11 (b) for Case V-5, the groundwater velocities at those three elevations z=3, 5, and 9 m are 1.95×10^{-8}, 5.09×10^{-7}, and 8.84×10^{-7} m/s, respectively, which are equal to approximately 0.5, 13, and 23 % of the background groundwater flow, respectively. These reductions in the groundwater velocities within the IAS influence zone for Cases V-2 and V-5 are proportional to gas saturation levels.

In Figure 5.11, as the groundwater flow velocity highly reduces in the vicinity of air injection points, some portion of the groundwater detours below the air injection points. This detour is more serious in Case V-5 than in Case V-2: i.e., the greater injection rate results in the larger diversion of the groundwater. The lateral detour of the groundwater flow also occurs on x-y plane at z=9 m in Figure 5.11. These lateral and vertical detours may result in accelerating the spreading of dissolved contaminants or uncontrolled movement of the contaminants [Nyer and Suthersan, 1993]. In addition, excessive air injection may reduce the efficiency of IAS systems by decreasing a mixing ratio that is a ratio of the treated groundwater volume to the injected air volume.

(a) Darcy velocity of groundwater at air injection rate, 10 m^3/hr

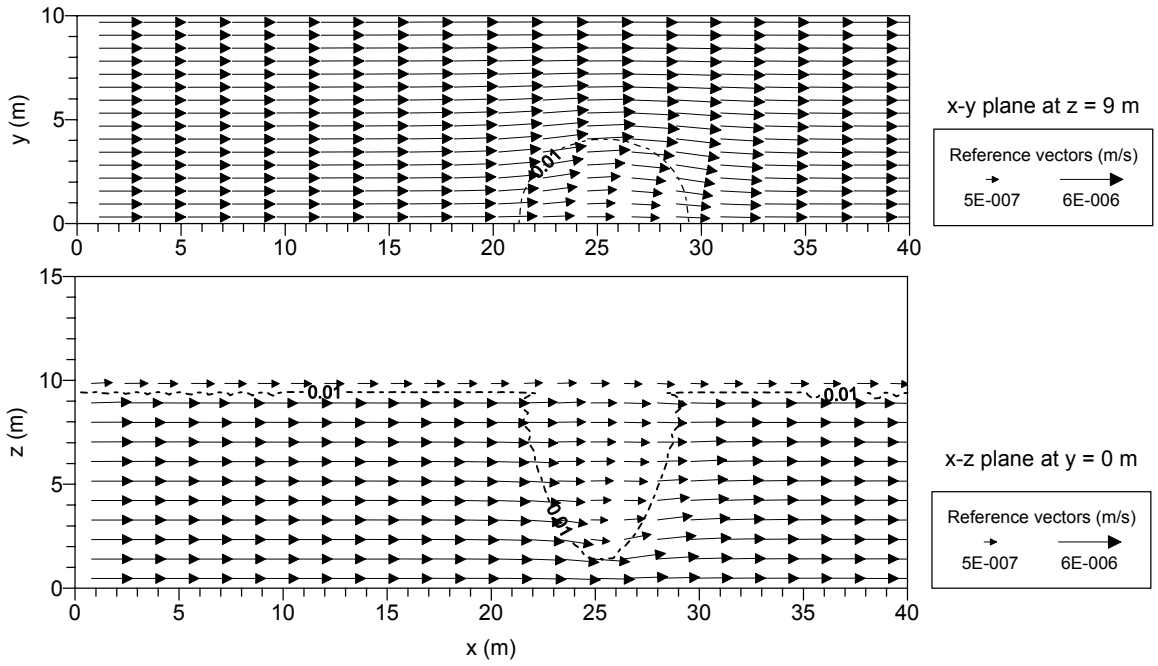

(b) Darcy velocity of groundwater at air injection rate, 60 m^3/hr

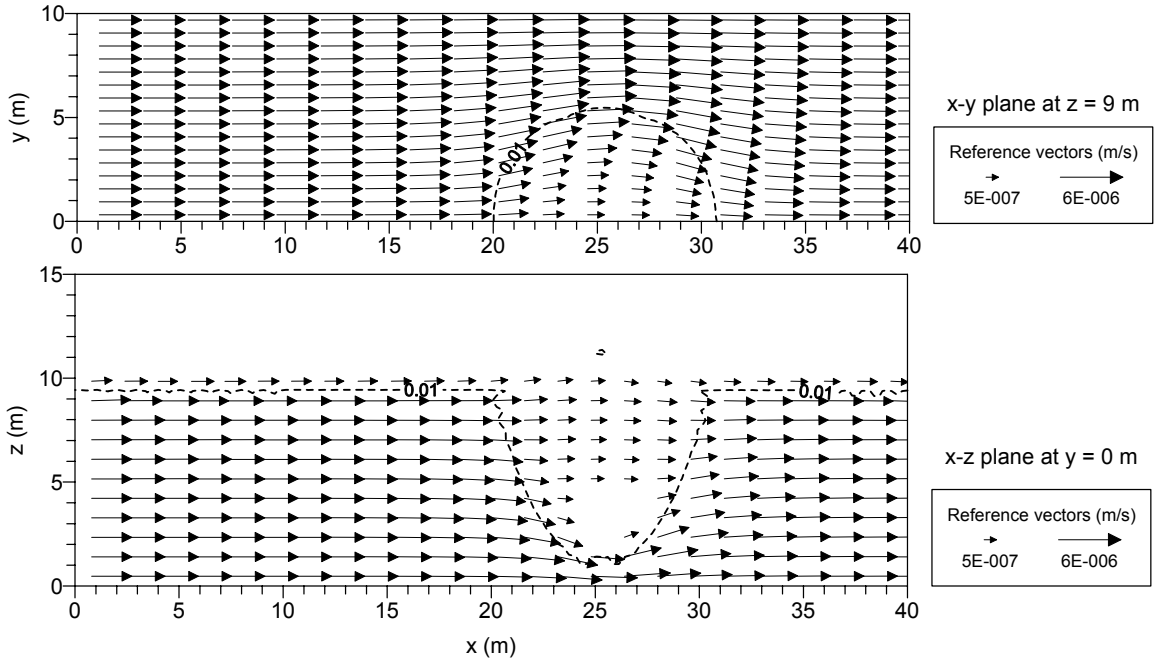

Figure 5.11 Darcy velocity of the groundwater at two air injection rates (10 and 60 m^3/hr) for Case V-2 and V-5. Dashed lines indicate a gas saturation level of 0.01.

As seen in Figure 5.8 to 5.11, the distribution of gas saturation, ROI, and flow velocities of gas and water phases are linked with each other and these parameters are important factors to determine the remedial efficiency of IAS systems. At contaminated sites, optimum values of operational parameters such as injection rates may be selected based on remediation performance results of various field test and/or IAS simulations. In this study, for IAS systems with single injection well, the remedial performances of five cases listed in Table 5.4 are investigated in terms of contaminant concentration reduction (Figure 5.12) and overall contaminant mass reduction within the modeling domain (Figure 5.13).

In Figure 5.12, temporal concentration profiles of dissolved TCE on the *x*-*y* plane at *z*=9 m and the *x*-*z* plane at *y*=0 m are given because these two planes contain the highest concentration profiles of dissolved TCE. Since the concentration of vaporized TCE in gas phase is very small (less than 0.001 g/L) through the domain, its concentration profiles are not presented in this chapter. However, total mass of vaporized TCE is considered in calculating the efficiency of IAS systems, discussed later.

In this study, the remedial performance of each IAS simulation case will be discussed in terms of three main aspects: (i) ROI of an injection well for contaminated groundwater plumes; (ii) the contaminant-concentration reduction compared to a target value; and, (iii) the lateral or vertical detours of contaminated plumes around the cone of IAS influence occurs.

In Figure 5.7 (d), initial dissolved TCE plumes with its concentration ≥ 0.001 g/L are located within *y* = 0-4 m on *x*-*y* plane, which are inside the ROI of 1 % gas saturation for Case V-2 and V-5 in *y*-direction: In Figure 5.9, the ROI values for the two cases are

4.05 ($r' = 0.57$) and 5.3 m ($r' = 0.75$), respectively. The ROI values of 10 % gas saturation for Case V-2 and V-5 are 2.15 ($r' = 0.3$) and 4.25 m ($r' = 0.6$), respectively, which implies the latter ROI value for Case V-5 covers initial contaminant plumes on *x*-*y* plane in *y*-direction but the former ROI does not. In this study, dissolved TCE plume shown in Figure 5.7 will expand out laterally and vertically due to dispersion along with the groundwater flow, and its expansion may be accelerated due to the diverted groundwater flow around injection wells shown in Figure 5.11. The size of remedial zones (effective ROI) could be evaluated from spatial contaminant concentration profiles around injection wells over time. Contaminant concentrations in aqueous phase can be non-dimensionalized as follows:

$$C' = \frac{C_w}{C_{w,\max}} \tag{5.3}$$

where C' is a dimensionless contaminant concentration, C_w is a dissolved contaminant concentration (g/L), and $C_{w,\max}$ is a maximum concentration (or solubility) of a contaminant as a characteristic concentration (g/L). In this study, the $C_{w,\max}$ for TCE is 1.33 g/L as shown in Table 3.4. The remedial target concentration of TCE (0.001 g/L) corresponds to a dimensionless concentration $C' = 0.00075$. Since dimensionless concentrations of TCE (or dissolved TCE concentrations) vary over time and location due to transport processes including advection, dispersion, and partitioning, the effective ROI (or r') mentioned above are complicatedly coupled with gas flow and contaminant transport processes. The effective ROI (or r') also changes over time. Therefore, it is difficult to define a specified relationship between C' and effective ROI (or r'). Instead, among temporal values of effective ROI during remedial periods, its minimum value can

be selected as a representative effective ROI of an injection well, which may be used in designing IAS systems.

Temporal variations of concentration of dissolved TCE are given in Figure 5.12, in which dissolved TCE concentrations are illustrated as dimensional values (g/L). For both Cases V-2 and V-5, the concentration of dissolved TCE decreases over time due to the operation of IAS systems. In Figure 5.12 (A3), at 20 days for Case V-2, some dissolved TCE plumes with the concentration of 0.001 g/L ($C' = 0.00075$) on *x*-*z* plane at *y*=0 m pass through the zone of IAS influence shown in Figure 5.8 (a). In a zone (*x*=25 m and *z*=8-9.5 m on the *x*-*z* plane in Figure 5.12 (A3)) through which the TCE plumes pass, gas saturation levels for Case V-2 are between 10 and 20 % as shown in Figure 5.8 (a). In that zone, gas saturation levels for Case V-5 are between 30 and 40 % as shown in Figure 5.8 (b), and gas saturation levels for Case V-3 are from 20 and 30 % (Figures for Case V-3 are not presented here). In Cases V-3 (Q=30 m^3/hr and $1/N_g = 0.31$) and V-5 (Q=60 m^3/hr and $1/N_g = 0.61$), the concentration reductions of dissolved TCE on *x*-*z* plane at *y*=0 m are higher than in Case V-2, and, in Cases V-3 and V-5, no dissolved TCE with the concentration of 0.001 g/L ($C' = 0.00075$) passes through the air sparging zone on the plane. These imply that, if single injection well is used in this study, gas saturation of more than 20 % should be provided in the zone (*x*=25 m and *z*=8-9.5 m on *x*-*z* plane at *y*=0 m), through which the highest-concentration TCE plumes pass, to clean up the contaminant plumes shown in Figure 5.6 (b) below the target concentration of 0.001 g/L ($C' = 0.00075$) on *x*-*z* plane at *y*=0 m.

Regarding the detour of contaminant plumes for Cases V-2 and V-5, dissolved TCE concentration plots at 5 days on *x*-*y* plane at *z* = 9 m are shown in Figure 5.12 (A1)

and (B1). At 5 days, the contaminant spreading in *y*-direction on *x*-*y* plane at z = 9 m is greater in Case v-5 than in Case V-2, which is also observed in Figure 5.12 (B2) and (B3). In IAS modeling with one vertical well of this study, the detour of contaminated groundwater plumes becomes larger as air injection rates increase: This may be due to the higher groundwater velocity reduction within IAS influence zones at the higher injection rate as shown in Figure 5.11.

In Case V-2, due to the detour of the groundwater on *x*-*y* plane at z = 9 m, the concentration contour of 0.001 TCE g/L ($C' = 0.00075$) exceeds the ROI of 1 % gas saturation (4.05 m and $r' = 0.57$) in *y*-direction at 5 days in Figure 5.12 (A1). At 20 and 30 days in Figure 5.12 (A3) and (A4), respectively, some contaminant plumes migrate over the IAS influence zone.

In Case V-5, the concentration contour of 0.001 TCE g/L ($C' = 0.00075$) exceeds the ROI of 1 % gas saturation (5.3 m and $r' = 0.75$) in *y*-direction at 10 days in Figure 5.12 (B2). In Figure 5.12 (B3) and (B4), some portion of dissolved TCE plumes on *x*-*y* plane at z=9 m bypasses the IAS influence zone. The detour of dissolved TCE plumes around the IAS influence zone on *x*-*y* plane at z=9 m occurred for all five cases listed in Table 5.4.

In Figure 5.12 (B3), while contaminant plumes move around the injection well, some portion of the plumes are remediated to below 0.001 TCE g/L ($C' = 0.00075$) level within some high gas saturation zones near the injection well. The point M, which indicates the limit of those high gas saturation zones, is located at 4 m in *y*-direction ($r' = 0.57$) and corresponds to approximately 10 % gas saturation limit shown in Figure 5.8 (b). The 10 % gas saturation at point M implies that, if gas saturation of up to 10 % is

provided beyond point M in the increasing y-direction, the detoured contaminant plumes that have not completely remediated on x-y plane at z=9 m will be successfully treated below the target TCE concentration (0.001 g/L or $C' = 0.00075$).

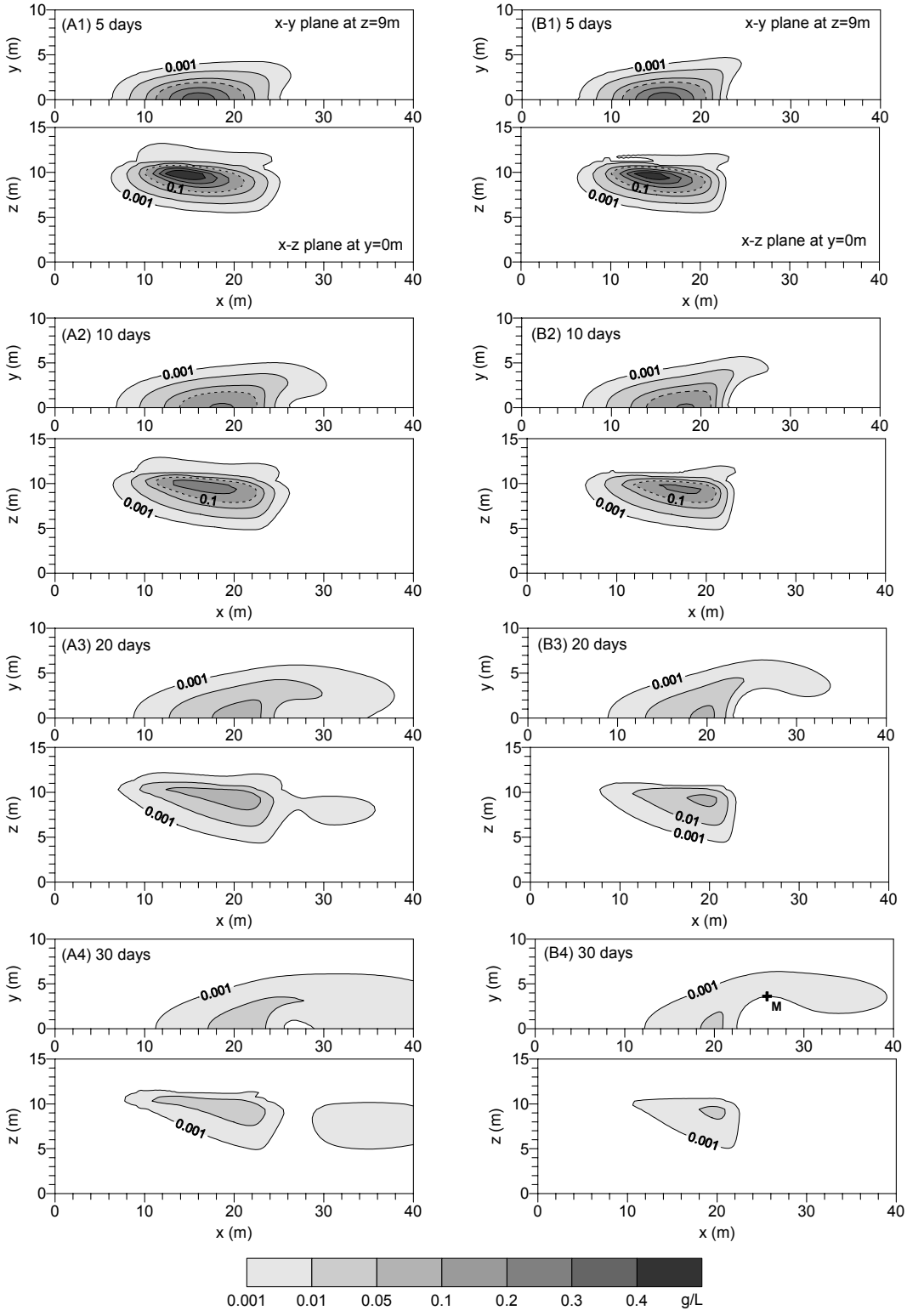

Figure 5.12 Dissolved TCE concentrations (g/L) at Cases V-2 and V-5

In Figure 5.12, the removal of dissolved TCE on *x*-*z* plane at *y*=0 m are successful if air injection rate is equal to or greater than that of Case V-3 (30 m^3/hr). For the all five cases listed in Table 5.4, however, the removal of dissolved TCE on *x*-*y* plane at *z*=9 m fails to achieve the remedial target (0.001 TCE g/L). In order to overcome problems related with the detoured contaminant plumes, we may have questions like "is air injection rate not sufficient yet?" or "should other approaches such as multiple vertical wells or horizontal wells be implemented?" These questions can be answered by investigating overall contaminant mass removal for the all five cases.

In Figure 5.13, the overall removal efficiency rises with the increase in air injection rates. The removal efficiencies of TCE in the domain for Cases V-1 (injection rate 5 m^3/hr), V-2 (10 m^3/hr), V-3 (30 m^3/hr), V-4 (50 m^3/hr), and V-5 (60 m^3/hr) are about 70, 80, 89, 91, and 91.9 % at 60 days. The increases in air injection from 5 to 10 m^3/hr and from 10 to 30 m^3/hr raise TCE removal efficiencies by 10 and 9 %, respectively. However, the increase in air injection from 30 to 60 m^3/hr generates the increase of less than 3 % in TCE removal efficiency. These implies that, in this study, the continuous increase in air injection rates at one injection well shown in Table 5.4 may have a limit in raising TCE removal efficiency. That limit may be due to the failure of one-injection well systems in capturing and cleaning up the detoured contaminated groundwater plumes on *x*-*y* plane at *z*=9 m shown in Figure 5.12. Therefore, to remediate the detoured contaminated groundwater plumes on that plane, multiple vertical wells or horizontal wells should be used. In addition, in Figure 5.13, the overall removal efficiencies profiles indicates that more than air injection rate of 30 m^3/hr does not have a significant effect in increasing the efficiency. Air injection rates more than 30 m^3/hr will

be excessive for one vertical well in this study. Thus, for multiple vertical well systems discussed in the next section, air injection rates per well are limited up to 30 m^3/hr.

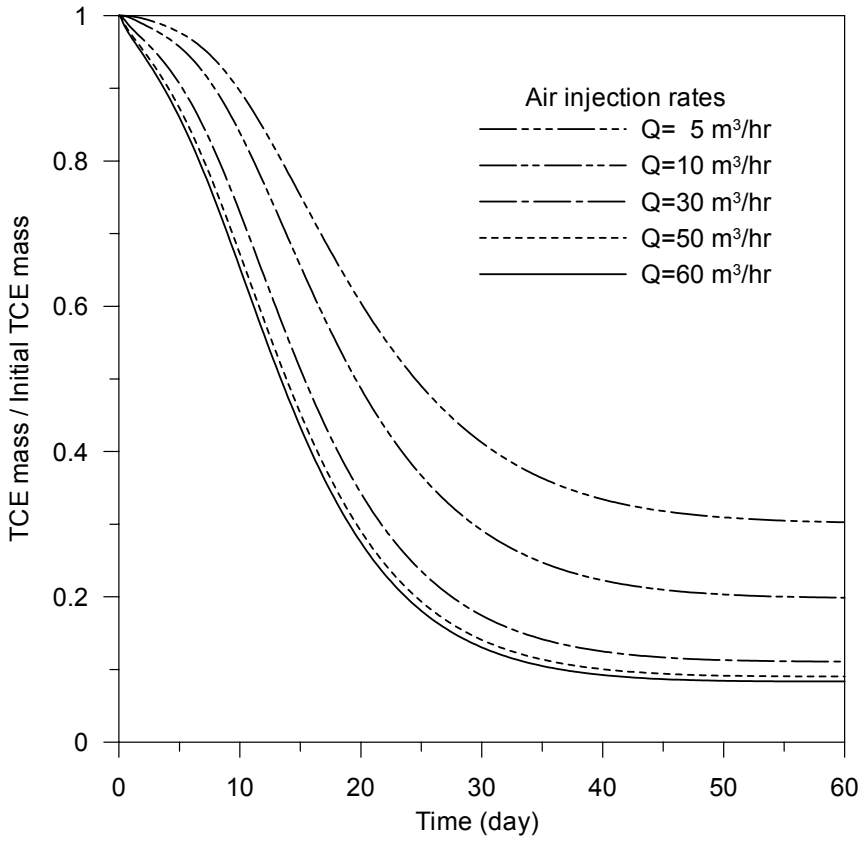

Figure 5.13 Removal of TCE by IAS operations with one vertical injection well

5.3.3 TCE Removal by IAS Systems with Multiple Vertical Wells

In Figure 5.12, IAS systems with one vertical injection well missed some portion of dissolved TCE plumes on x-y plane at z=9 m. Thus, multiple-injection-well systems will be one of the options to capture and clean up the missed contaminant plumes on the x-y plane. As listed in Table 5.5, two scenarios for IAS with three injection and three extraction wells are set. In the multiple-well systems, the second and third wells (Well No. 2 and 3) will support the first well (Well No. 1). The first well is located at the middle of TCE plume at y=0 m, and the second and third wells are located at y= +5 and -5 m, respectively, to capture the contaminant plumes that are not covered by the first well. To facilitate the capture of the detoured plumes, the second and third wells are located 1 m upstream (x=24 m) the location of the first well (x=25 m). The distance between the first and second wells is about 5.1 m. Based on gas saturation distributions given in 5.8, the expected gas saturation levels in the middle of the first and second wells (on x-y plane at z=9) are approximately 13 and 24 % for Cases MV-1 and MV-2, respectively.

Table 5.5 Scenarios for IAS systems with six vertical wells

Case No.	Flow rates (m^3/hr)		Screen locations of injection (Inj.)/extraction (Ext.) wells
	Injection	Extraction	
MV-1	10	15	Inj. well 1: *x*=25-25.5, *y*=0, *z*=2-3 m Ext. well 1: *x*=25-25.5, *y*=0, *z*=11-12 m
MV-2	30	45	Inj. well 2 & 3: *x*=24-24.5, *y*=+5/-5, *z*=2-3 m Ext. well 2 & 3: *x*=24-24.5, *y*=+5/-5, *z*=11-12 m

The distributions of gas saturation in multiple-injection-well systems are given in Figure 5.25 and are discussed later. In this section, our attention will be on contaminant removal for the detoured groundwater plumes on x-y plane at z=9 m. Concentration profiles of dissolved TCE over time for Cases MV-1 and MV-2 are presented in Figure 5.13. In the both cases, dissolved TCE plumes on x-y plane at z=9 m are captured and remediated by IAS with multiple wells. Overall, in Figure 5.14, multiple-well IAS systems successfully clean up the contaminant plumes shown in Figure 5.7 below the target concentration of dissolved TCE 0.001 g/L (or $C' = 0.00075$). In a comparison of concentration profiles of Cases MV-1 and MV-2 over time, the concentrations of dissolved TCE in the domain are lower in the latter case than in the former case. The advance (penetration) of contaminant plumes into the IAS influence zones in the groundwater flow direction is also greater in Case MV-1 than in Case MV-2. As expected, the larger injection rate contributes to the faster reduction in TCE concentration.

Multiple-well systems (Cases MV-1 and MV-2) also enhance contaminant removal in high concentration zones. For example, in Figure 5.12 (A3) for Case V-2 at 20 days, some portion of TCE plumes ($C_w \geq 0.001$ g/L or $C' \geq 0.00075$) pass through the IAS influence zone on *x*-*z* plane at *y*=0 m, however, this passage does not occur in Figure 5.14 (A2) for Case MV-1. The synergetic effects of multiple injection wells on remediation will help to reduce the requirement of air injection rates at each well of IAS systems in this study. Those synergetic effects will vary with many parameters such as well interval, injection rate, well layout, groundwater flow, and heterogeneous soil properties.

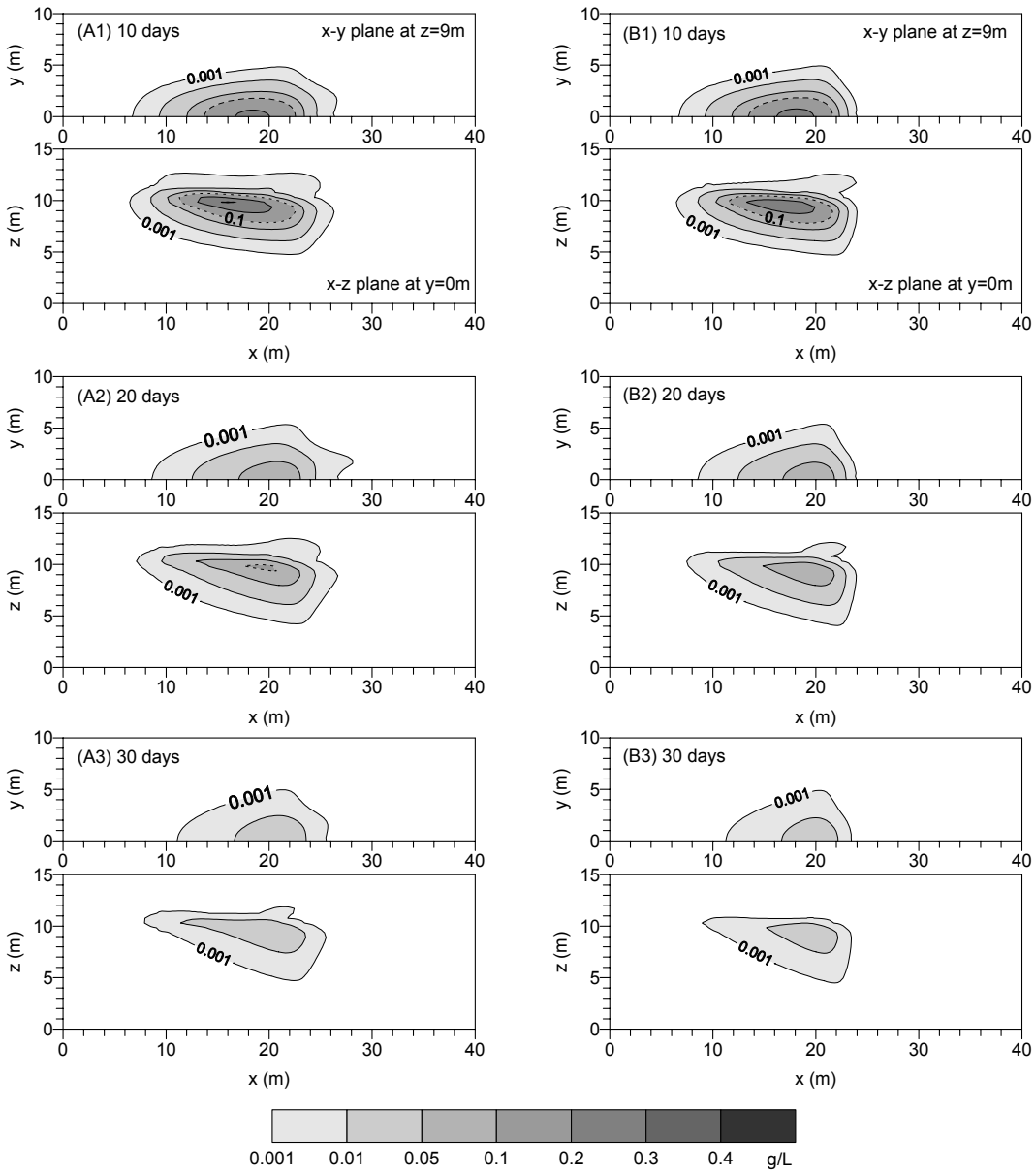

Figure 5.14 Concentration profiles of dissolved TCE (g/L) at IAS with multiple injection wells: (A) Case MV-1 and (B) Case MV-2

Overall removal efficiency of TCE in Cases MV-1 and MV-2 is given in Figure 5.14. In this study, IAS systems with multiple injection wells appear to be effective in cleaning up the contaminated groundwater in the modeling domain. The removal efficiencies of Cases MV-1 and MV-2 reach up to 96 and 97.2 % at 60 days, respectively. Even though total injection rate (30 m^3/hr) of Case MV-1 is half the injection rate (60 m^3/hr) of Case V-5 (for one injection well), the removal efficiency of the former case (96 %) is greater than that of the latter case (91.9 %). This implies that, under the contamination situations used here, well dispatched multiple sparging wells can be more effective than one sparging well in capturing a contaminant plume and cleaning up contaminated groundwater.

As mentioned earlier, the remedial performance of multiple-well IAS systems depends on many parameters. Especially, when the velocity of the groundwater flow or the concentration of contaminants increase, remedial burdens imposed to each well will rise. In such cases, high flow rates or more injection wells may be required. The design and operation of IAS systems with multiple wells will be determined based on multiple factors such as hydrogeological conditions of contaminated sites, spatial distributions of contaminants, physicochemical properties of contaminants, and remedial goals.

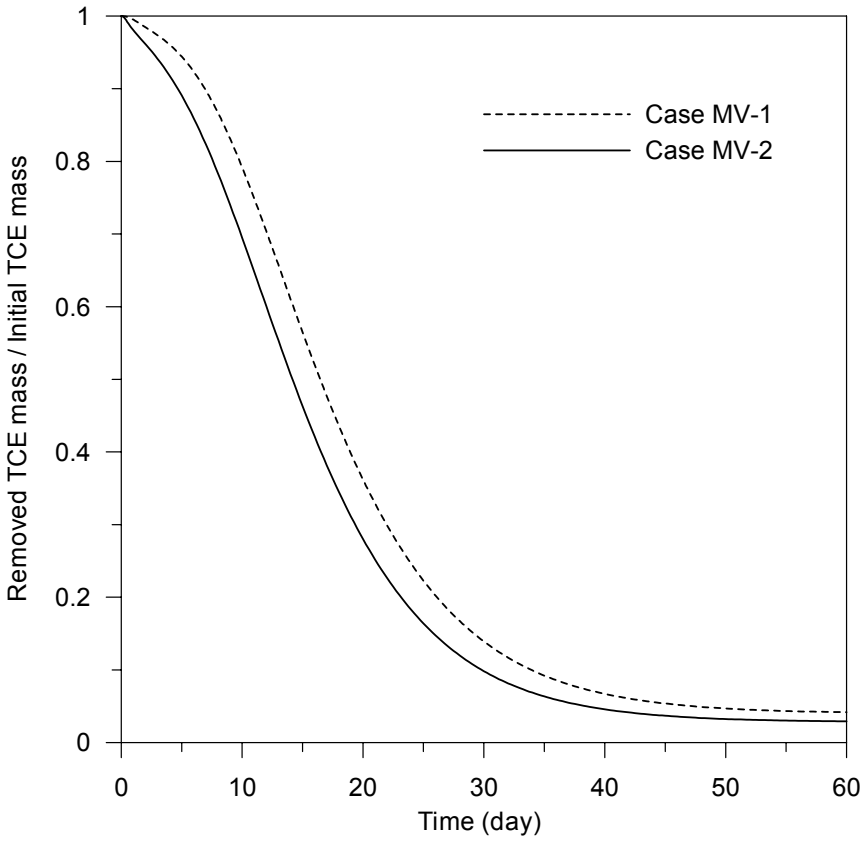

Figure 5.15 Removal of TCE by IAS with multiple vertical injection wells: Case MV-1 and MV-2

5.3.4 Multiphase Flow and Contaminant Removal by IAS Systems with One Horizontal Well

In IAS systems, horizontal wells are selected because these are expected to produce uniform gas distribution in the saturated zone and yield good contact between injected air and a contaminant plume [Unger et al., 1995]. A horizontal well can be extended laterally to cover wide contaminant plumes. To examine the flow of gas and groundwater and the removal efficiency of TCE by IAS systems with one horizontal well, three scenarios are set as listed in Table 5.6. The horizontal injection/extraction wells are located along with *y*-direction from *y* = -5 to +5 m as seen in Figure 5.6, and, in the numerical modeling domain of this study, the horizontal wells are at *y* = 0 to 5 m. Air is assumed to be released uniformly through an injection well screen.

Table 5.6 Scenarios for IAS with one horizontal well

Case No.	Flow rates (m^3/hr)		Well screen location
	Injection	Extraction	
H-1	20	40	Injection well: *x*=25-25.5, *y*=-5-+5, *z*=2.5-3 m Extraction well: *x*=25-25.5, *y*=-5-+5, *z*=11.5-12 m
H-2	60	120	
H-3	100	200	

The profiles of stabilized gas saturation for Cases H-1 and H-2 are given in Figure 5.16. On x-z plane (at y=0 m), the gas distribution profiles show parabolic shapes, and on x-y plane (at z=9 m) the gas distribution contours appear along with horizontal wells. In both Cases H-1 and H-2, gas saturation on y-z plane (at x=25 m) distributes more widely than that in the vertical-well air injection cases shown in Figure 5.8. That wide distributions in horizontal-well IAS will would be good to cover contaminant plumes

uniformly. On y-z plane (at x=25 m), gas saturation levels become higher as gas injection rates increase: Case H-1 shows gas saturation of around 10 % in the region containing the groundwater with high dissolved TCE concentration (y=0-5 m and z=5-9.5 m), and Case H-2 has that of around 20 % in the region. Since air injection through a horizontal well occurs over a wider screen area than that through a vertical well, gas saturation in the vicinity of air sparging points is lower at Case H-2 (Figure 5.16 (b)) than at Case V-5 (Figure 5.8 (b)) at the same injection rate of 60 m^3/hr. The lower gas saturation will help to reduce the diversion of the groundwater flow around air injection points. The comparison in gas saturation between Case V-5 (vertical injection) in Figure 5.5 (b) and Case H-2 (horizontal injection) in Figure 5.16 (b) demonstrates that, under a homogeneous soil conditions used here, the horizontal air injection can provide more uniform and wider mixing zone, in which injected air contacts with the groundwater, than the vertical air injection.

Flow and Darcy velocity of gas phase and groundwater are shown in Figure 5.17. Darcy velocity of gas phase around the horizontal injection well for Case H-2 is much less than that around a vertical injection well for Case V-5 under the same injection rate of 60 m^3/hr: For Case H-2, the maximum velocity is approximately 0.7 cm/s while for Case V-5 the velocity is about 4 cm/s. Within IAS influence zones, the reduction of groundwater velocity is also less in Case H-2 than in Case V-5. So, the movement of contaminant plumes will be faster in Case H-2 than in Case V-5 when the plumes pass through the middle of IAS influence zones.

(a) Case H-1

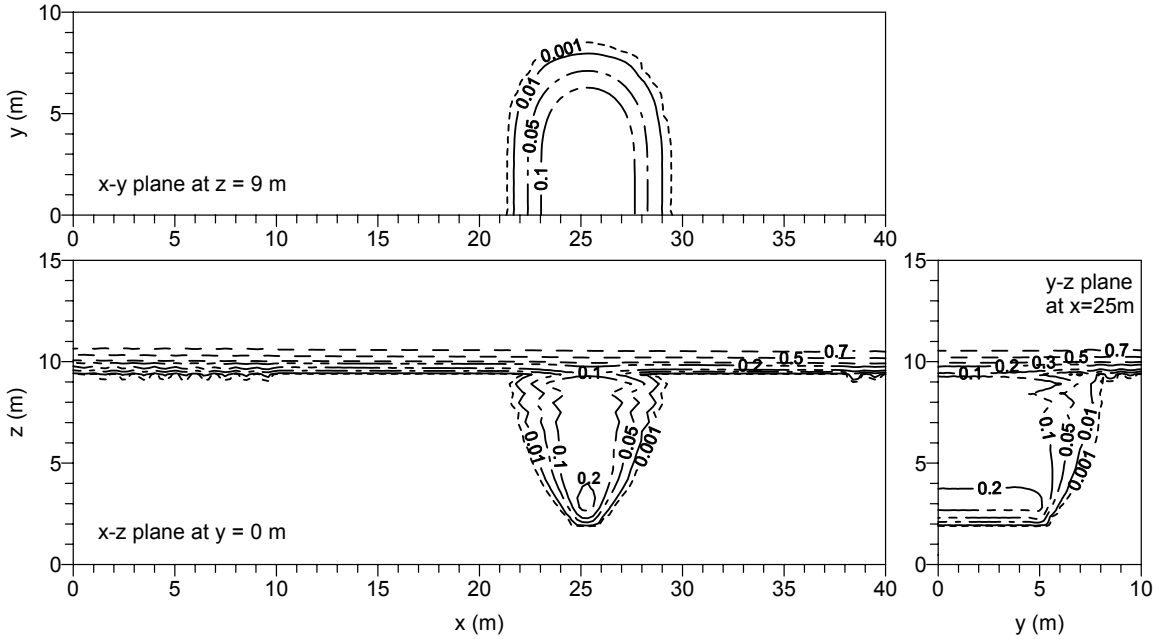

(b) Case H-2

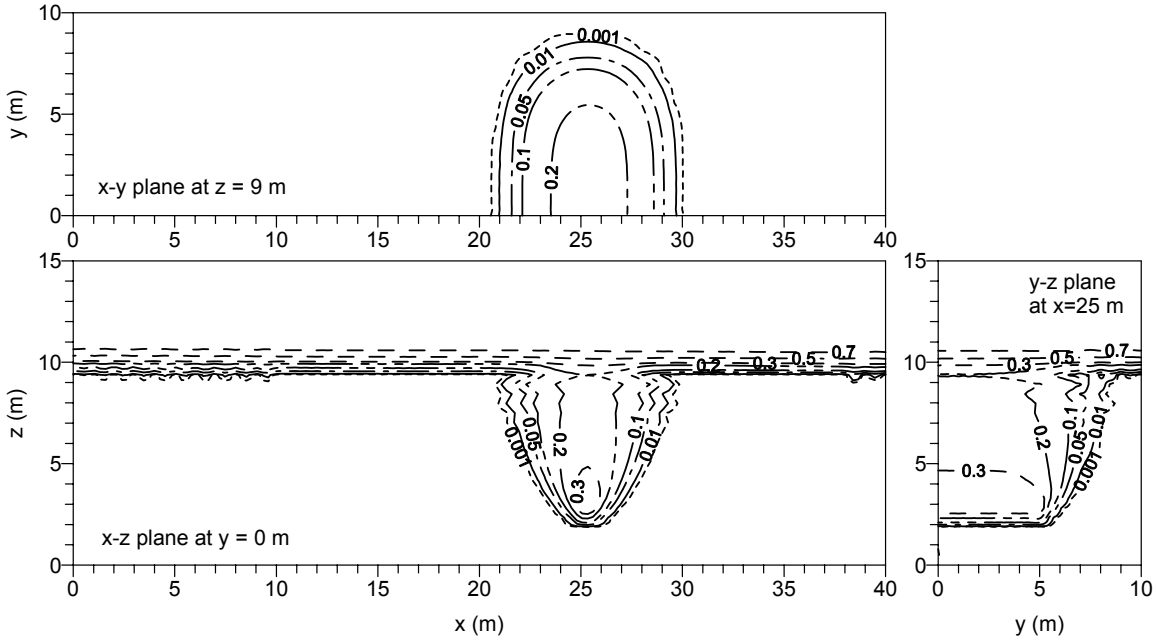

Figure 5.16 Air saturation under air injection through one horizontal well: Cases H-1 and H-2

(a) Darcy velocity of gas phase

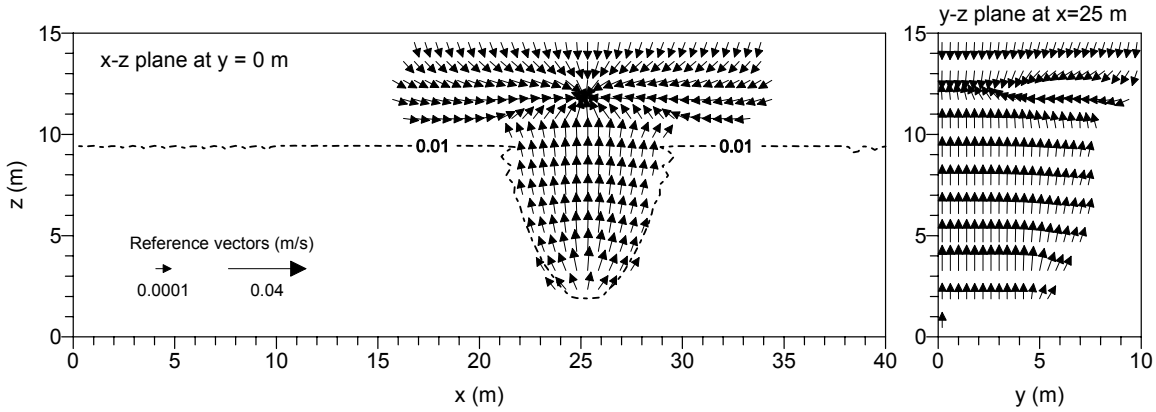

(b) Darcy velocity of groundwater

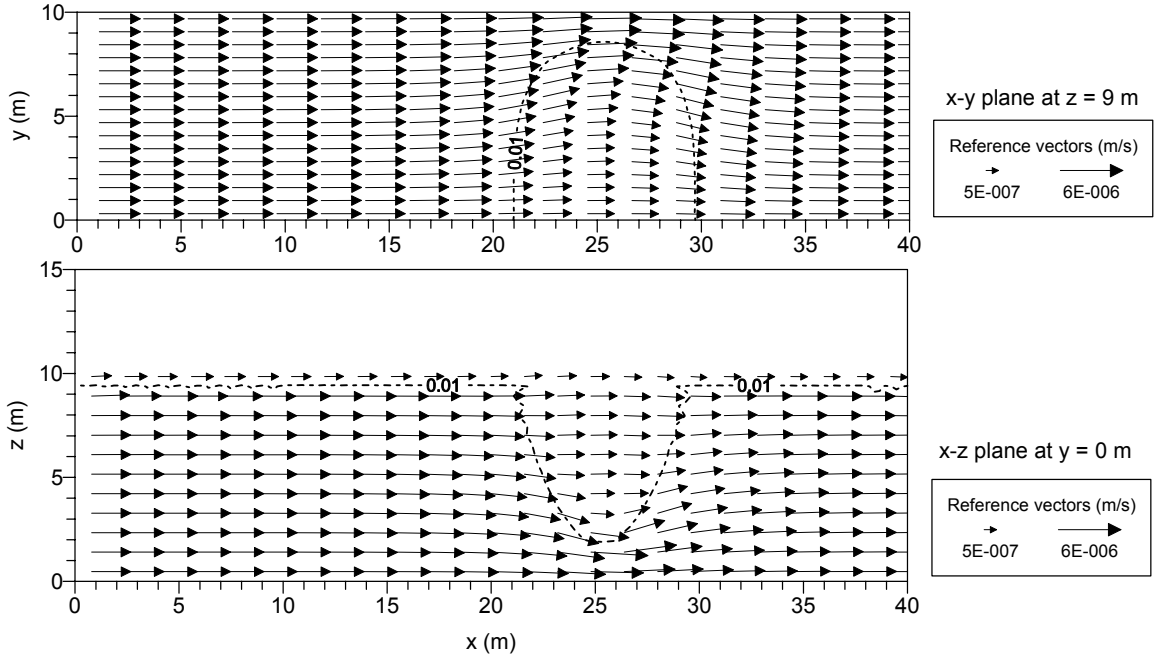

Figure 5.17 Darcy velocities of gas and groundwater at Case H-2. Dashed lines indicate a gas saturation level of 0.01.

In the application of IAS with a horizontal well, our attentions are on (i) whether the influence zone of a horizontal injection well covers all contaminant plumes and (ii) whether air injection rates are enough to clean up the plumes.

For Cases H-1 and H-2, the variations in dissolved TCE concentration are given in Figure 5.18. The migration of contaminant plumes shown on x-y plane (at z=9 m) in Figure 5.18 demonstrate that the influence zones in the two cases cover all contaminated plumes: No contaminant plume detours the influence zones of horizontal IAS wells. In Case H-1, however, some contaminant plumes with dissolved TCE concentration of 0.001 mg/L (or $C' = 0.00075$) pass through the sparging zones at 20 and 30 days. At Case H-2, dissolved TCE plume is successfully removed to below its target concentration of 0.001 g/L (or $C' = 0.00075$) by IAS operation. In Figure 5.18 (A2) and (A3) for Case H-1, the passage of some contaminant plumes through the air sparging zone occurs at relatively high concentration regions (dissolved TCE concentration ≥ 0.01 g/L or $C' = 0.0075$) among the whole plumes shown in Figure 5.7. This indicates that, in Case H-1, gas saturation of 10-20 % in the approximate main remedial-reaction zones of y=0-4 m and z=6-9.5 m at x=25 m is not sufficient to clean up highly polluted groundwater plumes (approximately dissolved TCE concentration ≥ 0.01 g/L or $C' = 0.0075$) passing the zones below the target concentration of 0.001 TCE g/L (or $C' = 0.00075$). In Case H-2, however, the contaminant loads passing the main reaction zones are successfully removed under gas saturation of 20-30 % in the zones. Nyer and Suthersan [1993] pointed out that very low air injection rates may not be sufficient for IAS to work. The evolution of contaminant concentration in Cases H-1 and H-2 shows that the ratio of contaminant loads to be remediated and injected gas volume is an important factor on the

removal of dissolved TCE. Contaminant loads may depend mostly on contaminant concentration and the groundwater flow.

Overall removal efficiency of TCE by one-horizontal-injection-well systems is given in Figure 5.19. The efficiencies for Cases H-1, H-2, and H-3 are approximately 93.9, 96.6, and 97 % at 60 days, respectively. The efficiency in Case H-2 is much higher than that obtained by air sparging through one vertical well (Case V-5), shown in Figure 5.13. The efficiency of 96.6 % in Case H-2 (injection 60 m^3/hr) is a little higher than that of 96.0 % in Case MV-1 (total injection 30 m^3/hr for three wells). The efficiency of 97 % in Case H-3 (injection 100 m^3/hr) is similar to the efficiency of 97.2 in Case MV-2 (total injection 90 m^3/hr for three wells). In this study, the efficiency results of IAS systems with horizontal wells or multiple injection wells suggest that the IAS systems can be good options to remediate the contaminant plumes shown in Figure 5.7 below a target concentration of 0.001 g/L dissolved TCE (or $C' = 0.00075$).

The difference in the efficiency between Case H-1 and H-2 is greater than that between Cases H-2 and H-3. The increase in injection flow rates from 60 to 100 m^3/hr contributes to only 0.4 % increase in the removal efficiency. If a target concentration of dissolved TCE using IAS systems is 0.001 mg/L (or $C' = 0.00075$), the flow rate of 100 m^3/hr would be excessive air injection in this study.

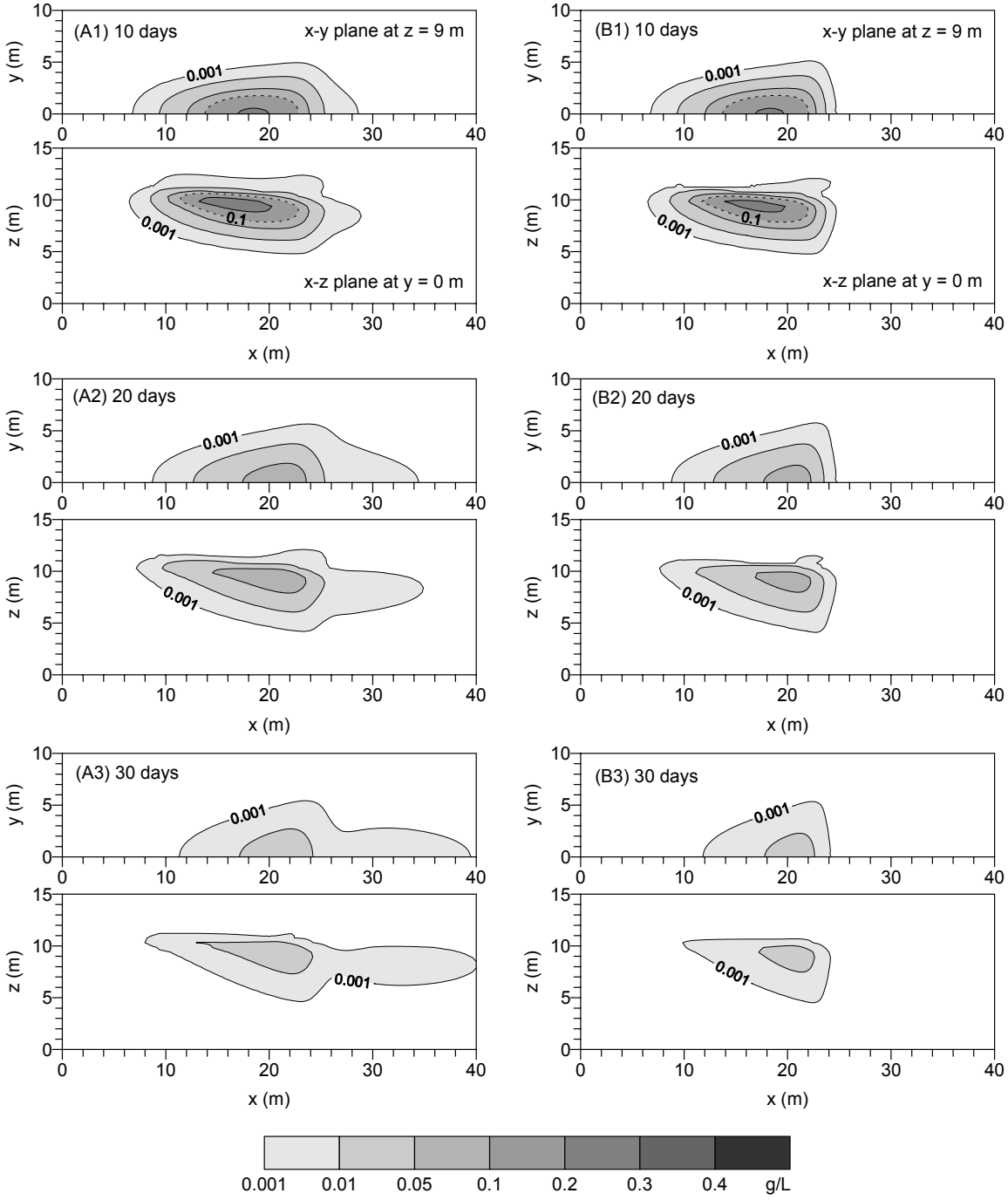

Figure 5.18 Concentration profiles of dissolved TCE (g/L) for (A) Case H-1 and (B) Case H-2.

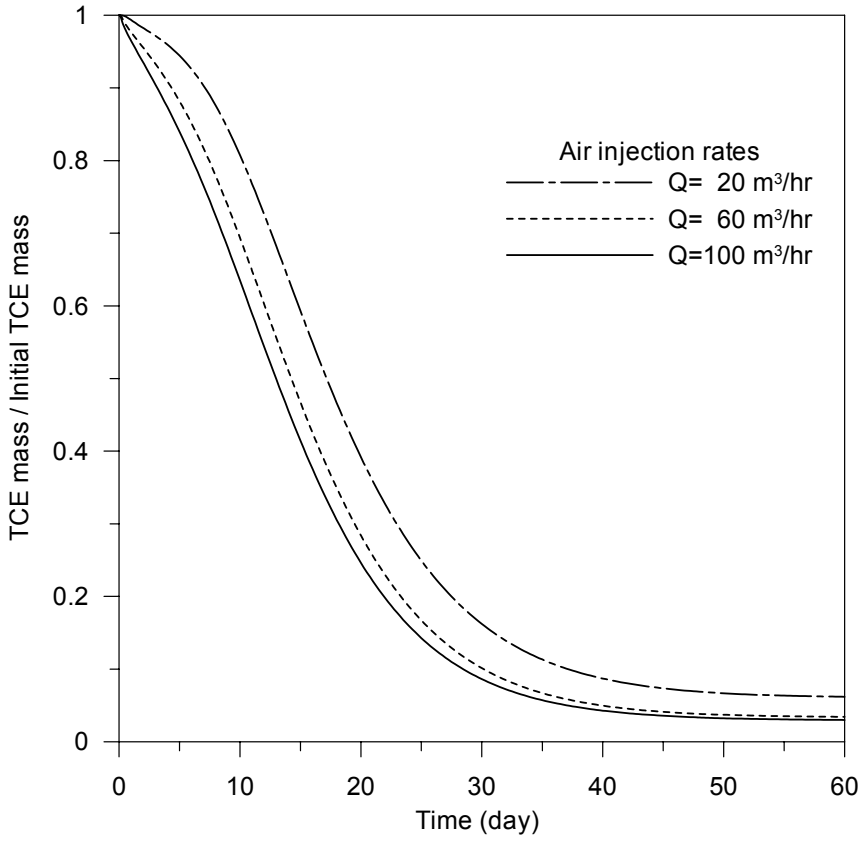

Figure 5.19 Removal of TCE by air sparging through one horizontal well

5.3.5 Effect of Depth of a Vertical Sparging Well on Contaminant Removal by IAS

A depth of air injection depends on the contaminant distribution in groundwater systems. Nyer and Suthersan [1993] suggested that a depth of injection should be at least 1 or 2 feet deeper than the deepest known point of contamination. In the industry, a recommended depth of air injection is less than 30 (9.1 m) to 40 feet (12.2 m). At depths greater than 40 feet, nested injection points are recommended [Nyer and Suthersan, 1993]. As a depth of air injection becomes deeper, ROI may increase, but also the potential for channeling due to the presence of higher permeability becomes larger. In field applications, air sparging at deeper depth requires safety considerations due to the high air pressures involved.

As seen in initial concentration profiles of dissolved TCE in Figure 5.7, the deepest point of dissolved TCE is about z=6 m (approximately 3.5m below the groundwater table). In this section, in order to investigate the effect of air injection depth on contaminant removal and the detour of contaminated plumes around the sparging points, three cases with different depths of air injection are considered as listed in Table 5.7. For simulations for the three cases, an IAS system with one vertical injection well is used at the same injection rate, 20 m^3/hr.

In the three cases shown in Table 5.7, the increase in well screen elevation (or the decrease in the depth of injection points below the water table) results in the reduction in ROI of an injection well. As the distance between injection points and contaminant plumes reduces due to the reduction in the depth of injection points, some contaminant plumes may be exposed to a fast gas flow in the vicinity of injection points, so mass transfer between water and gas phases may enhanced. Due to the reduction in the depth

of injection points, however, the detour of contaminant plumes can be accelerated by the diversion of the groundwater flow around the injection points. The profiles of gas and groundwater flow velocity at injection rate 10 m^3/hr are already shown in Figures 5.10 (a) and 5.11 (a), respectively.

Table 5.7 Scenarios for air sparging at different depths

Case No.	Well screen elevation (Injection well)	Well screen location	Flow rates (m^3/hr)
SE-1	z=2-3 m (*Depth bgw: 7 m)	Injection well: x=25-25.5, y=0 Extraction well: x=25-25.5, y=0, z=11-12 m	Injection: 10 Extraction: 20
SE-2	z=3-4 m (*Depth bgw: 6 m)		
SE-3	z=4-5 m (*Depth bgw: 5 m)		

*Depth bgw denotes an approximate depth of the center of well screen below the groundwater table

In Figure 5.20, concentration profiles of dissolved TCE are shown for Cases SE-1, SE-2, and SE-3 at 20 and 30 days. The development of dissolved TCE plume on x-z plane at y=0 m is greater at Cases SE-2 and SE-3 than at Case SE-1. Especially, for Cases SE-2 and SE-3, the spreading of contaminant plumes on x-z plane at y=0 m is distinct in Figure 5.20 (b) and (c). That spreading is mostly due to the downward movement of the groundwater flow around a sparging well shown in Figure 5.11. In Figure 5.20, as a depth of air injection becomes shallow, the remediation performance of IAS systems becomes worse: dissolved TCE plumes passing through the air sparging zones on x-z plane at y=0 m become bigger. The ROI of an injection well for 1% gas saturation in Cases SE-1, SE-2, and SE-3 is 4.05, 3.9, and 3.65 m, respectively. In the three cases, as the ROI of an injection well reduces, the detour of contaminated groundwater plumes on x-y plane at

z=9 m increases. Among the three cases, Case SE-3 (the shallowest depth of air sparging) shows the highest concentration profiles on the x-y plane at z=9 m.

Overall removal efficiency of TCE for the three cases is given in Figure 5.21. The efficiencies for Case SE-1, SE-2, and SE-3 are approximately 80, 76, and 71 % at 60 days, respectively. The results of the three cases indicate that, in the contaminated site conditions used here, the elevation of air injection should be at least less than z=3 m: This elevation is 3 m deeper than the deepest point of initial dissolved TCE contamination.

Regardless contaminant removal efficiency of the three cases, a major problem in Case SE-2 and SE-3 will be the downward spreading of dissolved TCE, which should be avoided in the application of IAS. In determining a depth of air injection, the downward detour (diversion) of the groundwater flow around air sparging points should be considered. In this study, under specified conditions used here, air sparging points of z=2-3 m seem to be good for IAS systems used. The degree of groundwater diversion may vary over contaminated sites and will be influenced by various parameters such as geological properties, gas saturation levels, and air injection rates. Thus, the depth of air sparging points can be selected through site investigations and experiments and/or modeling for target sites.

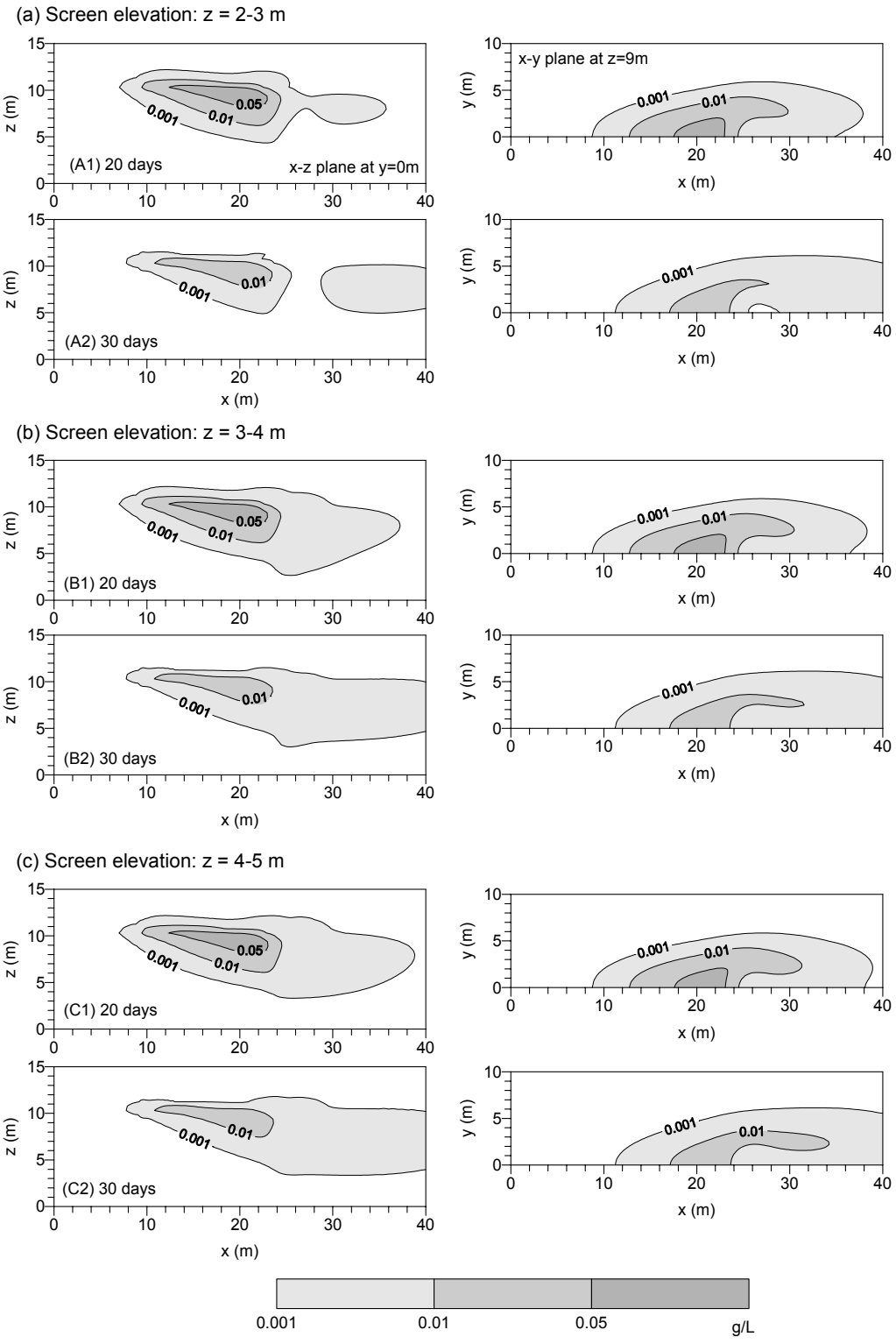

Figure 5.20 TCE concentration profiles (g/L) for Cases SE-1 (Screen elevation *z*= 2-3 m), SE-2 (Screen elevation *z*= 3-4 m), and SE-3 (Screen elevation *z*= 4-5 m)

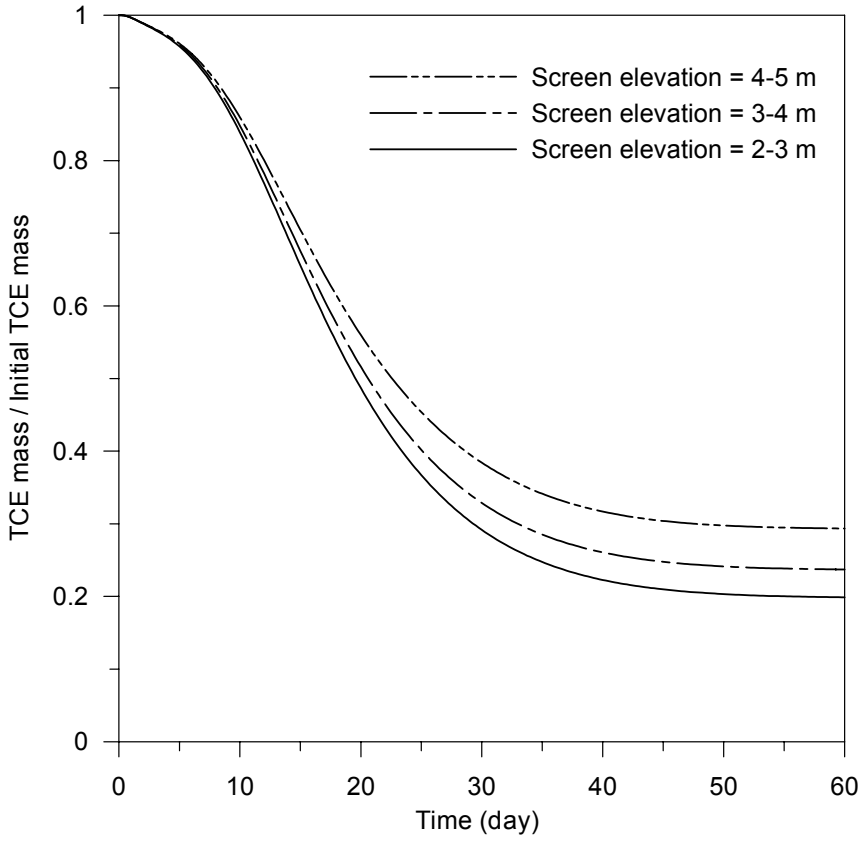

Figure 5.21 Removal efficiency of TCE for Cases SE-1, SE-2, and SE-3

5.3.6 Comparison of Continuous and Pulse Air Injection

Pulse air injection was proposed to improve the performance of air sparging systems by increasing the contact between contaminated groundwater and injected air and the mixing between treated and untreated groundwater within the cone of IAS influence [Rutherford and Johnson, 1996; Heron et al., 2002]. Based laboratory experimental results for the removal of tetrachloroethylene, Heron et al. [2002] reported that pulse air sparging produces five to eight times higher contaminant removal for each energy units applied than continuous air sparging. Pulsing periods of 8 to 24 hours is recommended for field applications. Nyer and Suthersan [1993] suggested that pulse air injection can be used to overcome the diversion of groundwater flow around the cone of IAS influence. When an IAS system is off, contaminated groundwater can move into the zone of IAS influence without the reduction in the groundwater flow velocity due to air sparging. When the system is on, the contaminants within the zone can be removed.

To examine the effect of pulse air injection on TCE removal, two pulse air sparging cases listed in Table 5.8 are considered, and the results of the pulse air injection cases are compared with those of the continuous air injection cases (H-1 and H-2) which are shown in section 5.3.4.

Table 5.8 Scenarios for pulse IAS systems

Case No.	Pulse cycle	Flow rates (m^3/hr)		Well screen location
		Injection	Extraction	
P-1	12 hrs	20	40	Horizontal injection well: x=25-25.5, y=0-5, z=2.5-3 m Horizontal extraction well: x=25-25.5, y=0-5, z=11.5-12 m
P-2	12 hrs	60	120	
H-1	Continuous injection	20	40	
H-2		60	120	

In this study, the pulse injection cases listed in Table 5.8 will produce two different situations from the continuous injection cases: (i) the contact time between the groundwater and injected gas will reduce to approximately half (12 hrs per day); and, (ii) contaminant migration in the zone of IAS influence will be accelerated while IAS is off. Darcy velocities of the groundwater flow at a location (x=25, y=0, z=9 m) are 2.07×10^{-6} and 1.48×10^{-6} m/s for Cases H-1 (or P-1), and H-2 (or P-2), respectively while the background velocity (or under no air injection) is 3.9×10^{-6} m/s. So, at that location, contaminant migration under no air sparging will be more than twice that under air sparging of Case P-2. Therefore, pulse air-injection methods will increase contaminant loads that should be removed while air sparging is on.

Since upward velocities of gas phase in *z*-direction for Cases H-1 and H-2 vary over location within the zone of IAS influence when IAS is on, the residence time of injected air highly depends on its rising pathway from an injection point to the unsaturated zone. The shortest distance of gas trajectory in the saturated zone may equal to the depth of an injection point below the groundwater table. In fact, the traveling distance of gas phase will be always greater than the injection-point depth due to the tortuosity of porous media. In a modeling domain, an averaged residence time can be calculated by dividing air volumes stored in the air sparging zone by injection rates. In this study, the overall averaged residence times for Cases H-1 and H-2 are approximately 13 and 20 minutes when IAS is on. The residence times of injected air decrease with the increase in air injection rates in this study. The longer residence time of gas phase in the saturated zone will provide more contact time for mass transfer of contaminants between gas and liquid phases. However, the reduction in rising velocity of gas phase (the longer

residence time of gas phase in the saturated zone) decreases the magnitude of a mass transfer coefficient as shown in Equation (5.1).

The removal efficiency of TCE for Cases P-1 and P-2 is compared with that for continuous air sparging Cases H-1 and H-2 in Figure 5.22. According to injection flow rates (20 or 60 m^3/hr), pulse IAS shows different responses in TCE removal efficiency. At 20m^3/hr (the smaller injection rate), Case P-1 (Pulse IAS) shows much lower efficiency than Case H-1 (Continuous IAS) throughout the simulation period: At 60 days, the total removal of TCE for Cases P-1 and H-1 is 86.7 and 93.9 %, respectively. In Figure 5.18, Case H-1 failed in removing high-concentration TCE plumes passing through the zone of IAS influence, so we stated air injection 20 m^3/hr (in Case H-1) is not sufficient for IAS to work. Under those situations (air injection 20 m^3/hr), the application of pulse operation results in the increase in contaminant loads per injected air volume, and thus TCE contaminant removal efficiency in pulse air sparging of Case P-1 becomes worse as shown in Figure 5.22.

At 60m^3/hr (the larger injection rate), continuous IAS (Case H-2) was successful to meet our remediation goal (dissolved TCE < 0.001 g/L or $C' < 0.00075$) as shown in Figure 5.18. At that flow rate, pulse IAS (Case P-2) is also effective in contaminant removal (Figure 5.22): At 60 days, the removal efficiency of Case P-2 and H-2 is 98.2 and 96.6 %, respectively. In a comparison of temporal contaminant removal for Cases H-2 and P-2, the superiority of each case on TCE removal depends on time: Until around 30 days, the overall removal of TCE is greater at continuous IAS (Case H-2) than at pulse IAS (Case P-2) even though the difference in TCE removal between the two cases diminishes over time. During that period, the difference between the two cases is less

than 10 %, and approximately 90 % of TCE is removed. That difference may be due to a time lag for pulse IAS not to work while it is off: In this IAS modeling, continuous IAS is operated 24 hrs a day, but pulse IAS 12 hrs a day. In Figure 5.18, as dissolved TCE mass in the domain decreases with time due to IAS operation, contaminant loads per injected air volume reduce with time. Until around 30 days, the temporal reduction in contaminant loads helps to diminish the difference in TCE removal between Cases H-2 and P-2. After 30 days, the overall removal in pulse IAS (Case P-2) becomes greater than that in continuous IAS (Case H-2): At 60 days, the difference in the overall removal is approximately 1.5 %. This enhancement in contaminant removal of Case P-2 over that of Case H-2 may result from contaminant migration under no air injection: While pulse IAS is off, more untreated contaminant plumes enter into the IAS influence zone (that generated under air injection) and then will be removed by pulse IAS operations.

In Cases P-2 and H-2, remediation rates over time (or remediation times) do not show significant differences because the migration of TCE to be removed within the zone of IAS influence mostly depends on the background groundwater flow even though the groundwater flow velocities vary within the influence zone.

For both Cases P-2 and H-2, air injection rate is sufficient for IAS to remediate contaminated groundwater plumes: The 12-hour-interval pulse IAS of injection 60 m^3/hr corresponds to continuous air injection rate of 30 m^3/hr, which is half the injection rate of Case H-2. The difference between Cases P-2 and H-2 is at total volume of injected air (or total air injection time), which may related with the operational cost of IAS systems. The simulation cases listed in Table 5.8 is too limited to decide the superiority of continuous or pulse operations on remedial performance. Remedial performance and applicability of

these operations will depend on site conditions. Under specified conditions for this IAS study including groundwater flow and contaminant plumes shown in Figure 5.6 and Figure 5.7, respectively, Case P-2 may be selected as a better option over Case H-2 in saving the operation cost of IAS systems.

A pulse period of IAS (Periodicity of pulse air sparging) will be a factor to determine temporal remedial performance of IAS application because pulse periodicity may change temporal/spatial contaminant loads for injected air. As mentioned earlier in this section, pulse periods of IAS implemented at contaminated sites varied according to site conditions. In this study, one operation interval (12 hrs) is considered as shown in Table 5.8. Shorter intervals of pulse IAS (for example, 4- or 6-hour intervals) may help to equalize contaminant loads per injected air volume and may change a final contaminant removal efficiency. At contaminated sites, based on overall remedial performance results at different periodicity of pulse IAS through laboratory/field experiments and/or numerical simulations, optimal intervals of pulse IAS will be determined.

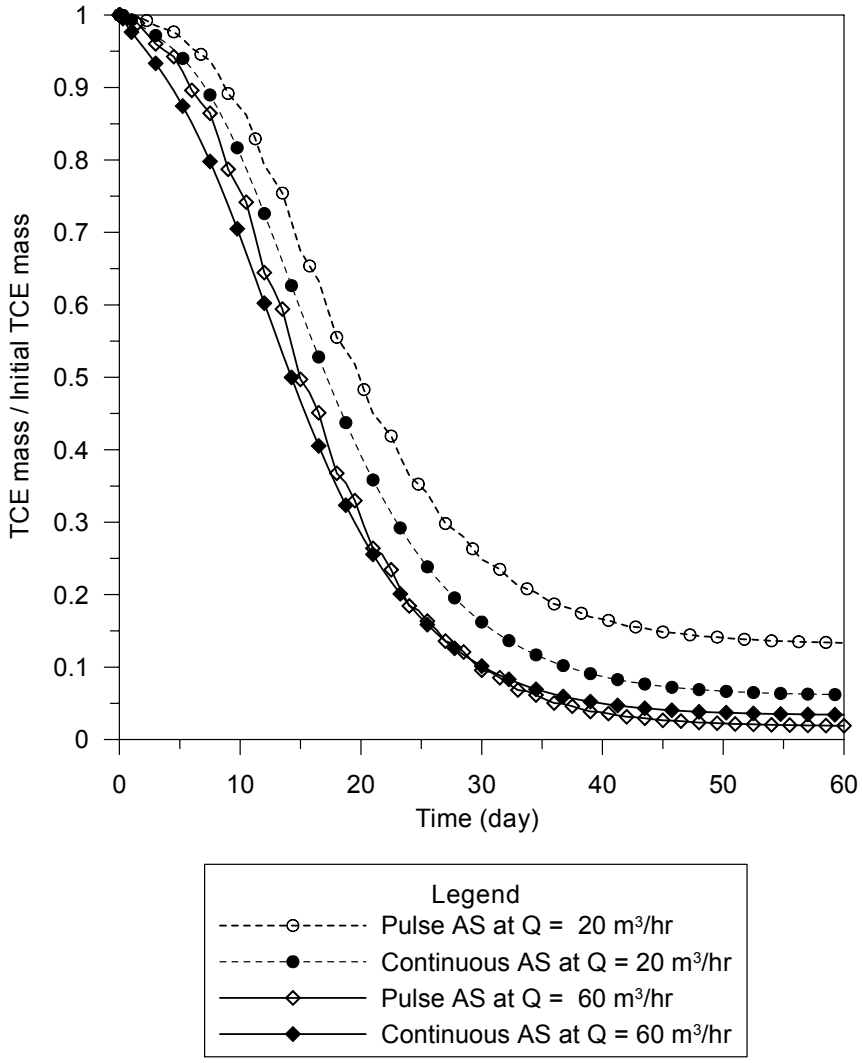

Figure 5.22 A comparison of removal efficiency of TCE by continuous or pulse air injection.

5.3.7 Biological Transformation of TCE under IAS Systems

Biological degradation of contaminants is one of main mechanisms for IAS operation. Kinetics of biological processes can be of major practical importance for IAS application when biological transformations of contaminants are very active processes at contaminated sites.

TCE can be microbially degraded under anaerobic conditions by dechlorination processes discussed in Chapter IV and under aerobic conditions by cometabolic transformation reactions. In IAS, since injected air generates aerobic conditions within the zone of IAS influence where remedial processes occur, only cometabolic reactions are considered in IAS modeling of this study. Cometabolic transformations are catalyzed by microbial enzymes and yield no carbon or energy used by the microorganism [Horvath, 1972]. Methanotrophs are the most widely studied bacteria for TCE cometabolism, and the kinetics of the cometabolism has been extensively investigated by many researchers [Alvarez-Cohen and Speitel, 2001].

Among kinetic coefficients for metanotrophic cometabolism of TCE summarized by Alvarez-Cohen and Speitel [2001], as shown in Table 5.9, two cases (low and high bioreaction coefficients) are selected to examine the effect of TCE cometabolism on TCE removal efficiency by IAS systems. Since TCE cometabolism occurs under aerobic conditions, the cometabolism is considered in the region containing gas saturation of greater than 0.001 % in the domain. Cometabolic processes may depend on many parameters such as microorganism population and diversity, concentration of contaminants and nutrients, and temperature. In this study, however, reaction rates of TCE cometabolism depend only on contaminant concentrations under uniform biomass

population in the domain and are expressed by Michaelis-Menten kinetics. As reference cases (or no bioreaction cases), Cases H-1 and H-2, which are already discussed in section 5.3.4, are used here in Table 5.9.

Table 5.9 Scenarios for biological transformations of TCE under IAS systems

Case No.	Michaelis-Menten kinetics [a]		Flow rates (m^3/hr)		Well screen location
	k_B [b] (mg/L d)	K_s (mg/L)	Injection	Extraction	
B-1	0.0012	4.7	20	40	Horizontal injection well: x=25-25.5, y=0-5, z=2.5-3 m Horizontal extraction well: x=25-25.5, y=0-5, z=11.5-12 m
B-2	0.275	19	20	40	
B-3	0.0012	4.7	60	120	
B-4	0.275	19	60	120	
H-1	No bioreaction		20	40	
H-2			60	120	

[a] Michaelis-Menten kinetic coefficients from Alvarez-Cohen and Speitel [2001]
[b] k_B is calculated with a biomass concentration of 5 μg/L.

In Figure 5.23, temporal variations of TCE concentration in IAS (air injection 20 m^3/hr) considering TCE cometabolic processes are given. The comparison of concentration profiles of Case H-1 (no bioreaction) in Figure 5.18 and Case B-1 (low bioreactivity) in Figure 5.23 shows that biological transformations of TCE in Case B-1 help to reduce the contaminant plume development (TCE concentrations), but the reduction in TCE concentration distributions is minor. For Case B-2 in Figure 5.23, the cometabolic processes of TCE have significant effects on the reduction in dissolved TCE concentration. Temporal reduction in TCE concentration for Case B-2 (Q=20 m^3/hr with high bioreactivity) is much greater than that for Case H-2 (Q=60 m^3/hr with no

bioreaction). Stimulating biological processes may contribute to the increase in the remedial capability without causing the spreading of contaminants in the domain. In Cases H-1 and H-2, the increase in air injection flow rate from 20 to 60 m^3/hr helps to raise the capability of IAS in treating contaminant loads. In Figure 5.18, the raised capability is sufficient to block the downstream migration of contaminant plumes but is not effective to reduce the lateral spreading of TCE on x-y plane at z=9 m: In Figure 5.18 (A2) and (B2), the spreading of contaminant plumes in y-direction on x-y plane at z=9 m is similar in both Cases H-1 and H-2. In the both cases, contaminant plumes reach up to about 6 m in y-direction in Figure 5.18 (A2) and (B2). In Figure 5.23, however, high-rate biotransformation of TCE in Case B-2 has significant effects on the reduction in the lateral and vertical spreading of contaminant plumes.

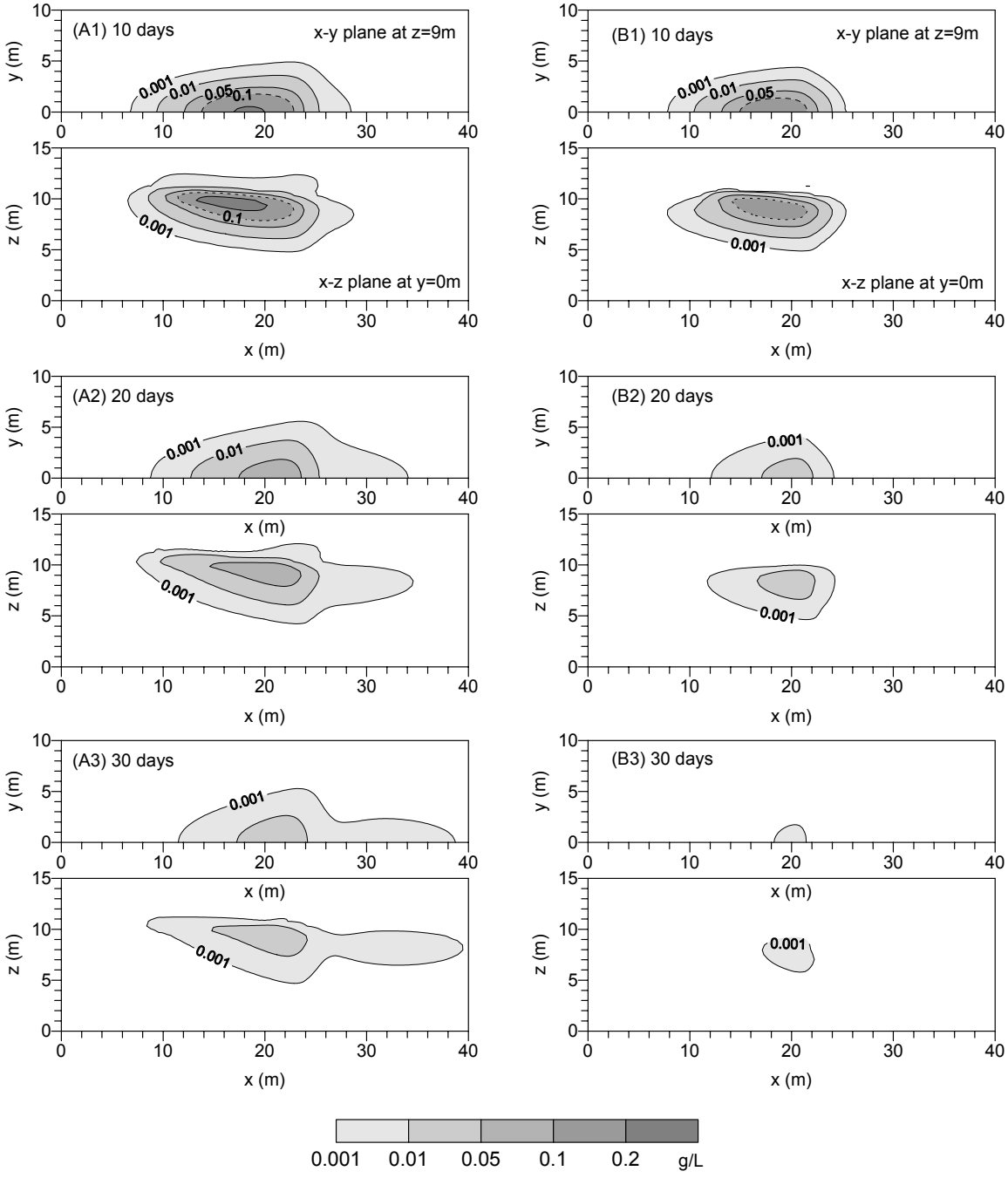

Figure 5.23 TCE concentration profiles in IAS considering TCE cometabolism at air injection rate Q=20 m^3/hr: Bioreaction Case 1 (B-1) and Case 2 (B-2).

In Figure 5.24, the overall TCE removal efficiencies for six cases listed in Table 5.9 are compared. At the air injection rate 20 m^3/hr, the overall efficiencies for Cases H-1, B-1, and B-2 are 93.9, 94.8 and 99.8 %, respectively. Temporal TCE mass reduction profiles for Cases H-1, B-1, and B-2 demonstrate high variability in bioreaction capabilities: At 30 days in Figure 5.24 (a), the contributions of TCE cometabolism on its removal are less than 1% for Case B-1, however, for Case B-2 these reach up to 15 %, which is greater than the contributions of approximately 5 % due to air injection increase from 20 (Case H-1) to 60 m^3/hr (Case H-2) at 30 days. At the injection rate of 60 m^3/hr in Figure 5.24 (b), the effect of biodegradation on TCE removal is significant in Case B-4. The results of Case B-2 and B-4 show that high-rate biological processes could save a remediation time. The simulations conducted in this section show the potential capability of biological processes in IAS under simplified condition used here.

In IAS applications at contaminated sites, the evaluation of the bioreactivity of contaminants including cometabolic processes could be accomplished through detailed field investigations and tests.

(a) Air injection flow rate, 20 m^3/hr

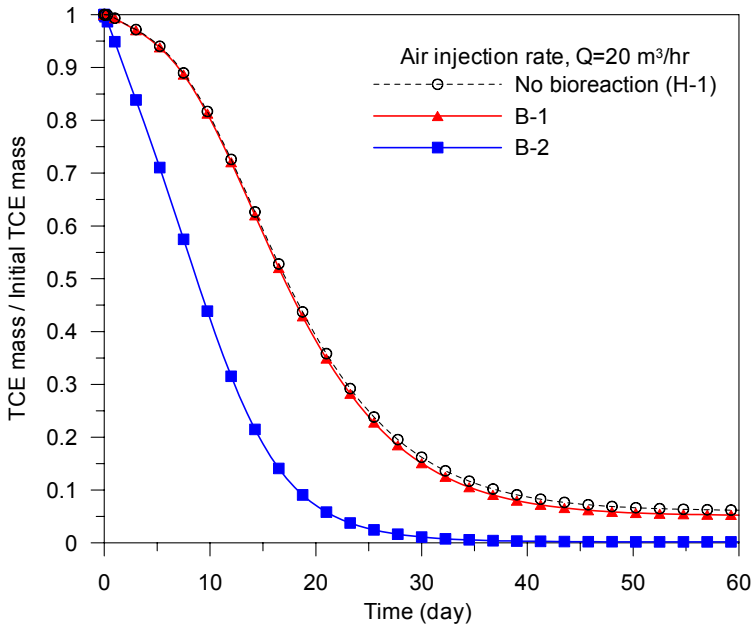

(b) Air injection flow rate, 60 m^3/hr

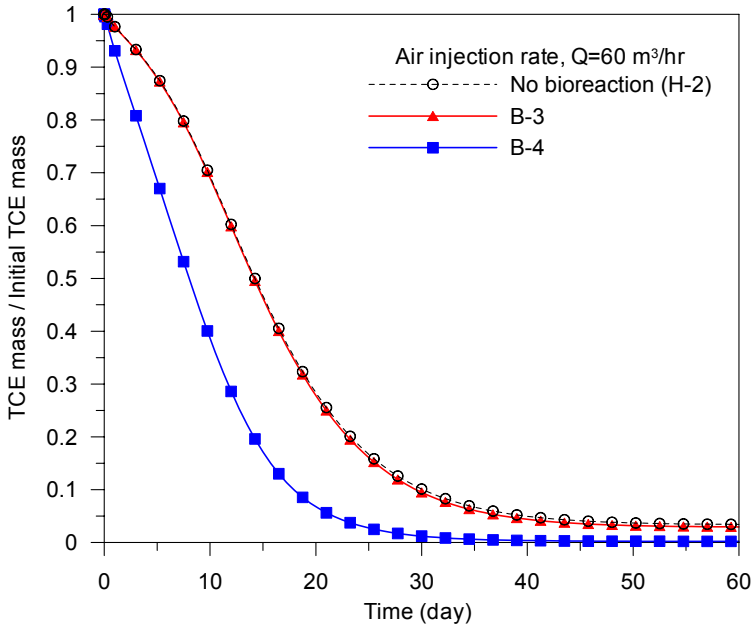

Figure 5.24 Bioreaction effects on TCE removal

5.3.8 Distance between Wells at Multiple Vertical Well Systems

In section 5.3.3, IAS systems with multiple vertical wells have been effective to clean up the groundwater contaminated with TCE. In designing IAS systems, the distance between injection wells is of importance in determining the removal efficiency of contaminants and the cost of IAS systems. The distance between the wells plays a key role in determining the overlapping degree of ROI of two injection wells, the distribution of gas saturation at locations between the two wells, and contaminant removal capacity of IAS depends on the gas-saturation distribution. Optimized distance between injection wells will make the performance of an IAS system to meet remediation criteria at contaminated sites, and will also allow us to save the cost of the IAS system. In this section, the effect of a distance between injection wells on TCE removal is investigated to find out a maximum allowable distance in cleaning up the contaminated groundwater below a target concentration of dissolved TCE, 0.001 g/L, in this study. Three scenarios are considered as listed in Table 5.10: The distances of the three cases are chosen based on ROI results shown in Figure 5.9 and TCE concentration profiles in Case MV-2 (the distance of 5.1 m between injection wells). From ROI results at injection rate 30 m^3/hr shown in Figure 5.9, we can expect that the ROI of two injection wells (No. 1 and 2) for Case W-2 (well-to-well distance = 7.1 m) will be overlapped at approximately 10 % gas saturation (ROI at 10 % gas saturation=3.6 m); For Case W-3, the ROI of each injection well (No. 1 and 2) at Case W-3 (well-to-well distance = 8.1 m) will be overlapped at about 5 % gas saturation (ROI at 5 % gas saturation=4.15 m). For all cases, air is injected continuously, and biological transformations of TCE are not included here.

IAS with multiple injection wells is used to increase the contaminant removal efficiency by remediating the detoured contaminant plumes shown in Figure 5.12 and to reduce air injection rates at each well. The study in this section focuses on gas-saturation distribution and contaminant removal.

Table 5.10 Scenarios for IAS systems with multiple wells

Case No.	Distance* (m)	Well No. 2 (Screen location)			Well No. 1 (Screen location)
		x (m)	y (m)	z (m)	
W-1	6.1	24-24.5	6	Injection well: z=2-3 Extraction well: z=11-12	Injection well: x=25-25.5, y=0, z=2-3 m Extraction well: x=25-25.5, y=0, z=11-12 m Injection rate: 30 m^3/hr Extraction rate: 30 m^3/hr
W-2	7.1	24-24.5	7		
W-3	8.1	24-24.5	8		

*Distance indicates the distance between the centers of injection well No. 1 and No. 2.

In Figure 5.25, the distribution of gas saturation is given for Cases W-1, W-2, and W-3. The overlap of influence zones of two injection wells (Injection well No. 1 and No. 2) happens in the middle of the distance between the wells. As the distance between the wells increases, the overlap of gas saturation becomes less. The degree of gas saturation is an indicator of contaminant remedial capacity at locations. Since contaminant loads (i.e., contaminant concentrations) vary over location and time, in the application of IAS, it is hard to determine the degree of gas saturation, which is sufficient to treat contaminant loads every point in the domain through whole remediation periods. By analyzing the development of contaminant plumes over time in the domain, we can determine whether gas saturation under a specified IAS conditions is enough or not.

For Case W-1, the gas saturation overlaps of two injection wells on x-y plane at z= 9 m are given in Figure 5.25 (A1); the cross-sectional gas saturation profiles between two wells on y-z plane x=24.5 m are presented in Figure 5.25 (A3); and, gas saturation profiles of injection well No. 1 are shown in Figure 5.25 (A2). The gas saturation profiles shown in Figure 5.25 (A3), (B3), and (C3) are useful to identify the variation of gas saturation over depth at the overlapped regions.

In the gas saturation distributions shown in Figure 5.25, the overlapped regions vary for the three cases in Table 5.10. The overlapped regions are located at approximately y=1.3-5, 2.3-5, 3.3-5 m for Cases W-1, W-2, and W-3, respectively on y-z plane x=24.5 m. Those overlapped regions draw our attentions since the regions are the pathway of the detoured contaminant plumes as shown in Figure 5.12. As the distances between injection wells increase, gas saturation levels in the overlapped regions decrease and the sizes of the overlapped regions become smaller. In Figure 5.25 (A1), (B1), and (C1), the gas saturation levels in the middle of the distance between two wells are at approximately 10-20, 10-15, and 5-10 % for Cases W-1, W-2, and W-3, respectively on x-y plane z=9 m. In Figure 5.25 (A3), (B3), and (C3), the vertical profiles of overlapped gas saturation at z=6-9.5 m in the middle of the distance between two wells are at approximately 10-20, 1-15, and 0.1-8.5 % for Cases W-1, W-2, and W-3, respectively on y-z plane x=24.5 m.

The effectiveness of the three cases (Cases W-1, W-2, and W-3) can be evaluated based on the removal and spreading of TCE. Concentration profiles of dissolved TCE for Case W-2 and W-3 are compared in Figure 5.26. The both cases are successful to reduce dissolved TCE below its concentration of 0.001 g/L on x-z plane at y=0 m. At x-y plane

at z=9 m, Case W-2 is successful to achieve the target TCE concentration, but Case W-3 fails: In Figure 5.26 (B4) and (B6) for Case W-3, some portion of the contaminated groundwater penetrates the gas saturation zones overlapped by two injection wells and leaves the zones downstream as the incompletely-treated groundwater. This indicates that the degree of gas saturation in the overlapped zone of Case W-3 is not sufficient for IAS systems to remove dissolved TCE below its target concentration (0.001 g/L). In Figure 5.25 (B1) for Case W-2, the gas saturation at the center of the overlapped region on x-y plane at z=9 m is approximately 15 %, and in Figure 5.25 (C1) for Case W-3, the gas saturation at the center point is less than 10 %. In this study, if multiple injection vertical wells are used under the flow rate and layout conditions given in Table 5.10, the maximum allowable distance between injection wells is approximately 7 m to achieve the specified remediation goal (dissolved TCE < 0.001 g/L).

In deciding the distance between injection wells, we may use gas saturation distributions and ROI profiles of each injection well, shown in Figures 5.8 and 5.9 (b), respectively: ROI profiles at different gas saturation levels will be useful to predict effective ROI at different contaminant concentrations. Gas saturation distributions within the zone of IAS influence can be used to estimate an approximate remedial capacity of each injection well. A multi-injection-well IAS system is a combination of single-injection-well IAS systems. Gas distribution data around single injection well will allow us to estimate the distributions of gas saturation at the overlapped regions between injection wells in multi-injection-well IAS systems. The gas saturation distributions at the overlapped regions will vary with distances between injection wells, injection rates, injection depths, and geological conditions in subsurface systems. Usually, as

contaminant concentrations are different over locations, the required gas saturation levels will change over location in successfully completing a target remediation goal. Furthermore, under heterogeneous subsurface environments at contaminated sites, the prediction of gas saturation distribution between wells would be much more difficult. The simulation results (gas saturation distributions and contaminant plume developments) of the three cases given in Figures 5.25 and 5.26 may be used to enhance our understandings on multiple-injection-well IAS systems and to demonstrate the diversion problems of contaminant plumes in the systems.

The temporal variations in overall removal efficiencies of the three cases are presented in Figure 5.27. These efficiencies do not show significant difference: At 60 days, these are 96.9, 95.1, and 92.9 % for Case W-1, W-2, and W-3, respectively. The difference in contaminant removal efficiency between Cases W-2 and W-3 produces after 15 day in Figure 5.27. That difference may result mostly from the detoured contaminant plumes of Case W-3 shown in Figure 5.26 (B4) and (B6).

(a) Case W-1

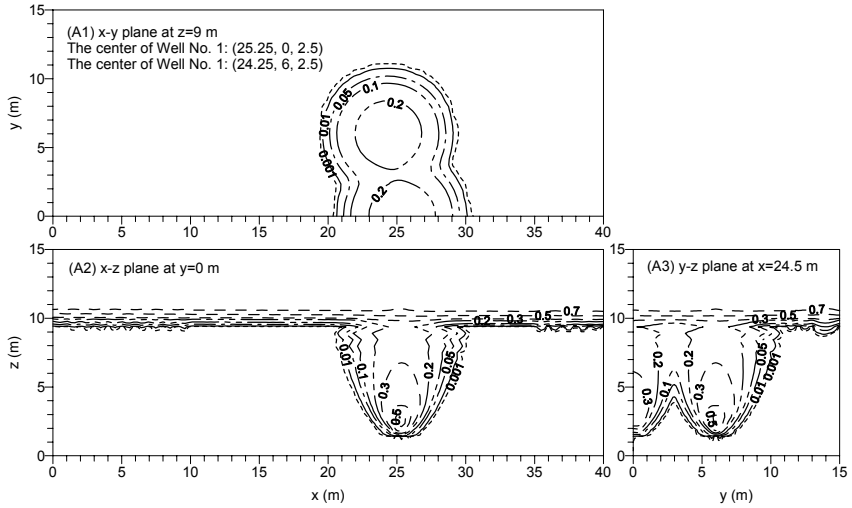

(b) Case W-2

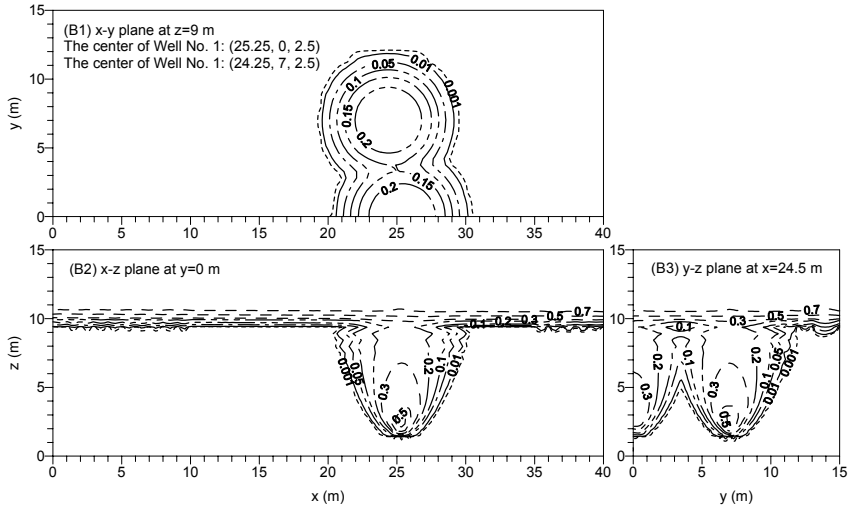

(C) Case W-3

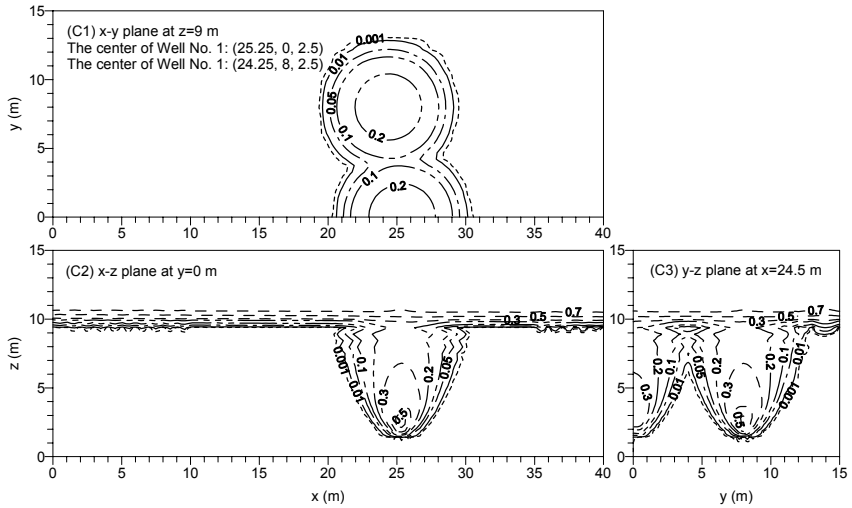

Figure 5.25 Gas saturation distributions at IAS systems with multiple wells

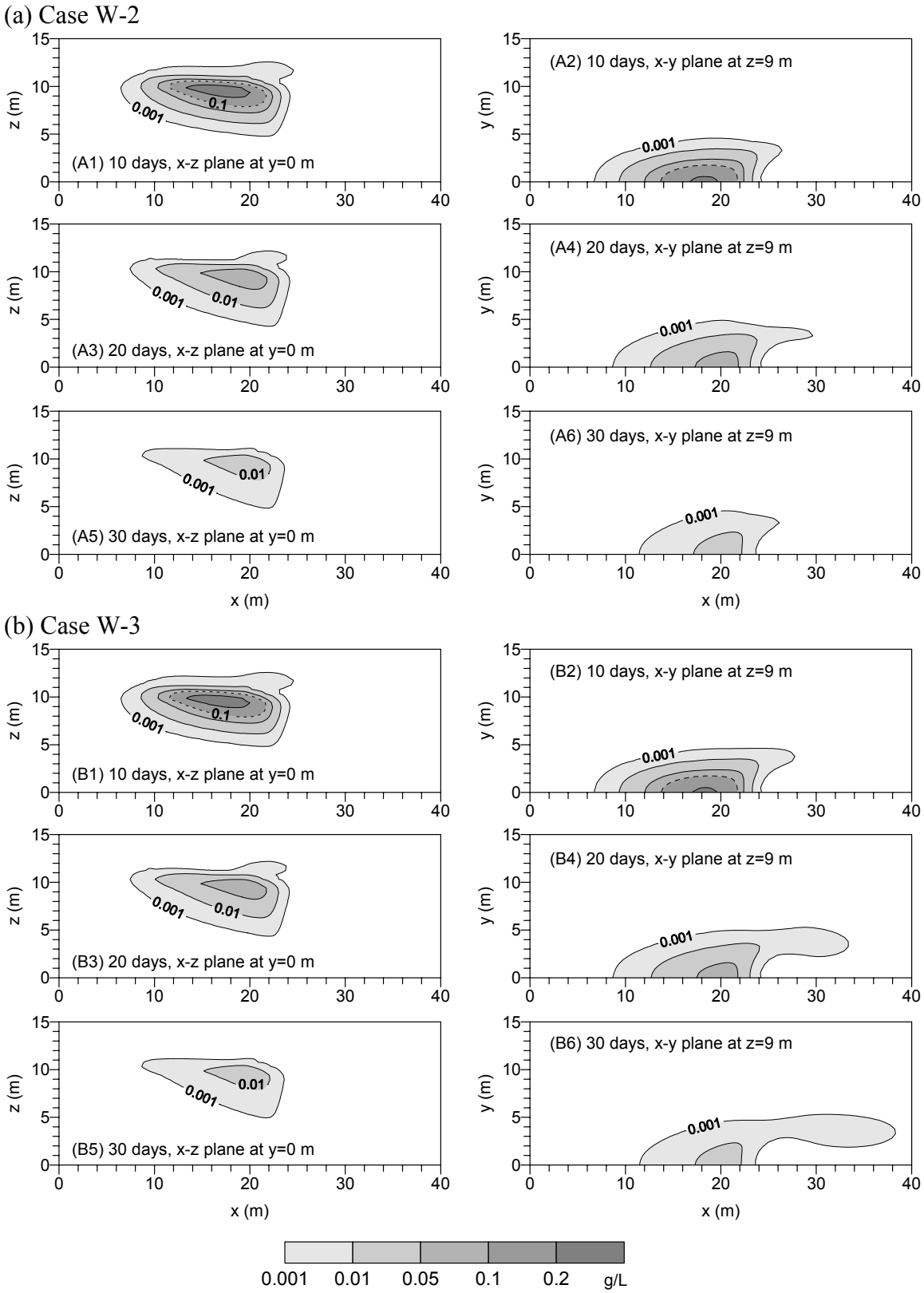

Figure 5.26 Concentration profiles of dissolved TCE at Cases W-2 and W-3

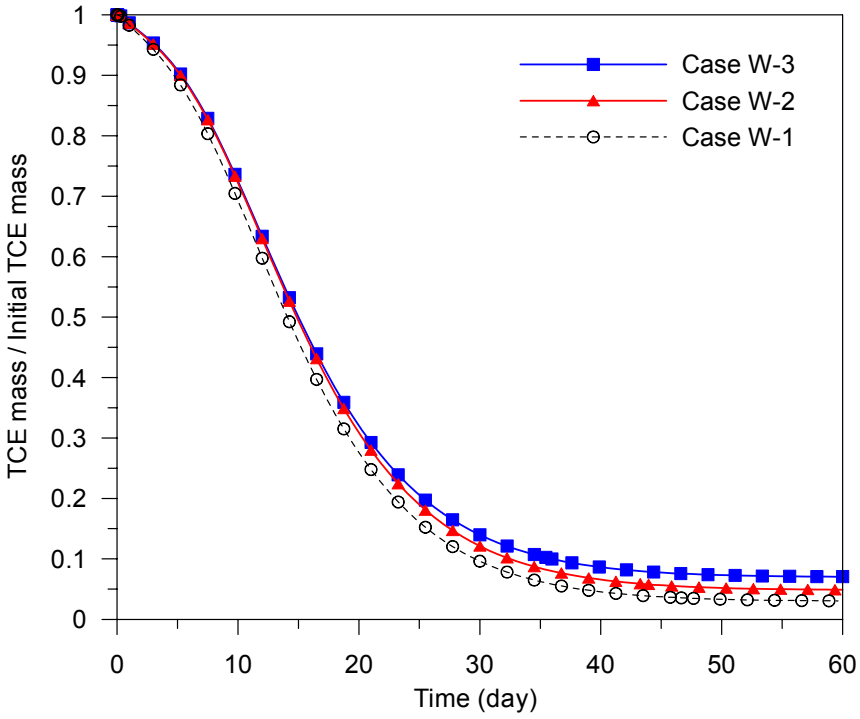

Figure 5.27 Reduction in TCE mass over time for Cases W-1, W-2, and W-3

5.4 Summary

In this chapter, the flow of gas and groundwater as a multiphase flow was investigated under IAS with vertical or horizontal wells, and the spreading of contaminant plumes and the removal efficiency of TCE by IAS operations were analyzed. TechFlow^{MP} model developed here was successfully verified using gas injection/extraction problems in the unsaturated zone and air sparging simulation data reported by van Dijke et al. [1995]. Under specified conditions including initial contaminant distributions and hydrogeological parameters used herein, many scenarios for IAS systems were simulated to evaluate remedial performance of the systems in terms of several IAS-related factors, such as injection well types (vertical-type vs. horizontal-type), flow rates, injection well depths, injection methods (continuous vs. pulse), and biological transformations. From the results of the simulations conducted herein, the followings can be summarized:

(i) In the study on the flow of gas and the groundwater under single-injection-well IAS, the increase in air injection flow rates leaded to the increase in the radius of IAS influence (or the size of the cone of IAS influence) and gas saturation level within the cone. The increase in gas saturation in the initially saturated zone accelerated the upward gas flow in the zone. Regardless of injection rates, gas volume stored in the cone was stabilized after its sharp linear increase during approximately 15 minutes. As injected air replaces pore water in soil matrix below the groundwater table, the air caused to reduce velocities of the groundwater flow and to divert some portion of the groundwater around the zone

of IAS influence. The reduction in the groundwater velocities was proportional to air injection rates (or gas saturation levels). In this study, since a homogeneous medium is used, the flow of groundwater and injected air through porous media did not show preferential pathways. However, if heterogeneous or stratified media are present in the domain, the flow may show different patterns.

(ii) In the simulations conduced here for IAS systems with one vertical injection well, the increase in injection flow rates helped to raise the removal efficiency of TCE: At injection rates of greater than 20 m^3/hr, the IAS systems were good enough to clean up contaminant plumes close to an injection well. Due to the diversion of contaminant plumes around an injection well, however, the systems were not successful to remove TCE below a concentration of 0.001 g/L through the whole contaminant plumes.

(iii) In the simulations carried out here for IAS systems with multiple vertical wells, the systems were successful to capture the detoured contaminant plumes generated around injection wells and helped to raise contaminant removal efficiency by IAS. In this study, the distance between injection wells determined the overlapped regions of the influence zones of the wells and the degree of gas saturation in the regions. Thus, the distance played a key role in determining the success of IAS systems with multiple vertical wells in capturing the detoured contaminant plumes. In IAS modeling of this study, at the distance between injection wells $\geq$ 7 m, the IAS systems with multiple vertical wells remediated

polluted groundwater below a dissolved TCE concentration of 0.001 g/L and showed high removal efficiency more than 95 %. The results of simulations conducted for multiple-injection-well IAS suggested that, under the modeling conditions used here, IAS systems with multiple injection wells having small injection rates are superior over IAS systems with one injection well having a large injection rate. Of course, at contaminated sites, the remedial performance of each IAS system will vary upon contaminant concentrations and site conditions.

(iv) Under air injection conditions used for vertical and horizontal wells in this study, air injection through a horizontal well generated wider influence zone than that through a vertical well. The horizontal-well air injection also produced relatively uniform gas saturation on wide *y*-*z* plane along with a horizontal injection well in *x*-direction. At the same injection rate used here, the velocities of air flow released from well screens were much smaller in the horizontal-well air injection than in the vertical-well air injection. That may reduce a diversion of the groundwater flow in the vicinity of injection wells for horizontal-well systems. The IAS systems with a horizontal well fully covered all contaminant plumes, but, at a low flow rate (20 m^3/hr), the contaminant removal by the systems failed to decrease dissolved TCE concentration below 0.001 g/L at some high-concentration plumes. At a high flow rate (60 m^3/hr), the remediation performance of the systems was sufficient to achieve our remedial goal. In this study, air injection rates for the horizontal wells will be determined by the ratio of contaminant loads to required air volumes at the highest-concentration zones within the contaminant plumes.

(v) The depth of injection wells should be deep enough to avoid a diversion of contaminated groundwater plumes below air injection wells. In this study, when the top of injection well screens is deeper about 3 m than the deepest point of the contaminant plumes, the diversion did not occur. The required distance between injection points and contaminated plumes will vary over air injection rates applied.

(vi) For modeling for pulse IAS in this study, a pulse-air-injection method was successful when injection flow rates are sufficient (60 m^3/hr at one horizontal well). If an injection rate is not enough (20 m^3/hr at one horizontal well), the remedial efficiency of pulse IAS was worse than that of continuous IAS. However, the injection rate is sufficient, the overall efficiency of pulse IAS was better than that of continuous IAS at the same flow rate.

(vii) Michaelis-Menten kinetics was used to describe an aerobic cometabolism of TCE. In IAS modeling of this study, the effect of biological transformations on the remedial efficiency of IAS systems was highly variable according to the bioreactivity of a contaminant. In a case that biodegradation of TCE is high, the cometabolic transformation contributed to enhancing the removal efficiency of IAS systems: At that case, the efficiency reached more than 99 % at a low injection rate 20 m^3/hr. However, at low bioreactivity, the contribution of TCE cometabolism to TCE removal was minor. The four scenarios conducted here

demonstrated the potential capability of bioreactions on contaminant removal. At contaminated sites, the potential may be evaluated through site-specified investigations.

(viii) Dimensionless variables representing injection rates, ROI, and contaminant concentrations in modeling systems were defined and used under limited simulation cases in this study. Under various modeling conditions including different injection-screen areas, injection depths, and intrinsic permeabilities, those dimensionless variables will be very useful in characterizing the relationships between air injection rates and ROI under IAS. Those dimensionless variables may be used to predict the remedial potential of each gas saturation level in the initially saturated zone under specific conditions, but, we need to note that there are complexly-coupled nonlinear relationships between gas saturation levels and contaminant removal rates in whole modeling domains.

CHAPTER VI

THERMAL-ENHANCED VENTING

Thermal-enhanced venting (TEV) uses heated air to remove a nonaqueous phase liquid (NAPL) from contaminated soils in the unsaturated zone. Due to heated air injection into the zone, the temperature of the injection zone in the subsurface increases as a function of time. In these applications, heat transfer in porous media as well as gas flow and multiphase contaminant transport in subsurface systems should be considered. In this chapter, governing equations for heat energy transport in a porous medium are developed and solved along with the contaminant transport equations described earlier. Using TEV experimental data published in the literature, TechFlow^{MP} is validated for heat transport in a porous medium, and, based on the results of several TEV applications, the effect and efficiency of TEV on NAPL contaminant removal is investigated.

6.1 Introduction

TEV is different from traditional soil venting because heated air instead of air at ambient conditions is applied to the contaminated zone. Due to the application of heated air at the contamination zone, the temperature will increase in this zone and this in turn will raise the evaporation rates of residual NAPL contaminants. Therefore, TEV is a suitable method to enhance removal or recovery of medium- or less-volatile residual hydrocarbon contaminants in the unsaturated zone [Kaluarachchi and Islam, 1995]. A schematic of TEV is shown in Figure 6.1.

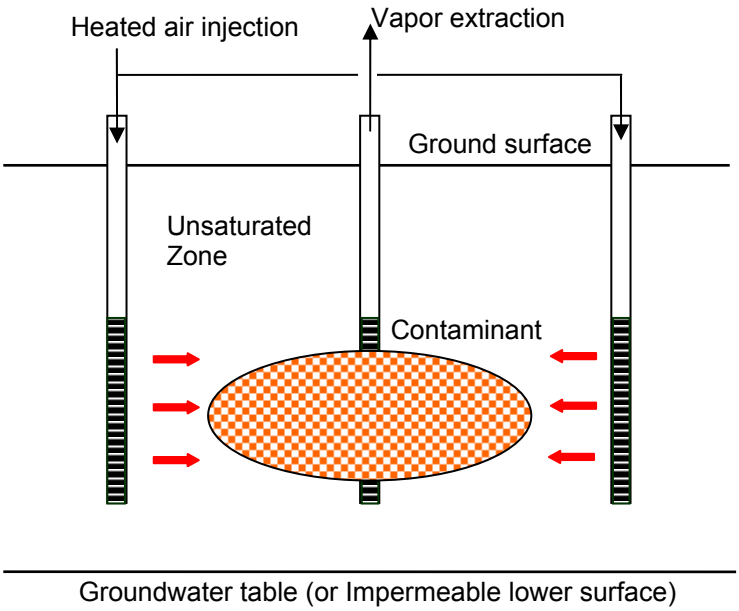

Figure 6.1 Schematic of a thermal-enhanced venting system.

Contaminated subsurface environments include the following phases: water, gas, soil, and NAPL. The physicochemical and thermal properties of each phase including thermal conductivity and heat capacity are dependent on temperature. Density and viscosity of gas phase, and vapor pressure of VOCs are significantly influenced by the variation in temperature. In Figure 6.2, the change in vapor pressure of TCE as a function of temperature is given.

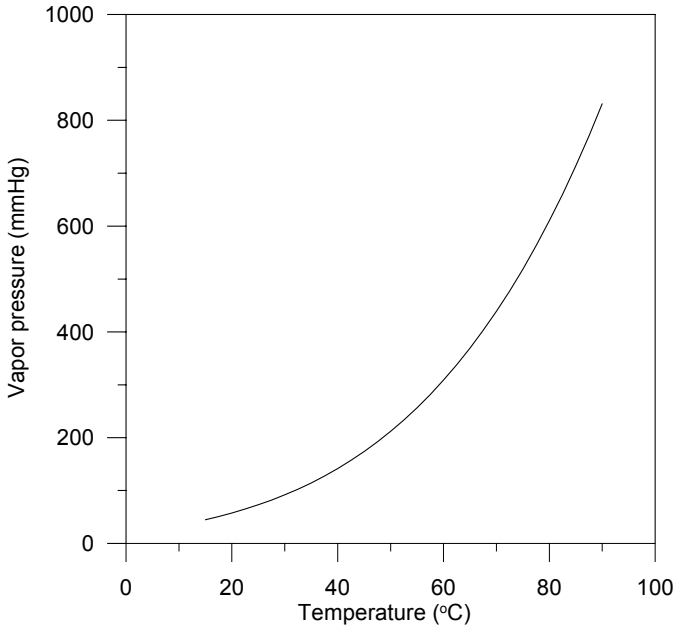

Figure 6.2 Vapor pressure of TCE

In this chapter, heat energy transport equations are developed to describe temperature variations due to heated air injection, water vaporization/condensation, and contaminant vaporization from NAPL to gas phase. Under non-isothermal conditions, the changes in temperature-dependent properties of gas and contaminants are considered in gas flow and contaminant transport in subsurface environments. In the unsaturated zone, since the velocity of soil water is very small, water phase is assumed to be stationary. In applications of TEV in this chapter, flow of gas phase, saturation changes of NAPL and water phases, and transport of contaminants in gas phase are considered. The change in saturation of water phase occurs due to evaporation or condensation, and the reduction in NAPL saturation results from vaporization of contaminants. TCE is a target contaminant in NAPL and gas phase.

The purpose of this study is to investigate heat transport in porous soil matrix and to evaluate the performance of TEV systems in removing residual TCE NAPL in

unsaturated subsurface environments. Two main parameters are considered: air injection flow rates and relative humidity (or water vapor density) in injected air. Air flow rates determine gas velocity in a porous medium. Water vapor (steam) is very effective in carrying heat energy due to heat capacity of water vapor (approximately 4 kJ/kg ^{o}C) and heat of evaporation (more than 2000 kJ/kg ^{o}C).

6.2 Heat Energy Transport Equation

In the subsurface, heat energy transport occurs by conductive and convective heat fluxes. Conductive heat flux in soil matrix depends in a complex fashion on properties of multiple phases (solid, water, gas, and NAPL), and convective heat flux is generated mainly by gas phase flow. In this study, heat energy transport is analyzed under the assumption of local thermal equilibrium between all phases and parallel heat conduction. The governing equation for the conservation of heat energy can be written as [Glascoe et al., 1999]

$$\begin{aligned}&(1-\phi)\frac{\partial}{\partial t}(\rho_s h_s)+\frac{\partial}{\partial t}\left(\sum_{f=w,g,n}\phi s_f \rho_f h_f\right)+\frac{\partial}{\partial t}(\phi s_g \rho_v h_v)+\frac{\partial}{\partial t}(\phi s_g \rho_o h_o)\\&+\nabla\cdot(q_g \rho_g h_g)+\nabla\cdot(J_v h_v)+\nabla\cdot(J_o h_o)\\&-\nabla\cdot(K_A \nabla T)+Q_S=0\end{aligned} \tag{6.1}$$

where h_f is specific enthalpy of phases (subscript s = solid soil, w = liquid water, n = NAPL, g = air in gas, v = water vapor, and o = organic chemical vapor) (J/kg); s is saturation of phases; ρ_v and ρ_o are densities of water vapor (water vapor concentration in gas phase) and organic vapor (contaminant concentration in gas phase) (kg/m^3), respectively; q_g are Darcy velocity of gas phase (m/s); J_v and J_o are the flux of water

vapor and organic vapor in gas phase ($kg/m^2/s$), respectively; K_A is an overall thermal conductivity ($W/m/K$); T is absolute temperature (K); and, Q_S is heat source/sink per unit volume due to heated air injection/extraction ($J/m^3/s$). The first two terms represent the enthalpy accumulation in solid soil and fluid phases (liquid water, air in gas, and NAPL). The third and fourth terms are the enthalpy accumulation for water vapor and organic chemical vapor, respectively: These terms include heat transfer due to condensation/evaporation of water and vaporization of organic chemicals. The fifth term represents a flux of air enthalpy. The sixth and seventh terms are for fluxes of water vapor enthalpy and organic vapor enthalpy, respectively. The seventh term indicates multiphase thermal conduction.

Specific enthalpies can be expressed as linear functions of temperature and the respective specific heat capacities [Glascoe et al., 1999]:

$$h_s = c_s\left(T - T_{ref}\right) \tag{6.2a}$$

$$h_w = c_w\left(T - T_{ref}\right) \tag{6.2b}$$

$$h_g = c_g\left(T - T_{ref}\right) \tag{6.2c}$$

$$h_n = c_n\left(T - T_{ref}\right) \tag{6.2d}$$

$$h_v = h_{Lat,water} + c_v\left(T - T_{ref}\right) \tag{6.2e}$$

$$h_o = h_{Lat,organic} + c_o\left(T - T_{ref}\right) \tag{6.2f}$$

where c is specific heat capacity ($J/kg/K$) for each component; $h_{Lat,water}$ and $h_{Lat,organic}$ are specific enthalpies of vaporization of water and an organic chemical, respectively; and, T_{ref} is a reference absolute temperature. Since enthalpy is a relative quantity, T_{ref}

can be any temperature (for example, 0 ^{o}C) as long as the temperature value is used consistently in all heat calculations.

Mass flux of two components (water vapor and organic vapor) in gas phase can be represented by advection and dispersion. The flux terms in Equation (6.1) will be expressed as,

$$J_v = q_g \rho_v - \theta_g D_v \nabla \rho_v \tag{6.3a}$$

$$J_o = q_g \rho_o - \theta_g D_o \nabla \rho_o \tag{6.3b}$$

where D_v and D_o are dispersion coefficients for water vapor and organic vapor in gas phase, respectively. Dispersion coefficients can be calculated by Equation (3.21).

Combining Equations (6.1) through (6.3) yields the following heat transport equation:

$$\begin{aligned} &\frac{\partial}{\partial t}\left[S_h\left(T - T_{ref}\right) + \phi s_g \rho_v h_v + \phi s_g \rho_o h_o\right] + \\ &+ \nabla \cdot q_g \left[\rho_g \left(T - T_{ref}\right) + \rho_v h_v + \rho_o h_o\right] + \nabla \cdot \left[\phi s_g D_v \nabla\left(\rho_v h_v\right) + \phi s_g D_o \nabla\left(\rho_o h_o\right)\right] \\ &- \nabla \cdot \left(K_A \nabla T\right) + Q_S = 0 \end{aligned} \tag{6.4}$$

where S_h is an overall heat capacity ($J/m^3/K$). In multiphase systems, volume-averaged overall heat capacity under thermodynamic equilibrium can be estimated as follows [Bear, 1972; Kaluarachchi and Islam, 1995; Kaviany, 1995; Nield and Bejan, 1999]:

$$S_h = \left(1 - \phi\right)\rho_s c_s + \phi \sum_{f=w,g,n} s_f \rho_f c_f \tag{6.5}$$

In TEV systems, since gas flows are derived by injection and extraction pressures, advective transport of water vapor and organic vapor in gas phase would be much greater than dispersive transport of these components. Thus, the heat transport terms for

dispersion (the terms in the third square bracket in Equation (6.4)) may be neglected and are not considered in this study.

The overall (effective) thermal conductivity, K_A, in Equation (6.4) depends on several parameters, such as soil-grain thermal conductivity, a water thermal conductivity, a gas thermal conductivity, a NAPL thermal conductivity, porosity, saturation of phases, and geometry of media [Nield and Bejan, 1999]. One of the methods to calculate overall thermal conductivity of porous media is a simple parallel conduction model. In the model, heat conduction in a soil matrix (including solid and fluid phases) is assumed to occur in parallel, and overall conductivity, K_A, is obtained as a weighted arithmetic mean of the conductivities of phases as follows [Bear, 1972; Nield and Bejan, 1999].

$$K_A = (1-\phi)K_s + \phi \sum_{f=w,g,n} s_f K_f \tag{6.6}$$

where K_f is heat conductivity of each phase ($W/m/K$), and subscript f indicates solid soil (s), water (w), gas (g), and NAPL (n) phases. The parallel method has been commonly used in nonisothermal subsurface simulations [Falta et al., 1992; Adenekan et al., 1993; Kaluarachchi and Islam, 1995]. In Equation (6.6), overall thermal conductivity is dominated by thermal conductivity of soil (rock), followed by that of liquids. Gas has a least effect on the overall conductivity, and the effect is negligible; thermal conductivity of a liquid is 10-100 times larger than that of a gas [Adenekan et al., 1993].

Since the contribution of radiation on heat transport is very small in the subsurface [Kaluarachchi and Islam, 1995], the effect of radiation is ignored. Although heat may be regained by condensation of contaminant vapor, it is not considered here.

6.3 Model Verification: Thermal Venting in a One-dimensional Soil Column

For TEV, Lingineni and Dhir [1992] conducted one-dimensional column experiments to investigate the effect of heat application on the removal of ethanol in a glass bead-filled column. The experiment column is vertically 60-cm long with a square cross section with a width of 18 cm. Heat was supplied directly to soil media and incoming air by a resistance heater. Two cases of soil venting experiments were carried out: air injection at ambient conditions (Case I) and air injection with a heat source (Case II). In the experiments, temperature variations were measured through the column. The published temperature profiles of the two cases are used to verify TechFlow^{MP} model developed in this study.

The initial temperature and residual saturation of ethyl alcohol in the column were 23 ^{o}C and 13 %, respectively. In Case I, air at ambient conditions was injected at a flow rate of 234 L/min. In Case II, a resistance heater with a heat input of 130 W was installed at the inlet of the column in order to heat porous media in the column and air injected at a flow rate of 140 L/min.

In this study, in order to simulate the experiments of Lingineni and Dhir [1992], an one-dimensional domain with 60-cm length is used, which is discretized with a uniform mesh size of 1 cm. Parameters used here are: porosity ϕ = 0.4, a first order coefficient for ethanol evaporation λ_v= 13 s^{-1}, thermal conductivity of a medium in the column = 1.4 W/m/K, and heat storage capacity of the medium = 2.3×10^6 J/m^3/K. Enthalpy of ethanol evaporation $h_{ethanol}$ is calculated using the following regression equation given by Yaws [1999]:

$$h_{ethanol} = 1.984 \times 10^3 \left(1 - T / 516.25\right)^{0.079} \quad (6.7)$$

In the simulations, the equations for gas flow, ethanol saturation, contaminant transport in gas phase, and heat energy transport are solved. The run time is up to 1500 sec with a constant time step of 1 sec. Local thermal equilibrium is assumed throughout the experimental column.

In Cases I, latent heat of ethanol evaporation in the column is absorbed from the injected air and the packed media in the column: Under no heat source (no heater), thermal energy of the injected air and the packed media at an ambient temperature is consumed by ethanol evaporation. So, the vaporization of ethanol results in temperature drops of the injected air and porous media in the column. In Figure 6.3, the measured temperature profiles of the injected air (or the packed media) in the column are given: At 1500 sec, the measured maximum temperature drop of the injected air is approximately 32 ^{o}C. Simulation results of this study for Case I are compared with the published experimental data of Lingineni and Dhir [1992] in Figure 6.3. Overall, the experimental data and the numerical results of this study show good agreement. Lingineni and Dhir [1992] stated that the location of the lowest temperature in the column at each time step indicates the evaporation front of ethanol. The lowest-temperature location in the column moves from the inlet (distance=0 m) towards the exit (distance = 0.6 m) over time. Since thermal energy delivered to the evaporation front by the flowing gas (air) becomes less with the movement of the evaporation front toward the exit because some portion of thermal energy of the injected gas is consumed to heat the media in the column before the gas reaches the evaporation front. Therefore, as the evaporation front in the column moves toward the exit, the temperature of the column (Temperature of the injected

gas/the packed media) at the evaporation front becomes lower. In Figure 6.3, the temperature drop at the evaporation front at 500 sec is much smaller in the simulation results of this study than in the experimental data. The simulation results show good agreement with the experimental data around the evaporation fronts, especially, downstream from the evaporation fronts.

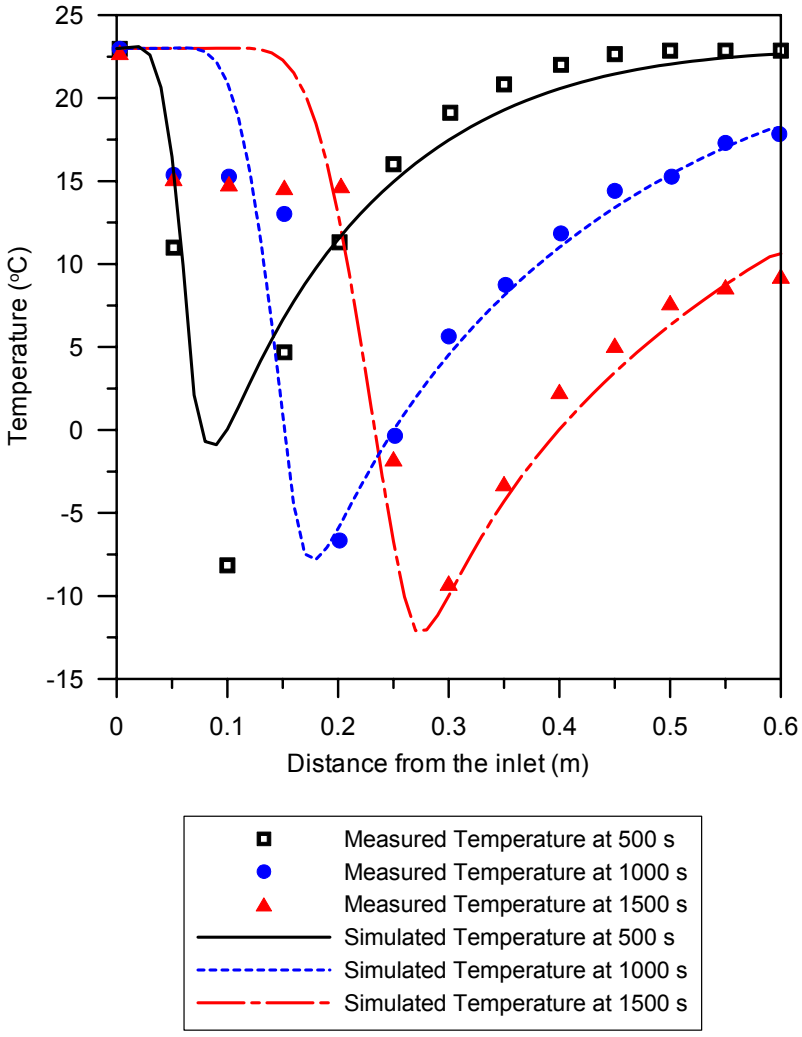

Figure 6.3 A comparison of temperature profiles between experimental data and simulation results for Case I (Air injection experiments without a heat source), Q=234 L/min.

In Case II, thermal energy is provided by a resistance heater at the inlet of the column, and the energy is transported through conduction and convection processes. The propagation of heat energy due to convection mostly depends on gas flow, and, since heat propagation by conduction in the column is very slow, the heating of the packed medium downstream of the inlet region is primary due to thermal energy delivered by heated gas [Lingineni and Dhir, 1992]. The convective heat transfer of gas phase also helps raise the temperature at ethanol-evaporation fronts. The lowest temperature of about -1 ^{o}C in Figure 6.4 (Case II) is higher than the lowest temperature of approximately -9 ^{o}C in Figure 6.3 (Case I). In Figure 6.4 for Case II, the simulation results of this study show good agreement with the experiment data of Lingineni and Dhir [1992]. In Case II, due to heat supply by a resistant heater, the temperature in the inlet of the column reaches more than 80 ^{o}C. The temperature drops due to ethanol evaporation in the column are much smaller in Case II than in Case I.

In Figure 6.4, the experimental data between distances from 0.12 to 0.18 m at t = 1500 sec show somewhat horizontal temperature profiles, which are not observed at the simulation results of this study. Lingineni and Dhir [1992] pointed out that the left-side end of the horizontal temperature profiles indicates the propagation of thermal fronts, at which the temperature becomes above the ambient temperature due to heat energy supplied at the inlet of the column. The propagation of thermal fronts primarily depends on the ratio of energy contents of air and soil and air injection rates [Lingineni and Dhir, 1992]: Increasing the heat input at the inlet of the column will raise the temperature of the incoming ambient air passing through the heater, but the contribution of the heated air to the propagation of thermal fronts will be minor.

One of the methods to increase the ratio of energy contents of air and soil is to use humidified air (the mixture of dry air and steam). As discussed in Chapter II, the heat capacity of steam, which is four times that of air, and heat of water evaporation will contribute to the increase in convective heat transfer rates. In the following section including TEV simulations of this study, humidified air is used to effectively transport thermal energy from air injection points to contaminated zones through porous media.

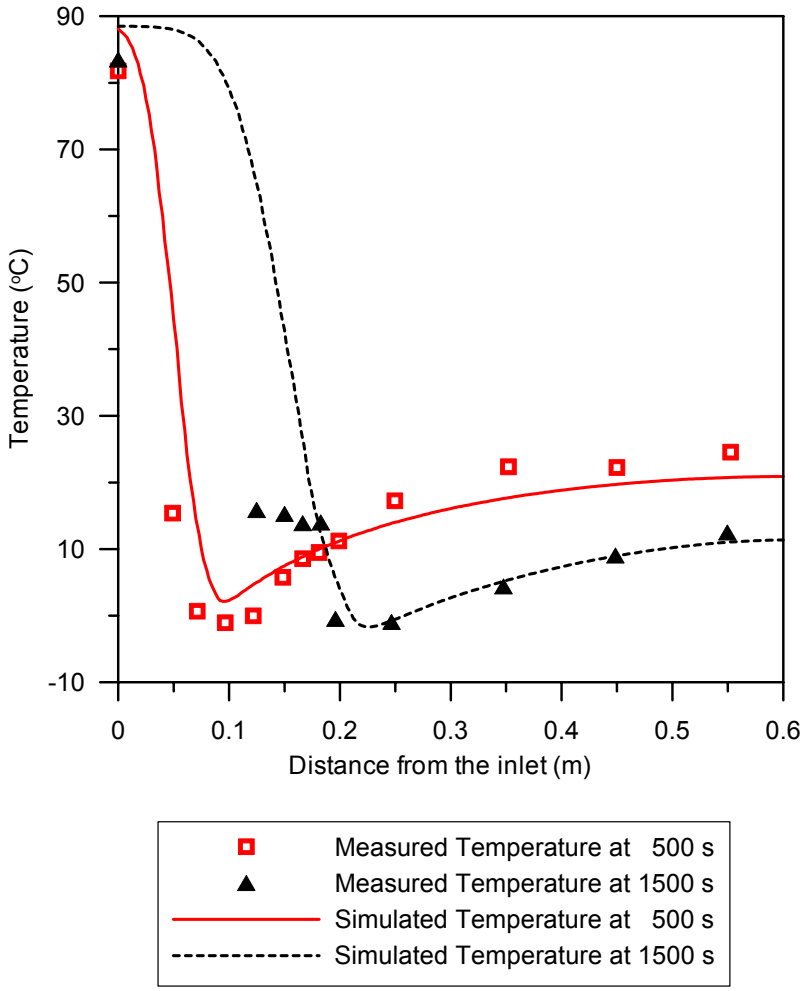

Figure 6.4 A comparison of temperature profiles between experimental data and simulation results of this study for Case II (Air injection experiments with a heat source), Q=140 L/min.

6.4 Application of Thermal-Enhanced Venting

6.4.1 Modeling Domain and Parameters

A two-dimensional unsaturated domain shown in Figure 6.5 is used in TEV modeling of this study to investigate the effect of TEV on NAPL contaminant removal and the transport of thermal energy in subsurface environments. In a TEV system shown in Figure 6.1, which describes a contaminated region containing NAPL between injection and extraction wells, heated humid air is injected into the unsaturated zone at the bottom (the inlet) of the domain, and contaminated gas (the mixture of air, water vapor, and vaporized TCE) is withdrawn from the top (the exit) by vapor extraction systems. While heated air travels from the inlet to the exit, a contaminant as NAPL phase partitions into gas phase, and then the contaminant in gas phase is removed out of subsurface systems.

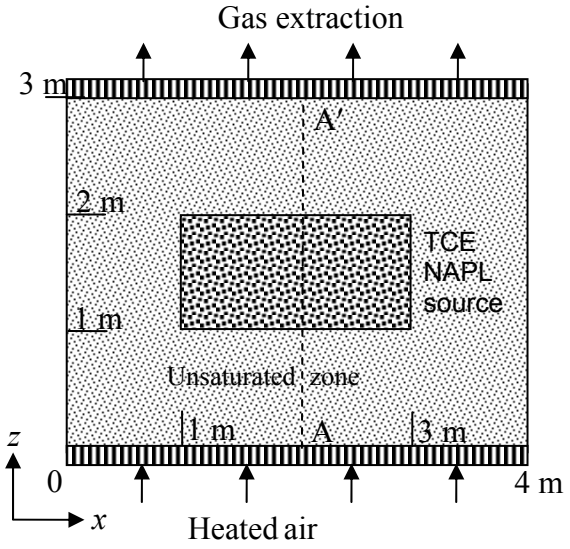

Figure 6.5 A model domain for TEV modeling

In Figure 6.5, TCE, as an immobilized NAPL contaminant source in pore spaces, is located at x = 1-3 m and z = 1-2 m in the unsaturated zone. The initial saturation of TCE residual is 10 %.

In Figure 6.5, boundary conditions for gas flow equation are as follows: specified pressure-head gradient conditions (type II) are assigned at the bottom and the top boundaries for injection and extraction wells (z=0 and 3 m, respectively), and no flux condition is given at the left- and right-hand side boundaries (x=0 and 4 m). For contaminant transport in gas phase, initial and boundary conditions are: an initial TCE concentration in gas phase is zero within the domain; the injected air contains no TCE; and, zero-dispersive flux (type II) on all boundaries. For heat transport, initial temperature of the domain is 10 ^{o}C. Since heated air at constant temperature of 80 ^{o}C is injected into the domain, total heat-energy flux (Cauchy or type III) is used at the inlet boundary (z = 0 m), and a specified heat-energy flux (type II) is used at the outlet boundary (z = 3 m). These heat boundary conditions were also used by Kaluarachchi and Islam [1995].

The properties of a soil medium in the domain are: intrinsic permeability k = 5.0×10^{-11} m^2, porosity $\phi = 0.35$, bulk density of soil matrix = 1600 kg/m^3, residual water saturation $s_m = 0$, longitudinal dispersivity $\alpha_L = 0.1$, transverse dispersivity $\alpha_T = 0.001$, coefficients for $P_c - s - k_r$ relationships of van Genuchten model (Equations (2.8) and (2.9)) $n = 2$, and $\alpha_{gw} = 3\,\text{m}^{-1}$. The molecular diffusion coefficients of TCE and water vapor in gas phase are 7.87×10^{-6} and 2.33×10^{-5} m^2/s, respectively. The first-order mass transfer coefficients for vaporization of TCE and water are 0.01 and 0.001 s^{-1}, respectively. The temperature-dependent properties of TCE and air in gas phase are

estimated using regression equations listed in Table 6.1. Thermal conductivity of soil particles is 0.48 W/m/K, and the regression equations for other thermal properties used herein are presented in Table 6.2.

In TEV simulations, a system of decoupled equations for gas flow, saturation of liquid water and TCE NAPL, transport of TCE and water vapor in gas phase, and heat transport in porous media are sequentially solved and iterated until the solutions of all equations converge within specified criteria. The criteria (ε_a and ε_r in Equations (3.41)-(3.42)) are 10^{-3} for flow and heat transport equations and 10^{-4} for transport equations for TCE and water vapor in gas phase. The partitioning of TCE into pore water phase is not considered here.

Table 6.1 Regression equations for properties of air and TCE in gas phase

Property	Estimating equations
$\rho_{air}(T)$	Ideal gas law, $PV = nRT$
$\rho_{TCE}(T)$	Ideal gas law, $PV = nRT$
$\rho_{gas\,mixture}$	Density of gas mixture, Equation (3.9)
$\mu_{air,gas}$ (micropoise)*	$\mu_{air,gas} = 50.153 + 4.8062\times10^{-1}T - 1.0967\times10^{-4}T^2$
$\mu_{TCE,gas}$ (micropoise)**	$\mu_{TCE,gas} = -23.621 + 4.2164\times10^{-1}T - 6.8948\times10^{-5}T^2$
$\mu_{gas\,mixture}$	Wilke's semi-empirical method***, Equation (3.15)

*From Yaws and Braker [2001]
**From Yaws [1999]
***From Reid et al. [1987]

Table 6.2 Regression equations for thermal properties

Thermal property	Regression equations
Thermal conductivity of water*, W/m/K	$K_{water,liquid} = -0.2758 + 4.612\times10^{-3}T - 5.5391\times10^{-6}T^2$
Thermal conductivity of air*, W/m/K	$K_{air,gas} = 0.00512 + 7.2342\times10^{-5}T - 9.2207\times10^{-9}T^2$
Thermal conductivity of NAPL (TCE)*, W/m/K	$K_{TCE,Liquid} = 10^{-2.1042+1.4428\times(1-T/571)\text{^}(2/7)}$
Specific heat capacity of water*, J/mol/K	$c_{water,liquid} = 92.053 - 3.9953\times10^{-2}T - 2.1103\times10^{-4}T^2 + 5.3469\times10^{-7}T^3$
Specific heat capacity of air**, J/mol/K	$c_{air,gas} = \left\{0.2896\times10^{-5} + 0.0939\times10^{-5}\left[\frac{3.012\times10^{-3}}{T}/\sinh\left(\frac{3.012\times10^{-3}}{T}\right)\right]^2 + 0.0758\times10^{-5}\left[\frac{1484}{T}/\cosh\left(\frac{1484}{T}\right)\right]^2\right\}\div1000$
Specific heat capacity of water vapor**, J/mol/K	$c_{water,gas} = \left\{0.3336\times10^{-5} + 0.2679\times10^{-5}\left[\frac{2.6105\times10^{-3}}{T}/\sinh\left(\frac{2.6105\times10^{-3}}{T}\right)\right]^2 + 0.089\times10^{-5}\left[\frac{1169}{T}/\cosh\left(\frac{1169}{T}\right)\right]^2\right\}\div1000$
Specific heat capacity of soil***	$c_{soil} = 0.48(1-\phi)\left[1 + 0.000611(T-298)\right]$
Specific heat capacity of NAPL (TCE)*, J/mol/K	$c_{TCE,liquid} = 58.916 + 0.4725T - 1.4035\times10^{-3}T^2 + 1.8353\times10^{-6}T^3$
Latent heat of vaporization of water*, kJ/mol	$h_{Lat,water} = 52.053(1-T/647.13)^{0.321}$
Latent heat of vaporization of TCE (NAPL)*, kJ/mol	$h_{Lat,TCE} = 46.915(1-T/571)^{0.396}$

*From Yaws [1999]
**From Perry et al.[1984]
***From Hart and Couvillion [1986]

Run time is up to 30 hours with variable time steps of 2-6 seconds. Mass balance calculations for TCE mass are performed to determine the removal of TCE by TEV systems and TCE distribution in the domain. For all simulations of TEV, accumulated mass balance errors for TCE were less than 0.5 % during simulation periods. Peclet (Pe) and Courant (Cr) numbers were less than 2 and 1, respectively.

To evaluate the performance of TEV in removing TCE in NAPL, eight application cases are investigated as shown in Table 6.3: Two cases of soil venting at ambient conditions and six cases of TEV with different humidity and flow rates. The water vapor concentration in injected humid air of each case is approximately 6.4 g/m^3 at 50 % relative humidity and 15 ^{o}C and 48.7, 121.6, and 218.9 g/m^3 at 20, 50, and 90 % relative humidity at 80 ^{o}C, respectively.

Table 6.3 Scenarios for TEV applications

Type	Case No.	Injected air temperature (^{o}C)	Relative humidity (%)	Flow rate (m^3/hr)
Normal venting	N-1	15	50	12.6
	N-2	15	50	21.0
Thermal-enhanced venting (TEV)	TA-1	80	20	12.6
	TA-2	80	50	12.6
	TA-3	80	90	12.6
	TB-1	80	20	21.0
	TB-2	80	50	21.0
	TB-3	80	90	21.0

In Table 6.3, the increase in relative humidity of injected humid air will proportionally raise heat capacity of injected humid air. As mentioned earlier in Chapter II, heat capacity of water vapor is four times that of dry air (approximately 1 kJ/kg ^{o}C)

and heat of evaporation is more than 2000 kJ/kg [Davis, 1997]. Air inject rates are also an important factor in determining soil temperature rise under TEV since convective heat transfer in soil venting depends on gas flow rates in porous media. The flow rates of 12.6 and 21.0 m^3/hr correspond to three and five pore volumes in the domain per hour, respectively, which are approximately 8.75×10^{-3} and 1.46×10^{-2} m/s as Darcy velocities of gas phase, respectively.

Due to nearly unidirectional gas flow (from the bottom to the top in *z*-direction) in the domain shown in Figure 6.5, soil temperature rise and TCE NAPL saturation reduction occur mostly along with the increasing z-direction. Thus, we will focus on the variations in soil temperature and NAPL saturation in *z*-direction. To support our analysis on heat transport and TCE removal (NAPL saturation reduction), simulation results (profiles of temperature and NAPL saturation) on A-A′ line (at x=2 m) in Figure 6.5 will be presented. In calculating overall TCE removal, all TCE mass in the domain is considered.

6.4.2 Results of TEV Simulations

The increase in soil temperature plays an important role in enhancing the vaporization of TCE at the contaminant source zone. For normal venting and thermal-enhanced venting cases listed in Table 6.3, the evolution of soil temperature in the domain is shown in Figure 6.6. Since the temperature of injected air (15 or 80 ^{o}C) is higher than initial temperature of the domain (10 ^{o}C), the injected air contributes to raise soil temperature in the domain. The degree of temperature rise depends on injected-air temperature, injection flow rate (Q), and relative humidity (RH). For instance, in Figure

6.6, soil temperatures at the inlet of the domain (z=0 m) at 3 hrs are 61, 73, and 75 ^{o}C for Cases TA-1 (RH=20 %, Q=12.6 m^3/hr), TA-2 (RH=50 %, Q=12.6 m^3/hr), and TB-1 (RH=20 %, Q=21 m^3/hr), respectively.

In Figure 6.6, the evaporation of TCE at the source zone (z=1-2 m) causes to decrease soil temperature at the zone. In Figure 6.6 (a1) for Case N-1, minimum soil temperature within the source zone drops over time. The locations of the lowest temperature move downstream with time until the end of the source zone (z = 2 m): For example, the locations are at 1.2, 1.4, and 2.0 m in z-direction (at x=2) for 3, 9, and 15 hours, respectively even though the locations are not noticeable in Figure 6.6 (a1). In Figure 6.3 for ethanol evaporation experiments, the minimum-temperature locations are clearly recognized, however, in Figure 6.6 (a1), until 12 hrs, soil temperature drops occur at fairly similar degree within the source zone except the temperature rise around z=1 m over time due to thermal energy of injected air. The difference in temperature profiles between ethanol (in Figure 6.3) and TCE (in Figure 6.6 (a1)) comes from the fact that evaporation of ethanol occurs mostly at the minimum-temperature location, however, evaporation of TCE occurs somewhat uniformly over the whole source zone. In section 6.3, the evaporation front of ethanol corresponds to the minimum-temperature location (in Figure 6.3), however, in this section regarding TCE, the location of the lowest temperature does not match the evaporation front of TCE. For instance, at t = 21 hrs of Case N-1, the lowest temperature is observed at z = 2 m (Figure 6.6 (a1)), but, at that time, the evaporation front of TCE is at the beginning of the source zone, z = 1 m, (Figure 6.7 (a1)).

In normal venting cases listed in Table 6.3, since the temperature of injected air (15 ^{o}C) is higher than the initial soil temperature (10 ^{o}C), the increase in an injection rate results in more heat supply to the contaminated zone. In Figure 6.6 (a1) and (b1), at t = 21 hrs, soil temperature at the beginning of the contaminated zone (z = 1 m) is higher in Case N-2 (Q=21.0 m^3/hr) than in Case N-1 (Q=12.6 m^3/hr): The temperatures for the former and latter cases are 13.6 and 8.7 ^{o}C, respectively. At that time, the soil temperature at the end of the contaminated zone (z = 2 m) is approximately 1.1 and 1.5 ^{o}C in Cases N-1 and N-2, respectively.

In TEV cases listed in Table 6.3, heated air (80 ^{o}C) at different relative humidity is supplied to enhance TCE evaporation. Relative humidity is defined as the ratio of actual water vapor density to saturated water vapor density at a specified temperature. The increase in relative humidity implies the increase in specific heat capacity of injected humid air. The higher relative humidity in injected gas derives the higher soil temperature in the contaminated zone. For example, in Figure 6.6 (a2)-(a4) at t = 9 hrs, soil temperature at z = 1 m is 27.4, 56.7, and 76.5 ^{o}C for Cases TA-1 (RH=20 %), TA-2 (RH=50 %), and TA-3 (RH=90 %), respectively.

The degree of relative humidity has influence on patterns of temperature increase. At t = 12 hrs in Figure 6.6 (a3), the temperature profiles of Case TA-2 (RH=50 %) can be divided into three stages: The first stage is at z = 0-0.8 m, the second one is at z = 0.8-1.2 m, and the third one is at z > 1.2 m. On the second stage, soil temperature variations are very small and relatively horizontal. The second stage is noticeable at a relative humidity of 50 % (Case TA-2 and TB-2), but that is not clear at 20 or 90 % relative humidity

cases. In Figure 6.4 (TEV for ethanol evaporation), some horizontal temperature profiles appear on the experimental data between distances from 0.12 to 0.18 m at t = 1500 sec.

Based on temperature profiles shown in Figure 6.6, we may compare relative impacts of flow rates and relative humidity on soil temperature rise. In this study, the temperature increment due to the injection rate increase (from 12.6 to 21 m^3/hr) at each relative humidity (RH=20, 50, or 90 %) are greater than that due to the increase in relative humidity (RH=20 to 50 % or RH=50 to 90 %) at the injection rate 12.6 m^3/hr. For example, at z=1.6 m, 6 hrs in Figure 6.6, the injection rate increase (from 12.6 to 21 m^3/hr) generates the temperature increment of 6 (i.e., 8.5 to 14.5 ^oC), 26 (i.e., 13.5 to 39.5 ^oC), and 41.7 ^oC (i.e., 28.3 to 70 ^oC) for RH = 20, 50, and 90 %, respectively. At an injection rate of 12.6 m^3/hr, the temperature increments (at z=1.6 m, 6 hrs) are: 5 ^oC when RH increases from 20 to 50 %; 15 ^oC when RH increases from 50 to 90 %. These data also indicate that the temperature increment becomes larger as relative humidity increases. In addition, the effect of relative humidity on temperature increments is higher at the higher injection rate Q=21 m^3/hr than Q=12.6 m^3/hr: At a injection rate of 21 m^3/hr, the temperature increments (at z=1.6 m, 6 hrs) are: 25 ^oC when RH increases from 20 to 50 %; 30.5 ^oC when RH increases from 50 to 90 %.

Temperature profiles shown in Figure 6.6 are estimated in the simplified model domain shown in Figure 6.5 even though thermal properties of phases (gas, liquid, and soil) change with temperature. At contaminated sites, the prediction of temperature variations in the subsurface may require information on more parameters such as soil-media heterogeneity, infiltration, and the groundwater table.

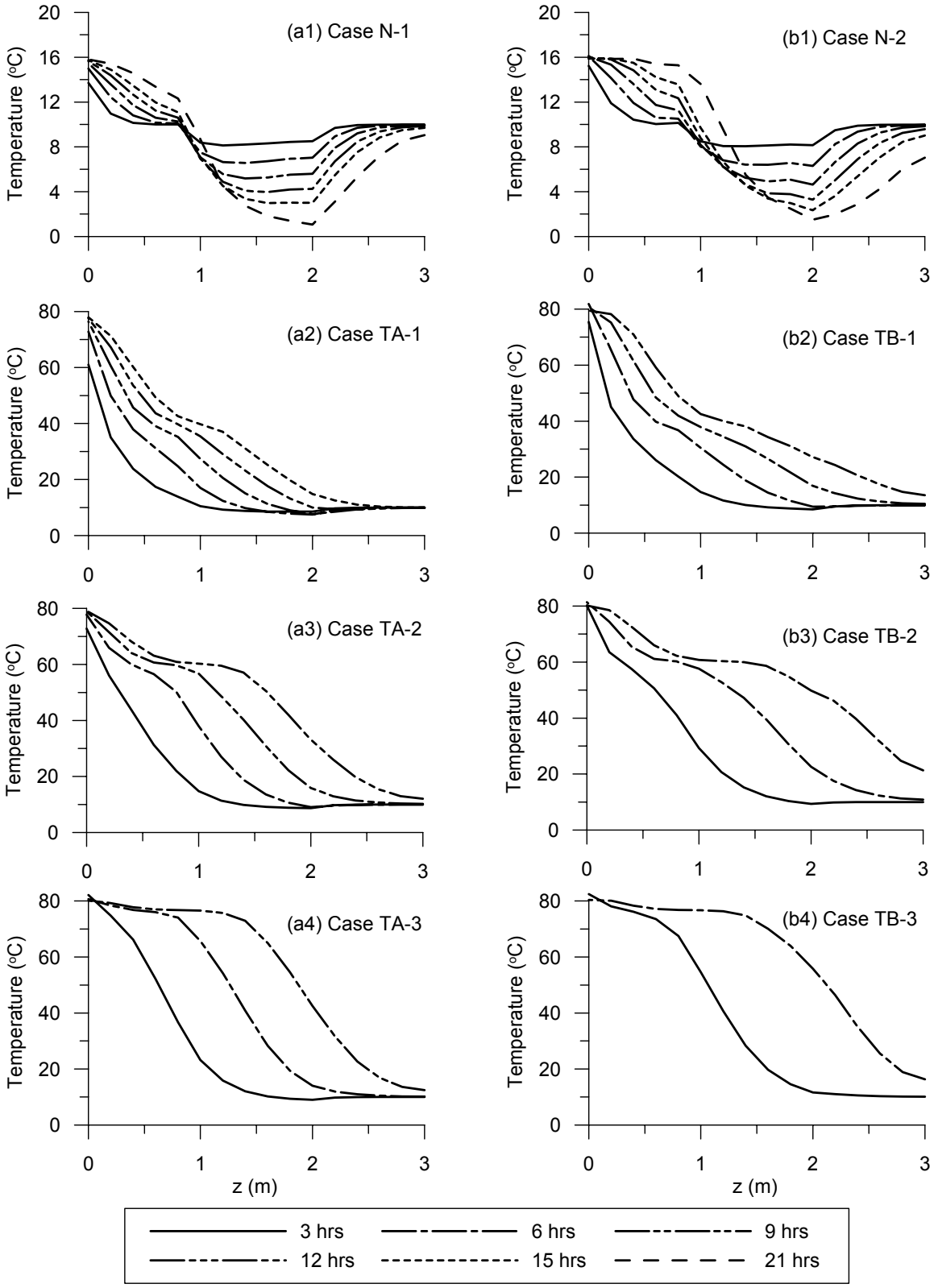

Figure 6.6 Temperature profiles over time during TEV on A-A′ line (at x=2 m)

Temporal saturation changes of TCE NAPL at the source zone (z=1-2 m on A-A′) are given in Figure 6.7. The reduction in the saturation of TCE NAPL starts from the beginning points of the source zone (z=1 m) because mass transfer rates at the points are highest within the source zone and the increase in soil temperature by heat transport occurs along with gas flow (in increasing z-direction).

In Figure 6.7, compared to the normal venting, TEV (the application of heated air) improves the reduction in TCE NAPL saturation: In Case TA-1 (Q=12.6 m^3/hr and RH=20 %), all TCE at z=1 m is removed at 12 hrs while at that time TCE NAPL saturation at z=1 m in Case N-1 (Q=12.6 m^3/hr) is approximately 0.37. At normal venting, the increase in injection rates contributes the reduction of TCE NAPL saturation: At 12 hrs, the saturation (at z=1 m) in Case N-2 (Q=21 m^3/hr) is about 0.33.

In TEV modeling of this study, the higher flow rate produces the greater increase in soil temperature as already seen in Figure 6.6 and the greater reduction in TCE NAPL saturation in Figure 6.7. For example, in Figure 6.7 (a2) for Case TA-1 (Q=12.6 m^3/hr) at 6 hrs, TCE NAPL saturations at z = 1 and 2 m are 0.062 and 0.078, and, in Figure 6.6 (a2), the corresponding soil temperatures are 17.0 and 7.5 ^oC, respectively. In Figure 6.7 (b2) for Case TB-1 (Q=21.0 m^3/hr) at 6 hrs, NAPL saturations at z = 1 and 2 m reduce to 0.048 and 0.074, respectively, and the corresponding temperatures (in Figure 6.6 (b2)) are 30.5 to 9.5 ^oC, respectively.

The increase in relative humidity of injected air is not directly related with the variation of TCE NAPL saturation even though water condensation may change gas saturation levels. However, since the relative humidity increase produces soil temperature rise that determines the increment of TCE vapor pressures (Figure 6.2), the relative

humidity of injected air is an important factor to determine TCE removal (or the reduction in TCE NAPL saturation). The increase in relative humidity of injected air prompts the reduction in TCE NAPL saturation at the source zone. In Figure 6.7 for Cases TAs (TA-1, TA-2, and TA-3) at 6 hrs, when the relative humidity of injected air increases from 20, 50, to 90 %, the NAPL saturation at z = 1 m reduces from 0.062, 0.045 to 0.0. At air injection rate of 12.6 m^3/hr, operation times required to completely remove TCE at z = 1 m are less than 21, 12, 8, and 6 hours for Cases N-1, TA-1, TA-2, and TA-3, respectively. The NAPL saturation profiles of Case TA-2 at 8 hrs are not presented in Figure 6.7.

In Figure 6.7, the difference between the NAPL saturation reductions of each case listed in Table 6.3 at 3 hrs is much smaller than the difference at 6 hrs. That is due to a heat transporting time, which is required for heat to be transferred from the inlet of the domain (z=0 m) to the beginning of the source zone (z=1 m). The slope of each NAPL saturation line at time steps become larger with time, and the overall slopes in TEV cases significantly rise with the increase in relative humidity of injected air even though the slope varies over locations. As simplified indicators for the slopes, we may compare the difference in NAPL saturation levels at z=1 and 2 m for Cases TA-1, TA-2, and TA-3. In Figure 6.7, the saturation levels at z=1 and 2 m at 6 hrs are: 0.062 and 0.078 in Cases TA-1, respectively; 0.045 and 0.079 in Case TA-2, respectively; and, 0 and 0.083 in Case TA-3, respectively. As expected, the difference between the two NAPL saturation levels at z=1 and 2 m becomes larger with the increase of RH in injected air. Among those saturation levels, we need to note the saturation levels at z=2 m: As RH increases, the saturation levels at z=2 m increase (TCE removal becomes smaller) while those at z=1 m

decrease. These phenomena are due to heat energy applied. For Cases TA-1, TA-2, and TA-3, as soil temperature gradients (negative values) within the contaminated zone in Figure 6.6 become steeper due to the increase in relative humidity of injected air, NAPL saturation gradients (positive values) in Figure 6.7 also become steeper. In Case TA-2, the temperatures at z=1 and 2 m are approximately 38 and 9.1 ^{o}C, respectively, at which maximum TCE vapor concentrations are approximately 0.88 and 0.25 kg/m^3, respectively; If TCE concentration within injected air (gas phase) due to TCE NAPL evaporation increases up to 0.25 kg/m^3 before the gas reaches z=2 m, the evaporation of TCE NAPL at z=2 m will be minor because a driving force for TCE NAPL evaporation (the difference between a maximum TCE concentration and a current TCE concentration in gas phase) diminishes. Therefore, the larger difference in temperature between z=1 and 2 m will result in the lower evaporation of TCE NAPL at z=2 m. The evaporation of TCE also depends on the magnitude of vaporization-rate coefficients of TCE as shown in Equation (3.18). The smaller vaporization rate will reduce the mass of vaporized TCE over distance and may decrease the difference in NAPL saturation reductions over distance.

In Figure 6.7, for Q=21 m^3/hr, NAPL saturation at z=2 m, 6 hrs in Case TB-3 is smaller than Cases TB-2 and TB-1: The saturation levels are 0.053, 0.075, and 0.074, respectively. That may be due to strong heat transport in Case TB-3: At 6 hrs, all TCE NAPL up to z=1.6 m are removed (Figure 6.7 (b4)).

In TEV simulation cases used here, only two temperatures are considered. In TEV application at contaminated sites, the temperature of injected air will also be an important factor for heat transfer in soil matrix and contaminant removal. In subsurface systems,

evaporation of NAPL results from complex relationships of physical and chemical parameters such as temperature, porosity and pore size in soil matrix, and mass transfer between phases.

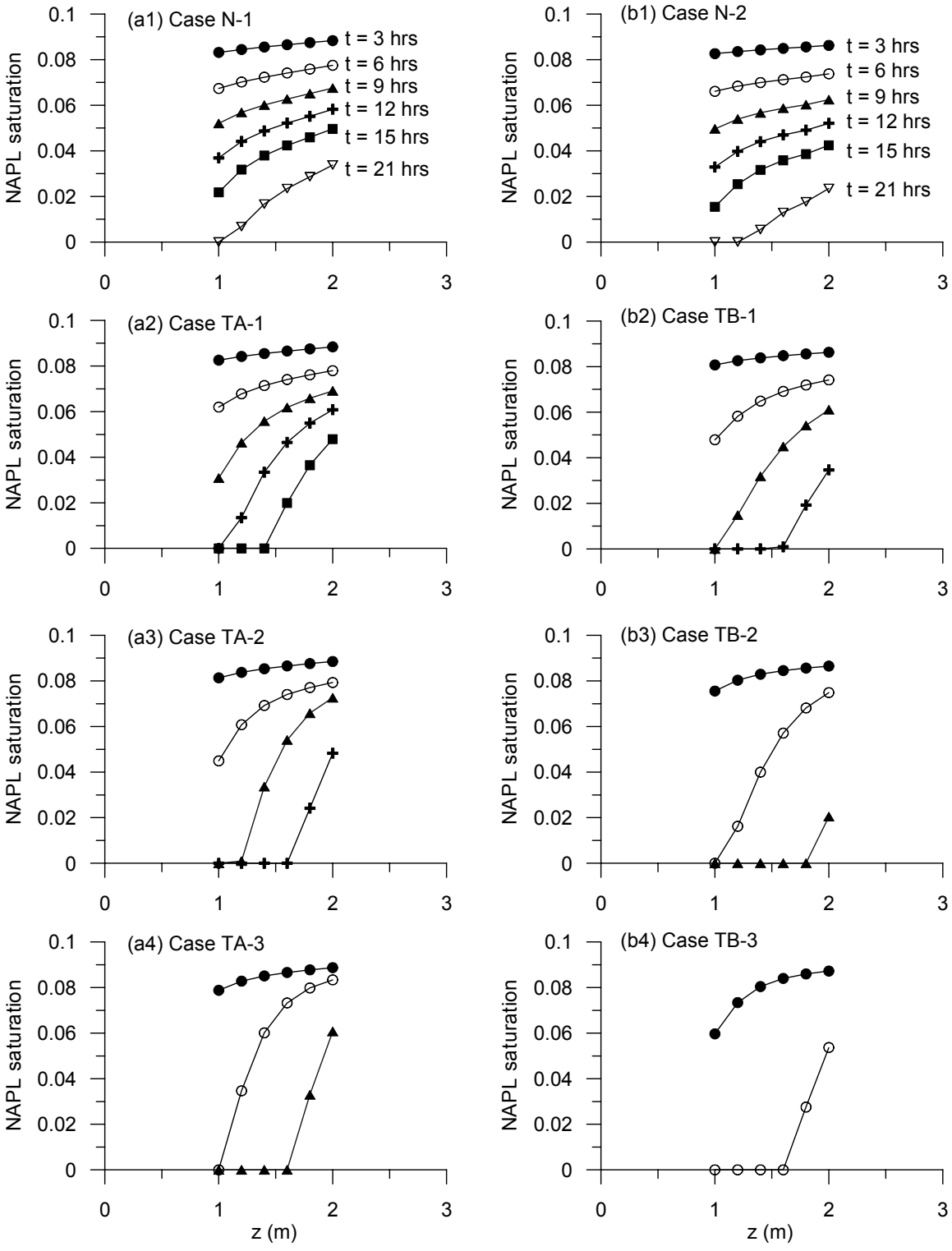

Figure 6.7 The changes in TCE NAPL saturation over time on A-A′ line (at x=2 m)

The temporal reduction of TCE mass in the domain is illustrated in Figure 6.8. The increases in relative humidity of injected air and/or injection rate of air reduce remediation times required to remove all NAPL at the source zone. At an injection rate of 12.6 m^3/hr (Figure 6.8 (a)), the required operation times are 32, 20, 14, and 11 hours for Cases N-1, TA-1, TA-2, and TA-3, respectively. Under that flow rate, TEV reduces the times by 38 and 66 % in Case TA-1 and TA-3, respectively compared to Case N-1. At an injection rate of 21.0 m^3/hr (Figure 6.8 (b)), the required operation times are 27, 14, 9.5, and 7 hours for Cases N-2, TB-1, TB-2, and TB-3, respectively: The operation times reduced by 48 and 74 % for Case TB-1 and TB-2, respectively compared to Case N-2. In this study, the application of heat energy reduces operation times by at least 12 hours compared to the normal venting cases shown in Table 6.3. At Cases N-1 and N-2, the increase in flow rates from 12.6 to 21.0 m^3/hr reduces the operation time by about 15.6 % (5 hrs). Under the conditions used herein, the overall reduction profiles of TCE NAPL mass shown in Figure 6.8 suggest that the application of thermal energy is effective in enhancing a remedial performance of TCE in the domain.

In the domain shown in Figure 6.5, there is a time lag between a heat input at the inlet and the enhancement in TCE NAPL removal at the contaminated zone. The variation of temperature within the source zone (z=1-2 m) depends on air injection rates and relative humidity applied for each case as shown in Figure 6.7, so the time lag vary over simulation cases shown in Table 6.3. In the simulation cases, since the higher flow rate yields the more heat energy transport to the source zone, the higher flow rate reduces the time lag observed in this TEV modeling.

In temporal profiles of TCE mass reduction in the domain shown in Figure 6.8, the time lag may be approximately estimated from the diversion of TCE mass reduction profiles of TEV cases from the mass reduction profiles of normal venting cases (Cases N-1 and N-2): The time lag is about 3 and 2 hours for injection rates of 12.6 and 21.6 m^3/hr, respectively.

At contaminated sites, the performance of TEV systems may be related with may operation parameters including air injection rates and relative humidity and temperature of injected air. In achieving a target performance of TEV systems, various combinations of operational parameters might be available. Among the simulation cases considered in this study, Cases TA-2 (Q=12.6 m^3/hr and RH=50 %) and TB-1 (Q=21.0 m^3/hr and RH=20 %) show similar performances in terms of a removal efficiency of TCE and a operation time required to remove all TCE in the domain (Figure 6.8): For the two cases, maximum differences in the removal efficiency and operation times to achieve each efficiency level are less than 5 % and 0.5 hour through simulation periods, respectively. Since the two cases produce nearly same results, either can be selected to remove TCE NAPL in this TEV modeling.

In the application of TEV systems to remove NAPL in the unsaturated zone, the selection of optimal settings for field remediation systems may be chosen based on removal efficiency of each setting and other factors such as applicability of each option at contaminated sites, costs for installation and operation, and safety.

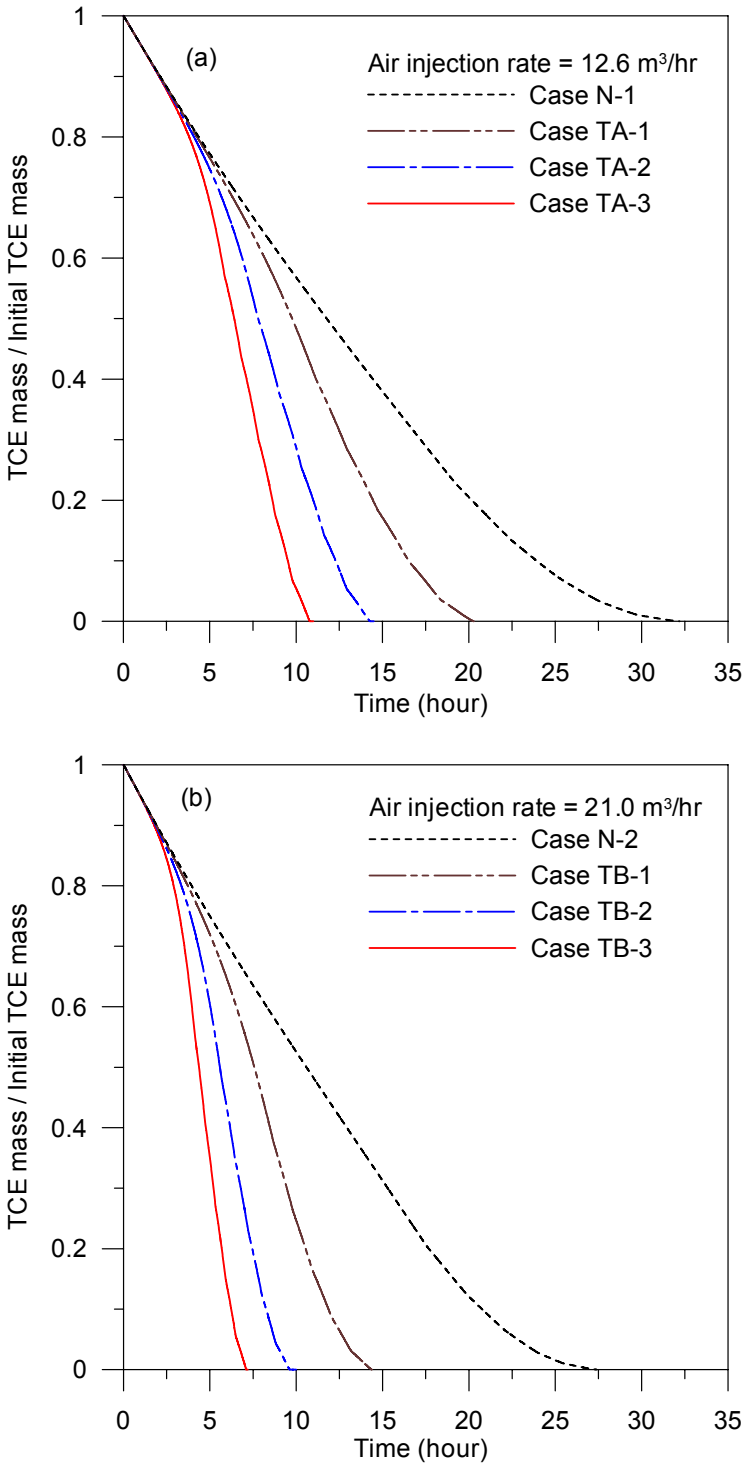

Figure 6.8 Reduction of NAPL saturation over time by TEV at two different flow rates: (a) air injection rate = 12.6 m^3/hr and (b) air injection rate = 21.0 m^3/hr

6.5 Summary

In this chapter, for TEV systems, heat energy transport equations are formulated and solved with other equations for gas flow and contaminant transport in gas phase. TechFlow^{MP} model developed in this study is verified using experimental data published in the literature. Under considerations for temperature-dependent parameters such as density and viscosity of gas phase, eight applications are studied to investigate heat transport in porous media and TCE NAPL removal by normal venting and thermal-enhanced venting. Through the application studies of TEV, the effects of air injection rates and injected-air relative humidity on TCE removal are analyzed. From the results of the eight-application studies, the followings can be summarized:

(i) Since heat energy required by evaporation of TCE at the contaminated zones is absorbed mostly from the incoming air and solid soil, TCE evaporation decreased soil temperature at the contaminated zone. Soil temperature drop at the source zone was greater in normal venting at ambient conditions than in TEV. At normal venting, maximum drop of soil temperature occurred downstream at the end of the contaminated zone, and the larger injection flow rate produced the higher increase in soil temperature at the contaminated zone.

(ii) TEV using heated air with three different levels of relative humidity (20, 50, and 90 %) was effective in transporting heat energy from the inlet to the contaminated zone. As heat energy delivered compensates heat consumption for evaporation of TCE at the contaminated zone, soil temperature at the contaminated zone did not

show significant drop throughout simulation periods. In TEV applications of this study, maximum temperature drop was less than two Celsius degree. Water vapor in gas phase played an important role in the increase in energy content of gas phase. Thus, the higher relative humidity in injected air resulted in the greater increase in soil temperature in the model domain. As expected, the larger flow rate enhanced the increase in soil temperature and the reduction in TCE NAPL saturation in the domain. In simulations of TEV cases of this study, as the transport of thermal energy by conduction and convection processes moves ahead the evaporation fronts, the reduction rate of TCE NAPL at the contaminated site was proportional to the magnitude of heat energy input into the domain.

(iii) Operating times required to completely remove TCE in the domain decreased with the increase in relative humidity of injected air and injection rates. The results of the simulations carried out in this study showed that, under the modeling conditions used here, TEV systems can reduce remediation times by at least 38 % compared to normal venting systems. In this study, water vapor in injected air played an important role in raising energy contents of the injected air and in transporting heat energy to the contaminated zone. In TEV modeling conducted here, the relative humidity of 50 % in injected air reduced more than 50 % of the operation time required by normal venting systems

CHAPTER VII

CONCLUSIONS

Groundwater contamination with volatile organic compounds (VOCs) has become a major environmental concern. In order to preserve groundwater resources from such contamination and to clean up sites contaminated with VOCs, the understanding of fate and transport of contaminants in the subsurface systems and evaluation of remediation technologies is essential. To enhance this understanding, the study presented in this thesis addressed four important topics: (i) multiphase flow and contaminant transport in subsurface environments; (ii) biological transformations of contaminants; (iii) in-situ air sparging (IAS); and (iv) thermal-enhanced venting (TEV). Among VOCs, trichloroethylene (TCE) is one of the most commonly detected chemicals at contaminated sites. In this study, TCE and its daughter products (dichloroethylene (cDCE) and vinyl chloride (VC)) are chosen as target contaminants. A three-dimensional numerical model, called TechFlow^{MP}, has been developed to conduct numerical modeling involving the four topics mentioned above. The model has been verified and validated using analytical solutions and experimental data published in the literature.

In the first part of this thesis, density-driven transport of TCE in subsurface environments was studied. Vaporization of TCE as a nonaqueous phase liquid (NAPL) generated density-driven advection of gas phase. Under modeling conditions used in this study, the density-driven advection played a key role in the spread of TCE in the unsaturated zone near contaminant source area and in the transport of TCE into the groundwater in the saturated zone. The advection increased the contaminant release into

the atmosphere and also enhanced the reduction of NAPL saturation at contaminant source area. In the down-gradient saturated zone, as the density-driven advection accelerated the release of TCE from the contaminated groundwater to the atmosphere, the density-driven advection helped to reduce the development of dissolved contaminant plume in the zone. Infiltration applied in this study lowered gas flow velocity in the unsaturated zone but raised contaminant transport into the saturated zone by accelerating the downward movement of pore water in the unsaturated zone. In terms of permeability, the higher permeability of soil matrix created stronger density-driven advection in gas phase. The study on density-driven transport of contaminants helped us find the effect of the density-driven advection of gas phase on groundwater pollution in the upstream and downstream zones. The findings will be used to plan monitored natural attenuation and/or to design active remediation strategies at contaminated sites.

In the second part of this thesis, the effects of biological transformations of dissolved contaminants on their transport were investigated. First-order relationships and Michaelis-Menten kinetics were used to describe sequential biotransformations of TCE, cDCE, and VC. Biotransformation of TCE reduced its spreading in a variably saturated zone and introduced new contaminants in subsurface systems. The greater bioreaction coefficient of TCE produced the greater reduction in TCE concentration and the greater production of cDCE. Since Michaelis-Menten kinetics becomes a zero-order or first-order relationship according to contaminant concentrations, the kinetics was more complicated than a first-order relationship in predicting concentration profiles of cDCE and VC. According to bioreaction kinetics, the locations of the highest concentration zones of cDCE and VC varied. For example, in first-order relationships, the highest

concentration zones of cDCE were located just above the groundwater table while, in Michaelis-Menten kinetics, the zones appeared in the down gradient saturated zone. In a case that biotransformation rates of TCE and cDCE were equal and were much greater than those of VC, VC concentrations were higher than cDCE concentrations in the system, which might represent competition between multispecies for dechlorination processes. The study in the second part of this thesis emphasized the importance of biological transformations of contaminants in their fate and transport in subsurface systems for long-term simulations. The fate and transport of reactive contaminants in multiphase flow highly depended on the kinetics of biotransformations and the magnitude of bioreaction coefficients. The findings of this study can be used to set up long-term remediation plans for bio-reactive contaminants. Since physical, chemical, and biological parameters of subsurface systems are highly site-specific, field experiments and investigations should be conducted to estimate the subsurface parameters as well as biotransformation coefficients.

In the third part of this thesis, IAS modeling was conducted to analyze two important topics: (i) interactive movement of injected air and groundwater, as multiphase flow, in three-dimensional domains and (ii) remedial performance of a variety of IAS systems for contaminated groundwater. In IAS modeling, air flow generated by air injection was stabilized after a short period of IAS operation time. The injected air caused the reduction in groundwater velocity in the influence zone of air sparging. Some portion of groundwater flow detoured around the influence zone. Under IAS modeling conditions used in this study, IAS through multiple injection wells were superior over IAS through one injection well in capturing dissolved-contaminant plumes and cleaning up the

contaminated groundwater. Air injection using a horizontal well created uniform gas saturation in wider influence zones than that using a vertical well. The single-horizontal-injection-well IAS used in this study covered all contaminant plumes, and the required air injection rate of the IAS was 60 m^3/hr to achieve a target performance in contaminant removal (TCE < 0.001 g/L). The detour of groundwater flow below injection points may cause uncontrolled migration of contaminants. To avoid this detour, the depth of injection wells should be deep enough below contaminant plumes. In this study, the minimum distance between the top of injection well screens and the deepest point of contaminant plumes was approximately 3 m. A pulse air injection method was very effective to capture contaminant plumes under air injection rate $\geq$ 60 m^3/hr in this study. The effect of biodegradation on contaminant removal was highly variable according to bioreaction activity. In IAS systems with multiple vertical wells, the distance between injection wells is an important design parameter. Wells should be close enough to ensure the performance of IAS systems. In this study, the maximum distance between vertical injection wells was approximately 7.1 m in removing dissolved TCE below its concentration 0.001 g/L in the modeling domain.

Up to now, the change in groundwater flow due to IAS has not been much studied and ignored in IAS study even though the groundwater flow is one of important factors that determine remedial efficiency of IAS. This study on IAS elucidated interactive flows of injected air and groundwater as multiphase flow and transport and removal of a contaminant under IAS in a subsurface system. The results of the IAS study can be used in designing effective, optimal IAS systems for contaminated sites.

In the last part of this thesis, under TEV in the unsaturated zone, heat transport through porous media and the effect of TEV on TCE NAPL removal were examined. Under the conditions used in this TEV modeling, thermal energy of injected air was effective in raising soil temperature at the contaminated zones, so TEV increased contaminant removal rates and reduced remediation times. The performance of TEV improved with the increase in injection flow rate and/or relative humidity of injected air. The TEV simulation results, including spatial, temporal variations in temperature and NAPL saturation degree under several TEV operations, will help us not only to identify the best operation conditions among the scenarios used herein but also to build optimal TEV strategies for contaminated sites.

The first and second parts of this thesis focused on natural contaminant movement in subsurface environments: i.e., the fate and transport of conservative or reactive contaminants under no-human interruption. The results of those two parts allow us to well understand the impacts of transport mechanisms on the development of contaminant plumes and to delineate future soil and groundwater contamination at target sites. These outcomes will be one of fundamental data in decision-making processes for remedial actions such as monitored natural attenuation, pump-and-treatment, and IAS.

The third and fourth parts of this thesis discovered in detail fluid flow and contaminant transport under human-induced remedial activities of IAS and TEV, respectively. The results of these two parts can be used to make practical guidelines for the application of the two remedial technologies, IAS and TEV. For example, the guidelines for IAS may include maximum air injection rates, well-to-well distances, injection types, and multiple-

well layouts at contaminated sites. For TEV, humidity and temperature of injected gas mixtures can be additionally considered.

Based on the findings of the study presented in this thesis, the following research topics can be recommended as further research areas:

(i) Density-driven transport with gas and water phases in heterogeneous porous media;

(ii) Transport of contaminants with convergent reactions;

(iii) IAS in heterogeneous and/or stratified subsurface systems;

(iv) Investigations on TCE fate and transport in the presence of other co-contaminants; and

(v) Gas flow and heat transport in a three-dimensional domain under TEV.

APPENDIX A

A THREE-DIMENSIONAL ISOPARAMETERIC RECTANGULAR PRISM ELEMENT AND A LINEAR INTERPOLATION FUNCTION

A rectangular prism element (Eight-node-linear element, Rectangular parallelopiped element, Trilinear hexahedral element, or brick) shown in Figure A.1 is a basic element for three-dimensional domains and is used in TechFlow^{MP} model. In a natural coordinate system (ξ,η,ζ), a shape function (basis function) for a rectangular prism element with eight nodes can be written as follows [Hinton and Owen, 1979; Hughes, 1987; Zienkiewicz and Taylor, 1989]:

$$w_i = \frac{1}{8}(1+\xi_i\xi)(1+\eta_i\eta)(1+\zeta_i\zeta) \tag{A.1}$$

where $\xi_i,\ \eta_i,\ \zeta_i = \pm 1$.

The element has faces $\xi = \pm 1$, $\eta = \pm 1$ and $\zeta = \pm 1$ as shown in the Figure A.1. Local coordinates of eight nodes are given in Table A.1.

Each basis function (shape function) has a value of 1 at its own node, and 0 at the other eight nodes. A property of the basis functions for an element is that

$$\sum w_i\ (\xi,\eta,\zeta) = \sum_{i=1}^{8} w_i\ (\xi,\eta,\zeta) = 1 \tag{A.2}$$

and

$$w_i\ (\xi_j,\eta_j,\zeta_j) = \begin{cases} 1 & if\ i = j \\ 0 & if\ i \neq j \end{cases} \tag{A.3}$$

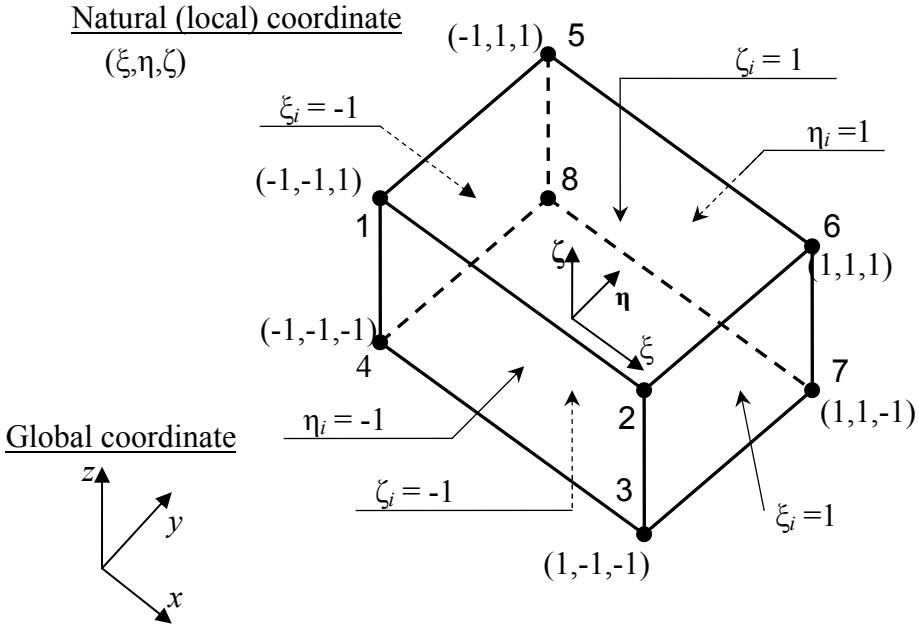

Figure A.1 Rectangular prism element

Table A.1 Local coordinates of eight nodes

Local node number	ξ_i	η_i	ζ_i
1	-1	-1	1
2	1	-1	1
3	1	-1	-1
4	-1	-1	-1
5	-1	1	1
6	1	1	1
7	1	1	-1
8	-1	1	-1

APPENDIX B

MODIFIED PICARD METHOD

Water flow equation in a variably saturated zone can be written as follows [Bear and Bachmat, 1990; Diersch and Perrochet, 1999]:

$$s_w S_s \frac{\partial \psi_w}{\partial t} + \phi \frac{\partial s_w}{\partial t} = \nabla \cdot \left[\frac{\rho_w k_m k_{rw} g}{\mu_w} \left(\nabla \psi_w + \nabla z \right) \right] + Q_w \tag{B.1}$$

where subscript w represents water phase, $S_s = \left[(1-\phi)\alpha + \phi \beta_w \right] \rho_w g$ is a specific volumetric storativity (L^{-1}), $\psi_w = P_w / \rho_w g$ is water-equivalent pressure head of water phase (L), $\beta_w = (1/\rho_w)(d\rho_w / dP_w)$ is compressibility of water under an isothermal condition (LT^2/M), $\alpha = (1/V_t)(dV_t / dP_w)$ is soil matrix compressibility (LT^2/M), V_t is a bulk volume of porous media element (L^3), and $Q_w = Q_w^{'} / \rho_w$ is strength of sources/sinks of water phase (L^{-1}).

Using the backward Euler approximation, the time-derivative of water saturation at the second term on the left-hand side of Equation (B.1) can be expanded,

$$\phi \frac{\partial s_w}{\partial t} = \phi \frac{s_w^{t+1,m+1} - s_w^t}{\Delta t} \tag{B.2}$$

where superscript t is a time level, and superscript m denotes an iteration level at t+1 time level, and Δt is a length of time step. By applying the approximation of the mixed form, proposed by Celia et al. [1990], to two mobile-phase (gas-water) system, the term $s_w^{t+1,m+1}(\psi_w, \psi_g)$ in Equation (B.2) can be expanded in a truncated Taylor series with respect to ψ_w:

$$\phi s_w^{t+1,m+1} \approx \phi s_w^{t+1,m} + c_{ww}^{t+1,m}(\psi_w^{t+1,m+1} - \psi_w^{t+1,m}) + c_{wg}^{t+1,m}(\psi_g^{t+1,m+1} - \psi_g^{t+1,m}) \tag{B.3}$$

with

$$c_{ij} = \phi \frac{\partial s_i}{\partial \psi_j}, \quad i,\ j = g, w \tag{B.4}$$

where c is a specific fluid capacity defined by Parker et al. [1987]. The specific fluid capacities can be evaluated by either analytical derivative equations or chord slope approximations [Parker et al., 1987; Rathfelder and Abriola, 1994; Diersch and Perrochet, 1999]. The chord slope approximations have some limitations; it is not applicable in the region with the steep and near-discontinuous pressure gradient around $\psi_f = 0$ [Paniconi and Putti, 1994]. TechFlow^{MP} is capable of handling both methods, and the analytical method is used in this study. The analytical evaluation for specific fluid capacities in two mobile-phase (air-water) system can be done by [Parker et al., 1987],

$$c_{ww} = \phi \alpha_{gw}(n-1)(1-s_m)(s_{we})^{1/m}\left[1-(s_{we})^{1/m}\right]^m \tag{B.5}$$

$$c_{gg} = c_{gw} = c_{ww} \tag{B.6}$$

$$c_{wg} = -c_{ww} \tag{B.7}$$

Finally, combining Equations (B.2) and (B.3) and then inserting them into equation (B.1) yields,

$$\begin{aligned} & s_w S_s \frac{\partial \psi_w}{\partial t} + \phi \frac{s_w^{t+1,m} - s_w^t}{\Delta t} + \frac{c_{ww}^{t+1,m}}{\Delta t}\left(\psi_w^{t+1,m+1} - \psi_w^{t+1,m}\right) + \frac{c_{wg}^{t+1,m}}{\Delta t}\left(\psi_g^{t+1,m+1} - \psi_g^{t+1,m}\right) \\ & = \nabla \cdot \left[\frac{\rho_w k_i\, k_{rw} g}{\mu_w}\left(\nabla \psi_w + \nabla z\right)\right] + Q_w^{'} \end{aligned} \tag{B.8}$$

For gas phase flow, its equation for a variably saturated zone can be written as follows as shown in Equation (3.13):

$$\begin{aligned}&\phi s_g\left(\frac{\rho_w g M_g}{RT}\frac{\partial \psi_g}{\partial t}+\sum_{i=1}^{N}\left(1-\frac{\rho_{air}}{\rho_v^i}\right)\frac{\partial C_g^i}{\partial t}\right)+\phi\rho_g\frac{\partial s_g}{\partial t}\\&=\nabla\left[\frac{\rho_g k_m k_{rg}}{\mu_g}\rho_w g\left(\nabla\psi_g+\frac{\rho_g}{\rho_w}\nabla z\right)\right]+\sum_{i=1}^{N}\phi s_g\left[\lambda_V^i\left(C_{ge}^i-C_g^i\right)+\lambda_H^i\left(HC_w^i-C_g^i\right)\right]+Q_g\end{aligned} \tag{B.9}$$

In the same manner applied to water flow equation, the equation for gas-phase flow can be rewritten as,

$$\begin{aligned}&\phi s_g\left(\frac{\rho_w g M_g}{RT}\frac{\partial \psi_g}{\partial t}+\sum_{i=1}^{N}\left(1-\frac{\rho_{air}}{\rho_v^i}\right)\frac{\partial C_g^i}{\partial t}\right)\\&+\phi\rho_g\frac{s_g^{t+1,m}-s_g^t}{\Delta t}+\frac{c_{gg}^{t+1,m}}{\Delta t}\rho_g\left(\psi_g^{t+1,m+1}-\psi_g^{t+1,m}\right)+\frac{c_{gw}^{t+1,m}}{\Delta t}\rho_g\left(\psi_w^{t+1,m+1}-\psi_w^{t+1,m}\right)\\&=\nabla\left[\frac{\rho_g k_m k_{rg}}{\mu_g}\rho_w g\left(\nabla\psi_g+\frac{\rho_g}{\rho_w}\nabla z\right)\right]+\sum_{i=1}^{N}\phi s_g\left[\lambda_V^i\left(C_{ge}^i-C_g^i\right)+\lambda_H^i\left(HC_w^i-C_g^i\right)\right]+Q_g\end{aligned} \tag{B.10}$$

APPENDIX C

CONTINUOUS DARCY'S VELOCITY APPROXIMATION

Flow velocities of gas and water phase are required in solving contaminant transport equations. The velocities can be expressed using Darcy's law. Globally continuous velocities of gas and water phase can be obtained by implementing a finite element method to solve Darcy's law equation [Yeh, 1981]. Fluid velocity in porous media, q, can be written as follows:

$$q_f = -\frac{\mathbf{k}\, k_{rf}}{\mu_f} \cdot \left[\nabla P_f - \rho_f \mathbf{g}\right] \tag{C.1}$$

where subscript f = fluid phase(g for gas and w for water), $\mathbf{k}$ = intrinsic permeability tensor (L^2), k_{rf} = relative permeability of β phase in a porous medium, μ_f = dynamic viscosity of β phase (M/LT), P_f = pressure in f phase (M/LT^2), $\mathbf{g}$ = vector of gravitational acceleration directed downward (L/T^2), $P_f = \psi_f \rho_R g$, and ρ_R = reference water density.

Equation (C.1) can be expanded for a three-dimensional domain:

$$q_{fx} = -\frac{\rho_R g K_{xx} k_{rf}}{\mu_w}\frac{\partial \psi_f}{\partial x} - \frac{\rho_R g K_{xy} k_{rf}}{\mu_w}\frac{\partial \psi_f}{\partial y} - \frac{\rho_R g K_{xz} k_{rf}}{\mu_w}\left(\frac{\partial \psi_f}{\partial z} + \frac{\rho_f}{\rho_R}\frac{\partial z}{\partial z}\right) \tag{C.2}$$

$$q_{fy} = -\frac{\rho_R g K_{yx} k_{rf}}{\mu_w}\frac{\partial \psi_f}{\partial x} - \frac{\rho_R g K_{yy} k_{rf}}{\mu_w}\frac{\partial \psi_f}{\partial y} - \frac{\rho_R g K_{yz} k_{rf}}{\mu_w}\left(\frac{\partial \psi_f}{\partial z} + \frac{\rho_f}{\rho_R}\frac{\partial z}{\partial z}\right) \tag{C.3}$$

$$q_{fz} = -\frac{\rho_R g K_{zx} k_{rf}}{\mu_w}\frac{\partial \psi_f}{\partial x} - \frac{\rho_R g K_{zy} k_{rf}}{\mu_w}\frac{\partial \psi_f}{\partial y} - \frac{\rho_R g K_{zz} k_{rf}}{\mu_w}\left(\frac{\partial \psi_f}{\partial z} + \frac{\rho_f}{\rho_R}\frac{\partial z}{\partial z}\right) \tag{C.4}$$

In Equation (C.2), Darcy velocity and pressure head can be approximated by

$$q_{fx}(x,y,z,t) \approx \hat{q}_{fx}(x,y,z,t) = \sum_{j=1}^{8} q_{fx,j} w_j(x,y,z) \quad j=1,2,\ldots,8 \tag{C.5}$$

$$\psi(x,y,z,t) \approx \tilde{\psi}(x,y,z,t) = \sum_{j=1}^{8} \psi_j w_j(x,y,z) \quad j=1,2,\ldots,8 \tag{C.6}$$

where w is an approximation function. When Equations (C.5) and (C.6) are substituted into Equation (C.2), the residual for Equation (C.2) can be written by

$$\begin{aligned} R(x,y,z,t) = \hat{q}_{fx} &+ \frac{\rho_R g K_{xx} k_{rf}}{\mu_w} \frac{\partial \hat{\psi}_f}{\partial x} + \frac{\rho_R g K_{xy} k_{rf}}{\mu_w} \frac{\partial \hat{\psi}_f}{\partial y} \\ &+ \frac{\rho_R g K_{xz} k_{rf}}{\mu_w} \left(\frac{\partial \hat{\psi}_f}{\partial z} + \frac{\rho_f}{\rho_R} \frac{\partial z}{\partial z} \right) \end{aligned} \tag{C.7}$$

For the Galerkin residual technique, the weighted residual equations are of the general form:

$$\int_\Omega R(\hat{q}_f(x,y,z,t)) w_i(x,y,z) dxdydz = 0 \qquad i = 1,2,3,\ldots,N \tag{C.8}$$

where Ω is a three-dimensional domain, and N is total number of nodes.

Substitution of Equation (C.7) into the residual $R(\hat{q}_f(x,y,z,t))$ yields:

$$\begin{aligned} \int_\Omega \Bigg\{ &\sum_{j=1}^{8} V_{fxj} w_j + \frac{\rho_R g K_{xx} k_{rf}}{\mu_w} \frac{\partial}{\partial x} \left(\sum_{k=1}^{8} \psi_{fk} w_k \right) + \frac{\rho_R g K_{xy} k_{rf}}{\mu_w} \frac{\partial}{\partial y} \left(\sum_{k=1}^{8} \psi_{fk} w_k \right) \\ &+ \frac{\rho_R g K_{xz} k_{rf}}{\mu_w} \left(\frac{\partial}{\partial z} \left(\sum_{k=1}^{8} \psi_{fk} w_k \right) + \frac{\rho_f}{\rho_R} \frac{\partial z}{\partial z} \right) \Bigg\} w_i d\Omega = 0 \end{aligned} \tag{C.9}$$

Equation (C.9) can be rewritten in the form of element matrix:

$$\left[A^e\right] \left\{q_{fx}\right\} = \left\{B^e\right\} \tag{C.10}$$

where

$$\left[A^e\right] = \int_{\Omega^e} w_i w_j d\Omega^e \tag{C.11}$$

$$\left\{B^e\right\} = -\int_{\Omega^e} \left\{ \frac{\rho_R g K_{xx} k_{rf}}{\mu_w} \left(\sum_{k=1}^{8} \psi_{fk} \frac{\partial w_k}{\partial x} \right) + \frac{\rho_R g K_{xy} k_{rf}}{\mu_w} \left(\sum_{k=1}^{8} \psi_{fk} \frac{\partial w_k}{\partial y} \right) + \frac{\rho_R g K_{xz} k_{rf}}{\mu_w} \left(\left(\sum_{k=1}^{8} \psi_{fk} \frac{\partial w_k}{\partial z} \right) + \frac{\rho_f}{\rho_R} \frac{\partial z}{\partial z} \right) \right\} w_i d\Omega^e \tag{C.12}$$

If principal permeability directions match with principal coordinate directions, K_{xy}, K_{xz}, K_{yx}, K_{yz}, K_{zx}, and K_{zy} become zero. Finally, the form of element matrix in all directions (*x*-, *y*-, and *z*-direction) can be summarized as follows:

In *x*-direction,

$$\left[A^e\right] \left\{q_{fx}\right\} = \left\{B^e\right\} \tag{C.13}$$

where

$$\left\{B^e\right\} = -\int_{\Omega^e} \left\{ \frac{\rho_R g K_{xx} k_{rf}}{\mu_w} \left(\sum_{k=1}^{8} \psi_f \frac{\partial w_k}{\partial x} \right) \right\} w_i d\Omega^e \ . \tag{C.14}$$

The form of element matrix in *y*- and *z*-direction can be obtained in the same manner done in *x*-direction. In *y*-direction,

$$\left[A^e\right] \left\{q_{fy}\right\} = \left\{B^e\right\} \tag{C.15}$$

where

$$\left\{B^e\right\} = -\int_{\Omega^e} \left\{ \frac{\rho_R g K_{yy} k_{rf}}{\mu_w} \left(\sum_{k=1}^{8} \psi_f \frac{\partial w_k}{\partial y} \right) \right\} w_i d\Omega^e \ . \tag{C.16}$$

For *z*-direction,

$$\left[A^e\right] \left\{V_{fz}\right\} = \left\{B^e\right\} \tag{C.17}$$

where

$$\left\{B^e\right\} = -\int_{\Omega^e} \left\{ \frac{\rho_R g K_{zz} k_{rf}}{\mu_w} \left(\left(\sum_{k=1}^{8} \psi_f \frac{\partial w_k}{\partial z} \right) + \frac{\rho_f}{\rho_R} \frac{\partial z}{\partial z} \right) \right\} w_i d\Omega^e \ . \tag{C.18}$$

APPENDIX D

TIME DERIVATIVES IN FLOW AND TRANSPORT EQUATIONS

Contaminant transport equation (Parabolic equation) can be expressed in the form of element matrix as follows:

$$[M_{\text{conductance}}]\{C\} + [M_{mass}]\left\{\frac{\partial C}{\partial t}\right\} = \{\mathbf{F}\} \tag{D.1}$$

where the conductance matrix $[M_{\text{conductance}}] = [M_{Diffusion}] + [M_{Advection}]$ and $[M_{mass}]$ is a mass storage matrix for a time derivative. The most commonly used method for solving Equation (D.1) is the *α family of approximation*, in which a weighted average of the time derivative of a dependent variable is approximated at two consecutive time steps by linear interpolation of the values of the variable at the two steps [Reddy, 1984]:

$$\alpha\left\{\frac{\partial C}{\partial t}\right\}_{s+1} + (1-\alpha)\left\{\frac{\partial C}{\partial t}\right\}_{s} = \frac{\{C\}_{s+1} - \{C\}_{s}}{\Delta t_{s+1}} \qquad for\ 0 \le \alpha \le 1 \tag{D.2}$$

where $\{\}_s$ refers the value of the enclosed quantity at time $t = t_s = \sum_{i=1}^{s} \Delta t_i$, and $\Delta t_s = t_s - t_{s-1}$ is the *s*th time step. If the time interval [0, T_0] is divided into equal time steps then $t_s = s\Delta t$.

Equation (D.2) can be interpreted as Taylor's expansion or finite difference. Using Taylor's expansion,

$$C\ (x_0 + h) = C(x_0) + hf(x_0, C(x_0)) + \frac{h^2}{2!} f'(x_0, C(x_0)) + \ldots + \frac{h^n}{n!} f^{n-1}(x_0, C(x_0)) \tag{D.3}$$

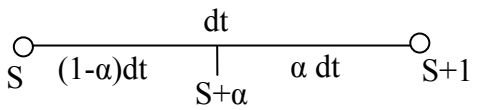

Figure D.1 Schematic for time derivatives

The $C_{S+\alpha}$ can be estimated in two ways as follows:

$$C_{S+\alpha}(t) = C_S(t_0) + (1-\alpha)\ dt\ f(t_0, C(t_0)) + \frac{((1-\alpha)\,dt)^2}{2!} f'(t_0, C(t_0)) + \ldots\ldots \tag{D.4}$$

$$C_{S+\alpha}(t) = C_{S+1}(t_1) - \alpha\, dt\, f(t_1, C(t_1)) + \frac{(-\alpha\, dt)^2}{2!} f'(t_1, C(t_1)) + \ldots\ldots \tag{D.5}$$

Ignoring from the second derivative in both Equations (D.4) and (D.5) and subtracting from Equation (D.4) to Equation (D.5) yield

$$\alpha\, f(t_1, C(t_1)) + (1-\alpha) f(t_0, C(t_0)) = \frac{C_{S+1}(t_1) - C_S(t_0)}{dt} \tag{D.6}$$

Using the finite difference technique,

$$\{C\}_{s+1} = \{C\}_s + \Delta t \left\{\frac{\partial C}{\partial t}\right\}_{s+\alpha} \tag{D.7}$$

$$\left\{\frac{\partial C}{\partial t}\right\}_{s+\alpha} = (1-\alpha)\left\{\frac{\partial C}{\partial t}\right\}_s + \alpha\left\{\frac{\partial C}{\partial t}\right\}_{s+1} \quad for\ 0 \le \alpha \le 1 \tag{D.8}$$

For different values of α, we obtain the following well-known numerical integration schemes [Reddy, 1984]:

$$\alpha = \begin{cases} 0, & \text{the forward difference (or Euler) scheme (Conditionally stable);}\ O(\Delta t) \\ \dfrac{1}{2}, & \text{the Crank - Nicolson scheme (stable)} : O((\Delta t)^2) \\ \dfrac{2}{3}, & \text{the Galerkin method (stable);}\ O((\Delta t)^2) \\ 1, & \text{the backward difference scheme (stable);}\ O(\Delta t) \end{cases} \tag{D.9}$$

Equation (D.2) can be used to reduce Equation (D.1) to algebraic equations among C at time t_{s+1}. Since Equation (D.1) is valid for any $t > 0$, it is valid for $t = t_s$ and $t = t_{s+1}$:

$$\left[M_{\text{conductance}}\right]_s \{C\}_s + \left[M_{mass}\right]\left\{\frac{\partial C}{\partial t}\right\}_s = \{\mathbf{F}\}_s \quad \text{at time step } t = t_{s+1} \tag{D.10}$$

$$\left[M_{\text{conductance}}\right]_{s+1}\{C\}_{s+1}+\left[M_{mass}\right]\left\{\frac{\partial C}{\partial t}\right\}_{s+1}=\{\mathbf{F}\}_{s+1}\quad\text{at time step } t=t_{\text{s}} \tag{D.11}$$

where it is assumed that mass matrix $[M_{\text{mass}}]$ is independent of time.

We multiply both sides of Equation (D.2) with $[M_{\text{mass}}]$ and obtain

$$\alpha\left[M_{mass}\right]\left\{\frac{\partial C}{\partial t}\right\}_{s+1}+(1-\alpha)\left[M_{mass}\right]\left\{\frac{\partial C}{\partial t}\right\}_{s}=\frac{\left[M_{mass}\right]\{C\}_{s+1}-\left[M_{mass}\right]\{C\}_{s}}{\Delta t_{s+1}} \tag{D.12}$$

Substituting for $\left[M_{\text{mass}}\right]\left\{\frac{\partial C}{\partial t}\right\}_{s+1}$ and $\left[M_{\text{mass}}\right]\left\{\frac{\partial C}{\partial t}\right\}_{s}$ from Equation (D.10) and (D.11) into Equation (D.12) yields

$$\begin{aligned}&\alpha\left(\{\mathbf{F}\}_{s+1}-\left[M_{\text{conductance}}\right]_{s+1}\{C\}_{s+1}\right)+(1-\alpha)\left(\{\mathbf{F}\}_{s}-\left[M_{\text{conductance}}\right]_{s}\{C\}_{s}\right)\\&=\frac{\left[M_{mass}\right]\{C\}_{s+1}-\left[M_{mass}\right]\{C\}_{s}}{\Delta t_{s+1}}\end{aligned} \tag{D.13}$$

Rearranging the terms into known and unknown ones, finally we obtain

$$\begin{aligned}&\left(\alpha\left[M_{\text{conductance}}\right]_{s+1}+\frac{\left[M_{mass}\right]}{\Delta t_{s+1}}\right)\{C\}_{s+1}\\&=\left((\alpha-1)\left[M_{\text{conductance}}\right]_{s}+\frac{\left[M_{mass}\right]}{\Delta t_{s+1}}\right)\{C\}_{s}+(1-\alpha)\{\mathbf{F}\}_{s}+\alpha\{\mathbf{F}\}_{s+1}\end{aligned} \tag{D.14}$$

If $\{\mathbf{F}\}$ is invariant over time and Δt is constant, Equation (D.14) can be simplified as follows:

$$\left(\alpha\left[M_{\text{conductance}}\right]_{s+1}+\frac{\left[M_{mass}\right]}{\Delta t}\right)\{C\}_{s+1}=\left((\alpha-1)\left[M_{\text{conductance}}\right]_{s}+\frac{\left[M_{mass}\right]}{\Delta t}\right)\{C\}_{s}+\{\mathbf{F}\} \tag{D.15}$$

APPENDIX E

MATERIAL BALANCE CALCULATION

Mass balance calculation is used to determine the fate (distribution) of contaminants in each phase over time and to verify mass conservation in the model. The calculation scheme was well described by Huyakorn and Pinder [1983], and it was used by Mendoza and Frind [1990]. As an example, consider the transport of a reactive species in the variably saturated zone. The governing equation can be written as

$$\nabla\left[\phi s D\,\nabla C\right]-\nabla\left(qC\right)-\frac{\partial}{\partial t}\left(\phi s R C\right)-\phi s\lambda C-M=0 \tag{E.1}$$

where ϕ is porosity, s is saturation degree, D is a dispersion coefficient [L^2T^{-1}], C is contaminant concentration [ML^{-3}], q is Darcy velocity [LT^{-1}], R is a retardation coefficient, λ is a decay coefficient [T^{-1}], and M is the contribution of point sources/sinks in domains. The M can be expressed as

$$M=\sum_{l=1}^{n_w} Q_i\delta\left(x-x_l,y-y_l,z-z_l\right)C_l^* \tag{E.2}$$

where Q and C^* are the flow rate [L^3T^{-1}] and concentration at wells, n_w is the number of wells, and δ is the Dirac delta function.

The mass balance over the whole domain Ω is obtained by integrating equation (E.1) and applying Green's theorem to both the dispersive and advective terms. Thus we obtains

$$\int_\Gamma\left(qC-\phi sD\nabla C\right)n_i d\Gamma+\int_\Omega\frac{\partial}{\partial t}\left(\phi sRC\right)d\Omega+\int_\Omega\phi s\lambda C d\Omega+\sum_{l=1}^{n_w}\left(Q_l C_l^*\right)=0 \tag{E.3}$$

where n_i is the outward vector normal to the boundary. The first term in Equation (E.3) represents the net material flux across the whole boundary. The second and third integrals represent, respectively, the rate of mass storage and the rate of mass decay in domain Ω. The last term represents the net rate of mass production owing to well injection and pumping.

If an approximate finite element solution $\hat{C} = C_j(t)w_j(x,y,z)$ is substituted, the rate of material loss $\dot{\varepsilon}_M$ can be evaluated as follows:

$$\dot{\varepsilon}_M \equiv \int_\Gamma \left(q\hat{C} - \phi s D \nabla \hat{C}\right) n_i d\Gamma + \int_\Omega \phi s \left(R\frac{\partial C_j}{\partial t} + \lambda C_j \right) w_j d\Omega + \sum_{l=1}^{n_w} \left(Q_l C_l^*\right) \tag{E.4}$$

The properties of the basis functions for element and boundary will be:

$$\sum_{i^*=1}^{n_B} w_{i^*}(x,y,z) = 1 \qquad \text{for all } x, y, z \text{ on } \Gamma \tag{E.5}$$

$$\sum_{i=1}^{n} w_i(x,y,z) = 1 \qquad \text{for all } x, y, z \text{ on } \Omega \tag{E.6}$$

where n_B is the number of nodes on the whole boundary and n is the total number of nodes in the whole solution region. Combination of equations (E.4)-(E.6) yields

$$\dot{\varepsilon}_M \equiv \sum_{i^*=1}^{n_B} \int_\Gamma \left(q\hat{C} - \phi s D \nabla \hat{C}\right) n_i w_{i^*} d\Gamma + \sum_{i=1}^{n} \int_\Omega \phi s \left(R\frac{\partial C_j}{\partial t} + \lambda C_j \right) w_i w_j d\Omega + \sum_{l=1}^{n_w} \left(Q_l C_l^*\right) \tag{E.7}$$

Equation (E.7) can be expressed in a simple form as

$$\dot{\varepsilon}_M \equiv \sum_{i^*=1}^{n_B} F_{i^*}^B + \sum_{i=1}^{n} \int_\Omega F_i^\Omega + \sum_{l=1}^{n_w} F_l^w \tag{E.8}$$

where

$$F_{i^*}^B = \int_\Gamma \left(q\hat{C} - \phi s D \nabla \hat{C}\right) n_i w_{i^*} d\Gamma \tag{E.9a}$$

$$F_i^{\Omega} = \int_{\Omega} \phi s \left(R \frac{\partial C_j}{\partial t} + \lambda C_j \right) w_i w_j d\Omega \tag{E.9b}$$

$$F_l^{w} = \sum_{l=1}^{n_w} \left(Q_l C_l^* \right). \tag{E.9c}$$

The F_i^{Ω} and F_l^{w} can be directly evaluated in elements. The boundary material flux, F_{i*}^{B}, is determined by boundary conditions.

[B.C. Type I] For a first-type boundary condition, the dispersive boundary nodal flux is not known explicitly and should be computed by back substitution of $\hat{C}$ into the nonboundary integral terms of the original finite element approximation of the transport equation at node *i**. Once the dispersive nodal flux, Q_{ci*}^{D}, has been computed, the outward advective flux is obtained from

$$q\hat{C}n_i = q_n C_i w_i \tag{E.10}$$

where q_n is the outward normal fluid flux distribution. The total boundary nodal flux is obtained from

$$F_{i*}^{B} \cong C_{i*} \int_{\Gamma} q_n w_i w_{i*} d\Gamma + Q_{ci*}^{D} \tag{E.11}$$

[B.C. Type II] For a second-type boundary condition, the outward dispersive flux distribution is prescribed as

$$-\phi s D \frac{\partial \hat{C}}{\partial n} = q_c^{D} \tag{E.11}$$

and the outward advective flux is obtained at equation (E.10).

The total boundary nodal flux is

$$F_{i*}^{B} = \int_{\Gamma} \left(q_n C_i \, w_i + q_c^{D} \right) w_{i*} d\Gamma \tag{2.13}$$

[B.C. Type III] For a third-type boundary condition, the total material flux distribution is prescribed as

$$\left(V_i \hat{C} - \phi D_{ij} \frac{\partial \hat{C}}{\partial x_j} \right) n_i = q_c^T \tag{E.14}$$

and thus F_{i*}^B is given explicitly by

$$F_{i*}^B = \int_\Gamma q_c^T w_{i*} d\Gamma \tag{E.15}$$

Cumulative mass balance error at a current time level, ε_M^{t+1}, will be computed by

$$\varepsilon_M^{t+1} = \sum_{k=1}^{t} \left(\dot{\varepsilon}_M \Delta t \right)^k \tag{E.16}$$

where *k* is the time level.

Either ε_M^{t+1} or its normalized form $\widetilde{\varepsilon}_M^{t+1}$ can be used as an indicator of the global accuracy of the numerical solution of the transport equation. The $\widetilde{\varepsilon}_M^{t+1}$ is defined as

$$\widetilde{\varepsilon}_M^{t+1} = \sum_{k=1}^{t} \left\{ \left(\dot{\varepsilon}_M \Delta t \right)^k \Big/ \left[\Delta t \left(\sum_{i=1}^{n} \left| F_i^{\Omega} \right| + \sum_{l=1}^{n_w} \left| F_{i'}^{w} \right| + \sum_{i*=1}^{n} \left| F_{i*}^{B} \right| \right) \right] \right\}. \tag{E.17}$$

REFERENCES

Abriola, L. M. (1989), Modeling Multiphase Migration of Organic-Chemicals in Groundwater Systems - a Review and Assessment, *Environmental Health Perspectives,* 83117-143.

Abriola, L. M., J. Lang, and K. Rathfelder. 1997. Michigan soil vapor extraction remediation (MISER) model: a computer program to model soil vapor extraction and bioventing of organic chemicals in unsaturated geological material. U.S. Environmental Protection Agency, Ada, OK.

Adenekan, A. E., T. W. Patzek, and K. Pruess (1993), Modeling of Multiphase Transport of Multicomponent Organic Contaminants and Heat in the Subsurface - Numerical-Model Formulation, *Water Resources Research,* 29(11), 3727-3740.

Aelion, C. M., and B. C. Kirtland (2000), Physical versus biological hydrocarbon removal during air sparging and soil vapor extraction, *Environmental Science & Technology,* 34(15), 3167-3173.

Aelion, C. M., B. C. Kirtland, and P. A. Stone (1997), Radiocarbon assessment of aerobic petroleum bioremediation in the vadose zone and groundwater at an AS/SVE site, *Environmental Science & Technology,* 31(12), 3363-3370.

Ahlfeld, D. P., A. Dahmani, and W. Ji (1994), A Conceptual-Model of Field Behavior of Air Sparging and Its Implications for Application, *Ground Water Monitoring and Remediation,* 14(4), 132-139.

Alexander, M. 1994. Biodegradation and bioremediation. Academic Press, San Diego.

Altevogt, A. S., D. E. Rolston, and R. T. Venterea (2003), Density and pressure effects on the transport of gas phase chemicals in unsaturated porous media, *Water Resources Research,* 39(3), 1061, doi:1010.1029/2002WR001338.

Alvarez-Cohen, L., and G. E. Speitel (2001), Kinetics of aerobic cometabolism of chlorinated solvents, *Biodegradation,* 12(2), 105-126.

Ataie-Ashtiani, B., S. M. Hassanizadeh, and M. A. Celia (2002), Effects of heterogeneities on capillary pressure-saturation-relative permeability relationships, *Journal of Contaminant Hydrology,* 56(3-4), 175-192.

ATSDR. 1997. Toxicological profile for trichloroethylene, United States. Agency for Toxic Substances and Disease Registry (ATSDR), Atlanta, Ga., U.S.

Auer, L. H., N. D. Rosenberg, K. H. Birdsell, and E. M. Whitney (1996), The effects of barometric pumping on contaminant transport, *Journal of Contaminant Hydrology,* 24(2), 145-166.

Barrio-Lage, G., F. Z. Parsons, and R. S. Nassar (1987), Kinetics of the Depletion of Trichloroethene, *Environmental Science & Technology,* 21(4), 366-370.

Bass, D. H., N. A. Hastings, and R. A. Brown (2000), Performance of air sparging systems: a review of case studies, *Journal of Hazardous Materials,* 72(2-3), 101-119.

Bear, J. 1972. Dynamics of fluids in porous media. American Elsevier, New York,.

Bear, J. 1979. Hydraulics of groundwater. McGraw-Hill International Book, New York.

Bear, J., and Y. Bachmat. 1990. Introduction to modeling of transport phenomena in porous media. Kluwer Academic Publishers, Dordrecht ; Boston.

Benner, M. L., R. H. Mohtar, and L. S. Lee (2002), Factors affecting air sparging remediation systems using field data and numerical simulations, *Journal of Hazardous Materials,* 95(3), 305-329.

Benner, M. L., S. M. Stanford, L. S. Lee, and R. H. Mohtar (2000), Field and numerical analysis of in-situ air sparging: a case study, *Journal of Hazardous Materials,* 72(2-3), 217-236.

Blount, G. C., C. C. Caldwell, J. E. Cardoso-Neto, K. R. Conner, G. T. Jannik, C. E. M. Jr., D. C. Noffsinger, and J. A. Ross (2002), The Use of Natural Systems to Remediate Groundwater: Department of Energy Experience at the Savannah River Site, *Remediation,* 12(3), 43-61.

Borch, T., P. Ambus, F. Laturnus, B. Svensmark, and C. Gron (2003), Biodegradation of chlorinated solvents in a water unsaturated topsoil, *Chemosphere,* 51(2), 143-152.

Braida, W., and S. K. Ong (2000), Modeling of air sparging of VOC-contaminated soil columns, *Journal of Contaminant Hydrology,* 41(3-4), 385-402.

Brockman, F. J., W. Payne, D. J. Workman, A. Soong, S. Manley, and T. C. Hazen (1995), Effect of Gaseous Nitrogen and Phosphorus Injection on in-Situ Bioremediation of a Trichloroethylene-Contaminated Site, *Journal of Hazardous Materials,* 41(2-3), 287-298.

Brooks, R. H., and A. T. Corey (1964), Hydraulic Properties of Porous Media, *Hydrology Paper 3., 27 pp., Colorado State University, Fort Collins, Co.*

Bruce, C. L., C. D. Gilbert, R. L. Johnson, and P. C. Johnson. 1998. Methyl tert-butyl ether removal by in situ air sparging in physical model studies. in *International Conference on Remediation of Chlorinated Recalcitrant Compounds, Monterey*

California, May 18-21, 1998. edited by G. B. Wickramanayake and R. E. Hinchee, Battell Press

Burns, S. E., and M. Zhang (1999), Digital image analysis to assess microbubble behavior in porous media, *Journal of Computing in Civil Engineering,* 13(1), 43-48.

Celia, M. A., E. T. Bouloutas, and R. L. Zarba (1990), A General Mass-Conservative Numerical-Solution for the Unsaturated Flow Equation, *Water Resources Research,* 26(7), 1483-1496.

Celia, M. A., P. C. Reeves, and L. A. Ferrand (1995), Recent Advances in Pore Scale Models for Multiphase Flow in Porous-Media, *Reviews of Geophysics,* 331049-1057.

Chen, M. R., R. E. Hinkley, and J. E. Killough (1996), Computed tomography imaging of air sparging in porous media, *Water Resources Research,* 32(10), 3013-3024.

Clayton, W. S. (1999), Effects of pore scale dead-end air fingers on relative permeabilities for air sparging in soils, *Water Resources Research,* 35(10), 2909-2919.

Clement, T. P. 1997. RT3D-A modular computer code for simulating reactive multi-species reactive transport in 3-dimensional groundwater aquifers, Pacific Northwest National Laboratory Report, PNNL-11720.

Clement, T. P., C. D. Johnson, Y. W. Sun, G. M. Klecka, and C. Bartlett (2000), Natural attenuation of chlorinated ethene compounds: model development and field-scale application at the Dover site, *Journal of Contaminant Hydrology,* 42(2-4), 113-140.

Coleman, N. V., T. E. Mattes, J. M. Gossett, and J. C. Spain (2002), Phylogenetic and kinetic diversity of aerobic vinyl chloride-assimilating bacteria from contaminated sites, *Applied and Environmental Microbiology,* 68(12), 6162-6171.

Conant, B. H., R. W. Gillham, and C. A. Mendoza (1996), Vapor transport of trichloroethylene in the unsaturated zone: Field and numerical modeling investigations, *Water Resources Research,* 32(1), 9-22.

Corapcioglu, M. Y., and A. L. Baehr (1987), A Compositional Multiphase Model for Groundwater Contamination by Petroleum-Products .1. Theoretical Considerations, *Water Resources Research,* 23(1), 191-200.

Corapcioglu, M. Y., A. Cihan, and M. Drazenovic (2004), Rise velocity of an air bubble in porous media: Theoretical studies, *Water Resources Research,* 40(4), doi:10.1029/2003WR002618.

Cupples, A. M., A. M. Spormann, and P. L. McCarty (2004), Comparative evaluation of chloroethene dechlorination to ethene by Dehalococcoides-like microorganisms, *Environmental Science & Technology,* 38(18), 4768-4774.

Daus, A. D., E. O. Frind, and E. A. Sudicky (1985), Comparative Error Analysis in Finite-Element Formulations of the Advection-Dispersion Equation, *Advances in Water Resources,* 8(2), 86-95.

Davis, E. L. 1997. How heat can enhance in-situ soil and aquifer remediation: Importnat chemical properties and guidance on choosing the appropriate technique, Ground Water Issue EPA/540/S-97/502. U.S. EPA.

Davis, J. W., J. M. Odom, K. A. DeWeerd, D. A. Stahl, S. S. Fishbain, R. J. West, G. M. Klecka, and J. G. DeCarolis (2002), Natural attenuation of chlorinated solvents at Area 6, Dover Air Force Base: characterization of microbial community structure, *Journal of Contaminant Hydrology,* 57(1-2), 41-59.

Demond, A. H., and P. V. Roberts (1991), Effect of Interfacial Forces on 2-Phase Capillary Pressure-Saturation Relationships, *Water Resources Research,* 27(3), 423-437.

Diersch, H. J. G., and O. Kolditz (2002), Variable-density flow and transport in porous media: approaches and challenges, *Advances in Water Resources,* 25(8-12), 899-944.

Diersch, H. J. G., and P. Perrochet (1999), On the primary variable switching technique for simulating unsaturated-saturated flows, *Advances in Water Resources,* 23(3), 271-301.

Dinicola, R. S., United States. Navy. Engineering Field Activity Northwest., and Geological Survey (U.S.). 2002. Natural attenuation of chlorinated volatile organic compounds in ground water at Operable Unit 1, Naval Undersea Warfare Center, Division Keyport, Washington. U.S., Information Services distributor, Tacoma, Wash., Denver, Colo.

Domenico, P. A. (1987), An Analytical Model for Multidimensional Transport of a Decaying Contaminant Species, *Journal of Hydrology,* 91(1-2), 49-58.

Dyer, M. (2003), Field investigation into the biodegradation of TCE and BTEX at a former metal plating works, *Engineering Geology,* 70(3-4), 321-329.

El-kadi, A. I., and G. Ling (1993), The Courant and Peclet Number Criteria for the Numerical-Solution of the Richards Equation, *Water Resources Research,* 29(10), 3485-3494.

EPA. 1991. In Situ Steam/Hot-Air Stripping Technology, Applications Analysis Report, EPA 540/A5-90/008. *in*.

EPA. 1995a. Bioventing Principles and Practices: Bioventing Desing, EPA/540/R-95/534a, Office of Research and Development, US Environmental Protection Agency, Washington, DC., 80pp.

EPA. 1995b. In situ steam enhanced recovery process, Hughes Environmental Systems, Inc. EPA/540/R-94/510, U.S. Environmental Protection Agency.

EPA. 2000a. National water quality inventory, 1998 Report to Congress, Ground water and drinking water chapter, EPA 816-R-00-013. United States. Environmental Protection Agency (EPA). Office of Water, Washington, D.C. U.S.A.

EPA. 2000b. Title 40 - Protection of Environment, CHAPTER I--ENVIRONMENTAL PROTECTION AGENCY, PART 141--NATIONAL PRIMARY DRINKING WATER REGULATIONS.

EPA. 2004. How to Evaluate Alternative Cleanup Technologies for Underground Storage Tank Sites: A Guide for Corrective Action Plan Reviewers. (EPA 510-B-94-003; EPA 510-B-95-007; and EPA 510-R-04-002). United States. Environmental Protection Agency (EPA). Washington, D.C. U.S.A.

Essaid, H. I., B. A. Bekins, E. M. Godsy, E. Warren, M. J. Baedecker, and I. M. Cozzarelli (1995), Simulation of aerobic and anaerobic biodegradation processes at a crude oil spill site, *Water Resources Research,* 31(12), 3309-3327.

Falta, R. W. (2000), Numerical modeling of kinetic interphase mass transfer during air sparging using a dual-media approach, *Water Resources Research,* 36(12), 3391-3400.

Falta, R. W., I. Javandel, K. Pruess, and P. A. Witherspoon (1989), Density-Driven Flow of Gas in the Unsaturated Zone Due to the Evaporation of Volatile Organic-Compounds, *Water Resources Research,* 25(10), 2159-2169.

Falta, R. W., K. Pruess, and S. Finsterle. 1995. T2VOC User's Guide, Lawrence Berkeley Lab. Rep. LBL-36400 UC-400, Berkeley, CA.

Falta, R. W., K. Pruess, I. Javandel, and P. A. Witherspoon (1992a), Numerical Modeling of Steam Injection for the Removal of Nonaqueous Phase Liquids from the Subsurface .1. Numerical Formulation, *Water Resources Research,* 28(2), 433-449.

Falta, R. W., K. Pruess, I. Javandel, and P. A. Witherspoon (1992b), Numerical Modeling of Steam Injection for the Removal of Nonaqueous Phase Liquids from the

Subsurface .2. Code Validation and Application, *Water Resources Research,* 28(2), 451-465.

Fang, Y. L., G. T. Yeh, and W. D. Burgos (2003), A general paradigm to model reaction-based biogeochemical processes in batch systems, *Water Resources Research,* 39(4), -.

Fennell, D. E., and J. M. Gossett (1998), Modeling the production of and competition for hydrogen in a dechlorinating culture, *Environmental Science & Technology,* 32(16), 2450-2460.

Forsyth, P. A., and B. Y. Shao (1991), Numerical-Simulation of Gas Venting for Napl Site Remediation, *Advances in Water Resources,* 14(6), 354-367.

Fotinich, A., V. K. Dhir, and S. Lingineni (1999), Remediation of simulated soils contaminated with diesel, *Journal of Environmental Engineering-Asce,* 125(1), 36-46.

Freedman, D. L., and J. M. Gossett (1989), Biological Reductive Dechlorination of Tetrachloroethylene and Trichloroethylene to Ethylene under Methanogenic Conditions, *Applied and Environmental Microbiology,* 55(9), 2144-2151.

Frind, E. O. (1982), Simulation of long-term transient density-dependent transport in groundwater, *Advances in Water Resources,* 5(2), 73-88.

Frind, E. O. (1988), Solution of the Advection-Dispersion equation with free exit Boundary, *Numerical methods for partial differential equations,* 4301-313.

Gauglitz, P. A., J. S. Roberts, T. M. Bergsman, S. M. Carley, W. O. Heath, M. C. Miller, R. W. Moss, R. Schalla, M. H. Schlender, T. R. Jarosch, C. A. Eddy-Dilek, and B. B. Looney. 1994. Field test of six phase soil heating at the Savannah river site. *in* G. W. Gee and N. R. Wing, editors. Thirty-third Hanford symposium on health and the environment: In situ remediation: Scientific basis for current and future technolgies. Part 2.

Glascoe, L. G., S. J. Wright, and L. M. Abriola (1999), Modeling the influence of heat/moisture exchange during bioventing, *Journal of Environmental Engineering-Asce,* 125(12), 1093-1102.

Gossett, J. M. (1987), Measurement of Henrys Law Constants for C1 and C2 Chlorinated Hydrocarbons, *Environmental Science & Technology,* 21(2), 202-208.

Gudbjerg, J., T. O. Sonnenborg, and K. H. Jensen (2004), Remediation of NAPL below the water table by steam-induced heat conduction, *Journal of Contaminant Hydrology,* 72(1-4), 207-225.

Gwo, J. P., E. F. D'Azevedo, H. Frenzel, M. Mayes, G. T. Yeh, P. M. Jardine, K. M. Salvage, and F. M. Hoffman (2001), HBGC123D: a high-performance computer model of coupled hydrogeological and biogeochemical processes, *Computers & Geosciences,* 27(10), 1231-1242.

Gwo, J. P., and G. T. Yeh (1996), A parallel 3-dimensional HYDROGEOCHEM and an application to a proposed waste disposal site at the Oak Ridge National Laboratory, *EOS Transactions American Geophysics Union,* 77(46), F203.

Hart, D. P., and R. Couvillion. 1986. Earth-coupled heat transfer. National Water Well Association, Dublin, OH.

Haston, Z. C., and P. L. McCarty (1999), Chlorinated ethene half-velocity coefficients (K-s) for reductive dehalogenation, *Environmental Science & Technology,* 33(2), 223-226.

He, J. Z., K. M. Ritalahti, K. L. Yang, S. S. Koenigsberg, and F. E. Loffler (2003), Detoxification of vinyl chloride to ethene coupled to growth of an anaerobic bacterium, *Nature,* 424(6944), 62-65.

Hecht, V., D. Brebbermann, P. Bremer, and W. D. Deckwer (1995), Cometabolic Degradation of Trichloroethylene in a Bubble-Column Bioscrubber, *Biotechnology and Bioengineering,* 47(4), 461-469.

Hendrickson, E. R., J. A. Payne, R. M. Young, M. G. Starr, M. P. Perry, S. Fahnestock, D. E. Ellis, and R. C. Ebersole (2002), Molecular analysis of Dehalococcoides 16S ribosomal DNA from chloroethene-contaminated sites throughout north America and Europe, *Applied and Environmental Microbiology,* 68(2), 485-495.

Heron, G., J. S. Gierke, B. Faulkner, S. Mravik, L. Wood, and C. G. Enfield (2002), Pulsed air sparging in aquifers contaminated with dense nonaqueous phase liquids, *Ground Water Monitoring and Remediation,* 22(4), 73-82.

Heron, G., M. Van Zutphen, T. H. Christensen, and C. G. Enfield (1998), Soil heating for enhanced remediation of chlorinated solvents: A laboratory study on resistive heating and vapor extraction in a silty, low-permeable soil contaminated with trichloroethylene, *Environmental Science & Technology,* 32(10), 1474-1481.

Hinton, E., and D. R. J. Owen. 1979. An introduction to finite element computations. Pineridge Press, Swansea [Wales].

Horvath, R. S. (1972), Microbial Co-Metabolism and Degradation of Organic Compounds in Nature, *Bacteriological Reviews,* 36(2), 146-&.

Hughes, T. J. R. 1987. The finite element method : linear static and dynamic finite element analysis. Prentice-Hall, Englewood Cliffs, N.J.

Hughes, W. D., and P. I. Dacyk. 1998. Air sparging of chlorinated volatile organic compounds in a layered geologic setting. in *International Conference on Remediation of Chlorinated Recalcitrant Compounds, Monterey California, May 18-21, 1998*. edited by G. B. Wickramanayake and R. E. Hinchee, Battell Press

Huyakorn, P. S., S. Panday, and Y. S. Wu (1994), A 3-Dimensional Multiphase Flow Model for Assessing Napl Contamination in Porous and Fractured Media .1. Formulation, *Journal of Contaminant Hydrology,* 16(2), 109-130.

Huyakorn, P. S., and G. F. Pinder. 1983. Computational methods in subsurface flow. Academic Press, New York.

Islam, K. M. M., and J. J. Kaluarachchi (1995), Thermal Venting to Recover Less-Volatile Hydrocarbons from the Unsaturated Zone .2. Model Applications, *Journal of Contaminant Hydrology,* 17(4), 313-331.

Jang, W., and M. M. Aral (2003), Concentration Evolution of Gas Species within a Collapsing Bubble in a Liquid Medium, *Environmental Fluid Mechanics,* 3(3), 173-193.

Jellali, S., H. Benremita, P. Muntzer, O. Razakarisoa, and G. Schafer (2003), A large-scale experiment on mass transfer of trichloroethylene from the unsaturated zone of a sandy aquifer to its interfaces, *Journal of Contaminant Hydrology,* 60(1-2), 31-53.

Jellali, S., P. Muntzer, O. Razakarisoa, and G. Schafer (2001), Large scale experiment on transport of trichloroethylene in a controlled aquifer, *Transport in Porous Media,* 44(1), 145-163.

Ji, W., A. Dahmani, D. P. Ahlfeld, J. D. Lin, and E. Hill (1993), Laboratory Study of Air Sparging - Air-Flow Visualization, *Ground Water Monitoring and Remediation,* 13(4), 115-126.

Johan, E. T., V. Vlieg, and D. B. Janssen (2001), Formation and detoxification of reactive intermediates in the metabolism of chlorinated ethenes, *Journal of Biotechnology,* 85(2), 81-102.

Johnson, R. L., P. C. Johnson, D. B. Mcwhorter, R. E. Hinchee, and I. Goodman (1993), An Overview of in-Situ Air Sparging, *Ground Water Monitoring and Remediation,* 13(4), 127-135.

Jury, W. A., W. J. Farmer, and W. F. Spencer (1984), Behavior Assessment Model for Trace Organics in Soil .2. Chemical Classification and Parameter Sensitivity, *Journal of Environmental Quality,* 13(4), 567-572.

Jury, W. A., D. Russo, G. Streile, and H. Elabd (1990), Evaluation of Volatilization by Organic-Chemicals Residing Below the Soil Surface, *Water Resources Research,* 26(1), 13-20.

Jury, W. A., W. F. Spencer, and W. J. Farmer (1983), Behavior Assessment Model for Trace Organics in Soil .1. Model Description, *Journal of Environmental Quality,* 12(4), 558-564.

Kaluarachchi, J. J., and K. M. M. Islam (1995), Thermal Venting to Recover Less-Volatile Hydrocarbons from the Unsaturated Zone .1. Theory, *Journal of Contaminant Hydrology,* 17(4), 293-311.

Karapanagioti, H. K., P. Gaganis, and V. N. Burganos (2003), Modeling attenuation of volatile organic mixtures in the unsaturated zone: codes and usage, *Environmental Modelling & Software,* 18(4), 329-337.

Kaslusky, S. F., and K. S. Udell (2002), A theoretical model of air and steam co-injection to prevent the downward migration of DNAPLs during steam-enhanced extraction, *Journal of Contaminant Hydrology,* 55(3-4), 213-232.

Kaviany, M. 1995. Principles of heat transfer in porous media, 2nd edition. Springer-Verlag, New York.

Kerfoot, W. B., C. J. J. M. Schouten, and V. C. M. v. Engen-Beukeboom. 1998. Kinetic analysis of pilot test results of the C-SPARGE Process. in *International Conference on Remediation of Chlorinated Recalcitrant Compounds, Monterey California, May 18-21, 1998*. edited by G. B. Wickramanayake and R. E. Hinchee, Battell Press

Kirtland, B. C., and C. M. Aelion (2000), Petroleum mass removal from low permeability sediment using air sparging/soil vapor extraction: impact of continuous or pulsed operation, *Journal of Contaminant Hydrology,* 41(3-4), 367-383.

Kirtland, B. C., C. M. Aelion, and P. A. Stone (2005), Assessing in situ mineralization of recalcitrant organic compounds in vadose zone sediments using delta C-13 and C-14 measurements, *Journal of Contaminant Hydrology,* 76(1-2), 1-18.

Kirtland, B. C., C. M. Aelion, and M. A. Widdowson (2001), Long-term AS/SVE for petroleum removal in low-permeability Piedmont saprolite, *Journal of Environmental Engineering-Asce,* 127(2), 134-144.

Lee, C. H., J. Y. Lee, W. Y. Jang, Y. H. Jeon, and K. K. Lee (2002), Evaluation of air injection and extraction tests at a petroleum contaminated site, Korea, *Water Air and Soil Pollution,* 135(1-4), 65-91.

Lehmann, F., and P. H. Ackerer (1998), Comparison of iterative methods for improved solutions of the fluid flow equation in partially saturated porous media, *Transport in Porous Media,* 31(3), 275-292.

Leij, F. J., W. B. Russell, and S. M. Lesch (1997), Closed-form expressions for water retention and conductivity data, *Ground Water,* 35(5), 848-858.

Lendvay, J. M., F. E. Loffler, M. Dollhopf, M. R. Aiello, G. Daniels, B. Z. Fathepure, M. Gebhard, R. Heine, R. Helton, J. Shi, R. Krajmalnik-Brown, C. L. Major, M. J. Barcelona, E. Petrovskis, R. Hickey, J. M. Tiedje, and P. Adriaens (2003), Bioreactive barriers: A comparison of bioaugmentation and biostimulation for chlorinated solvent remediation, *Environmental Science & Technology,* 37(7), 1422-1431.

Lenhard, R. J., M. Oostrom, C. S. Simmons, and M. D. White (1995), Investigation of Density-Dependent Gas Advection of Trichloroethylene - Experiment and a Model Validation Exercise, *Journal of Contaminant Hydrology,* 19(1), 47-67.

Lenhard, R. J., J. C. Parker, and J. J. Kaluarachchi (1989), A Model for Hysteretic Constitutive Relations Governing Multiphase Flow .3. Refinements and Numerical Simulations, *Water Resources Research,* 25(7), 1727-1736.

Li, C. W. (1993), A Simplified Newton Iteration Method with Linear Finite-Elements for Transient Unsaturated Flow, *Water Resources Research,* 29(4), 965-971.

Lingineni, S., and V. K. Dhir (1992), Modeling of Soil Venting Processes to Remediate Unsaturated Soils, *Journal of Environmental Engineering-Asce,* 118(1), 135-152.

Lorah, M. M. 1997. Natural attenuation of chlorinated volatile organic compounds in a freshwater tidal wetland, Aberdeen Proving Ground, Maryland. U.S., Branch of Information Services distributor, Baltimore, Md., Denver, CO.

Lundegard, P. D., and G. Andersen (1996), Multiphase numerical simulation of air sparging performance, *Ground Water,* 34(3), 451-460.

Lunn, M., R. J. Lunn, and R. Mackayb (1996), Determining analytic solutions of multiple species contaminant transport, with sorption and decay, *Journal of Hydrology,* 180(1-4), 195-210.

Mackay, D., W. Y. Shiu, and K. C. Ma. 1992. Illustrated handbook of physical-chemical properties and environmental fate for organic chemicals. Lewis Publishers, Boca Raton.

Mackay, D., W. Y. Shiu, A. Maijanen, and S. Feenstra (1991), Dissolution of Nonaqueous Phase Liquids in Groundwater, *Journal of Contaminant Hydrology,* 8(1), 23-42.

Marley, M. C., D. J. Hazebrouck, and M. T. Walsh (1992), The Application of Insitu Air Sparging as an Innovative Soils and Ground-Water Remediation Technology, *Ground Water Monitoring and Remediation,* 12(2), 137-145.

Marulanda, C., P. J. Culligan, and J. T. Germaine (2000), Centrifuge modeling of air sparging -- a study of air flow through saturated porous media, *Journal of Hazardous Materials,* 72(2-3), 179-215.

Maymo-Gatell, X., Y. T. Chien, J. M. Gossett, and S. H. Zinder (1997), Isolation of a bacterium that reductively dechlorinates tetrachloroethene to ethene, *Science,* 276(5318), 1568-1571.

McCray, J. E. (2000), Mathematical modeling of air sparging for subsurface remediation: state of the art, *Journal of Hazardous Materials,* 72(2-3), 237-263.

McCray, J. E., and R. W. Falta (1996), Defining the air sparging radius of influence for groundwater remediation, *Journal of Contaminant Hydrology,* 24(1), 25-52.

McCray, J. E., and R. W. Falta (1997), Numerical simulation of air sparging for remediation of NAPL contamination, *Ground Water,* 35(1), 99-110.

McWhorter, D. B. (1990), Unsteady Radial Flow of Gas in the Vadose Zone, *Journal of Contaminant Hydrology,* 5(3), 297-314.

Mei, C. C., Z. Cheng, and C. O. Ng (2002), A model for flow induced by steady air venting and air sparging, *Applied Mathematical Modelling,* 26(7), 727-750.

Mendoza, C. A., and E. O. Frind (1990a), Advective-Dispersive Transport of Dense Organic Vapors in the Unsaturated Zone .1. Model Development, *Water Resources Research,* 26(3), 379-387.

Mendoza, C. A., and E. O. Frind (1990b), Advective-Dispersive Transport of Dense Organic Vapors in the Unsaturated Zone. 2. Sensitivity Analysis, *Water Resources Research | Water Resour. Res. | Water Resour Res,* 26(3), 388-398.

Mendoza, C. A., and T. A. Mcalary (1990), Modeling of Groundwater Contamination Caused by Organic-Solvent Vapors, *Ground Water,* 28(2), 199-206.

Metcalfe, D. E., and G. J. Farquhar (1987), Modeling Gas Migration through Unsaturated Soils from Waste-Disposal Sites, *Water Air and Soil Pollution,* 32(1-2), 247-259.

Miller, C. T., G. Christakos, P. T. Imhoff, J. F. McBride, J. A. Pedit, and J. A. Trangenstein (1998), Multiphase flow and transport modeling in heterogeneous porous media: challenges and approaches, *Advances in Water Resources,* 21(2), 77-120.

Miller, C. T., M. M. Poiriermcneill, and A. S. Mayer (1990), Dissolution of Trapped Nonaqueous Phase Liquids - Mass-Transfer Characteristics, *Water Resources Research,* 26(11), 2783-2796.

Millington, R. J., and J. P. Quirk (1961), Permeability of porous solids, *Transactions of the Faraday Society,* 571200-1207.

Mohtar, R. H., R. B. Wallace, and L. J. Segerlind, editors. 1994. Finite Element Simulation of Oil Spill Cleanup Using Air Sparging. Kluwer Academic, Boston.

Molins, S., J. Carrera, C. Ayora, and M. W. Saaltink (2004), A formulation for decoupling components in reactive transport problems, *Water Resources Research,* 40(10), -.

Montgomery, J. H. 2000. Groundwater chemicals desk reference, 3rd edition. CRC Lewis Publishers, Boca Raton.

Mualem, Y. (1976), New Model for Predicting Hydraulic Conductivity of Unsaturated Porous-Media, *Water Resources Research,* 12(3), 513-522.

Mulligan, C. N., and R. N. Yong (2004), Natural attenuation of contaminated soils, *Environment International,* 30(4), 587-601.

Murphy, E. M., and T. R. Ginn (2000), Modeling microbial processes in porous media, *Hydrogeology Journal,* 8(1), 142-158.

Murphy, E. M., T. R. Ginn, A. Chilakapati, C. T. Resch, J. L. Phillips, T. W. Wietsma, and C. M. Spadoni (1997), The influence of physical heterogeneity on microbial degradation and distribution in porous media, *Water Resources Research,* 33(5), 1087-1103.

Murray, W. A., R. C. Lunardini Jr., F. J. Ullo Jr., and M. E. Davidson (2000), Site 5 air sparging pilot test, Naval Air Station Cecil Field, Jacksonville, Florida, *Journal of Hazardous Materials,* 72(2-3), 121-145.

Murray, W. D., and M. Richardson (1993), Progress toward the Biological Treatment of C(1) and C(2) Halogenated Hydrocarbons, *Critical Reviews in Environmental Science and Technology,* 23(3), 195-217.

Nield, D. A., and A. Bejan. 1999. Convection in porous media, 2nd edition. Springer, New York.

Nyer, E. K., and S. S. Suthersan (1993), Air Sparging - Savior of Ground-Water Remediations or Just Blowing Bubbles in the Bath Tub, *Ground Water Monitoring and Remediation,* 13(4), 87-91.

Panday, S., Y. S. Wu, P. S. Huyakorn, and E. P. Springer (1994), A 3-Dimensional Multiphase Flow Model for Assessing Napl Contamination in Porous and Fractured Media .2. Porous-Medium Simulation Examples, *Journal of Contaminant Hydrology,* 16(2), 131-156.

Paniconi, C., and M. Putti (1994), A Comparison of Picard and Newton Iteration in the Numerical-Solution of Multidimensional Variably Saturated Flow Problems, *Water Resources Research,* 30(12), 3357-3374.

Park, E., and H. B. Zhan (2001), Analytical solutions of contaminant transport from finite one-, two-, and three-dimensional sources in a finite-thickness aquifer, *Journal of Contaminant Hydrology,* 53(1-2), 41-61.

Parker, J. C., R. J. Lenhard, and T. Kuppusamy (1987), A Parametric Model for Constitutive Properties Governing Multiphase Flow in Porous-Media, *Water Resources Research,* 23(4), 618-624.

Pavlostathis, S. G., and M. T. Prytula (2000), Kinetics of the sequential microbial reductive dechlorination of hexachlorobenzene, *Environmental Science & Technology,* 34(18), 4001-4009.

Perry, R. H., D. W. Green, and J. O. Maloney. 1984. Perry's Chemical engineers' handbook, 6th edition. McGraw-Hill, New York.

Peterson, J. W., M. J. DeBoer, and K. L. Lake (2000), A laboratory simulation of toluene cleanup by air sparging of water-saturated sands, *Journal of Hazardous Materials,* 72(2-3), 167-178.

Peterson, J. W., P. A. Lepczyk, and K. L. Lake (1999), Effect of sediment size on area of influence during groundwater remediation by air sparging: a laboratory approach, *Environmental Geology,* 38(1), 1-6.

Pfiffner, S. M., A. V. Palumbo, T. J. Phelps, and T. C. Hazen (1997), Effects of nutrient dosing on subsurface methanotrophic populations and trichloroethylene degradation, *Journal of Industrial Microbiology & Biotechnology,* 18(2-3), 204-212.

Philip, J. R. (1998), Full and boundary-layer solutions of the steady air sparging problem, *Journal of Contaminant Hydrology,* 33(3-4), 337-345.

Plummer, C. R., J. D. Nelson, and G. S. Zumwalt (1997), Horizontal and vertical well comparison for in situ air sparging, *Ground Water Monitoring and Remediation,* 17(1), 91-96.

Powers, S. E., C. O. Loureiro, L. M. Abriola, and W. J. Weber (1991), Theoretical-Study of the Significance of Nonequilibrium Dissolution of Nonaqueous Phase Liquid in Subsurface Systems, *Water Resources Research,* 27(4), 463-477.

Rabideau, A. J., J. M. Blayden, and C. Ganguly (1999), Field performance of air sparging system for removing TCE from groundwater, *Environmental Science & Technology,* 33(1), 157-162.

Rathfelder, K., and L. M. Abriola (1994), Mass Conservative Numerical-Solutions of the Head-Based Richards Equation, *Water Resources Research,* 30(9), 2579-2586.

Rathfelder, K. M., J. R. Lang, and L. M. Abriola (2000), A numerical model (MISER) for the simulation of coupled physical, chemical and biological processes in soil vapor extraction and bioventing systems, *Journal of Contaminant Hydrology,* 43(3-4), 239-270.

Reddy, J. N. 1984. An introduction to the finite element method. McGraw-Hill, New York.

Reddy, J. N. 1993. An introduction to the finite element method. McGraw-Hill, New York.

Reddy, K. R., and J. A. Adams (2001), Effects of soil heterogeneity on airflow patterns and hydrocarbon removal during in situ air sparging, *Journal of Geotechnical and Geoenvironmental Engineering,* 127(3), 234-247.

Reid, R. C., J. M. Prausnitz, and B. E. Poling. 1987. The properties of gases and liquids, 4th edition. McGraw-Hill, New York.

Rifai, H. S., C. J. Newell, J. R. Gonzales, and J. T. Wilson (2000), Modeling natural attenuation of fuels with BIOPLUME III, *Journal of Environmental Engineering-Asce,* 126(5), 428-438.

Roosevelt, S. E., and M. Y. Corapcioglu (1998), Air bubble migration in a granular porous medium: Experimental studies, *Water Resources Research,* 34(5), 1131-1142.

Rutherford, K. W., and P. C. Johnson (1996), Effects of process control changes on aquifer oxygenation rates during in situ air sparging in homogeneous aquifers, *Ground Water Monitoring and Remediation,* 16(4), 132-141.

Schaerlaekens, J., D. Mallants, J. Simunek, M. T. van Genuchten, and J. Feyen (1999), Numerical simulation of transport and sequential biodegradation of chlorinated aliphatic hydrocarbons using CHAIN_2D, *Hydrological Processes,* 13(17), 2847-2859.

Schafer, D., R. Kober, and A. Dahmke (2003), Competing TCE and cis-DCE degradation kinetics by zero-valent iron - experimental results and numerical simulation, *Journal of Contaminant Hydrology,* 65(3-4), 183-202.

Schmidt, R., J. Gudbjerg, T. O. Sonnenborg, and K. H. Jensen (2002), Removal of NAPLs from the unsaturated zone using steam: prevention of downward migration by injecting mixtures of steam and air, *Journal of Contaminant Hydrology,* 55(3-4), 233-260.

Schmidt, S. K., S. Simkins, and M. Alexander (1985), Models for the Kinetics of Biodegradation of Organic-Compounds Not Supporting Growth, *Applied and Environmental Microbiology,* 50(2), 323-331.

Schwille, F. 1988. Dense chlorinated solvents in porous and fractured media : model experiments, English language edition. Lewis Publishers, Chelsea, MI.

Sellers, K. 1999. Fundamentals of hazardous waste site remediation. Lewis Publishers, Boca Raton.

Shan, C., and D. B. Stephens (1995), An Analytical Solution for Vertical Transport of Volatile Chemicals in the Vadose Zone, *Journal of Contaminant Hydrology,* 18(4), 259-277.

She, H. Y., and B. E. Sleep (1999), Removal of perchloroethylene from a layered soil system by steam flushing, *Ground Water Monitoring and Remediation,* 19(2), 70-77.

Shoemaker, C. A., T. B. Culver, L. W. Lion, and M. G. Peterson (1990), Analytical Models of the Impact of 2-Phase Sorption on Subsurface Transport of Volatile Chemicals, *Water Resources Research,* 26(4), 745-758.

Singh, H., F. E. Loffler, and B. Z. Fathepure (2004), Aerobic biodegradation of vinyl chloride by a highly enriched mixed culture, *Biodegradation,* 15(3), 197-204.

Sleep, B. E., and J. F. Sykes (1989), Modeling the Transport of Volatile Organics in Variably Saturated Media, *Water Resources Research | Water Resour. Res. | Water Resour Res,* 25(1), 81-92.

Smith, J. A., A. K. Tisdale, and H. J. Cho (1996), Quantification of natural vapor fluxes of trichloroethene in the unsaturated zone at Picatinny Arsenal, New Jersey, *Environmental Science & Technology,* 30(7), 2243-2250.

Smith, L. H., P. K. Kitanidis, and P. L. McCarty (1997), Numerical modeling and uncertainties in rate coefficients for methane utilization and TCE cometabolism by a methane-oxidizing mixed culture, *Biotechnology and Bioengineering,* 53(3), 320-331.

Smith, L. H., and P. L. McCarty (1997), Laboratory evaluation of a two-stage treatment system for TCE cometabolism by a methane-oxidizing mixed culture, *Biotechnology and Bioengineering,* 55(4), 650-659.

Solley, W. B., R. R. Perce, and H. A. Perlman. 1998. Estimated use of water in the united states in 1995. U.S. Dept. of the Interior Information Services [distributor], Reston, Va.

Srivastava, R., and T. C. J. Yeh (1992), A 3-Dimensional Numerical-Model for Water-Flow and Transport of Chemically Reactive Solute through Porous-Media under Variably Saturated Conditions, *Advances in Water Resources,* 15(5), 275-287.

Stone, H. L. (1970), Probability Model for Estimating 3-Phase Relative Permeability, *Journal of Petroleum Technology,* 22214-&.

Sun, Y., J. N. Petersen, and T. P. Clement (1999a), Analytical solutions for multiple species reactive transport in multiple dimensions, *Journal of Contaminant Hydrology,* 35(4), 429-440.

Sun, Y., J. N. Petersen, T. P. Clement, and R. S. Skeen (1999b), Development of analytical solutions for multispecies transport with serial and parallel reactions, *Water Resources Research,* 35(1), 185-190.

Suna, Y., J. N. Petersen, and J. Bearc (2001), Successive identification of biodegradation rates for multiple sequentially reactive contaminants in groundwater, *Journal of Contaminant Hydrology,* 51(1-2), 83-95.

Thibodeaux, L. J. (1981), Estimating the Air Emissions of Chemicals from Hazardous-Waste Landfills, *Journal of Hazardous Materials,* 4(3), 235-244.

Thomson, N. R., and R. L. Johnson (2000), Air distribution during in situ air sparging: an overview of mathematical modeling, *Journal of Hazardous Materials,* 72(2-3), 265-282.

Thomson, N. R., J. F. Sykes, and D. Van Vliet (1997), A numerical investigation into factors affecting gas and aqueous phase plumes in the subsurface, *Journal of Contaminant Hydrology,* 28(1-2), 39-70.

Travis, B. J., and N. D. Rosenberg (1997), Modeling in situ bioremediation of TCE at Savannah River: Effects of product toxicity and microbial interactions on TCE degradation, *Environmental Science & Technology,* 31(11), 3093-3102.

Tripathi, V. S., and G. T. Yeh (1993), A Performance Comparison of Scalar, Vector, and Concurrent Vector Computers Including Supercomputers for Modeling Transport

of Reactive Contaminants in Groundwater, *Water Resources Research,* 29(6), 1819-1823.

Unger, A. J. A., E. A. Sudicky, and P. A. Forsyth (1995), Mechanisms Controlling Vacuum Extraction Coupled with Air Sparging for Remediation of Heterogeneous Formations Contaminated by Dense Nonaqueous Phase Liquids, *Water Resources Research,* 31(8), 1913-1925.

USACE. 1995. Soil Vapor Extraction and Bioventing, EM 1110-1-4001. US Army Corps of Engineers, Department of Army, Washington, DC.

van Dijke, M. I. J., and S. E. A. T. M. van der Zee (1998), Modeling of air sparging in a layered soil: Numerical and analytical approximations, *Water Resources Research,* 34(3), 341-353.

van Dijke, M. I. J., S. E. A. T. M. van der Zee, and C. J. van Duijn (1995), Multiphase Flow Modeling of Air Sparging, *Advances in Water Resources,* 18(6), 319-333.

van Genuchten, M. T. (1980), A Closed-Form Equation for Predicting the Hydraulic Conductivity of Unsaturated Soils, *Soil Science Society of America Journal,* 44(5), 892-898.

Verce, M. F., and D. L. Freedman (2000), Modeling the kinetics of vinyl chloride cometabolism by an ethane-grown Pseudomonas sp., *Biotechnology and Bioengineering,* 71(4), 274-285.

Verce, M. F., C. K. Gunsch, A. S. Danko, and D. L. Freedman (2002), Cometabolism of cis-1,2-dichloroethene by aerobic cultures grown on vinyl chloride as the primary substrate, *Environmental Science & Technology,* 36(10), 2171-2177.

Vogel, T. M., C. S. Criddle, and P. L. McCarty (1987), Transformations of Halogenated Aliphatic-Compounds, *Environmental Science & Technology,* 21(8), 722-736.

Vogel, T. M., and P. L. McCarty (1985), Biotransformation of Tetrachloroethylene to Trichloroethylene, Dichloroethylene, Vinyl-Chloride, and Carbon-Dioxide under Methanogenic Conditions, *Applied and Environmental Microbiology | Appl. Environ. Microb.,* 49(5), 1080-1083.

Weber, W. J., and F. A. DiGiano. 1996. Process dynamics in environmental systems. Wiley, New York.

Weeks, E. P., D. E. Earp, and G. M. Thompson (1982), Use of Atmospheric Fluorocarbons F-11 and F-12 to Determine the Diffusion Parameters of the Unsaturated Zone in the Southern High-Plains of Texas, *Water Resources Research,* 18(5), 1365-1378.

Werth, C. J., and M. Reinhard (1997), Effects of temperature on trichloroethylene desorption from silica gel and natural sediments. 1. Isotherms, *Environmental Science & Technology,* 31(3), 689-696.

Wexler, E. J. 1992. Analytical solution for one-, two-, and three-dimensional solute transport in ground-water systems with uniform flow supplemental report : source codes for computer programs and sample data sets. Geological Survey (U.S.), Denver, CO.

Wiedemeier, T. H. 1998. Technical protocol for evaluating natural attenuation of chlorinated solvents in ground water. National Risk Management Research Laboratory Office of Research and Development, Cincinnati, Ohio.

Wiedemeier, T. H. 1999. Technical protocol for evaluating natural attenuation of chlorinated solvents in ground water. National Risk Management Research Laboratory Office of Research and Development, Cincinnati, Ohio.

Wiener, A. 1972. The role of water in development. McGraw-Hill, New York,.

Wilkins, M. D., L. M. Abriola, and K. D. Pennell (1995), An Experimental Investigation of Rate-Limited Nonaqueous Phase Liquid Volatilization in Unsaturated Porous-Media - Steady-State Mass-Transfer, *Water Resources Research,* 31(9), 2159-2172.

Wilson, D. J. (1992), Groundwater Cleanup by Insitu Sparging .2. Modeling of Dissolved Volatile Organic-Compound Removal, *Separation Science and Technology,* 27(13), 1675-1690.

Wilson, D. J. 1995. Modeling of in situ techniques for treatment of contaminated soils : soil vapor extraction, sparging, and bioventing. Technomic, Lancaster, Pa.

Wilson, D. J., C. Gomezlahoz, and J. M. Rodriguezmaroto (1994), Groundwater Cleanup by in-Situ Sparging .8. Effect of Air Channeling on Dissolved Volatile Organic-Compounds Removal Efficiency, *Separation Science and Technology,* 29(18), 2387-2418.

Witt, M. E., G. M. Klecka, E. J. Lutz, T. A. Ei, N. R. Grosso, and F. H. Chapelle (2002), Natural attenuation of chlorinated solvents at Area 6, Dover Air Force Base: groundwater biogeochemistry, *Journal of Contaminant Hydrology,* 57(1-2), 61-80.

Wu, C., and J. Schaum. 2001. Sources, emission, and exposure for trichloroethylene (TCE) and related chemicals. *in*. National Center for Environmental Assessment--Washington Office Office of Research and Development U.S. Environmental Protection Agency, Washington, DC.

Wu, W. M., J. Nye, M. K. Jain, and R. F. Hickey (1998), Anaerobic dechlorination of trichloroethylene (TCE) to ethylene using complex organic materials, *Water Research,* 32(5), 1445-1454.

Yaron, B., G. Dagan, and J. Goldshmid. 1984. Pollutants in porous media : the unsaturated zone between soil surface and groundwater. Springer-Verlag, Berlin ; New York.

Yaws, C. L. 1999. Chemical properties handbook : physical, thermodynamic, environmental, transport, safety, and health related properties for organic and inorganic chemicals. McGraw-Hill, New York.

Yaws, C. L., and W. Braker. 2001. Matheson gas data book, 7th edition. Matheson Tri-Gas, Parsippany, NJ.

Yeh, G. T. (1981a), On the Computation of Darcian Velocity and Mass Balance in the Finite-Element Modeling of Groundwater-Flow, *Water Resources Research | Water Resour. Res. | Water Resour Res,* 17(5), 1529-1534.

Yeh, G. T. (1981b), On the Computation of Darcian Velocity and Mass Balance in the Finite-Element Modeling of Groundwater-Flow, *Water Resources Research,* 17(5), 1529-1534.

Yeh, G. T., and V. S. Tripathi (1989), A Critical-Evaluation of Recent Developments in Hydrogeochemical Transport Models of Reactive Multichemical Components, *Water Resources Research,* 25(1), 93-108.

Yeh, G. T., and V. S. Tripathi (1991), A Model for Simulating Transport of Reactive Multispecies Components - Model Development and Demonstration, *Water Resources Research,* 27(12), 3075-3094.

Yeh, T. C. J., R. Srivastava, A. Guzman, and T. Harter (1993), A Numerical-Model for Water-Flow and Chemical-Transport in Variably Saturated Porous-Media, *Ground Water,* 31(4), 634-644.

Yu, S. H., M. E. Dolan, and L. Semprini (2005), Kinetics and inhibition of reductive dechlorination of chlorinated ethylenes by two different mixed cultures, *Environmental Science & Technology,* 39(1), 195-205.

Zienkiewicz, O. C., and R. L. Taylor. 1989. The finite element method, 4th edition. McGraw-Hill, London ; New York.

VITA

Wonyong Jang was born in Chinju, South Korea. He received his bachelor's degree in Environmental Engineering from Pusan National University, South Korea in 1993, and obtained a Master of Science degree in Environmental Engineering from Korea Advanced Institute of Science and Technology in 1995. After receiving his master degree, from 1995 to 1998 he worked for Research Institute of Technology, Samsung Construction and Engineering in Seoul, Korea as a research assistant. He participated in research projects involving landfills and contaminated site remediation. From 1998 to 1999, he worked as a researcher for Institute of Advanced Technology, Anyang University, Korea. He conducted research studies involving remedial technologies (in-situ air sparing and soil vacuum extraction) at petroleum-contaminated sites. In January 2000, he started his Ph.D. degree program in School of Civil and Environmental Engineering at Georgia Institute of Technology and received his Master of Science from the same school in December 2002. His research interests are on multiple phase flow, fate and transport of contaminants, and transport of thermal energy in subsurface systems.